Ice sheets, oceanic circulation & sea surface conditions: the NW European margin during the last 35,000 years

Lukas W.M. Becker

Thesis for the Degree of Philosophiae Doctor (PhD)
University of Bergen, Norway
2018

UNIVERSITY OF BERGEN

Ice sheets, oceanic circulation & sea surface conditions: the NW European margin during the last 35,000 years

Lukas W.M. Becker

Thesis for the Degree of Philosophiae Doctor (PhD)
at the University of Bergen

2018

Date of defence: 20.04.2018

Year: 2018

Title: Ice sheets, oceanic circulation & sea surface conditions: the NW European margin during the last 35,000 years

Name: Lukas W.M. Becker

Print: Skipnes Kommunikasjon / University of Bergen

"Through endurance we conquer."

Ernest Shackelton, polar explorer (1875 - 1922)

Scientific environment

The research leading to this dissertation was carried out at the Department of Earth Science, University of Bergen (UoB), Norway, between October 2013 and November 2017. This thesis was funded through a scholarship at the UoB (Stipendiat stilling) and, as an associated researcher, this PhD was linked to and received additional funding from the Initial Training Network GLANAM (GLAciated North Atlantic Margins). The project GLANAM (www.glanam.org) was itself funded through the People Programme (Marie Curie Actions) of the European Union's Seventh Framework Program FP7/2007-2013 under REA grant agreement no. 317217. Further funding was provided by the climate research schools ResClim and CHESS and "det alminnelige naturvitenskapelige forsknings fond" at the UoB. The supervisory committee consisted of Hans Petter Sejrup as the main-supervisor and the co-supervisors Berit O. Hjelstuen and Haflidi Haflidason, all based at the UoB.

Acknowledgements

First and foremost, I would like to sincerely thank my supervisors for their continuous support, near constant availability and knowledgeable input throughout the various stages of the projects. Especially Hans Petter, for his supervision, oversight and ideas during the early stages of the projects, his patience to look at "yet another" age model, his critical comments on paper drafts and the significant input during the writing process. Berit, for her detailed input on paper manuscripts, her critical eye on text structure, the preparation of seismic lines and for writing Paper III. Haflidi, for the hours of tephra counting he put into this project, the in-detail discussions of figures and the support during core description and bulk element scanning.

Furthermore, I would like to thank the Quaternary Earth Systems group at the UoB. Particularly, I thank Vigdis for the countless hours of counting and picking foraminifera, Eivind, Ulysses and Jostein for technical support and discussions. Dag Inge Blindheim for the time he spent counting ice rafted debris and for his consent to take part in the fight man versus machine, within the methodological study. In addition, I am truly thankful for the discussions, help and support that I got from my friends and fellow early-career researchers within the department, especially Benedict Reinardy, Benjamin Bellwald, Björn Morén, Jens Karstens, Nicklas Meinecke, Lisa Griem, Eoghan Reeves, Thomas Leutert, Johannes Werner, Willem van der Bilt, Anna Hughes, Fanny Ekblom Johansson, Torgeir Opeland Røthe, Tobias Zolles and Alexios Theofilopoulos. Hanno Kinkel, James Scourse, Alistair Seddon, Ulf Willén, G. Hansen, Andreas J.-G. Becker, Jannicke Kuvås, Johannes Wiest and Tobias Schwestermann are acknowledged for their laboratory help, advice and knowledge transfer.

Moreover, I would like to mention the GLANAM fellows, especially Riccardo Arosio, Elena Grimoldi, and Dimitrios Kteñas, who have made the annual GLANAM meetings and workshops to what they were.

Additionally, I am grateful for my old friends Simon Jost, Hjalmar Gienger, Ana Lucia Kempe, Nora Dunker and Wilhelm Brasch for being there when they are needed.

Finally, BSI Seiling, the UoBs' student sailing club, and all the people that come with it, particularly Vegard Guttormsen and Manuel Hempel, are thanked for providing

numerous options of distractions and for constantly reminding me that there is more to it then science.

However, none of the work would have been possible without the support and love from my parents, siblings and specifically Julie and our daughter Élise. I know, this was not always easy, something that I will be forever grateful for.

Abstract

The north-western European continental margin provides a key area for detailed investigations of changes within the inflow of Atlantic warm surface currents, fluctuations in continental ice sheets and the corresponding influence on sea surface conditions, such as (near) sea surface temperature and primary productivity. Knowledge of these fluctuations and forcing mechanisms is crucial to further our understanding of present day climate changes. This dissertation is principally based on continental slope cores, combined with shallow seismic lines and instrumentally measured data. The studied time interval is twofold, the last glacial cycle (35,000 - 15,000 years BP) and the mid- and late Holocene (the last 8000 years). During the last glacial cycle, the north-western European margin was exposed to the advancing and retreating continental ice sheets, resulting in thick glacial, hemipelagic deposits on the continental slope that provide a continuous sedimentary archive of ice sheet build-up, maximum and decay. In contrast, the mid- and late Holocene encompassed relatively stable climatic conditions, with unusually high accumulation rates on the mid-Norwegian margin, allowing for a high-resolution analysis of the regional sea surface conditions. In addition, this dissertation presents a new automated procedure for counting ice rafted debris (IRD), providing a faster, more precise alternative method compared to the current manual counting technique utilised by numerous palaeo-environmental studies. The multi-proxy approach of this thesis was achieved through a set of different analytical techniques, ranging from X-ray fluorescence core scanning, to grain size analysis and foraminifera assemblage counts to numerical analysis and seismic interpretation. The complex ice-ocean interaction along the NW European continental margin during the last glacial cycle and the more recent oceanographic changes observed in the Holocene are chronologically constrained through numerous new and published radiocarbon and $^{210}Pb/^{137}Cs$ dated samples and the identification of Icelandic tephra events, which were used as input parameters for Bayesian age modelling. The main results of the sedimentological and micro-palaeontological analysis indicate, that the proposed confluence of the British-Irish and the Fennoscandian ice sheets during the last glacial cycle, was likely later and shorter than previously anticipated, between

25.5 and 18.7 ka BP. Furthermore, the data indicated that the Norwegian Channel Ice Stream might have only been active between 23.3 and 19 ka BP. Moreover, the results, supported through seismic interpretations from the central North Sea, showed evidence of a glacial outburst flood, connected to the break-up of the ice sheet confluence. The distal deposits of this event, an ultra-rapidly deposited meltwater plume dated to 18.7 ka BP, were additionally investigated through numerical modelling, indicating a significant influence of ultra-rapid sedimentation on the gas hydrate stability zone. Within the mid- and late Holocene, the results of this dissertation demonstrate a strong link between relative calcium content and primary production, suggesting that high-resolution calcium data can be used as a relative productivity proxy within the south-eastern Nordic Seas. Finally, cross-correlation efforts found that the primary production in the region is inversely linked to the North Atlantic Oscillation, which might indicate that this link can be used for NAO reconstructions.

List of publications

Paper I

Becker, L.W.M., Hjelstuen, B.O., Støren, E.W.N. and Sejrup, H.P., 2017. Automated counting of sand-sized particles in marine records. Sedimentology. doi: 10.1111/sed.12407

Paper II

Becker, L.W.M., Sejrup, H.P., Hjelstuen, B.O., Haflidason, H. and Dokken, M., 2017. Ocean-ice sheet interaction along the SE Nordic Seas margin from 35 - 15 ka BP. Marine Geology (GLANAM Special Issue).
http://dx.doi.org/10.1016/j.margeo.2017.09.003

Paper III

Hjelstuen, B.O., Sejrup, H.P., Valvik, E., Becker, L.W.M., In Press. Evidence of an ice-dammed lake outburst in the North Sea during the last deglaciation. Marine Geology (GLANAM Special Issue). https://doi.org/10.1016/j.margeo.2017.11.021

Paper IV

Karstens, J., Haflidason, H., Becker, L.W.M., Berndt, C., Rüpke, L., Planke, S., Liebetrau, V., Schmidt, M., Mienert, J., In Press. Glacigenic sedimentation pulses triggered post-glacial gas hydrate dissociation. Nature communications.

Paper V

Becker, L.W.M., Sejrup, H.P., Hjelstuen, B., Haflidason, H., Kjennbakken, H., Werner, J., in prep. Holocene primary productivity fluctuations in the SE Nordic Seas. To be submitted to Paleoceanography.

Contents

Introduction

Rationale

The research within this dissertation is based on the analysis and interpretation of marine sediment archives, recovered from the south-eastern Nordic Seas. The records generally span from the instrumental time period, the last 50 years, to beyond the Last Glacial Maximum (35,000 years). The north-western European continental margin provides a stratigraphic archive of (1) changes in the inflow strength and the extent of the warm North Atlantic surface waters, entering the Nordic Seas, and (2) the variability of the last, marine-based section of the continental north-western European ice sheets. Marine sedimentary archives of the region have the advantage of being primarily continuously deposited and yet have sufficiently high resolution to resolve short lasting climatic events. The overarching reasoning behind this thesis is therefore to use such continuously deposited, high-resolution sediment archives to reconstruct climatic changes within the last 35,000 years on the north-western European continental margin. Two time frames are focused on, the transition through full glacial conditions of the last European glaciation and the comparatively steady conditions of the middle and late Holocene. The results of these studies provide input and validation parameters for ice sheet and climate models, to enable understanding of the complex interplay between oceanographic, terrestrial and atmospheric forcing parameters.

A large part of the initial work of this thesis was to find, sort, quality control and compile geological data that was acquired between the years 2000 and 2013 by various people. Some of this data was already published elsewhere, while some was hitherto unused. Additionally, various new analyses were performed on selected marine sediment cores, increasing the sampling resolution or adding new parameters. This lab-based part of the thesis benefitted greatly from easy access to the newly established EARTHLAB wet-sediment facilities (http://www.uib.no/en/BGF/EARTHLAB) at the Department of Earth Science at the UoB.

Finally, from an educational and career perspective, the PhD candidate benefitted from being an associated researcher within the GLANAM Initial Training Network (ITN). As part of an ITN, several transferrable skills courses were offered by GLANAM to all fellows and associated researchers, which addressed future challenges of Early Stage Researchers on the job market and highlighted opportunities of industry collaboration.

Study area

The study sites of this PhD thesis are all located on the north-western European continental margin, with slightly differing geographic focus (Figs. 1A and 1B). The bathymetry of the NW European continental margin is dominated by a drop-off along the continental slope, where water depths increase from around 400 m below sea level (bsl) to over 1000 m bsl (Fig. 1A). The Weichselian and Holocene deposits on the continental slope are primarily composed of hemipelagic sediments (Sejrup et al., 1981; Sejrup et al., 2005), interrupted by numerous glacial debris flows (Lekens et al., 2005; Nygård et al., 2007), deposited during times when the ice sheet was extending to the shelf edge. On the mid-Norwegian margin, a large submarine slide scar erodes into the continental slope and provides evidence of the Storegga slide event, dated to about 8000 years BP (Haflidason et al., 2005). East and south of the continental margin, depths on the continental shelf are relatively constant and shallow (100 - 400 m bsl), with the exception of the Norwegian Channel. The Norwegian Channel is an approximately 850 km long morphological feature, that is 70-150 km wide and 280-700 m deep (Rise et al., 2008). Studies found the morphology of the Norwegian Channel to be mainly the result of repeated periods of ice streaming of the Norwegian Channel Ice Stream (NCIS) within the last 1.1 million years (Sejrup et al., 2003; Nygård et al., 2005; Reinardy et al., 2017).

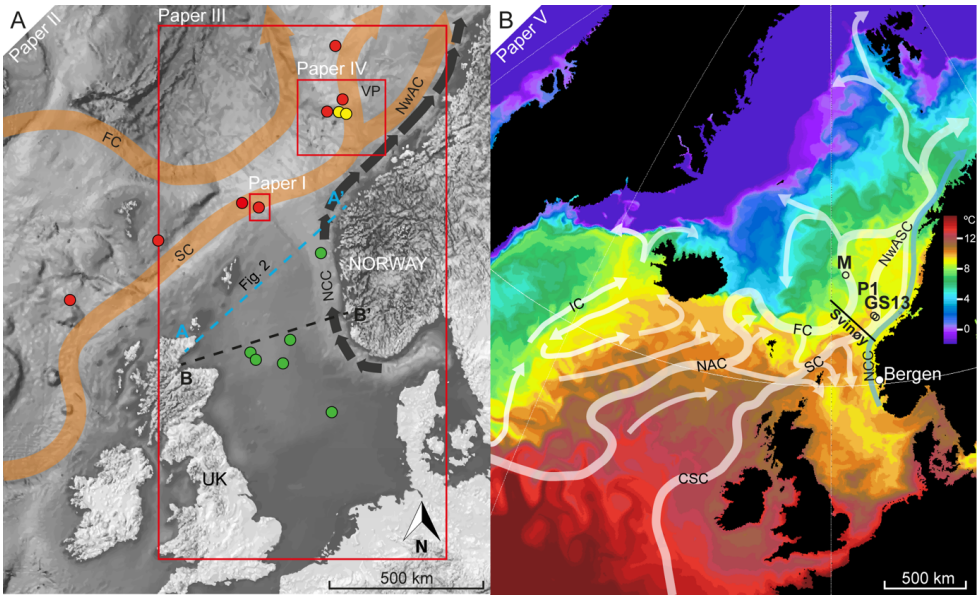

Fig. 1: Overview of the different study areas within the south-eastern Nordic Seas. (A) Location map of sediment cores presented in paper 2 (studied cores in red, reference cores in blue and marked as X1 and X2). For details see paper 2. The red triangles indicate specific study sites for paper 1, 3 and 4. Indicated (B) The investigated area of paper 5, with indicated modern surface currents as in (A), based on Hansen and Østerhus (2000). Continental Slope Current (CSC), North Atlantic Current (NAC), Farøe Current (FC), Slope Current (SC), Norwegian Atlantic Slope Current (NwASC), Norwegian Coastal Current (NCC), Irminger Current (IC). Background image denotes an early summer, daily mean SST field from the UK's Natural Environment Research Council's 1/12th degree, NEMO-based, ocean-only model courtesy of Dr. A.C. Coward from the National Oceanography Centre, Southampton.

For a large part of the last 35,000 years, the north-western European margin and its adjacent landmasses were under the influence of continental ice sheets (Paper I and II). Combined, these ice sheets were termed the Eurasian Ice Sheet (EIS) and consisted of the Fennoscandian (FIS), the British-Irish (BIIS) and the Barents Kara Ice Sheet. During maximum glacial extension, a large proportion of these ice sheets were marine-based

(Sejrup et al., 2005; Lee et al., 2012; Hughes et al., 2015). In terms of glacial dynamics forcing, the large marine-based fraction and the location of the EIS made it particularly vulnerable to changes in oceanographic conditions (Peck et al., 2006; Joughin et al., 2012). The inflow strength of the Atlantic Meridional Overturning Circulation and with it the changes in warm Atlantic surface water influx are proposed to have had an influence on glacial dynamics of the EIS (e.g. Rørvik et al., 2010) and vice versa (e.g. Alvarez-Solas et al., 2011) - Paper II.

The modern surface circulation in the investigated region is characterised by the inflow of warm Atlantic water, the branch of the Atlantic Meridional Overturning Circulation that enters the Nordic Seas via the Iceland - Scotland ridge. Most of the water enters through the Faroe-Shetland Channel as the North Atlantic Current (NAC), and flows northwards in two branches, the Faroe Current and the Shetland Current, summarised as the Norwegian Atlantic Current (NwAC) (Mork and Skagseth, 2010). The eastern branch, the Norwegian Atlantic Slope Current (NwASC), is a barotrophic current and passes over the Vøring Plateau (Fig. 1A), while the topographically confined western branch, the Norwegian Atlantic Front Current (NwAFC) is deflected around the perimeters of the Vøring Plateau (Hansen and Østerhus, 2000). Salinities of 35.0 - 35.3 psu and temperatures of around 5-10 ºC commonly define the Atlantic surface waters in the investigated region (Orvik et al., 2001), transporting in total 5.1±0.3 Sv northwards (Mork and Skagseth, 2010). To the east of the Atlantic surface waters, a less saline, coastal current flows northwards along the Norwegian coastline, the Norwegian Coastal Current (NCC). This current has large seasonal variations driven by terrestrial freshwater runoff and changes in wind directions, where prevailing northerly winds are proposed to lead to a westward extension during the summer months (Nilsen and Falck, 2006). During the last glacial cycle, the surface currents are thought to have followed a generally similar pattern, however, studies suggest variable position, speed and depth of the NAC (Rasmussen and Thomsen, 2008; Montelli et al., in press), comprising of sluggish speeds during stadials and increased flow speed during interstadials (Kissel et al., 1998; Dahlgren and Vorren, 2003). On the mid-Norwegian margin, evidence suggests, that the speed of the NAC is low immediately before the Last Glacial Maximum, while it increases when the ice sheet has reached the continental

shelf edge during the Last Glacial Maximum and is strongest at the onset of the last deglaciation (Dahlgren and Vorren, 2003).

While the maximum extent of the marine-based fraction of the EIS was confined by numerous studies (i.e. Dahlgren and Vorren, 2003; Sejrup et al., 2005; Clark et al., 2012; Hughes et al., 2015; Ottesen et al., 2016), the proposed timing and dynamics of build-up and deglaciation have a wide range of interpretations. A major part of the marine-based fraction of the EIS covered the central North Sea, connecting the FIS and the BIIS (Paper II). The central North Sea is a good example of the complexity of reconstructing marine-based ice sheet build-up and deglaciation history. Multiple evidences suggests the timing of the first offshore advance of the FIS and the BIIS to after the Ålesund interstadial at around 29 ka BP (Mangerud et al., 2003; Scourse et al., 2009; Clark et al., 2012), however, the timing and the dynamics of a possible confluence of both ice sheets is more challenging. The timing of the confluence was, until recently, generally accepted to be between 31 and 24 ka BP (Sejrup et al., 1994; Bradwell et al., 2008; Ehlers and Gibbard, 2008; Sejrup et al., 2009; Toucanne et al., 2010; Sejrup et al., 2015), but new evidence suggests to move the timing of confluence should be moved to before 23 ka BP until separation at around 18.5 ka BP (Sejrup et al., 2016). The authors suggest, that the separation of the FIS and the BIIS was initiated through 500 years of speed up in ice streaming through the NCIS, which resulted in a draw down and a thinning of the ice sheet in the central North Sea. Furthermore, the authors proposed, that the imminent separation followed at 18.5 ka BP through a collapse of the ice dam at the so-called Ling Bank drainage channel, holding back an ice-dammed lake on the southern ice margin (Paper III). North of the trough mouth of the Norwegian Channel, on the southern Vøring Plateau (Fig. 1A), an acoustically transparent unit, interpreted as a meltwater plume, was mapped by Hjelstuen et al. (2004) and later described in several studies (Lekens et al., 2005; Reiche et al., 2011) and in Paper II. This suspension plume is believed to originate from a point source in the direction of the Norwegian Channel (Lekens et al., 2005) and was likely deposited within only centuries. Paper III adds new detail to this. At the surface, on the southern Vøring Plateau, several hundreds of seafloor depressions, termed the Nyegga pockmark field (Vaular et al., 2010), mark the major gas hydrate province beneath the mentioned suspension plume. Studies found,

that the gas hydrate field also extends south, beneath the Storegga slide scar (Bünz et al., 2003), with the suspension plume having an important influence on the gas hydrate and slope stability (Paper IV).

Finally, during the Holocene, after the Storegga slide event, some basins within the Storegga slide scar (Fig. 1B) acted as a sediment trap due to the slide scar topography, resulting in thick, hemipelagic deposits of up to 25 m (Haflidason et al., 2005). The high accumulation rates combined with the favourable position, directly beneath the inflow of the NwASC and occasionally the NCC make this location an ideal study area for high-frequency, mid- and late Holocene climatic variabilities (Paper V).

Database and approach

The research within this thesis is primarily based on sedimentary, geochemical and micro-palaeontological data obtained from sediment cores recovered within the IMAGES V campaign aboard the R/V Marion-Dufresne in 1999 (Labeyrie et al., 1999) and within a UoB cruise aboard R/V G.O. SARS in 2013 (Hjelstuen et al., 2013). This data is combined with numerous other cores within the region, taken on earlier cruises. Furthermore, this data was combined with high-resolution, shallow seismic data and bathymetric images.

Sediment cores and sediment analysis

The database of this PhD thesis builds in the first place upon a compilation of published and un-published data acquired by several researchers, PhD and MSc students at the UoB within the last 18 years (Dokken and Jansen, 1999; Berstad, 2003; Haflidason et al., 2003; Hjelstuen et al., 2004; Lekens et al., 2005; Lekens et al., 2006; Rasmussen and Thomsen, 2008; Scourse et al., 2009; Brendryen et al., 2011; Hall et al., 2011; Risebrobakken et al., 2011; Dokken et al., 2013; Dokken et al., 2015b; Dokken et al., 2015a). Where possible, this data was quality checked, recalculated, partly re-analysed and at specific locations supplemented with additional measurements.

In total 48 m of sediment cores (the upper 15 m of MD99-2283 and MD99-2289 and the complete core GS13-182-01CC) were evaluated and scanned for their bulk elemental composition with the Itrax X-ray fluorescence (XRF) core scanner from COX Analytical Systems at the UoB (Paper II and V). All sections of core MD99-2283 were re-scanned, the same as two sections of MD99-2289, as they were already previously scanned in lower resolution (2 cm). Core GS13-182-01CC was scanned immediately after splitting, which revealed interesting oxidation features (Fig. 2). All runs were performed with the molybdenum X-ray tube with a resolution of 500 µm, while letting the cores warm up to room temperature prior to analysis. This non-destructive analysis results in semi-quantitative elemental counts, but the counts can be affected by various sediment parameters, like grain-size, water content or density (Croudace et al., 2006).

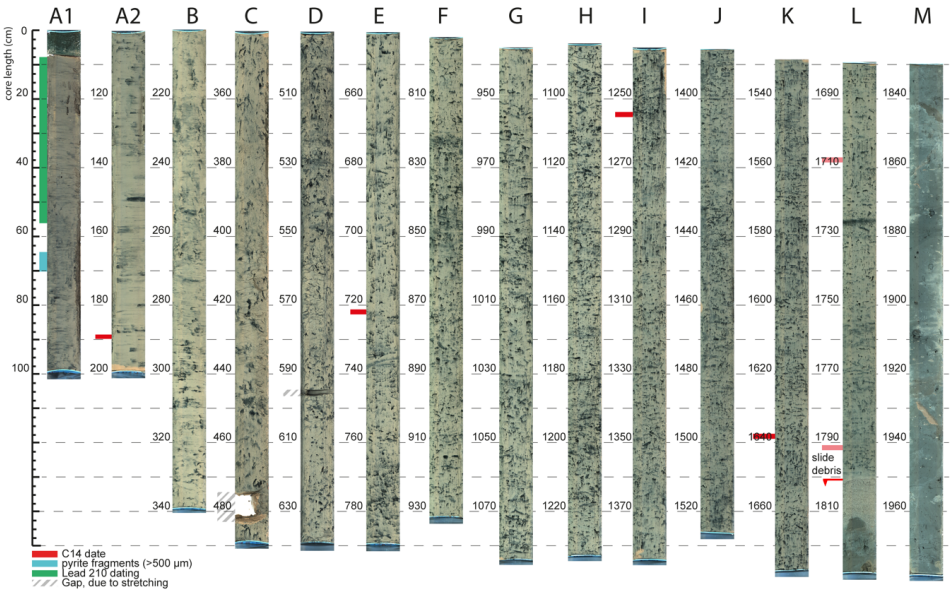

Fig. 2: Example of one sediment core, in this case GS13-182-01CC, used in Paper V. The sediment core was sliced in two halves and subsequently photographed using the ITRAX core scanner. The black oxidations vanish after a few hours and leave continuous, grey marine sediment. The lowermost section penetrated into the slide debris of the Storegga slide scar, as did the second last section, where a sorted fine sand layer overlies the slide debris. This image depicts the quality of recovered

material, with apparent continuous accumulation and only two gaps due to stretching during recovery. Coloured bars mark dated levels and specific finds.

To obtain information of changes in the type of accumulated sediment, high-resolution grain-size analysis of the sand fraction was performed with manual wet sieving every 0.5 cm for the first two meters and every 5 cm for the remainder of core GS13-182-01CC, resulting in approximately 720 samples (Paper V). Additionally to existing data, some grain-size analysis was performed on core MD99-2283, to increase the sampling resolution at critical depths (Paper I and II). The acquired sediment fractions could then be used for further analysis, such as counting of Ice Rafted Debris (IRD), foraminifera assemblages and radiocarbon dating of micro-fossils. A new, automated method was developed to make the classic method of manual IRD counting quicker, more comparable and less subjective (Paper I). About 350 samples of core MD99-2283 and MD99-2284 were counted with this new method (Paper I and II). New, additional and re-counting of the planktonic foraminiferal assemblage was carried out on cores MD99-2283, MD99-2289, MD99-2284 (Paper I and II) and on core GS13-182-01CC (presented elsewhere).

Finally, several statistical tools were used to smooth, filter and disentangle the information contained in the high-resolution datasets. Among those are the 'Stats' package (v.3.5.0) in R, the signal processing toolbox of MATLAB® (2016b, The MathWorks, Natick, MA, USA) and the jLab toolbox (v. 1.6.5) for data analysis (Lilly, 2017).

Age modelling

The base of all work with sediment records is to establish time control on the acquired archive. The approach of age model construction is crucial to be able to compare the event synchronicity between time series. A suite of different methods is currently being used in the marine realm, offering differing solutions. Most commonly benthic or planktonic foraminifera are Accelerator Mass Spectrometry (AMS) ^{14}C dated, while assuming or calculating a certain local marine reservoir effect correction (∂R). The local reservoir effect describes the age offset between terrestrial and marine carbon accumulation relative to the ^{14}C production rate. The carbon in the marine realm is inherently older, due to the slower carbon exchange of the oceans and the atmosphere, compared to the terrestrial environment. However, the size and variability of the local reservoir effect is debated with a wide spread of estimations, from 100 to 1700 years (e.g. Haflidason et al., 1995; Sejrup et al., 2010; Hall et al., 2011; 2011; Sarnthein et al., 2015a). Furthermore, the local reservoir effect is not constant through time. Additionally, some radiocarbon age models are tuned to stadial - interstadial changes in Greenland ice cores by using relative temperature changes indicated by concentration of the planktonic foraminifera species *N. pachyderma* sinistral (e.g. Scourse et al., 2009; Crocker et al., 2016; Rasmussen et al., 2016). Alternatively, others tuned the starting point of peaks of the anhysteretic remanent magnetization (ARM) or magnetic susceptibility (MS) with the initiation of Greenland interstadials (e.g. Dokken et al., 2013; Wary et al., 2016). However, the ARM/MS tuning is challenging at some locations, with highly variable sediment flux proximal to the shelf edge. Tephra ash layers or magnetic reversals are used as additional absolute tie-point support. Finally, precise dating of the last approximately 70 years can be done through $^{210}Pb/^{137}Cs$ dating of bulk sediment samples. Based on the assumption, that the core top represents the time of sampling, accumulation rates can be calculated. This can be confirmed and supported through spikes in the ^{137}Cs curve, evidencing known events of atomic radiation release (first atomic bomb tests, catastrophic nuclear accidents like in Chernobyl 1985 or the unfiltered release of ^{137}Cs rich cooling water into the North Atlantic, as happened at Sellafield, 1979).

One important factor of age model difference is the way of construction, that is, the degree of subjectiveness, ranging from high subjectiveness within a linear or a polynomial fit through all dated levels (e.g. Lekens et al., 2009), to little subjectiveness in Bayesian age modelling (Blaauw and Christen, 2011). Within this thesis, a range of these age modelling techniques was experimented with, but the best and most robust results were achieved by using the Bayesian age modelling tool "Bacon" (v.2.2), an R-based script written by Blaauw et al. (2011).

The input for the age models run with Bacon, that were then used as the base of the presented Papers II-V is a collection of about 250 AMS ^{14}C ages in total, with 37 of those newly presented within this thesis. The AMS ^{14}C dated samples were mainly picked from the planktonic foraminifera *N. pachyderma* sinistral (MD99-2283, MD99-2284, MD99-2289 - Papers II-IV) and *N. incompta* & *G. bulloides* (GS13-182-01CC) (Paper V). The dating was performed at Beta Analytic, Trondheim (AMS), Kiel AMS, Poznan Radiocarbon Laboratory and INSTAAR at the University of Colorado at Boulder. All radiocarbon ages were (re-)calibrated using the Marine13 calibration curve (Reimer et al., 2013) within Bacon, which includes a global reservoir correction of 405 years. Within Papers II-IV, no further local reservoir effect correction was applied, due to the above mentioned large discrepancies in the size of the local reservoir effect within the time period 30-15 ka BP. This is however different within the mid and late Holocene, due to the work of Sejrup at al. (2010; 2011), where the local reservoir effect was well constrained within the last 8000 years within the southern Norwegian Sea. We have therefore applied this correction within core GS13-182-01CC and P1-003MC&SC to achieve calendar ages (Paper V). Furthermore, the youngest part of core GS13-182-01CC was dated through ^{210}Pb/^{137}Cs dating of 25 two cm slices of sediment, same as in core P1-003MC&SC. The samples were ^{210}Pb/^{137}Cs dated at Eawag, ETH Zürich. Finally, a known tephra layer was found in core MD99-2283 (FMAZ II) additional to the same layer in MD99-2284 (Dokken et al., 2013) and MD99-2289 (Nilsen, 2014), which could be used as an absolute time marker in the sediments, but was not used in the age models (Paper II-IV). The age offset between the FMAZ II tephras and the modelled, uncorrected radiocarbon ages in Paper II however suggested a local reservoir effect of about 1000 years, supporting earlier findings (Davies et al., 2008). On the other

hand, several tephra layers (Hekla 1947, Katla 1918) were found and used to constrain the age model in core GS13-182-01CC, as already done for core P1-003MC&SC (Sejrup et al., 2011) (Paper V). Notably, the tephra layers in core GS13-182-01CC were discovered at almost exactly the depth suggested by the radiocarbon dated age model, supporting the size of the suggested local reservoir effect correction at that time. Further counting also revealed the likely Askja 1875 tephra layer within 5 years of the modelled weighted mean age model, giving even higher confidence in the chronology. This tephra layer is not included so far, as it awaits geochemical verification.

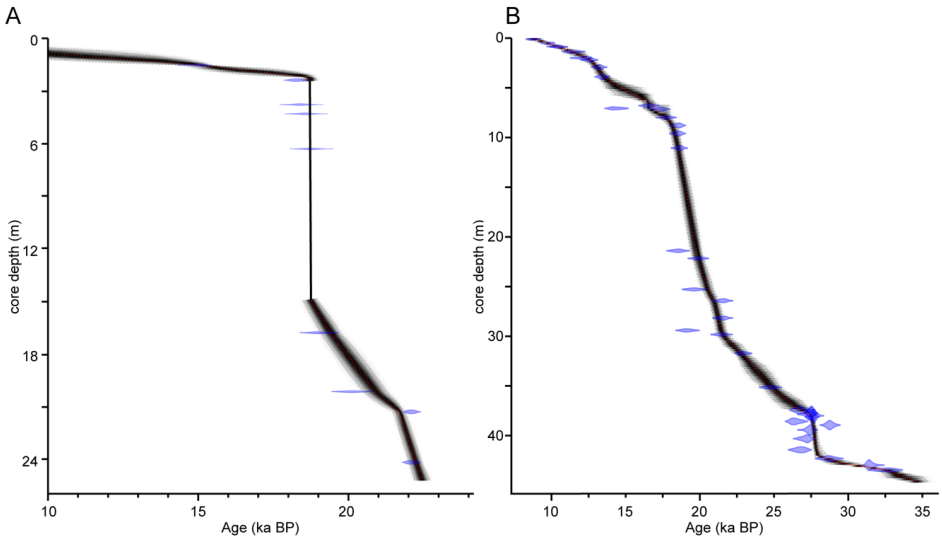

Fig. 3: An example of (A) the Bacon age model run for core MD99-2291, used in Paper II and III, and (B) the age model of the virtual core constructed for Paper IV. The blue dots mark individual AMS radiocarbon dates, the grey shading the total spread of age model ensembles and the red line marks the weighted mean age model, that was used in the respective studies.

All age models were constructed with a set accumulation rate distribution of 1.5 (Paper II-IV) and 3 (Paper V) and a student-t distribution, while the section thickness was changed depending on the need for flexibility in each core. This parameter was set to the smallest possible value, allowing the age model to run within the two-sigma standard deviation of most calibrated ^{14}C ages. Some samples were removed prior to

age modelling due to suspected reworking and in MD99-2283 the Laschamp palaeo-magnetic reversal (earlier published by Lekens et al., 2006) was added to constrain the age model in its oldest section. Core MD99-2291 proved especially challenging to model within Bacon, as such apparently sudden sedimentation rate changes like the meltwater plume event exceed the capabilities of the age modelling script. For the sake of age model construction, the deposits between the previously identified reflectors marking the start and end position of the plume deposit (Reiche et al., 2011), were regarded as instantaneous sedimentation (Paper II). The removed section was added back in as linear sedimentation after age modelling (Fig. 3A), resulting in an approximate duration of the deposition of this 12.2 m thick plume of less than the age model uncertainty of 230 years. The introduction of a virtual core, constructed out of 4 different cores along a seismo-stratigraphic framework in Paper IV finally simplified the modelling of this event, making the result more robust (Fig. 3B). Finally, performing age modelling by using Bayesian age modelling software like Bacon has an additional advantage, as it produces, depending on the amount of iterations, a certain amount of equally likely age models that can be used for further analysis. Applying for example a cross correlation of a certain comparison proxy time series to a measured proxy on the age model ensemble allows for a deeper understanding of synchronicity or lead/lag relationships between time series (Paper V).

Objectives

This PhD thesis is subdivided into two main projects with differing objectives: (i) Ocean - ice sheet interactions during the build-up, maximum and decay of the last glacial and (ii) high resolution Holocene climatic variability as recorded in a marine sediment archive.

(i) The main objectives of the first part are: (1) To compile and comprehensively present a series of well-dated cores from the south-eastern Nordic Seas continental margin and (2) relate the observed changes in the adjacent ice sheets to variability seen in the inflow of warm Atlantic water into the investigated area. (3) To investigate the onset, endpoint and last glacial maximum variability of the NCIS, while combining this with (4) new information and interpretation of the confluence of the BIIS and the FIS. Moreover, to (5) apply this new information in detailed studies of the Ling Bank glacial lake outburst flood and the (6) depositional influences of such an outburst plume event on the underlying gas hydrate stability zone.

(ii) The main objectives of the second part are: (1) To establish a sound chronological framework for core GS13-182-01CC by and (2) to combine instrumental and previously measured, unpublished data from a neighbouring core, to understand, establish and calibrate a high-resolution geochemical proxy-instrumental data connection. Finally (3) to use this new proxy to interpret possible climatic and environmental drivers of the signal and apply this to reconstruct this relationship for the time covered by the record.

Synthesis

Main findings and key implications

The results of this dissertation are a useful contribution to a wide range of future scientific work. Particularly in the light of the changing climate system and the accompanied discussions it is important to further our understanding of past ice sheets, to improve future ice sheet and climate modelling input and to understand ocean-atmosphere interactions in high-resolution beyond the time of instrumental measurements.

First and foremost, the proposed new method and workflow of automated sand-sized grain counting (Paper I) yielded a reasonably quick sample turnover time with compatible results and within controllable error sizes. The main findings of Paper II are, within the presented chronological framework, (1) a stadial/interstadial pattern of sediment deposition between 35 and 26 ka BP, indicating 500-1000 year long periods of increased, winnowing current speeds. (2) A later and shorter North Sea ice sheet confluence than previously suggested, between 25.5 ± 0.3 ka BP and 18.7 ± 0.2 ka BP. This is marked by a sharp drop in sedimentation rates along the margin, indicating a cut-off from southern sediment sources and the release and deposition of a meltwater plume, respectively. (3) Evidence suggesting sediment provenance changes between 25.5 and 24.5 ka BP, indicating an ice expansion of the BIIS beyond the coast of the Shetlands for possibly the first time during the Weichselian. (4) A Weichselian NCIS activity restricted to between 23.3 ± 0.5 ka BP and 19.0 ka BP, with the onset directly preceding a large-scale warm near-surface water intrusion along the continental margin, possibly indicating an NCIS initiation driven by ocean melt. (5) A high variability in the inferred streaming activity of the NCIS indicated by changing IRD flux on the margin. These episodes are interrupted by 500-600 yearlong halts/retreats and (6) coincide remarkably well with similar data off the western and eastern EIS margin, possibly indicating a common glacial forcing mechanism and/or atmospheric teleconnections. Finally, the glaciation history of the central North Sea, was

summarised in a glaciation curve (Fig. 4), updating previous versions by Sejrup et al. (1994; 2009).

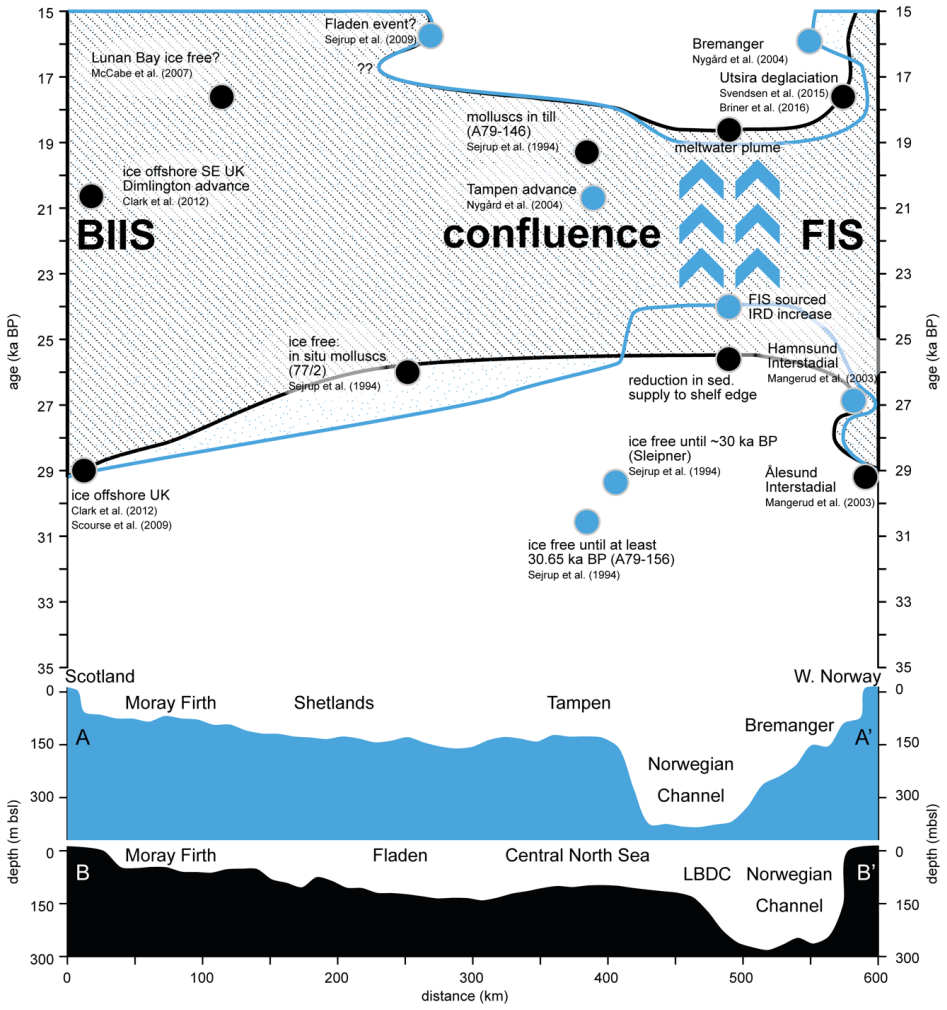

Fig. 4: The updated glaciation curve of the North Sea, showing ice extend into the North Sea from the British / Scottish side in the West and the Norwegian side in the East. The time of confluence and proposed timing of Norwegian Channel Ice Stream (NCIS) activity are indicated. Abbreviations include British-Irish Ice Sheet (BIIS), Fennoscandian Ice Sheet (FIS). The location of the profiles corresponds to Fig. 1A, all figure objects in blue correspond to the northern transect (A to A') and all black objects

to the southern transect (B to B'). The shaded areas indicate times of inferred glacial ice extension. Localised information on glacial ice state are given as dots with respective references. Blue arrows mark proposed NCIS activity.

The main findings from the detailed investigation into the Ling Bank glacial lake outburst flood at and during the separation of the BIIS and FIS at 18.7 ka BP are, (1) seismic evidence supporting the existence of an outburst flood in the North Sea (Paper III). Among those, a 12 m deep, 3 km wide incision at 56 m below present sea level at the north-eastern section of the Dogger Bank, combined with typical glacial lake outburst flood deposits like a 10 m thick prograding-aggrading unit deposited at the northern and southernmost part of the Ling Bank overlying erosional surfaces in the glacial sediments. (2) Peak discharge values were calculated to between 2.9×10^4 and 9.8×10^4 m^3s^{-1} in a first approximation, indicating that the Late Weichselian North Sea Lake outburst drained the proposed lake in about 5-15 months. (3) The flood is therefore interpreted to have been about 10 times smaller than estimated for the Glacial Lake Missoula located in todays' Montana, USA, but can be classified as a "major" jökulhlaup. (4) Finally, the meandering river system was found overlying the outburst sediments, indicating a fluvial-dominated environment following the outburst flood until the Ling Bank got submerged during the Younger Dryas, about 7000 years after the lake drainage.

Finally, numerical modelling of the base gas hydrate stability zone before, during and after the time the proposed meltwater, lake outburst flood plume is suggested to have arrived at the southern Vøring Plateau, resulting in the following main findings (Paper IV). (1) Changes in the rate of sedimentation are able to cause significant gas hydrate dissociation, without shifts in bottom water temperature or fluctuations in the relative sea level. (2) Even though no proof has so far been published of gas hydrate-related slope failures, many large slope failures occurred after proposed phases of increased sediment deposition. However, the results of this study show, that sedimentation-induced dissociation of gas hydrates might be an important part of the triggering or preconditioning mechanisms of slope failures due to pore-overpressure accumulation. (3) The large shifts of the base gas hydrate stability zone through changes

in sediment deposition result in a redistribution of large volumes of gas hydrates. This can lead to pore-overpressure, if the redistribution is hampered, potentially triggering focused fluid flow, which (4) discharges methane and has a significant impact on local and global carbon budget and fluxes. (5) The results highlight the world-wide importance of sedimentation changes to comprehend the development of focused fluid conduits and slope failures in gas hydrate provinces.

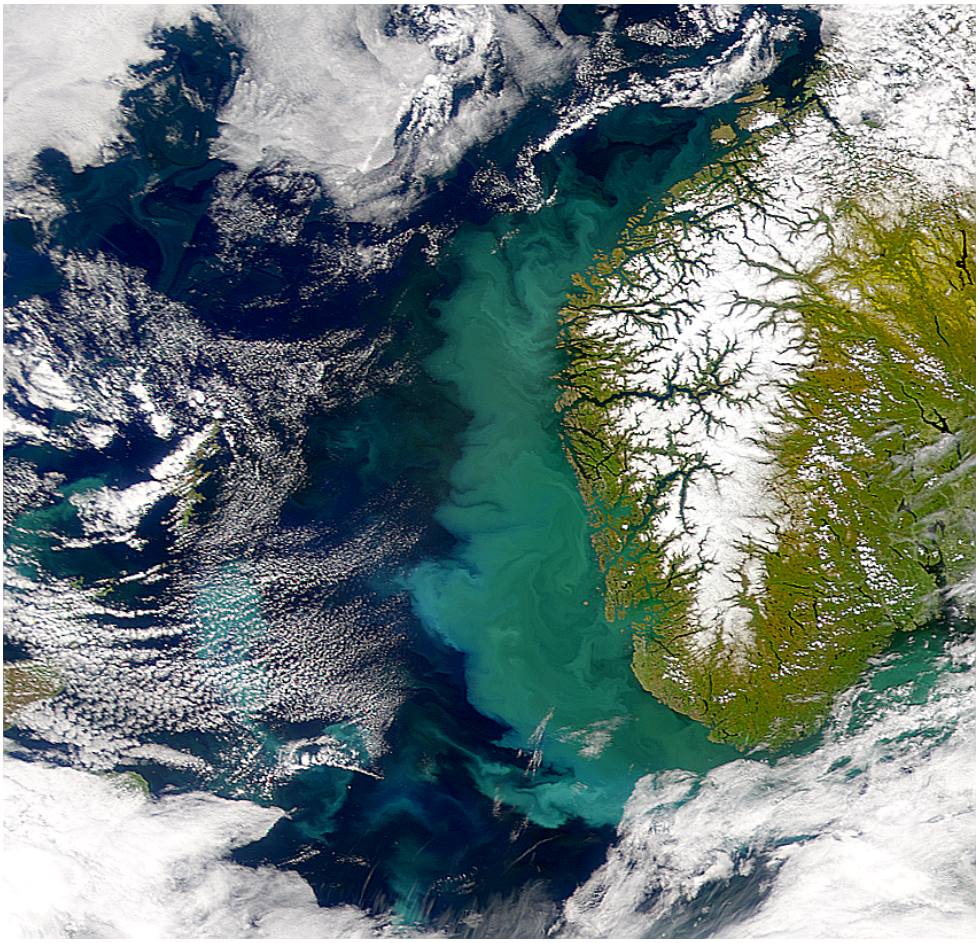

Fig. 5: The phytoplankton spring bloom along the south-western Norwegian coast. Source: SeaWiFS Project, NASA/Goddard Space Flight Center, ORBIMAGE.

Based on two, 8000 yearlong, sediment cores recovered from continuously deposited, hemipelagic sediments in the south-eastern Nordic Seas, the results of Paper V show, that (1) relative changes in calcium content, as seen in the Ca/Fe XRF data, are driven by calcium carbonate. The calcium carbonate content is (2) found to be principally contributed by the coccolithophore *C. pelagicus*. A significant link to instrumentally measured primary productivity strength could be shown (3) through the correlation with dissolved oxygen measurements between 1950 and 1992 AD. This is taken as an indication, that Ca/Fe might be used as a relative primary productivity proxy in the region, measuring essentially the strength of the phytoplankton spring bloom (Fig. 5). Furthermore, the results confirm previous findings of a significant anti-correlation (4) between the instrumentally analysed, atmospheric forcing pattern of the North Atlantic Oscillation (NAO) and the proposed proxy for primary productivity (Ca/Fe). Finally, comparing the Ca/Fe record to published NAO reconstructions indicates, that (5) it might be feasible to use this proxy to reconstruct past NAO changes within the south-eastern Nordic Seas on sub-decadal time scales within the last 8000 years.

Limitations

The assessments of limitations of the acquired data or the applied method is almost as important as the results it yielded. Essentially, knowing and stating the limitations of the presented data makes interpretations possible and renders them significant, - or not. The limitations of the proposed new, automated method of sand-sized particle counting (Paper I) are the physical loss of particles during the sample dispersion step, leading to lower total counts and the potential misidentification of particles within the post-processing, either decreasing or increasing the total counts. Whereas the first pitfall could simply be measured and yielded a relatively constant 9% sample loss, the latter depends on the skills of the user and is harder to constrain. However, this error is assumed to be negligible. Furthermore, specifically for the counting of IRD, there is a general discussion on which grain size fraction to use in such studies (Andrews, 2000), which opens up a range of other limitations, that go beyond the scope of the methodological study in Paper I.

The results of Paper II builds, in parts, upon data that was recovered within the last 18 years, by various people. This, especially with the relatively old and previously unpublished data, brings along a certain amount of uncertainty to how exactly samples were taken and how they were treated, even though all possible efforts were made to recover as much information as possible and quality check the data in regard to these issues. Furthermore, the interpretation of the proxy records are built on several assumptions. The synchronicity of events is built upon the assumption, that the 1000 km long transect of sediment records along the north-western European margin was influenced by the same magnitude of local reservoir effect at one time, and events are therefore seen as synchronous, when they overlap within the two-sigma age model uncertainty. However, there is a possibility for different reservoir effects along that transect, which could influence the synchronicity of the age models and the hereupon based interpretations. Even though the degree of subjectivity within the age modelling process is reduced to a minimum, a certain element of choice remains, especially, when interpreting abrupt changes in sedimentation rates. Potentially, this could lead to a misinterpretation of the depositional history, changing the inferred interpretations.

The chronological aspects of Paper III built upon previous studies and Paper II. The limitations of this study lie within the acquisition of the high-resolution shallow seismic profiles, which might conceal important features. Furthermore, the interpretation of these profiles requires a certain amount of assumptions, potentially leading to misinterpretation of seismic reflectors, which could change the size and extension of particular seismological units.

The results presented in Paper IV built on numerical simulations, which are limited by simplifications of the numerical code and the accuracy of the input parameters. The sediment temperature evolution is solely controlled by vertical, diffusive heat transport and neither considers the effects of various thermal properties within specific sediment layers causing anisotropic heat transport nor the transport of heat by advection of fluids. Furthermore, the code ignores the thermodynamic effects of gas hydrate dissociation or formation on pore pressure, methane solubility and pore fluid temperature. Considering these effects would have required detailed constraints about the hydraulic and thermal properties of the sediments and about the pore fluid geochemistry, which are not

available. While the sedimentation rates have been constrained in high resolution, parameters like the local subsidence, the thermal properties of the sediment and bottom-water-temperature fluctuations are based on a limited number of constraints from literature. However, the sensitivity analysis revealed that the uncertainty of these parameters has little impact on the overall simulation results.

Finally, Paper V builds upon the assumption of continuous sedimentation throughout the mid- and late Holocene, supported by visual core description and the age modelling results, however there may be sudden, short lasting accumulation rate increases that are beyond the resolution of the age model. Furthermore, the relative changes in bulk element concentration within the X-ray fluorescence core scanner data are measured in a resolution, giving up to 25 points per year are within at least the most recent 200 years. This appears to offer the chance for sub-seasonal measurements, but inter-annual variations in the sedimentation rates and different biogenic material production periods cannot be resolved by the presented age model, limiting the maximum resolution to annual. Additionally, as outlined in Paper V, the inferred calcium carbonate content might potentially be diluted by other factors than primary production of coccolithophores and foraminifera, like the previously proposed calcium carbonate precipitating bacterial activity (Heldal et al., 2012). This might add some uncertainty to using calcium carbonate, in the case of Paper V inferred from Ca/Fe counts, as primary production strength proxy in the sediments.

Outlook

In the following, the scientific contribution of the presented findings are considered with a focus on how they could be used in future work.

The different aspects of this dissertation, from methodological to proxy based palaeo-reconstructions, glacial to Holocene climates and wet sediment to modelling approaches, will enable a wide range of scientific application. From a technical point of view, the methodological Paper I, already successfully applied in Paper II, will be useful to, e.g. marine geologists and palaeo-oceanographers, aiding them during the quick acquisition of reliably and comparably counted datasets of e.g. IRD, while reducing the

bias of objectiveness. Moreover, the presented additional constraints on the timing and variability of the NCIS and the new interpretation of the timing of inter-North Sea ice sheet confluence (Paper II - III) will be a helpful contribution to further disentangle the complicated history of the north-western European and North Sea glaciation during the last glacial cycle. Parts of the chronological and palaeo-geographical reconstructions of Paper II could be used as an analogue to help forecast the future behaviour of todays' remaining ice sheets and ice streams. More directly, the results of Paper II-IV will be useful as a framework for future glacial and oceanographic reconstruction and modelling projects.

Specifically, several aspects within the glacial part of this dissertation will be pursued further, like the apparent common driver of marine and terrestrial terminating parts of the EIS during the last glacial maximum, mentioned in Paper II. Exploring these potentially atmospheric teleconnections further will shed a fresh light on the forcing mechanisms driving the internal variability of large continental ice sheets. Additionally, dates taken on mollusc samples in core MD99-2283 are not presented within this thesis. These dates however are from mollusc fragments found within the IRD influx episode, which is proposed to have a provenance from the shallow areas around the Shetlands (Paper II). The results of these dates need to be confirmed, but they appear to indicate, that our interpretation of a first Weichselian ice extension off the coast of the Shetlands after about 26 ka BP is correct.

Furthermore, with the presented new suite of ensembles of age models from seven cores along the inflow of the NAC in the southern Norwegian Sea (Paper II) it might be possible to further investigate the varying sizes of local reservoir effect in the region. As previously mentioned, the estimations range from 100 to several thousand years, depending on the type of record, the method and the location (Sarnthein et al., 2007; Davies et al., 2008; Franke et al., 2008; Hall et al., 2011; Sarnthein et al., 2015b). Using age model ensembles from Bayesian modelled chronologies combined with absolute tie-points, cross correlation and tuning efforts could add valuable insight.

The results of the high resolution sedimentary record presented in Paper V of this dissertation enabled a marine, deep-sea proxy-instrumental data correlation, in a resolution that was, to our knowledge not available before. This record and the

additional, so far unpublished data acquired from it, like the palaeomagnetic work by Sædis Ólafsdóttir, high-resolution foraminifera assemblages and oxygen isotopes on planktonic foraminifera, partly already presented in a MSc thesis (Rúnarsdóttir, 2016), will yield enough material for several additional papers potentially addressing sea surface conditions and inter-hemispheric relationships. A publication using the foraminifera assemblages and oxygen isotopic data is already in preparation. Last but not least, performing high-resolution coccolithophorid assemblage counts could be used to strengthen the presented relationship (Paper V) and sortable-silt analysis on the same core would offer opportunities for a detailed analysis and potentially a reconstruction of the dominant currents on the mid-Norwegian margin.

Finally, as a side project during my dissertation, I applied the same Bayesian age modelling approach as in Papers II-V for dating methods outside of the range of radiocarbon, published in Reinardy et al. (2017). Strontium isotope dating and a time coverage of the last three million years is far beyond what the age modelling script was originally written for (Blaauw and Christen, 2011). Exploring this age modelling approach further and enhancing it to include dating methods like strontium isotope or $^{210}Pb/^{137}Cs$ dating will be valuable for the palaeo-climate community.

References

Alvarez-Solas, J., Montoya, M., Ritz, C., Ramstein, G., Charbit, S., Dumas, C., Nisancioglu, K., Dokken, T. and Ganopolski, A., 2011. Heinrich event 1: an example of dynamical ice-sheet reaction to oceanic changes. Climate of the Past, 7(4): 1297-1306.

Andrews, J., 2000. Icebergs and iceberg rafted detritus (IRD) in the North Atlantic: facts and assumptions. Oceanography, 13(3): 100-108.

Berstad, I.M., 2003. Quaternary climate variability in the eastern Nordic Sea region inferred from speleotherm and deep-sea cores. PhD Thesis, University of Bergen, Bergen, Norway, 140 pp.

Blaauw, M. and Christen, J.A., 2011. Flexible Paleoclimate Age-Depth Models Using an Autoregressive Gamma Process. Bayesian Analysis, 6: 457-474.

Bradwell, T., Stoker, M.S., Golledge, N.R., Wilson, C.K., Merritt, J.W., Long, D., Everest, J.D., Hestvik, O.B., Stevenson, A.G., Hubbard, A.L., Finlayson, A.G. and Mathers, H.E., 2008. The northern sector of the last British Ice Sheet: Maximum extent and demise. Earth-Science Reviews, 88(3-4): 207-226.

Brendryen, J., Haflidason, H. and Sejrup, H.P., 2011. Non-synchronous deposition of North Atlantic Ash Zone II in Greenland ice cores, and North Atlantic and Norwegian Sea sediments: an example of complex glacial-stage tephra transport. Journal of Quaternary Science, 26(7): 739-745.

Briner, J.P., McKay, N.P., Axford, Y., Bennike, O., Bradley, R.S., de Vernal, A., Fisher, D., Francus, P., Fréchette, B., Gajewski, K., Jennings, A., Kaufman, D.S., Miller, G., Rouston, C. and Wagner, B., 2016. Holocene climate change in Arctic Canada and Greenland. Quaternary Science Reviews, 147: 340-364.

Bünz, S., Mienert, J. and Berndt, C., 2003. Geological controls on the Storegga gas-hydrate system of the mid-Norwegian continental margin. Earth and Planetary Science Letters, 209(3): 291-307.

Clark, C.D., Hughes, A.L.C., Greenwood, S.L., Jordan, C. and Sejrup, H.P., 2012. Pattern and timing of retreat of the last British-Irish Ice Sheet. Quaternary Science Reviews, 44: 112-146.

Crocker, A.J., Chalk, T.B., Bailey, I., Spencer, M.R., Gutjahr, M., Foster, G.L. and Wilson, P.A., 2016. Geochemical response of the mid-depth Northeast Atlantic Ocean to freshwater input during Heinrich events 1 to 4. Quaternary Science Reviews, 151: 236-254.

Croudace, I.W., Rindby, A. and Rothwell, R.G., 2006. ITRAX: description and evaluation of a new multi-function X-ray core scanner. In: R.G. Rothwell (Editor), New techniques in sediment core analysis. Geological Society of London, London, UK, pp. 51-63.

Dahlgren, K.I.T. and Vorren, T.O., 2003. Sedimentary environment and glacial history during the last 40 ka of the Vøring continental margin, mid-Norway. Marine Geology, 193: 93-127.

Davies, S.M., Wastegard, S., Rasmussen, T.L., Svensson, A., Johnsen, S.J., Steffensen, J.P. and Andersen, K.K., 2008. Identification of the Fugloyarbanki tephra in the NGRIP ice core: a key tie-point for marine and ice-core sequences during the last glacial period. Journal of Quaternary Science, 23(5): 409-414.

Dokken, T., Andersson, C. and Risebrobakken, B., 2015a. Relative abundance of planktic foraminifera and calculated SSTs and SST anomaly (11.1-25.5 ka BP) in sediment core MD95-2010. PANGAEA.DOI: 10.1594/PANGAEA.841922

Dokken, T., Andersson, C. and Risebrobakken, B., 2015b. Relative abundance of planktic foraminifera and calculated SSTs and SST anomaly (0-25.5 ka BP) in sediment core MD99-2284.DOI: 10.1594/PANGAEA.846924

Dokken, T.M. and Jansen, E., 1999. Rapid changes in the mechanism of ocean convection during the last glacial period. Nature, 401(6752): 458-461.

Dokken, T.M., Nisancioglu, K.H., Li, C., Battisti, D.S. and Kissel, C., 2013. Dansgaard-Oeschger cycles: Interactions between ocean and sea ice intrinsic to the Nordic seas. Paleoceanography, 28(3): 491-502.

Ehlers, J. and Gibbard, P., 2008. Extent and chronology of Quaternary glaciation. Episodes, 31(2): 211-218.

Franke, J., Paul, A. and Schulz, M., 2008. Modeling variations of marine reservoir ages during the last 45 000 years. Climate of the Past, 4: 125-136.

Haflidason, H., Sejrup, H.P., Kristensen, D.K. and Johnsen, S., 1995. Coupled Response of the Late-Glacial Climatic Shifts of Northwest Europe Reflected in Greenland Ice Cores - Evidence from the Northern North-Sea. Geology, 23(12): 1059-1062.

Haflidason, H., Sejrup, H.P., Berstad, I.M., Nygård, A., Richter, T., Bryn, P., Lien, R. and Berg, K., 2003. A Weak Layer Feature on the Northern Storegga Slide Escarpment, European Margin Sediment Dynamics.

Haflidason, H., Lien, R., Sejrup, H.P., Forsberg, C.F. and Bryn, P., 2005. The dating and morphometry of the Storegga Slide. Marine and Petroleum Geology, 22(1-2): 123-136.

Hall, I.R., Colmenero-Hidalgo, E., Zahn, R., Peck, V.L. and Hemming, S.R., 2011. Centennial- to millennial-scale ice-ocean interactions in the subpolar northeast Atlantic 18-41 kyr ago. Paleoceanography, 26(2): 1-18.

Hansen, B. and Østerhus, S., 2000. North Atlantic–Nordic Seas exchanges. Progess in Oceanography, 45: 109-208.

Heldal, M., Norland, S., Erichsen, E.S., Thingstad, T.F. and Bratbak, G., 2012. An unaccounted fraction of marine biogenic $CaCO^3$ particles. PLoS One, 7(10): e47887.

Hjelstuen, B., Sejrup, H.P., Haflidason, H., Nygård, A., Berstad, I.M. and Knorr, G., 2004. Late Quaternary seismic stratigraphy and geological development of the south Vøring margin, Norwegian Sea. Quaternary Science Reviews, 23: 1847-1865.

Hjelstuen, B.O., Monsen, S., Sejrup, H.P. and Haflidason, H., 2013. Report from calypso-coring at the Møre continental slope (Storegga slide). Report No. 100-05/13, Department of Earth Science, University of Bergen, Bergen, Norway.

Hughes, A.L.C., Gyllencreutz, R., Lohne, Ø.S., Mangerud, J. and Svendsen, J.I., 2015. The last Eurasian ice sheets – a chronological database and time-slice reconstruction, DATED-1. Boreas, 10(1111).

Joughin, I., Alley, R.B. and Holland, D.M., 2012. Ice-sheet response to oceanic forcing. Science, 338(6111): 1172-6.

Kissel, C., Laj, C., Mazaud, A. and Dokken, T., 1998. Magnetic anisotropy and environmental changes in two sedimentary cores from the Norwegian sea and the North Atlantic. Earth and Planetary Science Letters, 164(3-4): 617-626.

Labeyrie, L., Cortijo, E., Jansen, E. and Balut, Y., 1999. Les rapports de campagne a la mer a bord du Marion-Dufresne Campagne Interpole MD99-114/ IMAGES V.

Lee, J.R., Busschers, F.S. and Sejrup, H.P., 2012. Pre-Weichselian Quaternary glaciations of the British Isles, The Netherlands, Norway and adjacent marine areas south of 68˚N: implications for long-term ice sheet development in northern Europe. Quaternary Science Reviews, 44: 213-228.

Lekens, W.A.H., Sejrup, H.P., Haflidason, H., Petersen, G.O., Hjelstuen, B. and Knorr, G., 2005. Laminated sediments preceding Heinrich event 1 in the Northern North Sea and Southern Norwegian Sea: Origin, processes and regional linkage. Marine Geology, 216(1-2): 27-50.

Lekens, W.A.H., Sejrup, H.P., Haflidason, H., Knies, J. and Richter, T., 2006. Meltwater and ice rafting in the southern Norwegian Sea between 20 and 40 calendar kyr BP: Implications for Fennoscandian Heinrich events. Paleoceanography, 21(3): PA3013.

Lekens, W.A.H., Haflidason, H., Sejrup, H.P., Nygard, A., Richter, T., Vogt, C. and Frederichs, T., 2009. Sedimentation history of the northern North Sea Margin during the last 150 ka. Quaternary Science Reviews, 28(5-6): 469-483.

Lilly, J.M., 2017. A data analysis package for Matlab, v. 1.6.5, http://www.jmlilly.net/jmlsoft.html.

Mangerud, J., Løvlie, R., Gulliksen, S., Hufthammer, A.K., Larsen, E. and Valen, V., 2003. Paleomagnetic correlations between Scandinavian Ice-Sheet fluctuations and Greenland Dansgaard–Oeschger events, 45,000–25,000 yr B.P. Quaternary Research, 59: 213-222.

McCabe, A.M., Clark, P.U., Smith, D.E. and Dunlop, P., 2007. A revised model for the last deglaciation of eastern Scotland. Journal of the Geological Society, 164: 313-316.

Montelli, A., Dowdeswell, J.A., Ottesen, D. and Johansen, S.E., in press. 3D seismic evidence of buried iceberg ploughmarks from the mid-Norwegian continental margin reveals largely persistent North Atlantic Current through the Quaternary. Marine Geology.

Mork, K.A. and Skagseth, Ø., 2010. A quantitative description of the Norwegian Atlantic Current by combining altimetry and hydrography. Ocean Science, 6(4): 901-911.

Nilsen, J.E.Ø. and Falck, E., 2006. Variations of mixed layer properties in the Norwegian Sea for the period 1948–1999. Progress in Oceanography, 70(1): 58-90.

Nilsen, T.E., 2014. Kronologi, askestratigrafi og utbredelse av store askeutbrudd fra de siste 40 ka i kjerne MD99-2289 fra Norskehavet. MSc Thesis, University of Bergen, Bergen, 114 pp.

Nygård, A., Sejrup, H.P., Haflidason, H., Cecchi, M. and Ottesen, D., 2004. Deglaciation history of the southwestern Fennoscandian Ice Sheet between 15 and 13 ^{14}C ka BP. Boreas, 33: 1-17.

Nygård, A., Sejrup, H.P., Haflidason, H. and Bryn, P., 2005. The glacial North Sea Fan, southern Norwegian Margin: architecture and evolution from the upper continental slope to the deep-sea basin. Marine and Petroleum Geology, 22: 71-84.

Nygård, A., Sejrup, H.P., Haflidason, H., Lekens, W.A.H., Clark, C.D. and Bigg, G.R., 2007. Extreme sediment and ice discharge from marine-based ice streams: New evidence from the North Sea. Geology, 35(5): 395-398.

Orvik, K.A., Skagseth, O. and Mork, M., 2001. Atlantic infow to the Nordic Seas: current structure and volume fluxes from moored current meters, VM-ADCP and SeaSoar-CTD observations, 1995-1999. Deep-Sea Research I, 48: 937-957.

Ottesen, D., Stokes, C.R., Bøe, R., Rise, L., Longva, O., Thorsnes, T., Olesen, O., Bugge, T., Lepland, A. and Hestvik, O.B., 2016. Landform assemblages and sedimentary processes along the Norwegian Channel Ice Stream. Sedimentary Geology, 338: 115-137.

Peck, V.L., Hall, I.R., Zahn, R., Elderfield, H., Grousset, F., Hemming, S.R. and Scourse, J.D., 2006. High resolution evidence for linkages between NW European ice sheet instability and Atlantic Meridional Overturning Circulation. Earth and Planetary Science Letters, 243(3-4): 476-488.

Rasmussen, T.L. and Thomsen, E., 2008. Warm Atlantic surface water inflow to the Nordic seas 34-10 calibrated ka BP. Paleoceanography, 23(1).

Rasmussen, T.L., Thomsen, E. and Moros, M., 2016. North Atlantic warming during Dansgaard-Oeschger events synchronous with Antarctic warming and out-of-phase with Greenland climate. Nature Scientific Reports, 6: 20535.

Reiche, S., Hjelstuen, B.O. and Haflidason, H., 2011. High-resolution seismic stratigraphy, sedimentary processes and the origin of seabed cracks and pockmarks at Nyegga, mid-Norwegian margin. Marine Geology, 284(1-4): 28-39.

Reimer, P.J., Bard, E., Bayliss, A., Beck, J.W., Blackwell, P.G., Ramsey, C.B., Buck, C.E., Cheng, H., Edwards, R.L., Friedrich, M., Grootes, P.M., Guilderson, T.P., Haflidason, H., Hajdas, I., Hatte, C., Heaton, T.J., Hoffmann, D.L., Hogg, A.G., Hughen, K.A., Kaiser, K.F., Kromer, B., Manning, S.W., Niu, M., Reimer, R.W., Richards, D.A., Scott, E.M., Southon, J.R., Staff, R.A., Turney, C.S.M. and van der Plicht, J., 2013. Intcal13 and Marine13 Radiocarbon Age Calibration Curves 0-50,000 Years Cal Bp. Radiocarbon, 55(4): 1869-1887.

Reinardy, B.T.I., Hjelstuen, B.O., Sejrup, H.P., Augedal, H. and Jørstad, A., 2017. Late Pliocene-Pleistocene environments and glacial history of the northern North Sea. Quaternary Science Reviews, 158: 107-126.

Rise, L., Bøe, R., Ottesen, D., Longva, O. and Olsen, H.A., 2008. Postglacial depositional environments and sedimentation rates in the Norwegian Channel off southern Norway. Marine Geology, 251(1-2): 124-138.

Risebrobakken, B., Dokken, T., Smedsrud, L.H., Andersson, C., Jansen, E., Moros, M. and Ivanova, E.V., 2011. Early Holocene temperature variability in the Nordic Seas: The role of oceanic heat advection versus changes in orbital forcing. Paleoceanography, 26.

Rørvik, K.L., Laberg, J.S., Hald, M., Ravna, E.K. and Vorren, T.O., 2010. Behavior of the northwestern part of the Fennoscandian Ice Sheet during the Last Glacial Maximum – a response to external forcing. Quaternary Science Reviews, 29(17-18): 2224-2237.

Rúnarsdóttir, R.H., 2016. High-resolution δ18O and assemblage analysis between 1949- and 2000 AD based on planktonic foraminifera from the Storegga Slide, eastern Norwegian Sea. MSc Thesis, University of Bergen, Bergen.

Sarnthein, M., Grootes, P.M., Kennet, J.P. and Nadeau, M.-J., 2007. ^{14}C Reservoir Ages Show Deglacial Changes in Ocean Currents and Carbon Cycle, Geophysical Monograph Series. American Geophysical Union.

Sarnthein, M., Balmer, S., Grootes, P.M. and Mudelsee, M., 2015a. Planktic and Benthic C-14 Reservoir Ages for Three Ocean Basins, Calibrated by a Suite of C-14 Plateaus in the Glacial-to-Deglacial Suigetsu Atmospheric C-14 Record. Radiocarbon, 57(1): 129-151.

Sarnthein, M., Balmer, S., Grootes, P.M. and Mudelsee, M., 2015b. Planktic and benthic ^{14}C reservoir ages for three ocean basins, calibrated by a suite of ^{14}C plateaus in the glacial-to-deglacial suigetsu atmospheric ^{14}C record. Radiocarbon, 57(1): 129-151.

Scourse, J.D., Haapaniemi, A.I., Colmenero-Hidalgo, E., Peck, V.L., Hall, I.R., Austin, W.E.N., Knutz, P.C. and Zahn, R., 2009. Growth, dynamics and deglaciation of the last British-Irish ice sheet: the deep-sea ice-rafted detritus record. Quaternary Science Reviews, 28(27-28): 3066-3084.

Sejrup, H.P., Fjæran, T., Hald, M., Beck, L., Hagen, J., Miljeteig, I., Morvik, I. and Norvik, O., 1981. Benthonic foraminifera in surface samples from the Norwegian Continental margin between 62ºN and 65ºN. Journal of Foraminiferal Research, 11(4): 277-295.

Sejrup, H.P., Haflidason, H., Aarseth, I., King, E., Forsberg, C.F., Long, D. and Rokoengen, K., 1994. Late Weichselian glaciation history of the northern North Sea. Boreas, 23(1): 1-13.

Sejrup, H.P., Larsen, E., Haflidason, H., Berstad, I.M., Hjelstuen, B.O., Jonsdottir, H.E., King, E.L., Landvik, J., Longva, O., Nygard, A., Ottesen, D., Raunholm, S., Rise, L. and Stalsberg, K., 2003. Configuration, history and impact of the Norwegian Channel Ice Stream. Boreas, 32(1): 18-36.

Sejrup, H.P., Hjelstuen, B.O., Dahlgren, K.I.T., Haflidason, H., Kuijpers, A., Nygard, A., Praeg, D., Stoker, M.S. and Vorren, T.O., 2005. Pleistocene glacial history of the NW European continental margin. Marine and Petroleum Geology, 22(9-10): 1111-1129.

Sejrup, H.P., Nygard, A., Hall, A.M. and Haflidason, H., 2009. Middle and Late Weichselian (Devensian) glaciation history of south-western Norway, North Sea and eastern UK. Quaternary Science Reviews, 28(3-4): 370-380.

Sejrup, H.P., Lehman, S.J., Haflidason, H., Noone, D., Muscheler, R., Berstad, I.M. and Andrews, J.T., 2010. Response of Norwegian Sea temperature to solar forcing since 1000 AD. Journal of Geophysical Research-Oceans, 115.

Sejrup, H.P., Haflidason, H. and Andrews, J.T., 2011. A Holocene North Atlantic SST record and regional climate variability. Quaternary Science Reviews, 30(21-22): 3181-3195.

Sejrup, H.P., Hjelstuen, B.O., Nygard, A., Haflidason, H. and Mardal, I., 2015. Late Devensian ice-marginal features in the central North Sea - processes and chronology. Boreas, 44(1): 1-13.

Sejrup, H.P., Clark, C.D. and Hjelstuen, B.O., 2016. Rapid ice sheet retreat triggered by ice stream debuttressing: Evidence from the North Sea. Geology, 44(5): 355-358.

Svendsen, J.I., Briner, J.P., Mangerud, J. and Young, N.E., 2015. Early break-up of the Norwegian Channel Ice Stream during the Last Glacial Maximum. Quaternary Science Reviews, 107: 231-242.

Toucanne, S., Zaragosi, S., Bourillet, J.-F., Marieu, V., Cremer, M., Kageyama, M., Van Vliet-Lanoë, B., Eynaud, F., Turon, J.-L. and Gibbard, P.L., 2010. The

first estimation of Fleuve Manche palaeoriver discharge during the last deglaciation: Evidence for Fennoscandian ice sheet meltwater flow in the English Channel ca 20–18ka ago. Earth and Planetary Science Letters, 290(3-4): 459-473.

Vaular, E.N., Barth, T. and Haflidason, H., 2010. The geochemical characteristics of the hydrate-bound gases from the Nyegga pockmark field, Norwegian Sea. Organic Geochemistry, 41(5): 437-444.

Wary, M., Eynaud, F., Rossignol, L., Lapuyade, J., Gasparotto, M.-C., Londeix, L., Malaizé, B., Castére, M.-H. and Charlier, K., 2016. Norwegian Sea warm pulses during Dansgaard-Oeschger stadials: Zooming in on these anomalies over the 35–41 ka cal BP interval and their impacts on proximal European ice-sheet dynamics. Quaternary Science Reviews, 151: 255-272.

Thesis outline

Paper I is a methodological study, that proposes a novel method to automate the counting of sand- and gravel-sized particles in sediment records. The content and fluxes of ice-transported lithic particles in marine sediment cores are a common tool used to reconstruct glacial variability. IRD data sets are currently acquired in several different and often time-consuming ways, and within various grain-size fractions. The presented workflow updates a commonly used technique using an automated method to count IRD to reduce analysis time and subjectivity. This method is based on the instrument 'Morphologi G3' from Malvern Instruments Limited. The described workflow includes all pre-processing and post-processing steps. This particle characterisation tool is an automated microscope combined with a proprietary software package. In this study, the analysis was performed on the 150 to 1000 μm fraction. If desired, grain counts can be carried out on the entire sand and silt fractions. However, this would result in a considerably greater turn-over time. To test and validate this method, a total of 350 sediment samples from core MD99-2283, taken on the upper continental slope at the southern part of the north-east Atlantic margin, were counted with this automated method. In addition, a total of 161 samples were counted manually as a control on the reliability of the scanning. A linear correlation between automated and manually counted lithic and biogenic material revealed a convincing correlation between both methods ($R^2 = 0.97$ and 0.93 respectively). The turnover time per automatically counted sample is around 20 min, while requiring less experience and skills than manual counting. This study's results yielded a promising, time-saving new technique with which high-resolution IRD count datasets can be acquired, with acceptable error margins.

Paper II applies the method described in paper I and aims to contribute to our understanding of the timing of ice sheet advances and instabilities along the south-eastern Nordic Seas continental margin. The focus of this paper lies on the marine-based section of the FIS and the BIIS between 35,000 and 15,000 years BP. The variability of the FIS, the BIIS and the regional oceanic conditions are simultaneously archived in

sediment cores from the south-eastern Nordic Seas. This study is based on a compilation of new and published sedimentological, geochemical and micro-paleontological datasets within a revised, radiocarbon based, Bayesian modelled chronological framework. The presented data are acquired from cores MD99-2283, MD99-2284 and MD99-2289, retrieved along the upper continental slope between the Faroe-Shetland Channel and the Vøring Plateau. The results of this study show a possibly first Weichselian FIS/BIIS confluence at ca. 25,500 years BP in the central North Sea. This buttressed the BIIS to the east, potentially leading to a northwards deflection of the BIIS via the Shetlands. The proposed timing of confluence is several thousand years later than previously anticipated by earlier studies. Consequently, this study concludes, that the NCIS most likely only reached the shelf edge after 23,300 ± 500 years BP, perhaps for the first time during the Weichselian. The onset of the NCIS directly preceded a pronounced influx of warm Atlantic water to the northern North Sea margin, potentially implying a connection between the onset of the NCIS and forcing through ocean melt. Generally, this study finds a highly variable NCIS, with three ~1400 yearlong episodes of increased IRD flux, interrupted by ~600 yearlong minima. Comparing these findings to other parts of the EIS margin, even to the terrestrial terminating southern margin, these episodes appear to correlate well, suggesting a common forcing mechanism. In conclusion, the presented data of this study supports recent suggestions that the last glacial stage of the BIIS was more extensive in the central North Sea and the confluence later than previously thought.

Paper III focusses on the drainage event of the proposed ice-dammed lake within the southern North Sea at 18.7 ka BP, as outlined in paper II. This event was preceded by a retreat of the NCIS after ca. 19 ka BP and marks the separation of the BIIS and the FIS. The aim of this paper is to study this common deglaciation process in detail, as high-resolution evidence of such an event are rare within the marine realm. For this, high-resolution TOPAS profiles, bathymetric records and shallow borings are combined with recent reconstructions of the evolution of the BIIS and the FIS. The breaching point of the ice-dammed lake is suggested to have been in the north-eastern part of the Dogger Bank, marked by a 12 m deep and 3 km wide incision. The glacial

lake outburst flood waters continued northwards between the withdrawing BIIS and FIS, following the crest of the Ling Bank. Peak discharge rates are estimated to be 9.8 x 10^4 - 2.9 x 10^5 m^3s^{-1}, with the outburst lasting about 5-15 months. An up to 10 m thick sediment package with a prograding-aggrading sedimentation pattern, typical for ice-dammed lake outburst deposits, was deposited about 300 km downstream of the break-through point. This sediment package was deposited in a high-energy environment, immediately following extensive erosion of the underlying Last Glacial Maximum till unit. On the Norwegian continental margin, this outburst is connected to an oxygen isotope anomaly and an associated ultra-rapidly deposited meltwater plume dated to ca. 18.7 ka BP. During this time, evidence suggests a sea level at least 110 m lower than at present in the region. Therefore, this study proposes, that the Ling Bank Delta developed on top of the outburst deposits, when the sea level rose, following the disintegration of the Last Glacial Maximum ice sheets. The Ling Bank Delta indicates a sea level close to 80 m below present sea level and has an extent of 80 km. Up to 12 m deep fluvial channels are associated with the interpreted topset beds. This study concludes, that this fluvial environment may have lasted until the end of the Younger Dryas time period, when the Ling Bank was finally submerged and reached its present water depth.

Paper IV concentrates on another aspect of the described Ling Bank drainage event mentioned in paper II and III. The distal effect of this drainage event at 18.7 ka BP is the ultra-rapidly deposited meltwater plume on the Vøring plateau and on top of the Ormen Lange gas field. This paper aims to understand the effect of such high rates of sediment accumulation on the depth of the gas hydrate stability zone by combining several sedimentary archives and high-resolution shallow seismic datasets. This effect is of high importance, as large amounts of methane are stored in continental margins in the form of solid gas hydrates. The stability of gas hydrates is dependent on pressure and temperature. As long as the pressure is high and the temperatures are low, gas hydrates are stable, but variations in pressure and/or ocean temperature can destabilise gas hydrates rapidly. Consequently, gas hydrates can react sensitively to environmental changes. Previously, modelling of gas hydrate dynamics after the Last Glacial

Maximum considered mainly changes in bottom water temperature and/or sea level fluctuations. Detailed sediment accumulation rate reconstructions are often impossible, which is why this factor is usually not considered. However, the age models constructed within Paper II, combined into one virtual core in Paper IV, made a detailed reconstruction of sediment accumulation rates possible. The resulting numerical simulations of this study show, that pulses of increased sedimentation dominantly controlled gas hydrate stability during and after the Last Glacial Maximum at the mid-Norwegian margin. In turn, this implies widespread gas hydrate dissociation and high pore overpressure and explains the formation of ubiquitous blowout pipes in water depths of 600 to 800 m below sea level. Furthermore, the calculated maximum gas hydrate dissociation correlates spatially and temporally with the distribution and the formation or reactivation of associated pockmarks around 18,000 years BP. This was constrained by radiocarbon dating of authigenic carbonate crusts and *Isorropodon nyeggaensis* bivalve shells from sediment cores. The results of this study highlight that rapid changes of sedimentation at gas-hydrate hosting continental margins can have a strong impact on gas hydrate driven fluid flow dynamics, natural gas seepage activity as well as slope stability. These impacts have to be taken into account in climate change scenarios.

Paper V is a manuscript in preparation and concentrates on a more recent time frame, from 1992 AD to about 8000 years BP. The overlap with the instrumental period gives the opportunity to test specific parameters measured in high-resolution as a proxy value and apply this framework to climatic changes within the last 8000 years. Primary productivity in the SE Nordic Seas has been instrumentally measured since the 1950s. Its strength is dependent on irradiance, nutrients and temperature, rendering it closely linked to solar, atmospheric and oceanic forcing. Down-core calcium carbonate ($CaCO_3$) variability is a widely used parameter in marine pelagic archives to determine palaeo-oceanographic conditions and found to reflect the primary production strength of the $CaCO_3$ secreting biomass. Paper V aims to link $CaCO_3$ in sediment archives to high resolution, X-ray fluorescence scanned relative Ca content, verify this with robust chronological control against instrumentally measured primary production data in order

to infer palaeo-productivity changes within the last 8000 years and examine the potential of North Atlantic Oscillation (NAO) reconstruction. Based on two sediment cores from the mid-Norwegian continental slope, P1-003 with exceptional chronological control and GS13-182-01CC with three times higher resolution, this study presents continuous, relative Ca variations in sub-annual resolution of the last 8000 years. Bayesian modelled time uncertainties (2$\boldsymbol{\sigma}$) range from 2-15 years (last 200 years) to about 110 years (1800 AD - 6000 BC). The results show the Ca content to be driven primarily by $CaCO_3$ variations, contributed by the coccolithophore *C. pelagicus*. Cross-correlations of the Ca/Fe data to primary productivity measurements show a significant correlation ($p < 0.01$). Furthermore, the Ca/Fe data correlate significantly to the inverse, instrumental NAO ($p < 0.0001$), supporting earlier suggestions of inverse primary production and NAO phase fluctuations in the SE Nordic Seas. In conclusion, the findings suggest that the relative calcium content can be used as a palaeo-productivity proxy for $CaCO_3$ secreting organisms and might furthermore potentially be used for a NAO reconstruction in the SE Nordic Seas of the past 8000 years.

I

Automated counting of sand-sized particles in marine records

Lukas W.M. Becker, Berit O. Hjelstuen, Eivind W.N. Støren
and Hans Petter Sejrup

Published in Sedimentology (2017), doi: 10.1111/sed.12407

SEDIMENTOLOGY the journal of the International Association of Sedimentologists

Sedimentology (2017) doi: 10.1111/sed.12407

Automated counting of sand-sized particles in marine records

LUKAS W. M. BECKER*, BERIT O. HJELSTUEN*, EIVIND W. N. STØREN† and HANS PETTER SEJRUP*

**Department of Earth Science, University of Bergen, Allégaten 41, Bergen 5007, Norway (E-mail: lwmbecker@gmail.com)*

†Bjerknes Centre for Climate Research, Allégaten 70, 5007, Bergen, Norway

Associate Editor – Nick Lancaster

ABSTRACT

Content and fluxes of ice-transported sand-sized and gravel-sized, lithic particles in marine sediment cores are a common tool used to reconstruct glacial variability. Ice-rafted debris data sets are currently acquired in several different and often time-consuming ways, and within various grain-size fractions. This article proposes a novel workflow using an automated method to count ice-rafted debris to reduce analysis time and subjectivity. The described method is based on the instrument 'Morphologi G3' from Malvern Instruments Limited and includes all pre-processing and post-processing steps. This particle characterization tool is an automated microscope combined with a proprietary software package. In this study, the analysis was performed on the 150 to 1000 μm fraction. If desired, grain counts can be carried out on the entire sand and silt fractions. However, this would result in a considerably greater turnover time. A total of 350 sediment samples from core MD99-2283, taken on the upper continental slope at the southern part of the north-east Atlantic margin, were counted with this automated method. In addition, a total of 161 samples were counted manually as a control on the reliability of the scanning. The comparison of automated versus manually counted biogenic and lithic material shows a convincing correlation between the two methods. The turnover time per automatically counted sample is around 20 min, the method requiring less experience and skills than manual counting. The results yield a promising, time-saving new technique to achieve high-resolution ice-rafted debris counting records with acceptable error margins.

Keywords Automated, counting, glacial sediments, grain size, ice-rafted debris, IRD, North Atlantic.

INTRODUCTION

Terrestrial and especially marine-based ice sheets have been shown to be sensitive to changes in various climatic parameters (Vaughan & Arthern, 2007; Joughin *et al.*, 2014). The fluctuating output of ice sheets is archived in the accumulating sediment record in the marine and lacustrine realm. The palaeo-climatic significance of sand and gravel-sized, lithic particles in deep marine sedimentary records has been widely recognized and discussed since the recognition of Heinrich events (Heinrich, 1988; Broecker *et al.*, 1992) as periods of increased flux of ice-rafted debris (IRD) to the North Atlantic (e.g. Alley & Macayeal, 1994; Bond & Lotti, 1995; Andrews, 2000). Although sea ice is reported to be of some importance (Andrews, 2000; Darby *et al.*, 2009), the basic rationale is that ice rafting is the only possible transportation aid of sand and gravel-sized particles into the deep ocean, as long as mass flow deposits can be excluded with information from additional data.

The identification of IRD in sediment cores is done in several different ways, spanning from a full-spectrum grain-size distribution analysis to

counting of discrete sand and gravel-sized particles. The full-spectrum grain-size distribution can be acquired through manual sieving and weighing or by automated solutions like the Sedigraph (Micromeritics Instrument Corporation, Norcross, GA, USA), the Coulter Counter (Beckman Coulter Inc., Brea, CA, USA) and the Mastersizer (Malvern Instruments Limited, Worcestershire, UK), depending on the grain-size fraction in focus (McCave & Syvitski, 1991; Ryżak & Bieganowski, 2011). The significant amount of information derived from the relative bandwidth of grain-size distribution in each sample can be extended by counting of the particle content. This information combined with volumetric and density measurements can then further be used to calculate flux volumes (e.g. Scourse *et al.*, 2009). This set of size distribution and content data is in turn valuable in discussions of glacial variability and the modes of deposition.

Even though the majority of sediments derived from glacial erosion are of clay and silt size, the sand and gravel fractions are commonly used to deduce information about glacial activity. As Andrews (2000) pointed out, this specific fraction is preferentially used because grains are easier to count than those in smaller size fractions. The counting of IRD is commonly done either by counting 300 to 600 grains in a split of a specific fraction (such as >150 μm or >500 μm) under a light microscope and computing those counts into the IRD content of the total sample (Bornhold, 1983; Heinrich, 1988; Bond & Lotti, 1995; Haapaniemi *et al.*, 2010; Bailey *et al.*, 2012), or by counting IRD grains >2 mm on an X-ray picture of the split core as a less labour-intensive and time-consuming alternative (Grobe, 1987). The X-ray method gives a quick overview of a large core section, while yielding corresponding values compared with counting in separate fractions, but needs a "relatively high amount of large IRD particles" to work (Grobe, 1987).

In this study, a novel method and workflow to automate the process of IRD counting are presented and discussed. The measurements were performed with the particle characterization tool Morphologi G3 (M-G3), version 'MOR2400', from Malvern Instruments Limited (Malvern Instruments Limited, 2017). To be comparable, this study focuses on the commonly used grain-size fraction (>150 μm). However, the presented method offers the theoretical possibility to extend particle counting and shape analysis also into the silt fraction. All samples are from sediment core MD99-2283, taken on board the *R/V Marion Dufresne*, in a water depth of 707 m at the outlet of the Norwegian Channel, which was repeatedly occupied by the Norwegian Channel Ice Stream (Sejrup *et al.*, 2003). Other data from this core were previously published by, for example, Lekens *et al.* (2006). All control-counting and sample runs were performed at the Earth Surface Sediment Laboratory (EARTHLAB), Department of Earth Science, University of Bergen, Norway.

INSTRUMENT AND METHODS

The M-G3 (Fig. 1) is in essence an automated microscope with a connected software package (Malvern Instruments Ltd., 2017). Based on image analysis of systematically captured frames of a selected scan area, the instrument detects particles in dry or wet samples within a size range of 0·5 to 1000 μm. The individual sample size volume is limited to 20 mm^3, because larger sample volumes increase the chance of overlapping of single particles, which either slows down the post-processing workflow or makes a rerun with a smaller sample size necessary. The morphometric output parameters for the individual particles include length, width, area, perimeter, volume, diameter, shape (circularity, elongation, aspect ratio and convexity) and grey scale information (intensity mean).

Pre-processing workflow

All samples for automatic counting are pretreated in the same way as for manual counting. The samples are hence wet sieved and dried in fractions 63 to 150 μm, 150 to 1000 μm and >1000 μm. The fraction 150 to 1000 μm is split with a standard sample splitter until the split size reaches approximately 20 mm^3. Separate tests with samples <1000 μm, without any further fractionation, showed that such samples appear to be more complicated to interpret during the post-processing workflow due to poor spatial separation of particles during dispersion. The grains in the fraction >1000 μm were manually counted and added to the total number of particles during the post-processing operation. It should be noted that the fraction used for counting can, if needed, be changed to any other range during post-processing.

Set-up of the instrument

The standard operating procedure (SOP), which is defined before analysing the first sample,

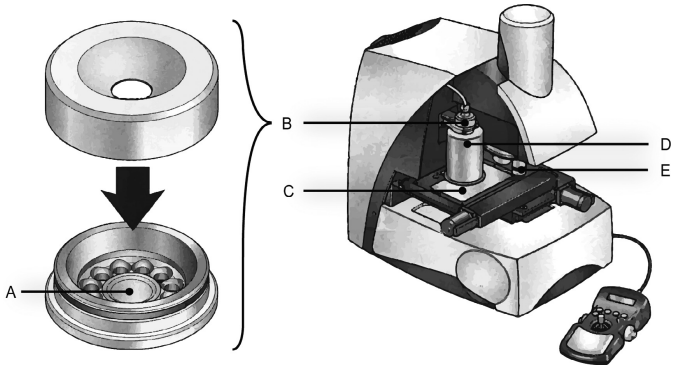

Fig. 1. Major components of the Morphologi G3: The sample well (A) in the bottom section of the sample entrainment spool (B). The glass plate (C) on which the sample is dispersed within the dispersion cylinder (D) and the optical unit with its five different lenses (E). Drawings are modified from the user manual of the instrument (Malvern Instruments Limited, 2013) on pages 4-3 and 3-3, respectively.

ensures that the dispersal and the measurement of all samples are performed with the same settings. See supporting information for details and screenshots of the described set-up procedure within the Malvern Instruments Limited proprietary software (version 8·12). The duration and energy of dispersal in the sample dispersion unit (Fig. 1B and D) were set to 'low' (2 bar over 20 sec with 5 sec settling time). The scan area (circular, 46 mm radius) was set to include the entire dispersed sample on the glass plate (Fig. 1C). The detection threshold was adjusted to capture the particles of interest. A threshold of 130 showed the best results for these types of sediments. The used objective lens (Fig. 1E) has a magnification of 2·5, covering particle sizes from 13 to 1000 μm (Malvern Instruments Ltd., 2017), and was run with a fixed focus that is automatically set during the calibration of the instrument at the start of each run. The function 'focus stacking' was disabled, because this made each measurement considerably quicker. Tests showed no significant loss in the total particle counts compared to the function being enabled. However, if one chooses to measure samples with a larger grain-size range than 150 to 1000 μm, it might be necessary to use different optics and 'focus stacking' during the same run, thus increasing the measuring time considerably. The light was set to an automatic calibration intensity of 80% and illuminates the sample from below (backfield). Because the dispersed sample was measured in single rectangles, it was inevitable that some particles were lying exactly on the border between two scanned rectangles and are split into two pieces. The function 'particle stitching' was therefore enabled, allowing the software to merge particle slices that are split into two shapes.

The collected data can be handled in two different ways within the included software: 'Classifications' allow exclusion or inclusion of particles to specific parameters, like a certain circularity or diameter. This can be done automatically during the sample run. 'Tags' allow marking of a specific particle with several separate labels manually, thus a particle could be marked as, for example, 'biogenic' and 'doublets' at the same time. To prepare the post-processing of the data, the 'classifications' settings were set to exclude all particles <150 μm, by setting 'length <150 μm (excluded)'. The majority of all biogenic material in the samples for this study (tag 'biogenic') consisted of foraminifera, which in these tests appeared to be well-classified as rounded ('circularity' >0·945) and opaque particles ('intensity mean' <25·00).

The overview of the total counts for overlapping particles (doublets and triplets), single lithic particles (single_d/t) and biogenic material (Fig. 2A to D) was prepared by setting 'tagged' = 'doublets', 'triplets', 'single_d/t' and 'biogenic', respectively, within the classifications menu. With this setting and after completed particle tagging, the number of counts for each tag group will be displayed on the records overview page. The overview page can be exported. Once all parameters were set, the SOP was saved as a

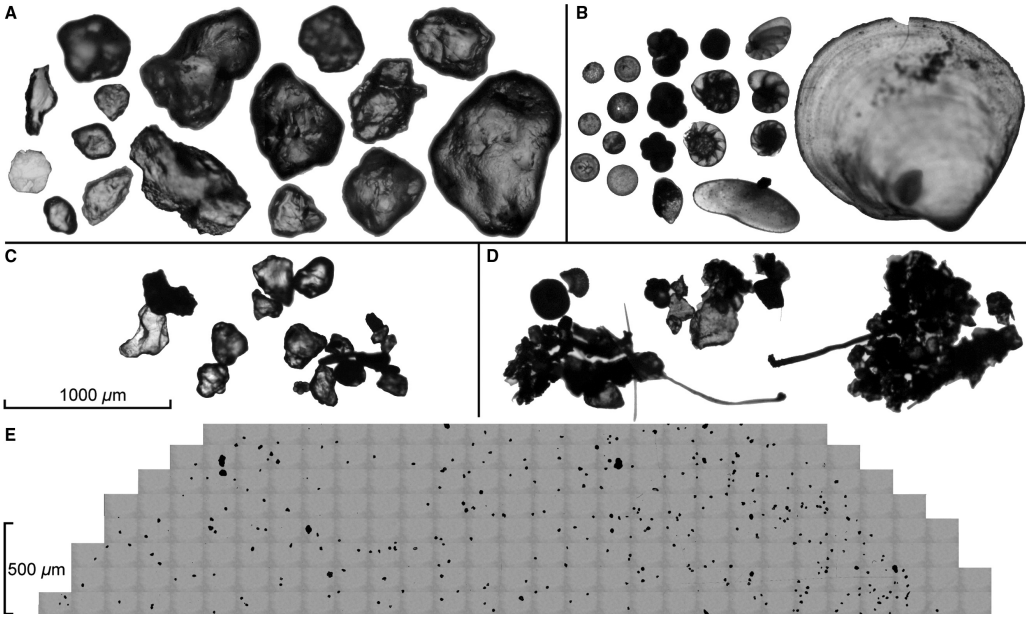

Fig. 2. Examples of different particles measured with the Morphologi G3. (A) Lithic grains of various types, shapes and sizes. (B) Various types of biogenic material. (C) Examples of doublets, triplets and multigrain shapes. (D) Uncountable particle clusters that led to rerun of the specific sample. (E) Example of a dispersed sample on the glass plate. The area composite consists of a collage of the rectangular images that were taken during the sample measurement.

'.vsop' file. This SOP was launched for every sample run, to produce a file with all morphological properties and predefined classifications of the detected particles. A run with these settings takes about 16 min to complete.

Sample run

The split sample is transferred into the dispersion unit entrainment spool of the M-G3 (Fig. 1B). This spool consists of a bottom and top section. The bottom section has a platform in the middle, the 'sample well' (Fig. 1A), which is surrounded by holes through which the sample will fall during the dispersal. The simplest and most exact way to transfer the split sample on to the sample well is to fill the split sample into a clean 11·5 mm standard glass vial, which in turn fits directly on the sample well. The sample entrainment spool is then closed with the top section of the spool and carefully inserted into the sample dispersion unit. Within the dispersion cylinder, the sample is automatically dispersed on to a glass plate (Fig. 1C, with sample in Fig. 2E) and subsequently scanned in one pass according to the SOP-given parameters. When one run is finished, the counted sample may be collected from the glass plate and stored together with the rest of the split sample.

Post-processing workflow

Although the procedure is automated, several simple steps are necessary to quality check the previously set classifications and with that to finally achieve the absolute number of particles within a scanned sample. Biogenic material has to be separated out and shapes that consist of multiple particles have to be accounted for. The following workflow was found to be most suitable for the samples in question and on average took about 8 min to complete. More time is needed with increasing sample size due to more frequent cases of overlapping particles, causing clusters of triplets and doublets (Fig. 2C).

Firstly, the particles classified as 'biogenic' in the SOP are sorted by decreasing circularity and are all selected. All particles falsely classified

(for example, Fig. 2A) are deselected, whereas the rest are tagged 'biogenic'. Usually, the falsely classified particles are those with the lowest circularity. Subsequently, artefacts (such as scratches on the glass plate or sample contamination such as hairs) and particle clusters (doublets and triplets – Fig. 2C) have to be manually excluded from the data set. This is easily done by sorting all identified particle shapes by decreasing circularity, displaying these elongated features at the top of the list. Every detected artefact is selected and 'manually excluded'. If particle clusters with an unknown number of particles are present (Fig. 2D), the sample run is rejected and a rerun has to be performed, where the sample had to be split at least one additional time before.

To control the whole sample for biogenic material that was not automatically classified (Fig. 2B), the tag 'biogenic' is deselected. In this way, all particles that are already tagged 'biogenic' are not shown and the control takes considerably less time. In particular, disc-shaped and non-opaque foraminifera, gastropods, molluscs and biogenic material within multiples are not automatically detected by the classification parameters set within the SOP. All discovered biogenic shapes are then consecutively tagged 'biogenic'. In special cases, where for example two foraminifera or shells are present within one shape, another non-foraminifera or shell shape is also tagged 'biogenic' so that the correct total of all biogenic material is counted. In a last step, to obtain the total particle count, all doublets are tagged 'doublets' and all triplets tagged 'triplets', irrespective of lithic grain or biogenic material.

If one particle cluster consists of, for instance, six shapes (Fig. 2C), another single shape would be tagged 'triplets' to account for the additional three grains. However, if a single shape is tagged 'doublets' or 'triplets', the absolute particle count only increases by one or two particles, respectively. This is due to the fact that the second/third particle normally is already being accounted for in the total particle count. A single shape tagged 'triplets' therefore 'counts' only for two instead of three particles. To accommodate for this, an additional 'single doublet/triplet (d/t)' tag is added to every single shape, which is tagged with 'doublets' or 'triplets'.

Finally, the processed file is saved with the extension '_processed'. The original file can therefore always be re-evaluated. The final result will be displayed on the records overview page with 'sample name', '#particles', '#doublets', '#triplets', '#single_d/t' and '#biogenic'. This page can be exported as a '.txt' file.

The actual content of IRD particles >150 μm per gram within a sample is calculated as follows:

$$\mathrm{IRD\,g^{-1}} = \frac{(((\mathrm{p} + \mathrm{d} + (2 \times \mathrm{t}) + \#\mathrm{single\_d/t} - \mathrm{b}) \times 2^{\#\mathrm{splits}}) + (\mathrm{p} > 1000\,\mu\mathrm{m}))}{\mathrm{dry\ weight\,(g)}} \quad (1)$$

where p = #particles, d = #doublets, t = #triplets and b = #biogenic. At the same time, the content of biogenic material can be calculated with:

$$\mathrm{biogenic\,g^{-1}} = \frac{\#\mathrm{biogenic} \times 2^{\#\mathrm{splits}}}{\mathrm{dry\ weight\,(g)}} \quad (2)$$

RESULTS

The above-described method was used to analyse and post-process a total of 350 samples from core MD99-2283. Roughly 800 to 6000 particles (2500 on average) were measured in each of the samples. To verify the automated counts, all lithic and biogenic particles were additionally manually counted under a light microscope in 33 samples. In addition, the biogenic content was control-counted in a further 128 samples, totalling 161 control-counted samples.

The control-counting appears to have a generally good fit with the respective automated and post-processed counts of the M-G3 (Fig. 3A and B). The lithic grain counts (n = 33) correlate with a linear coefficient of R = 0·97 (Fig. 3A). The biogenic material counts are separated into two sub-groups (Fig. 3B). In roughly one-third of the manual counts of biogenic material, only planktonic foraminifera were counted, rather than all biogenic material. This is apparent in the two differing linear coefficients (Fig. 3B). When considering all biogenic material counts (n = 161), the linear coefficient is slightly lower

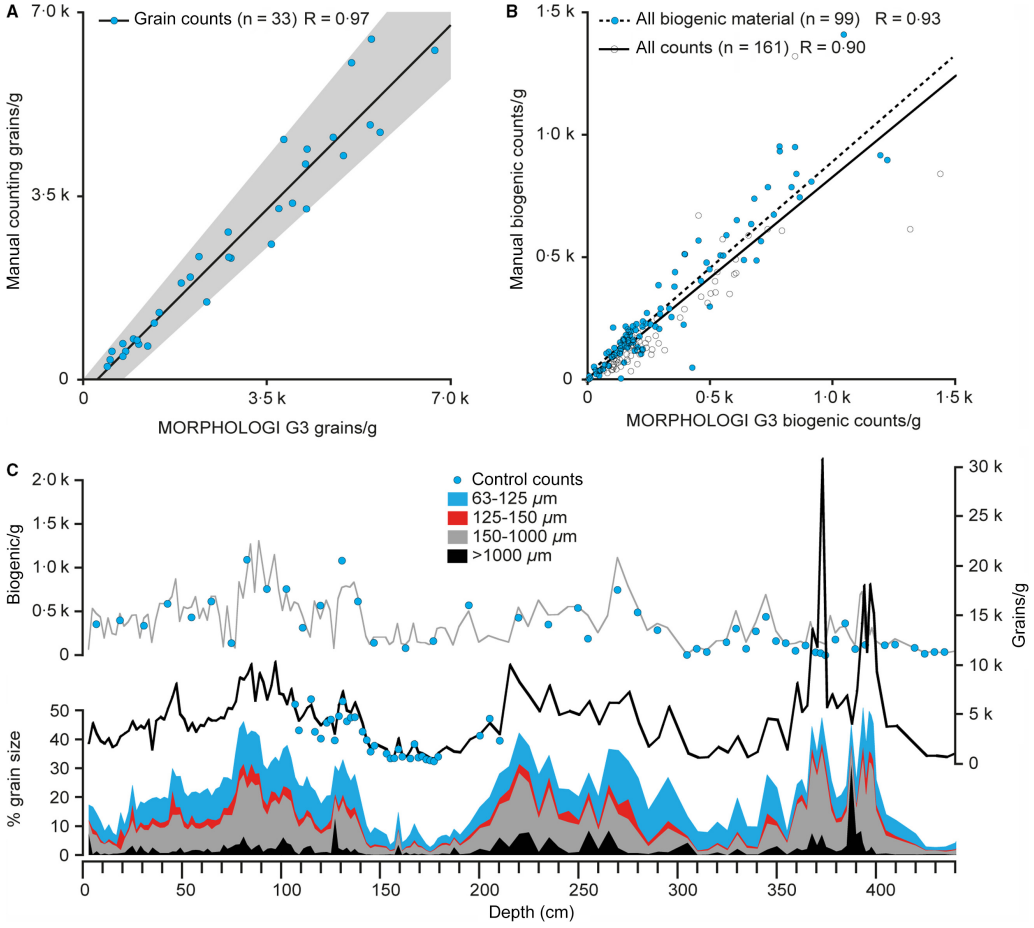

Fig. 3. Diagrams to illustrate and compare the validity of the Morphologi G3 counts versus manually counted samples. (A) Lithic grain counts, with the grey shade highlighting the maximum spread of the counted samples. (B) Biogenic material counts with two linear coefficients. One for all samples and one for only those samples, where all biogenic material was counted (n = 99), as opposed to counting only planktonic and benthic foraminifera. (C) The stratigraphic position of the manually counted 33 lithic and 161 biogenic particle counts in core MD99-2283, plotted, respectively, against the lithic grain counts (black line) and the biogenic counts (grey line) of the Morphologi G3. The cumulative grain-size distribution of all manually sieved and weighed samples is given in four different size fractions.

(R = 0·90), compared to R = 0·93 (n = 99), where all counts with only planktonic foraminifera are excluded (n = 62).

DISCUSSION

Despite the generally good fit (Fig. 3A), the automated and manual counts deviate increasingly with higher IRD content. This effect is also evident in Fig. 3C, when comparing the correlation between the post-processed lithic grain counts of the M-G3 (black line) and the manual counts (blue dots) within their stratigraphic position along core MD99-2283 (Fig. 3C). This could indicate a decrease in accuracy of one or potentially both methods with higher particle content. The picture is similar for the biogenic counts of

the M-G3 (grey line) and the respective control-counts (Fig. 3C). Although the M-G3 is restricted to a maximum sample size of 20 mm^3, the counts per sample are on average about a magnitude higher than during manual counting, where commonly about 300 counts are seen as statistically significant. Additionally, samples with high lithic grain content are likely to require more splits than other samples, increasing the potential for an underestimation or overestimation of the calculated total counts. The higher total counts of the M-G3 might minimize this risk compared to manual counting. Nonetheless, the M-G3 appears to slightly overestimate the IRD counts (Fig. 3A and C). This, however, may also be related to a loss of sample material during dispersion and collection of the sample in the M-G3, because the manual counts were performed on already automatically counted splits.

In summary, the apparent good correlation of the two methods to count lithic grains and biogenic material suggests a high reliability of the automated M-G3 counts. Thus, the counts of the M-G3 appear to be at least as representative as the manual counting.

The most distinctive feature that the M-G3 counted IRD data of core MD99-2283 revealed is the difference between the three apparent spikes in the cumulative grain-size distribution (Fig. 3C). The two spikes between 0 cm and 320 cm core depth, when the grain-size distribution is analysed, appear to be similar to the third spike between 320 cm and 420 cm core depth. However, the M-G3 data showed that the third spike contains about triple the amount of IRD and is almost barren of biogenic material. The palaeo-climatic interpretation of the acquired IRD data of MD99-2283 is, however, beyond the scope of this study, but a separate paper is in preparation, which will deal with this in detail.

In the tests described in this study, the single sample turnover time of the M-G3 and the manual counting were relatively similar. An average of 35 min including sample splitting (7 min), set-up (4 min), run (16 min) and post-processing (8 min) were needed for the M-G3 counting. About the same time was needed for sample splitting and counting during manual counting. The absolute sample turnover time of the M-G3 is, however, lower; this is because the sample run time can be used to post-process or split samples. This reduces the absolute work time per sample to around 20 min. Arguably, the time used for manual counting is also strongly dependent on the skill of the individual person. A non-skilled person would probably need more time per sample and could bias results through an element of subjectivity. In contrast, the M-G3 only requires a short introduction and can thereafter be easily operated. Due to the counting being done automatically, the automated method is objective and can be efficiently operated seven days a week, several hours a day, whereas the accuracy of manual counting probably decreases during long days. A practical advantage with automated counting is the relatively small file size of the counted samples on the computer, which can be archived and re-evaluated at any time if needed.

A disadvantage of the presented automated counting method is that lithic grains are not grouped into individual rock types, making provenance studies impossible. Additionally, the misidentification of particles could potentially lead to too high IRD counts. In particular, when counting in fractions <150 μm, airborne material like volcanic ash could falsely be identified as IRD. However, the capabilities of the M-G3 can be enhanced by adding Raman spectroscopy to the morphometric analysis, providing information on geochemistry and mineralogy, limiting potential misidentifications and enabling provenance studies. The instrument used for this study did not have this add-on installed.

The implementation of an algorithm could be a step to simplify the post-processing workflow of the M-G3 further. An algorithm, which counts, for example, macrofossils, already exists for other instruments, such as in the FlowCam VS (Fluid Imaging Technologies Inc., Scarborough, ME, USA), but is to the knowledge of the present authors not yet adapted for the M-G3.

Two potential pitfalls of the automated counting method became apparent during the sample runs. The possible misidentification of particles like foraminifera or shells could lead to too high lithic grain counts. However, the size of this error appeared negligible in the tests here. To completely eliminate this error, one could dissolve all biogenic matter in the sample, which would in turn improve the duration of post-processing significantly. However, this might have an effect on the grain-size distribution (Vasskog *et al.*, 2016) and would also dissolve lithic grains like chalk. Secondly, during the dispersion of the sample in the M-G3, the glass plate is raised to connect to the seal on the bottom of the dispersion cylinder. During the tests here, within a confidence interval of two sigma, 9·1 ± 2% of lithic grains and 9·4 ± 4% of

biogenic material per sample was getting stuck on the seal. This appears to be an inevitable, constructional, effect because a certain amount of material will always get lost on the seal of the dispersion cylinder, according to Malvern Instruments Limited (Willén, 2015). However, as the values of lost material were relatively constant throughout the performed tests, it appears that if one is interested in absolute IRD values, the relative amounts of lost material could be added to the total lithic grain and biogenic material counts.

Compared to other, more conventional instrumental techniques like laser diffraction analysis, the presented method is more time-consuming, but results in actual counts per sample weight and not a size fraction content in volume %. This offers the opportunity to calculate fluxes of the counted material. Furthermore, due to occasional high biogenic content, other methods would require chemical pretreatment to eliminate the biogenic components. As mentioned above, this can influence the grain-size distribution. In contrast, automatic filters and manual selection make it possible to separate biogenic material from lithic content in the M-G3. Finally, the presented workflow aims to simply automate a widely used technique and to remove an element of subjectivity. Through this, the method ensures direct comparability to new and previously published studies using manually counted IRD data sets.

CONCLUSIONS

The use of the 'Morphologi G3' (M-G3), in combination with the described post-processing workflow, offers an interesting and compatible option of acquiring high-resolution ice-rafted debris (IRD) flux records in a reasonable amount of time. Within the studied sedimentary setting, the acquired IRD content appears to be as representative as manually counted samples. The single sample turnover time is about 35 min on average, but because sample preparation or post-processing can be done simultaneously during the sample run, the absolute work time needed per sample is about 20 min. Two possible pitfalls were discovered during the sample runs, the potential misidentification of particles during post-processing and the loss of sample material during the dispersion step of the analysis could lead to an overestimation or underestimation of the counted IRD. However, the resulting error sizes appear to be constant and controllable. Other methods, such as laser diffraction analysis, could produce similar records more quickly, but not with absolute grain counts, inhibiting IRD flux calculations. Additionally, such methods would require chemical pretreatment of the samples, potentially influencing the grain-size distribution.

ACKNOWLEDGEMENTS

The research leading to these results has received funding from the GLANAM (GLAciated North Atlantic Margins) Initial Training Network, a People Program (Marie Curie Actions) of the European Union's Seventh Framework Program FP7/2007-2013 under REA grant agreement No. 317217. This work was additionally supported by the gender program ('likestillingsprogrammet') at the University of Bergen to B.O. Hjelstuen. All analyses were done at the national infrastructure EARTHLAB (NRC 226171) at the University of Bergen. The authors thank A. J.-G. Becker, J. Kuvås and D.I. Blindheim for their extensive laboratory work, U. Willén and G. Hansen at Malvern Nordic Sweden for discussion on the workflow, Helga (Kikki) Flesche Kleiven for comments on the manuscript and Benedict Reinardy for language editing. Additionally, we would like to thank the reviewers, Berg Flemming and Simon Blott for their valuable input.

REFERENCES

Alley, R.B. and **Macayeal, D.R.** (1994) Ice-rafted debris associated with binge/purge oscillations of the Laurentide Ice Sheet. *Paleoceanography*, **9**, 503–511.

Andrews, J. (2000) Icebergs and iceberg rafted detritus (IRD) in the North Atlantic: facts and assumptions. *Oceanography*, **13**, 100–108.

Bailey, I., **Foster, G.L.**, **Wilson, P.A.**, **Jovane, L.**, **Storey, C.D.**, **Trueman, C.N.** and **Becker, J.** (2012) Flux and provenance of ice-rafted debris in the earliest Pleistocene sub-polar North Atlantic Ocean comparable to the last glacial maximum. *Earth Planet. Sci. Lett.*, **341**, 222–233.

Bond, G.C. and **Lotti, R.** (1995) Iceberg discharges into the North Atlantic on millennial time scales during the last glaciation. *Science*, **267**, 1005–1010.

Bornhold, B.D. (1983) Ice-rafted debris in sediments from Leg-71, Southwest Atlantic-Ocean. *Init. Rep. Deep Sea Drilling Proj.*, **71**, 307–316.

Broecker, W., **Bond, G.**, **Klas, M.**, **Clark, E.** and **McManus, J.** (1992) Origin of the northern Atlantic's Heinrich events. *Clim. Dyn.*, **6**, 265–273.

Darby, D.A., **Ortiz, J.**, **Polyak, L.**, **Lund, S.**, **Jakobsson, M.** and **Woodgate, R.A.** (2009) The role of currents and sea ice in both slowly deposited central Arctic and rapidly

deposited Chukchi-Alaskan margin sediments. *Global Planet. Change*, **68**, 58–72.

Grobe, H. (1987) A simple method for the determination of ice-rafted debris in sediment cores. *Polarforschung*, **57**, 123–126.

Haapaniemi, A.I., **Scourse, J.D.**, **Peck, V.L.**, **Kennedy, H.**, **Kennedy, P.**, **Hemming, S.R.**, **Furze, M.F.A.**, **Pienkowski, A.J.**, **Austin, W.E.N.**, **Walden, J.**, **Wadsworth, E.** and **Hall, I.R.** (2010) Source, timing, frequency and flux of ice-rafted detritus to the Northeast Atlantic margin, 30-12 ka: testing the Heinrich precursor hypothesis. *Boreas*, **39**, 576–591.

Heinrich, H. (1988) Origin and consequences of cyclic ice rafting in the Northeast Atlantic Ocean during the past 130,000 years. *Quatern. Res.*, **29**, 142–152.

Joughin, I., **Smith, B.E.** and **Medley, B.** (2014) Marine Ice sheet collapse potentially under way for the Thwaites glacier basin, West Antarctica. *Science*, **344**, 735–738.

Lekens, W.A.H., **Sejrup, H.P.**, **Haflidason, H.**, **Knies, J.** and **Richter, T.** (2006) Meltwater and ice rafting in the southern Norwegian Sea between 20 and 40 calendar kyr BP: Implications for Fennoscandian Heinrich events. *Paleoceanography*, **21**, PA3013.

Malvern Instruments Ltd. (2013) Morphologi G3 user manual, issue 5, version MAN0410.

Malvern Instruments Ltd. (2017) Morphologi G3 - Advanced particle characterization made easy. Available at: http://www.malvern.com/en/products/product-range/morphologi-range/morphologi-g3/ (last accessed on 01.03.2017).

McCave, I.N. and **Syvitski, J.P.M.** (1991) Principles, methods, and application of particle size analysis. In: *Principles, Methods, and Application of Particle Size Analysis* (Ed. J.P.M. Syvitski), pp. 368. Cambridge University Press, Cambridge.

Ryżak, M. and **Bieganowski, A.** (2011) Methodological aspects of determining soil particle-size distribution using the laser diffraction method. *J. Plant Nutr. Soil Sci.*, **174**, 624–633.

Scourse, J.D., **Haapaniemi, A.I.**, **Colmenero-Hidalgo, E.**, **Peck, V.L.**, **Hall, I.R.**, **Austin, W.E.N.**, **Knutz, P.C.** and **Zahn, R.** (2009) Growth, dynamics and deglaciation of the last British-Irish ice sheet: the deep-sea ice-rafted detritus record. *Quatern. Sci. Rev.*, **28**, 3066–3084.

Sejrup, H.P., **Larsen, E.**, **Haflidason, H.**, **Berstad, I.M.**, **Hjelstuen, B.O.**, **Jonsdottir, H.E.**, **King, E.L.**, **Landvik, J.**, **Longva, O.**, **Nygard, A.**, **Ottesen, D.**, **Raunholm, S.**, **Rise, L.** and **Stalsberg, K.** (2003) Configuration, history and impact of the Norwegian Channel Ice Stream. *Boreas*, **32**, 18–36.

Vasskog, K., **Kvisvik, B.C.** and **Paasche, Ø.** (2016) Effects of hydrogen peroxide treatment on measurements of lake sediment grain-size distribution. *J. Paleolimnol.*, **56**, 365–381.

Vaughan, D.G. and **Arthern, R.** (2007) Why is it hard to predict the future of ice sheets? *Science*, **315**, 1503–1504.

Willén, U. (2015) Personal communication via e-mail on the 25th of August 2015. Global Sales Manager – Laser Diffraction & Imaging, Malvern Nordic Sweden.

Manuscript received 2 March 2017; revision accepted 3 August 2017

Supporting Information

Additional Supporting Information may be found in the online version of this article:

Figure S1. Set-up of the Standard Operating Procedure (SOP).
Figure S2. Set-up of the SOP (continued).
Figure S3. Set-up of the workspace.
Figure S4. Post-processing workflow (part 1).
Figure S5. Post-processing workflow (part 2).
Figure S6. Post-processing workflow (part 3).
Figure S7. Post-processing workflow (part 4).
Figure S8. Post-processing workflow (part 5).
Figure S9. Post-processing workflow (part 6).
Figure S10. Post-processing workflow (part 7).

Sedimentology

Supporting Information for:

Automated counting of sand sized particles in marine records

Lukas W. M. Becker, Berit Oline Hjelstuen, Eivind W. N. Støren, Hans Petter Sejrup

Department of Earth Science, University of Bergen

Contents of this file

Figures S1 to S10

Introduction

The described workflow of the Standard Operating Procedure (SOP) setup and the sample pre- and post processing is here supported with the corresponding screenshots from the Malvern Instruments Ltd. proprietary software “Morphologi”, version 8.12. The supplementary material can be used as a manual for the described workflow.

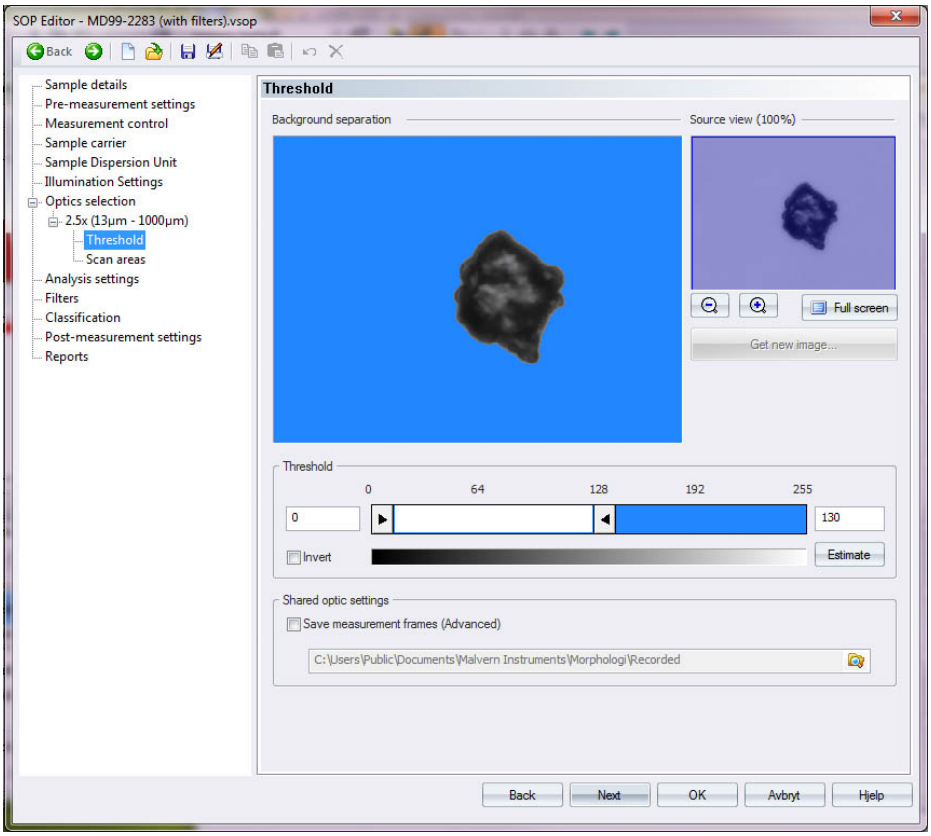

Figure S1. The setup-window of a Standard Operating Procedure (SOP). The sample details, Sample Dispersion Unit settings and the appropriate optics are set. The "Threshold" is set to a value which eliminates background noise and images the outline of the particle correctly. Usually, only a fine adjustment from the estimated ("Estimate" button) value has to be done. Note that a test sample has to be dispersed in the instrument to be able to set these parameters. A new SOP can be created via "File –> New –> SOP".

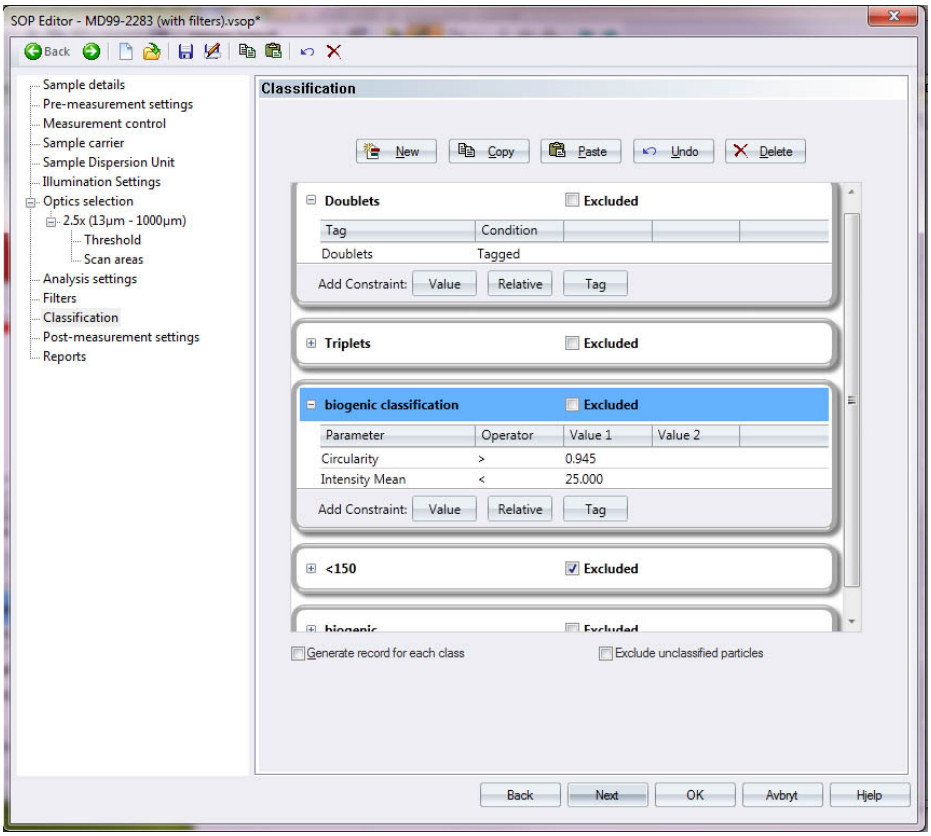

Figure S2. Setup of the SOP (continued). The desired classification parameters are set in this menu. Biogenic material is classified by circularity and intensity mean (degree of opaqueness) and all material < 150 µm is excluded. The post processing is prepared by including doublets, triplets, biogenic and single_d/t with the condition "tagged". This setting displays the sum of all counted particles within the respective tagging group as a "classification".

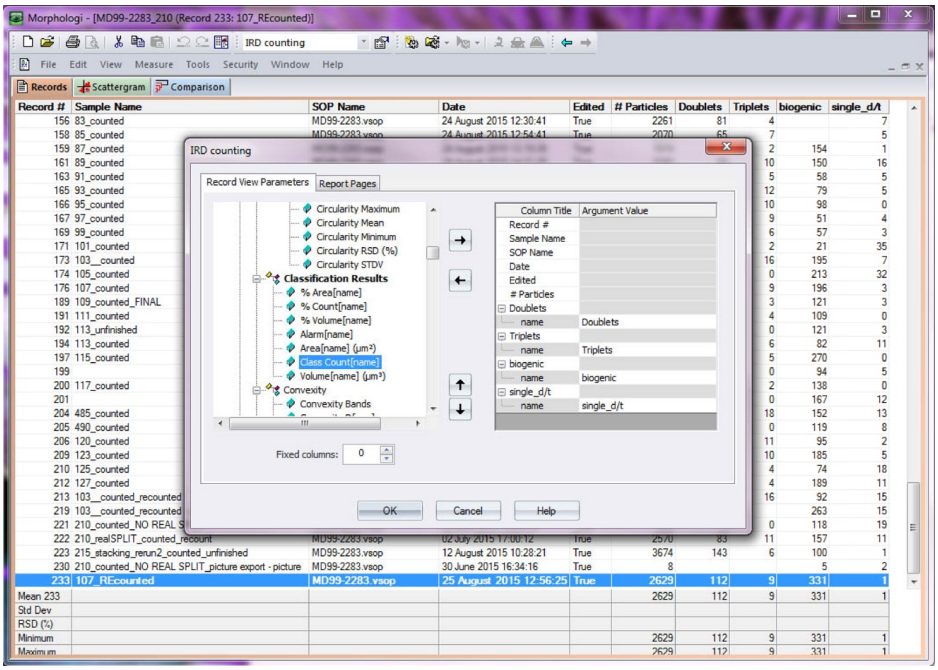

Figure S3. Setup of the workspace. The workspace displays the contents of the file in which all records are stored. The workspace can be exported as a txt file via “File -> Export -> Export Result”. All counts within a classification can be displayed in the workspace. The setting “Class Count [name]” is added for every classification that should be displayed. This setting can be found under “Measurement -> Morphology -> Classification Results”. Note that the “Argument Value” has to be exactly the same as the name of the classification in the SOP. A new workspace can be created via “View -> Workspace -> Add Workspace”.

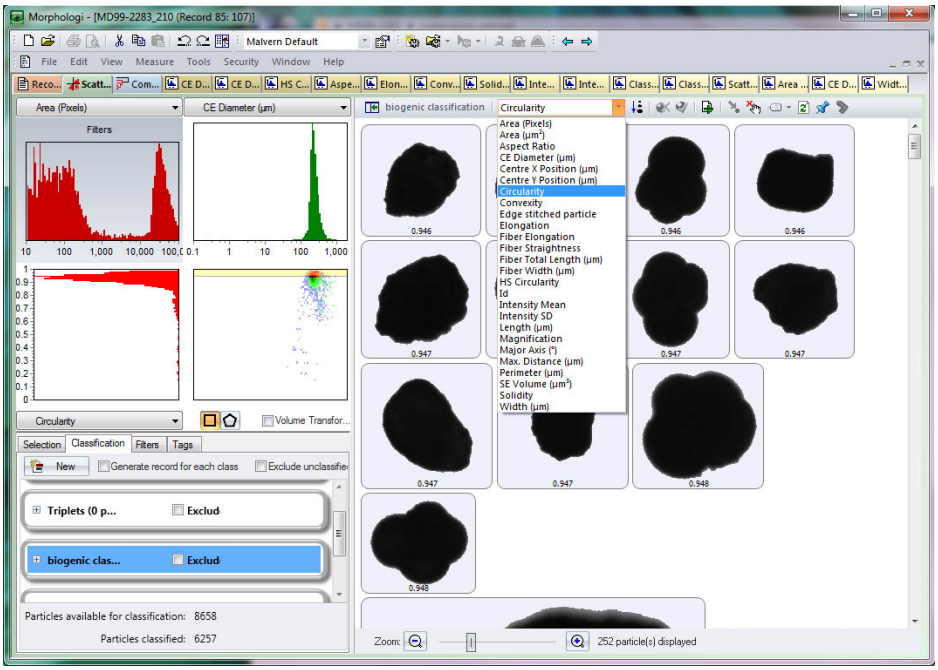

Figure S4. Post processing workflow (part 1). A sample run is opened and "biogenic classification" selected in the Classification menu. The particles are sorted by increasing circularity.

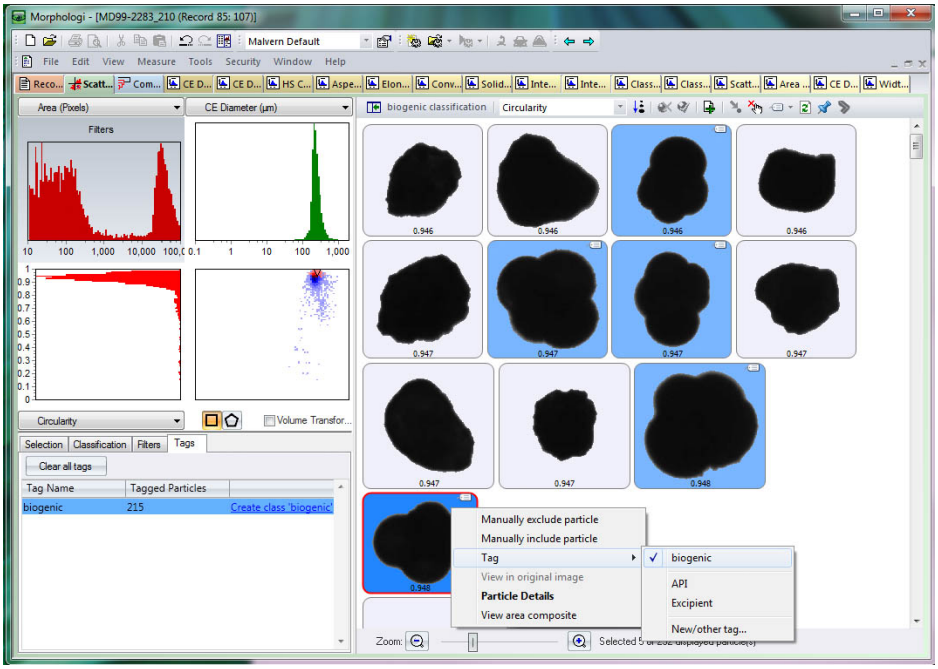

Figure S5. Post processing workflow (part 2). All particles are selected with the keys STRG + A. All particles which appear not to be biogenic are deselected without releasing the STRG key. By right-clicking on one of the biogenic particles the menu to tag the particles with “biogenic” will open. For each new sample the tag has to be created once during post-processing by clicking on “New/other tag…”. The spelling of the tag has to be exactly the same as earlier set in the SOP.

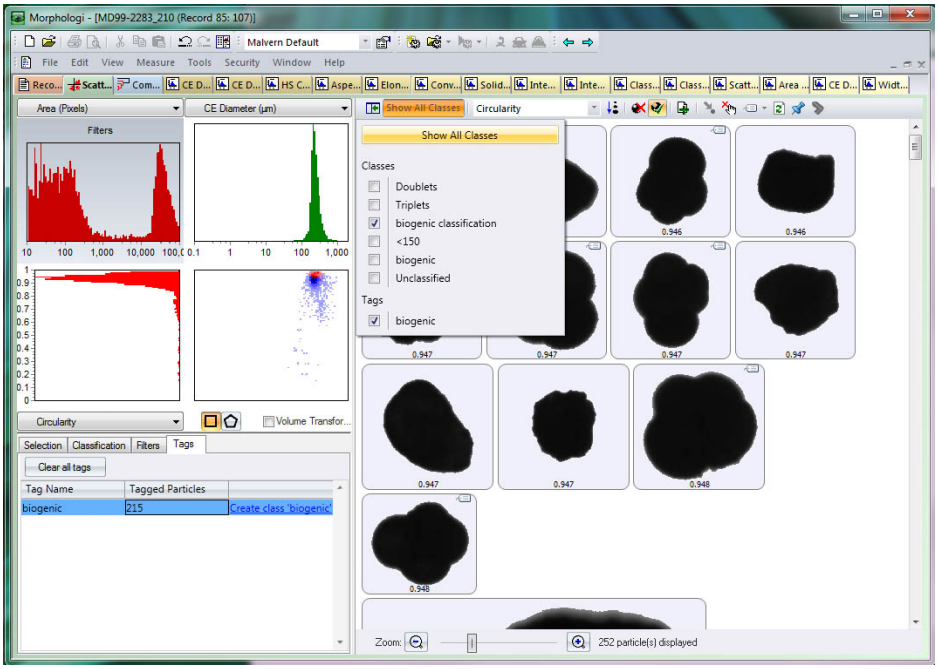

Figure S6. Post processing workflow (part 3). All particles of the currently opened record are displayed by clicking on “Show All Classes”. The sorting continues to be set on decreasing circularity.

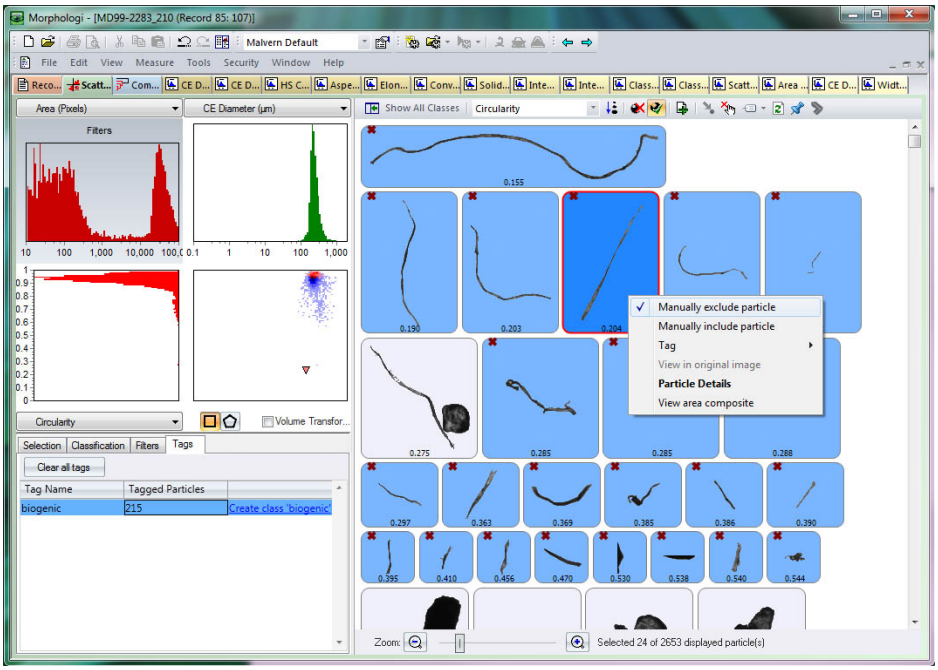

Figure S7. Post processing workflow (part 4). All artifacts, those with the lowest circularity values, are now displayed at the top. The artifacts are then selected and consecutively manually excluded by clicking on “Manually exclude particle”. The selected particles will be displayed with a red cross at first, but will automatically not be shown in the following step.

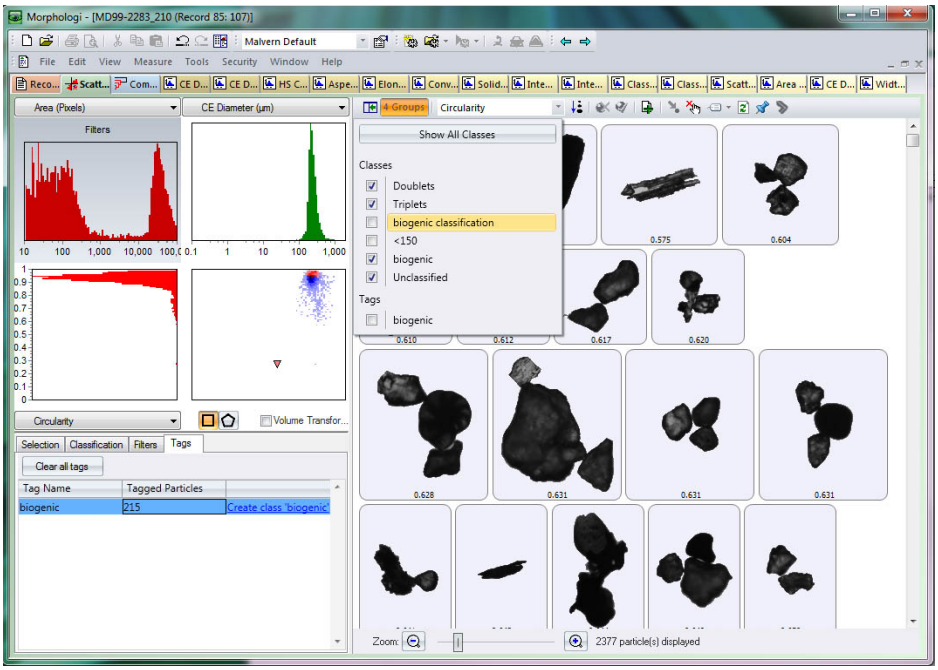

Figure S8. Post processing workflow (part 5). To complete the post processing the "biogenic classification" and "<150 µm" classes and the "biogenic" tags are disabled. All doublets and triplets should now be displayed at the top.

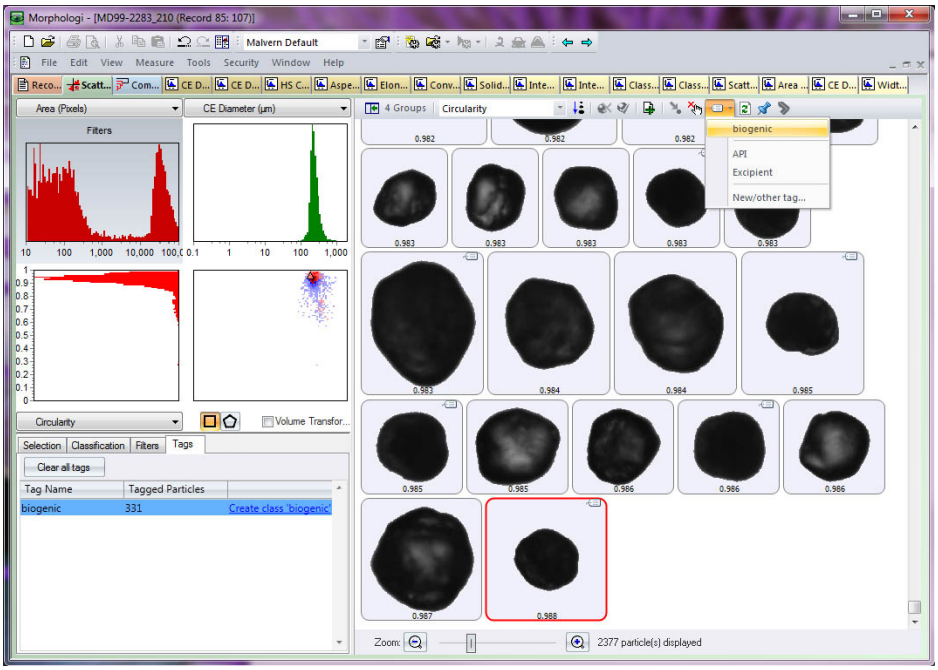

Figure S9. Post processing workflow (part 6). The tagging tool in the upper right hand corner is now selected with the tag “biogenic”. All additional biogenic particles, that were not already included in the “biogenic classification”, are tagged.

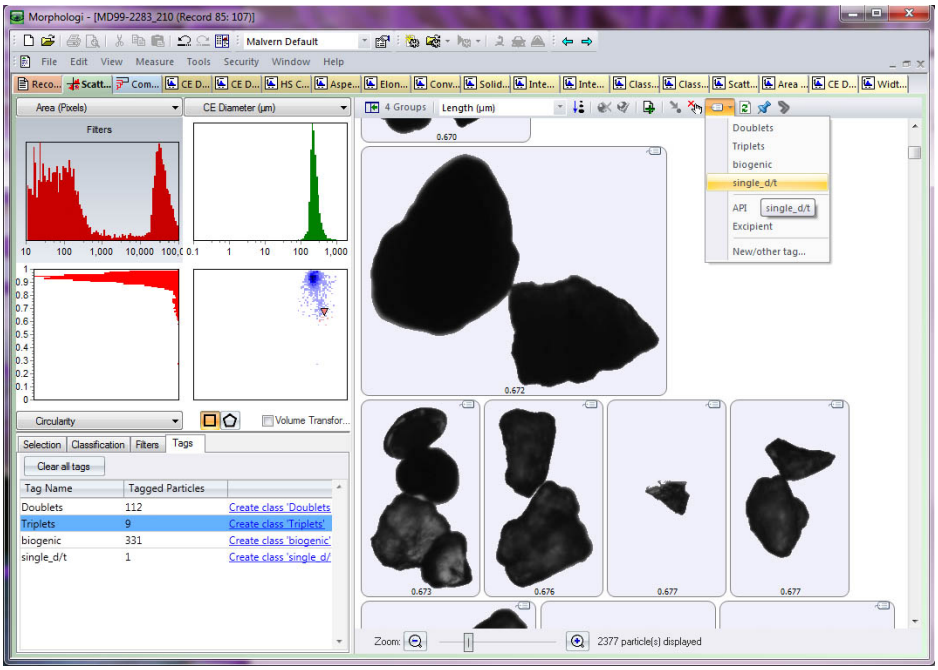

Figure S10. Post processing workflow (part 7). The same process as described in Figure S9 is repeated for doublets and triplets, where each tag has to be created again with the exact same spelling as set in the SOP. Shapes with four or more particles have to be split up into doublets and triplets. In this case the four particles on the lower left corner were tagged “Doublets” and the single particle on the right side was tagged with “Doublets” and “single_d/t” to account for the other two particles, as described in the manuscript. A click on the tab “record view” on the upper left corner displays again the workspace. A prompt appears to save the post processed file. The file is saved under the prior sample identification and the addition “_processed”.

II

Ocean-ice sheet interaction along the SE Nordic Seas margin from 35 to 15 ka BP

Lukas W.M. Becker, Hans Petter Sejrup, Berit O. Hjelstuen,
Haflidi Haflidason and Trond M. Dokken

In press in Marine Geology, GLANAM special issue,
http://dx.doi.org/10.1016/j.margeo.2017.09.003

Marine Geology xxx (xxxx) xxx–xxx

Contents lists available at ScienceDirect

Marine Geology

journal homepage: www.elsevier.com/locate/margo

Ocean-ice sheet interaction along the SE Nordic Seas margin from 35 to 15 ka BP

Lukas W.M. Becker[a,*], Hans Petter Sejrup[a], Berit O. Hjelstuen[a], Haflidi Haflidason[a], Trond M. Dokken[b,c]

[a] Department of Earth Sciences, University of Bergen, Norway
[b] Uni Research, Bergen, Norway
[c] Bjerknes Centre for Climate Research, Bergen, Norway

ARTICLE INFO

Keywords:
IRD
Multi-proxy
Norwegian Channel Ice Stream
NE Atlantic margin
Ice sheet variability
Last Glacial Maximum

ABSTRACT

Sediment cores from the south-eastern Nordic Seas simultaneously archive the variability of the Fennoscandian Ice Sheet (FIS), the British-Irish Ice Sheet (BIIS) and the regional oceanic conditions. This study aims to contribute to our understanding of the marine-based section of the FIS and the BIIS between 35,000 and 15,000 years BP, by using cores MD99-2283, MD99-2284 and MD99-2289, retrieved along the upper continental slope between the Faroe-Shetland Channel and the Vøring Plateau. For this, we present a revised, radiocarbon based, Bayesian modelled chronological framework and a compilation of new and published sedimentological, geochemical and micro-paleontological datasets. Our results show a possibly first Weichselian FIS/BIIS confluence at ca. 25,500 years BP in the central North Sea, which buttressed the BIIS to the East, potentially leading to a northwards BIIS deflection via the Shetlands. The Norwegian Channel Ice Stream (NCIS) most likely only reached the shelf edge after 23,300 ± 500 years BP, possibly for the first time during the Weichselian. The NCIS onset directly preceded a pronounced influx of warm Atlantic water to the northern North Sea margin possibly implying forcing through ocean melt. We find a highly variable NCIS, with three ~1400 yearlong episodes of increased ice rafted debris flux interrupted by ~600 yearlong minima. When compared to other sides of the European Ice Sheet, these episodes appear to correlate well, suggesting a common forcing mechanism. In conclusion, our data supports recent suggestions that the last glacial stage of the BIIS was more extensive in the central North Sea and the confluence later than previously thought.

1. Introduction

Large landmasses in the Northern Hemisphere have been covered repeatedly by continental ice sheets throughout the Quaternary. The world's last two continental ice sheets today, on Greenland and Antarctica, are experiencing an ongoing and, in terms of speed, possibly unprecedented loss of ice mass within the last decades, as emphasized in the last report by the Intergovernmental Panel on Climate Change (Vaughan et al., 2013). The retreat of these ice sheets, associated with potential sea level changes and the influence on the climate system, is assumed to have a large environmental impact worldwide (Vaughan et al., 2013). The increased freshwater delivery to the North Atlantic has the possible impact of reducing the strength of the Atlantic Meridional Overturning Circulation (Broecker et al., 1985; Rahmstorf et al., 2015; Liu et al., 2017), which is in turn proposed to result in large-scale restructuring of our climate system (Hall et al., 2006).

The understanding of the mechanisms controlling ice sheet decay and the associated speed of these processes, still remains fragmentary. Research on paleo-ice sheets and numerical modelling of ice sheets is today receiving increased attention in an effort to decipher the complex responses of present ice sheets to a warming climate. Within the last decade, there has been a growing focus on marine-based parts of ice sheets and their interaction with ocean circulation (Rise et al., 2005; Lekens et al., 2006; Knutz et al., 2007; Alvarez-Solas et al., 2011; Crocker et al., 2016; Wary et al., 2016). To be able to develop and test climate models, detailed knowledge about the timing and the mechanism behind the initiation, dynamics and decay of the marine-based fraction of continental ice sheets is essential (Bentley et al., 2014).

The aim of this study is to contribute to our understanding of the timing of ice sheet advances and instabilities along the south-eastern Nordic Seas continental margin. This is done by compiling a series of well-dated cores from the region (Fig. 1A), covering the Middle and Late Weichselian, focusing on the time period between 35 and 15 ka before present (BP). Additionally, the observed ice sheet variability will

* Corresponding author.
E-mail address: lwmbecker@gmail.com (L.W.M. Becker).

http://dx.doi.org/10.1016/j.margeo.2017.09.003
Received 21 April 2017; Received in revised form 23 August 2017; Accepted 4 September 2017

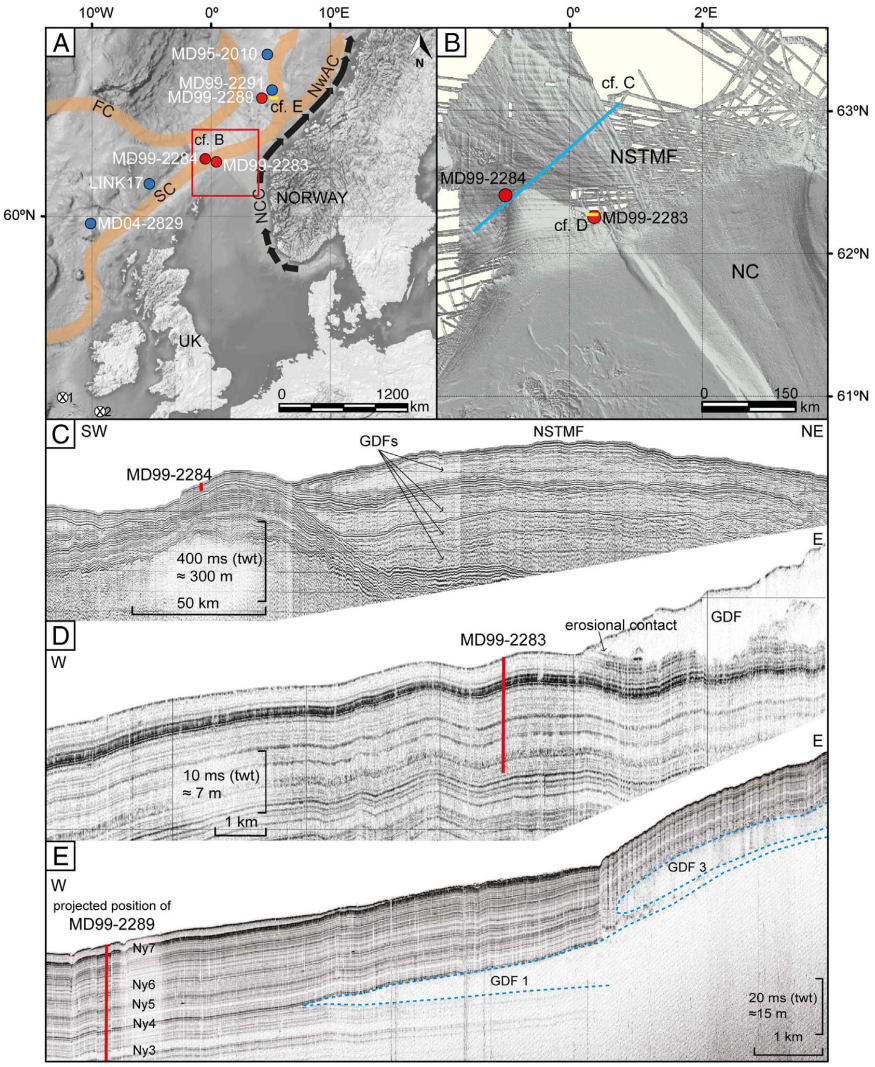

Fig. 1. (A) The southern Norwegian Sea, red dots indicate studied cores, blue dots reference cores. X1: MD01-2461 (Peck et al., 2006), X2: 300 km north of MD95-2002 (Toucanne et al., 2015). Modern surface currents, the Faroe- (FC), Shetland- (SC), Norwegian Atlantic- (NwAC) and the Norwegian Coastal Current (NCC) are indicated (Hansen and Østerhus, 2000). (B) Seabed character of the northern North Sea margin and the Norwegian Channel (NC); bathymetric data from Olex AS. MD99-2284 and MD99-2283 are separated by a submarine bulge. (C) A deep-tow boomer profile crossing the > 300 m thick North Sea Trough Mouth Fan (NSTMF), position indicated in B. The profile is reproduced with the permission of the British Geological Survey ©NERC. All rights reserved. (D) TOPAS high-resolution seismic profile, as indicated in B, demonstrating the position of MD99-2283 relative to the youngest described glacigenic debris flow (GDF). Several layers of sediment are visible below the GDF, which postdate the core top of MD99-2283. (E) TOPAS high-resolution seismic profile, as indicated in A, visualizing the stratigraphic position of MD99-2289 relative to the last GDFs. This profile is modified after Reiche et al. (2011). (For interpretation of the references to colour in this figure legend, the reader is referred to the web version of this article.)

be related to changes in ocean surface circulation in the south-eastern Nordic Seas. With this, a special focus will be set on the investigation of the timing of Norwegian Channel Ice Stream (NCIS) activity combined with new insights into the timing of British-Irish Ice Sheet (BIIS) and Fennoscandian Ice Sheet (FIS) confluence in the central North Sea.

2. Background

The Eurasian Ice Sheet, consisting of the FIS, the BIIS and the Barents-Kara Ice Sheet, encompassed a large marine-based section during maximum extension (Sejrup et al., 2005; Lee et al., 2012; Hughes et al., 2015). The location of the Eurasian Ice Sheet made it particularly vulnerable to ocean melt forcing through the inflow of warm Atlantic waters along the continental margin (Joughin et al., 2012). A high co-variability of the BIIS with changes in ocean sea surface temperature, that is, the position of the polar front, has been suggested (Scourse et al., 2009; Hall et al., 2011). Even though the maximum extension of the western oceanic border of the Eurasian Ice Sheet within the Last Glacial Maximum (LGM) is rather well documented (Dahlgren and Vorren, 2003; Sejrup et al., 2005; Clark et al.,

Table 1
Position, data origin and number of accelerator mass spectrometry radiocarbon dates of the cores used in this study including the individual original data sources. Reference cores are in italics.

Core	ID	Position	Water depth [mbsl]	Grain size distribution	IRD counts	Foraminifera counts	Isotope (∂18O) sampling	ITRAX data	C14 dating	Number of C14 dates	Age model	References
MD95-2010	*MD95*	*66.684167°, 4.566160°*	*1226*	–	(1)	(2) & *this study*	(1)	–	(1)	*26*	*This study*	(1) *Dokken and Jansen (1999)*; (2) *Dokken et al. (2015a)*
MD99-2291	*MD91*	*64.938667°, 5.592000°*	*577*	–	*This study*	(2)	(2)	–	(*1 & 2*)	*12*	*This study*	(1) *Hjelstuen et al. (2004)*; (2) *Lekens et al. (2005)*
MD99-2289	MD89	64.6680556°, 4.2263889°	1262	(1)	(2)	(2) & this study	(2)	This study	(2) & this study	25	This study	(1) Hafildason et al. (2003); (2) Berstad et al. (2003)
MD99-2283	MD83	62.261167°, 0.414000°	*707*	(1) & this study	This study	This study	(1)	This study	(1)	21	This study	(1) Lekens et al. (2006)
MD99-2284	MD84	62.374667°, −0.980167°	1500	This study	(2) & This study	(3) & this study	This study	This study	(1) & this study	27	This study	(1) Risebrobakken et al. (2011); (2) Dokken et al. (2013); (3) Dokken et al. (2015b)
LINK17	*LINK17*	*61.000000°, −5.000000°*	*1500*	–	(1)	(1)	(1)	–	(1)	*11*	*This study*	(1) *Rasmussen and Thomsen (2008)*
MD04-2829	*MD04*	*58.948830°, −9.571670°*	*1743*	–	(1)	(1)	(1)	–	(2)	*24*	*This study*	(1) *Scourse et al. (2009)*; (2) *Hall et al. (2011)*

2012; Hughes et al., 2015; Ottesen et al., 2016), the timing and structure of the build-up and deglaciation can still be refined further.

Until recently, it was widely accepted that the FIS and the BIIS were in confluence across the central North Sea between about 31–24 ka BP (Sejrup et al., 1994; Bradwell et al., 2008; Ehlers and Gibbard, 2008; Sejrup et al., 2009; Toucanne et al., 2010; Sejrup et al., 2015). Based on mapping of landforms and a compilation of data from sediment cores within the North Sea region, Sejrup et al. (2016) suggested that the two ice sheets were in confluence in the central North Sea at 23 ka BP until separating at 18.5 ka BP, but without stating the onset of confluence. Along the Mid-Norwegian margin the FIS is suggested to reach the shelf edge by 24 ka BP, marked by the deposition of glacigenic debris flows (Dahlgren et al., 2002; Dahlgren and Vorren, 2003; Hjelstuen et al., 2005).

The eastern section of the North Sea is characterized by the Norwegian Channel (Fig. 1A), a distinct ca. 850 km long morphological feature, 70–150 km in width and 280–700 m in depth (Rise et al., 2008). The morphology of the Norwegian Channel is to a large extent the product of multiple periods of ice streaming of the NCIS within the last 1.1 million years (Sejrup et al., 2003; Nygård et al., 2005; Reinardy et al., 2017). The last active period of the NCIS is reported to have taken place during the LGM and until the onset of deglaciation at around 19 ka BP (Lekens et al., 2006; Nygård et al., 2007), with estimated sediment fluxes of ca. 8000 cubic meters per year, per meter ice front (Nygård et al., 2007). However, the onset of NCIS ice streaming during the LGM or any inter-LGM variability remains unclear and challenging to determine, as with most paleo-ice streams (Margold et al., 2015).

The timing of retreat from the maximum LGM ice stand position, that is, the shelf edge, is assumed to have differed along the northwestern European margin. Studies agree on an early retreat of the BIIS along its western margin after 24 ka BP (e.g. Peck et al., 2006; Bigg et al., 2012), while the FIS along the northern North Sea margin is thought to have stayed grounded on the shelf edge until about 19 ka BP (King et al., 1998; Nygård et al., 2007; Sejrup et al., 2016). On the Mid-Norwegian margin the onset of retreat is reported to have been before 17 ka BP (Dahlgren and Vorren, 2003; Hjelstuen et al., 2005). Additionally, shell fragments in till on the same margin suggested grounded ice at the shelf edge until after 18.1 ka BP (Rokoengen and Frengstad, 1999). Following the retreat from the northern North Sea margin, recent work suggests that the NCIS had withdrawn to the innermost parts of the Norwegian Channel (Skagerrak) by 17.6 ka BP (Morén et al., 2017), which agrees with terrestrial data (Sejrup et al., 1998; Sejrup et al., 2009; Houmark-Nielsen et al., 2012; Anjar et al., 2014; Svendsen et al., 2015; Briner et al., 2016).

The along-shelf deglaciation signal is briefly halted on the Mid-Norwegian margin, where Nygård et al. (2004) describe a glacial re-advance (the Bremanger re-advance) around 16–17 ka BP onto the Måløy Plateau (Fig. 1A), which is believed to coincide with a re-advance from the Shetlands into the Fladen area (Sejrup et al., 2015).

The present-day surface current system in the studied region comprises of two branches of North Atlantic Water, the Shetland and the Faroe currents, entering the Nordic Seas across the Wyville-Thomson and the Iceland-Faroe Ridges (Hansen and Østerhus, 2000). The Shetland Current continues along the shelf edge northwards and across the Vøring Plateau as the Norwegian Atlantic Current (NwAC) (Fig. 1A). Additionally, along the coastline of Norway, the Norwegian Coastal Current transports Norwegian Coastal water northwards (Fig. 1A) (Hansen and Østerhus, 2000). Position, speed and depth of the NwAC were variable within the last glacial cycle (Rasmussen and Thomsen, 2008), with sluggish current speeds during stadials and increased flow, sorting deposits, within interstadials (Kissel et al., 1998; Dahlgren and Vorren, 2003). During the LGM, NwAC speeds along the Mid-Norwegian margin are reportedly low before the ice sheet reached the shelf edge, medium strong and able to sort sands during maximum ice advance, while strong after the onset of the last deglaciation, leading to winnowing and non-deposition (Dahlgren and Vorren, 2003).

3. Material and methods

3.1. Core locations

This study is based on a compilation of new and previously published data from the giant CALYPSO piston cores MD99-2283, MD99-2284, MD99-2289 (hereafter MD83, MD84 and MD89), raised from the south-eastern Nordic Seas margin in 1999 (Fig. 1A, Table 1). The sedimentological, geochemical, micro-paleontological and stable isotope records from these cores are compared to published data from cores MD04-2829, LINK17, MD99-2291 and MD95-2010 (Table 1) roughly taken along the approximate track of the NwAC (Fig. 1A). Together, these cores form a 1100 km long transect from Rosemary Bank, northeast of Scotland, to the northern Vøring Plateau in the eastern Norwegian Sea, enabling a spatial overview of the western margin of the Eurasian Ice Sheet, extending the work of Scourse et al. (2009) northwards.

A set of sub-bottom profiles is applied to illustrate the regional and depositional context of the studied cores (Fig. 1A and B). The profiles are a deep-towed boomer line made available by the British Geological Survey (Fig. 1C) and two 2D TOPAS high-resolution profiles (Fig. 1D and E), of which the latter is a modification of Fig. 2b in Reiche et al. (2011). To convert sediment two-way-travel time into meters, we have used the velocity of 1600 m/s.

Core MD84 was retrieved from a sediment package composed of acoustically well-laminated facies, suggesting hemipelagic deposits, that appear to drape an old, deep feature (Fig. 1B and C). The eastern section of the available boomer profile (Fig. 1C) cuts through the thick package of glacigenic debris flows forming the North Sea Trough Mouth Fan. These glacigenic debris flow deposits are assumed to reflect the long history of the NCIS throughout the Quaternary (King et al., 1996; Sejrup et al., 2003; Nygård et al., 2005). Cores MD83 and MD84 are located 75 km apart, but differ almost 800 m in water depth (Table 1). The location of core MD83 is about 40 km north-west of the shelf break, at the mouth of the Norwegian Channel (Fig. 1B) and thus downstream of the NCIS. The position of MD83 (Fig. 1D) is about 2 km west of the youngest identified glacigenic debris flows of the North Sea Trough Mouth Fan (Nygård et al., 2005).

The glacigenic debris flows appear to have protected the underlying hemipelagic sediments from the vigorous NwAC flowing along the margin (Fig. 1D), especially since the onset of the last deglaciation (Sejrup et al., 1981; Jansen et al., 1983). This can be observed by tracing the first identified reflector below the seabed from the core site of MD83 to the East (Fig. 1D), which reveals a maximum thickness of about 1.5 ms (~1 m) of hemipelagic deposits beneath the contact to the overlying glacigenic debris flow. This implies some additional time of hemipelagic sedimentation before deposition of the glacigenic debris flow, compared to the age of the core top of MD83. This observation fits well with previous work on the North Sea Fan, where the last glacigenic debris flows have been dated to have been deposited before 19.1 ka BP (King et al., 1998).

Core MD89 was raised from the south-western flank of the Vøring Plateau in a hemipelagic setting (Haflidason et al., 2003), about 100 km to the west of the last deposited glacigenic debris flows, identified on the southern part of the Vøring Plateau (Reiche et al., 2011).

3.2. Chronology

This study adds 33 new accelerator mass spectrometry (AMS) radiocarbon dates (Table 2) to the 113 previously published dates from the same cores (Table S1). In addition, the Faroe Marine Ash Zone (FMAZ) II, dated to 26.69 ± 0.39 ka BP (Davies et al., 2008) has in this study been identified in MD83 and previously in MD84 (Dokken et al., 2013) and MD89 (Nilsen, 2014) (Table 2).

Earlier studies in the region have either constructed age models based on radiocarbon dates (e.g. Haflidason et al., 1998; Lekens et al., 2005) or have relied on tuning proxy records to Greenland ice core stratigraphies (Haflidason et al., 1995; Seierstad et al., 2014). Such tuning to Greenland Stadials and Interstadials has been based on the variability in the relative abundance of sub-polar planktonic foraminifera (e.g. Scourse et al., 2009; Hall et al., 2011; Crocker et al., 2016; Rasmussen et al., 2016), magnetic susceptibility records (e.g. Stanford et al., 2011; Dokken et al., 2013; Wary et al., 2016) or

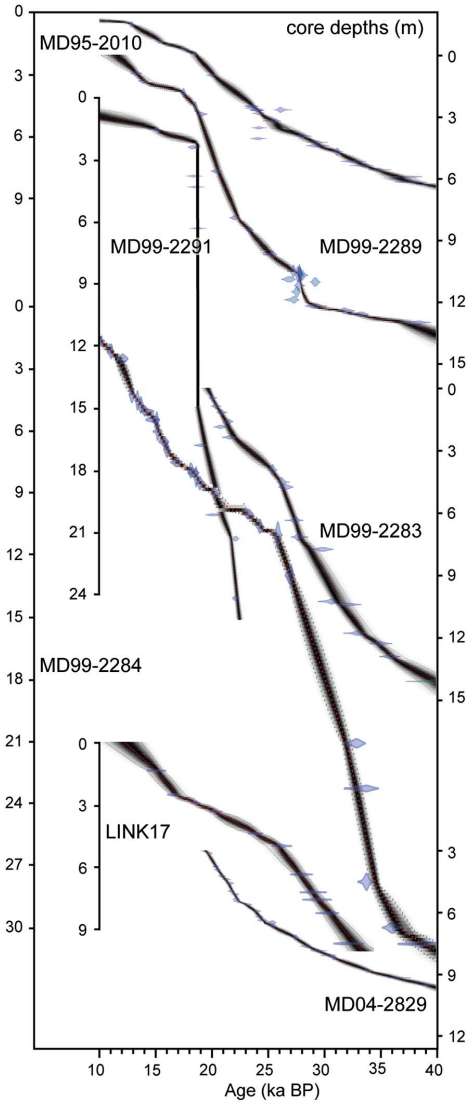

Fig. 2. Individual age models of all cores in this study. The age models are based on 142 accelerator mass spectrometry radiocarbon dates (Table S1) and are computed with the R-based script Bacon (Blaauw and Christen, 2011). The red line marks the weighted mean, the grey shaded area displays the two-sigma uncertainty of each depth in the core. The darker the grey tone, the higher the age model certainty. In core MD99-2283 the Laschamp magnetic reversal was used as an additional age model constraint. Core MD99-2291 was modelled without the proposed plume event (2.8–15 m core depth). No local reservoir correction was applied. (For interpretation of the references to colour in this figure legend, the reader is referred to the web version of this article.)

Table 2
New accelerator mass spectrometry radiocarbon dates for cores MD83, MD84 and MD89 including the identified Faroe Marine Ash Zone (FMAZ) II. Nps (*N. pachyderma* sinistral).

Core	Lab number	Core depth, void corrected (cm)	Material	14C Age, uncorrected (ka BP)	Calendar age (ka BP)	S.D. 1 σ (ka)	Calibrated, modelled age (cal ka BP)	S.D. 2 σ (ka)	Different between calendar and modelled age (ka)	Reference	Info
MD99-2289	ETH-55533	86.8	Nps	11.78		0.18	13.25	0.36		This study	
MD99-2289	Beta 414663	182.0	Planktonic foraminifera	14.72		0.04	17.39	0.19		This study	
MD99-2289	Beta 380040	248.8	Nps	15.63		0.05	18.47	0.14		This study	
MD99-2289	Beta 380041	850.1	Nps	19.79		0.07	23.29	0.28		This study	
MD99-2289	Beta 376421	1049.9	Nps	23.24		0.10	27.14	0.37		This study	
MD99-2289	Beta 376422	1059.8	Nps	24.08		0.09	27.64	0.17		This study	
MD99-2289	Beta 373227	1062.8	Nps	24.14		0.12	27.68	0.13		This study	
MD99-2289	FMAZ II	1063.8	Tephra		26.69	0.39	27.70	0.11	− 1.01	Nilsen (2014)	Not in age model
MD99-2289	Beta 365943	1064.8	Nps	23.83		0.11	27.71	0.10		This study	
MD99-2289	Beta 376423	1069.8	Nps	24.40		0.11	27.78	0.07		This study	
MD99-2289	Beta 380041	1072.8	Nps	24.20		0.09	27.79	0.07		This study	
MD99-2289	Beta 380043	1102.8	Nps	25.54		0.11	27.88	0.07		This study	
MD99-2289	Beta 380044	1171.8	Nps	27.79		0.13	28.24	0.21		This study	Rejected-reworked
MD99-2289	Beta 380045	1242.8	Nps	28.50		0.14	31.27	0.86		This study	
MD99-2283	ETH-72933	334.8	Nps	19.90		0.07	24.18	0.67		This study	Rejected-too young
MD99-2283	BETA-429895	392.3	Nps	21.51		0.07	25.37	0.28		This study	
MD99-2283	BETA-429889	449.4	Nps	22.48		0.08	26.14	0.23		This study	
MD99-2283	FMAZ II	634.4	Tephra		26.69	0.39	27.47	0.29	− 0.78	This study	Not in age model
MD99-2284	Tua-3305	450.5	Nps	11.96		0.09	13.42	0.15		This study	
MD99-2284	Tua-3987	472.5	Nps	12.24		0.08	13.73	0.17		This study	
MD99-2284	Tua-3988	502.5	Nps	12.60		0.13	14.17	0.35		This study	
MD99-2284	Tua-3989	543.5	Nps	12.98		0.13	14.92	0.25		This study	
MD99-2284	POZ-10154	546.5	Nps	13.08		0.06	14.94	0.23		This study	
MD99-2284	KIA-10678	600.5	Nps	13.15		0.07	15.30	0.22		This study	
MD99-2284	Tua-3306	650.5	Nps	13.55		0.10	15.77	0.24		This study	
MD99-2284	POZ-10155	687.5	Nps	13.71		0.06	16.09	0.19		This study	
MD99-2284	Tua-3990	749.5	Nps	14.32		0.12	17.00	0.35		This study	
MD99-2284	POZ-10156	788.5	Nps	15.33		0.07	18.11	0.24		This study	
MD99-2284	Tua-3307	800.5	Nps	15.55		0.19	18.41	0.25		This study	
MD99-2284	POZ-10157	819.5	Nps	15.73		0.07	18.64	0.17		This study	
MD99-2284	Tua-3991	849.5	Nps	16.11		0.12	19.04	0.24		This study	
MD99-2284	Tua-3308	900.5	Nps	17.20		0.09	20.22	0.27		This study	
MD99-2284	Tua-3309	1000.5	Nps	19.73		0.12	23.19	0.39		This study	
MD99-2284	BETA-429891	1058.5	Nps	20.59		0.08	24.26	0.27		This study	
MD99-2284	BETA-429890	1295.5	Nps	23.02		0.08	26.99	0.31		This study	
MD99-2284	FMAZ II	1407.5	Tephra		26.69	0.39	27.67	0.49	− 0.98	Dokken et al. (2013)	Not in age model

variations in relative Ca-concentration in X-ray Fluorescence (XRF) core scanner data (Lekens et al., 2006; Brendryen et al., 2010).

In this study, all age models are based solely on radiocarbon dates. The rationale behind this is to be able to compare the proxy records from the margin to the development of the marine-based parts of the FIS and the BIIS on the continental shelf, as these records are largely based on radiocarbon dates on marine carbonates (e.g. Sejrup et al., 2016). During the age model run all dates were (re-)calibrated with Marine13 (Reimer et al., 2013), including a 405-year global reservoir correction. No further local reservoir correction was applied. The changes in local reservoir effect are considered to be similar along the south-eastern Nordic Seas margin, making the presented cores comparable to each other within individual age model uncertainties.

The age models cover the time interval 40–10 ka BP (Fig. 2) and are constructed with the R-based, Bayesian age modelling script "Bacon" (v.2.2) (Blaauw and Christen, 2011). All age models were constructed with an accumulation rate distribution width of 1.5, a student-t distribution and a section thickness depending on the required flexibility in each core (Blaauw and Christen, 2011). The section thickness was set to the smallest possible value, which still allowed the age model to be run within the 2-sigma standard deviation of each calibrated radiocarbon date. Outliers were removed in core MD91 (reworking in 2 samples described in Lekens et al., 2005), in MD89 (one sample out of context) and in MD83 (two apparently too young ages). In core MD83 the Laschamp palaeomagnetic reversal (Lekens et al., 2006) was used to constrain the age model in its oldest section. The above described FMAZII tephra was not included in any age model run and is just used to validate the tentative tuning of the archives to the ∂ 18O data from the Greenland ice core GISP2.

The age model of core MD91 however required some additional measures, as a sudden, pronounced change in accumulation rate in the core surpasses the capabilities of Bacon. Nearly 14 m of the core is related to a rapidly deposited meltwater plume along the Mid-Norwegian margin, dated to about 18.5 ka BP (Hjelstuen et al., 2004; Lekens et al., 2005; Reiche et al., 2011; Sejrup et al., 2016; Hjelstuen et al., this issue). Thus, the previously identified "UNT6" (Reiche et al., 2011) between reflectors Ny7 (280.5 cm) and Ny6 (1720.5 cm) (Fig. 1E) was removed during age modelling in this study (Fig. 2). Through re-evaluation of core and TOPAS data, reflector Ny6 was moved to 1500 cm core depth in MD91. This section was afterwards added back into the depth scale and the sedimentation between the top and bottom point of the plume event was regarded as linear (Fig. 2). Any possible variability of the sedimentation rate within the plume can therefore not be resolved within this age model, as in fact the complete duration of the plume event itself likely lies within the age model uncertainties of about 230 years.

One of the major challenges while comparing different time series is the question of synchronicity of events, or the detection of potential leads or lags. To increase the comparability, all independent age models in this study are calculated with the same settings. Our assumption is that events are most likely synchronous if they overlap within the uncertainty of two-sigma in the age model. However, studies have attempted to solve this numerically (Werner and Tingley, 2015), or visually with "ghost plots" of any proxy within Bacon (Blaauw and Christen, 2011).

3.3. Analysis and proxies

The visual description of core MD83 was additionally supported through high resolution colour images taken with the ITRAX core scanner (COX Analytic Systems). In addition, analogue X-rays, previously taken on the split core (Lekens et al., 2006), were used to assess core stretch, voids and sediment composition.

Subsamples from all cores were wet sieved with an array of sieve sizes and in varying sampling intervals (Table 3). Most of the grain size data, however, has previously been published elsewhere. Lithic grains in the fraction >1 mm of cores MD89 and MD83 were counted manually, updating previous counts of core MD83 (Lekens et al., 2006) within the top 13 m (35–19 ka BP). Furthermore, all lithic grains in the 150–1000 μm fraction were counted in core MD83 using the automated light microscope "Morphologi G3" from Malvern Instruments (Malvern Instruments Ltd., 2017), applying a method described in Becker et al. (2017). In core MD84 lithic particles were manually counted in fractions >150 μm, all counts between 30 and 16.26 m core depth (35–29 ka BP) were previously published (Dokken et al., 2013). An additional 13 samples were counted in the same fraction in MD84 between 15 and 10.79 m core depth (28–25 ka BP) with the same method as for MD83. The interpretation of lithic grains >150 μm as ice rafted debris (IRD) is widely used in the literature (e.g. Bond and Lotti, 1995; Bailey et al., 2012), even though, there is an ongoing discussion on which grain size fraction should be regarded as IRD (Andrews, 2000). A study on the western Barents Sea margin associated an increased amount of IRD >500 μm with the advance and retreat of ice streams, while observing only little IRD at the maximum extension of the ice stream (Dowdeswell and Elverhøi, 2002). In this study, lithic grain counts >150 μm are interpreted as an IRD signal of a fluctuating, relatively proximal ice sheet margin.

The assemblage of planktonic foraminifera was counted in the 150–1000 μm fraction in core MD83 within the upper 13 m core depth (35–19 ka BP), with a resolution of 100–200 years. Additional samples were counted in MD89, increasing the resolution published by Berstad et al. (2003) to 200–500 years between 12.90 and 10.49 m core depth (35–27 ka BP). The high resolution (10–100 years) assemblage data from MD84 (Dokken et al., 2015b) were supplemented with 13 new counts between 11.44 and 10.79 m core depth (26–25 ka BP).

The relative concentrations of the polar species *Neogloboquadrina pachyderma* sinistral of $<90\%$ are widely used as an indication of influx of Atlantic water into the near surface of the Nordic Seas (Haflidason et al., 1995; Klitgaard-Kristensen et al., 2001; Austin et al., 2004; Scourse et al., 2009) indicating summer temperatures higher than 4 °C (Bé and Tolderlund, 1971; Kellogg, 1980; Pflaumann et al., 2003). Previous studies suggest a change from 90% to 50% *N. pachyderma* sinistral in this region to be comparable to a relative temperature variation of about 7 °C (e.g. Rasmussen and Thomsen, 2008; Dokken et al., 2013). Some data points, if based on counts of <200 planktonic foraminifera, were removed due to unreliability.

The oxygen stable isotope data used in this study were previously published elsewhere (Berstad, 2003; Lekens et al., 2006). The isotopes are reported in respect to the VPDB (Vienna Peedee Belemnite) standard and were measured on ca. 7 (MD83) or ca. 20 (MD84 and MD89) tests of *N. pachyderma* sinistral on the Finnigan MAT251 mass spectrometer at the Geological Mass Spectrometry laboratory at the University of Bergen with an accuracy of ± 0.07‰. This proxy is widely considered to partly reflect global ice volume and near-surface water freshening and/or temperature changes (e.g. Lekens et al., 2006; Rasmussen and Thomsen, 2008), where lighter values indicating fresher and/or warmer near-surface waters.

The upper 15 m of cores MD83 and MD89, covering the studied time interval, were analysed every 500 μm on the split core with the ITRAX core scanner (COX Analytic Systems). All XRF measurements were performed with the Molybdenum tube to produce a set of relative geochemical parameters, updating earlier measurements with 40 times the previous resolution (Berstad, 2003; Lekens et al., 2006). Core MD84 was scanned every 2 cm with similar settings, but on an AVAATECH XRF core scanner. The measured counts of Calcium (Ca) were normalized with the Iron (Fe) counts. The Ca/Fe ratios were further resampled on a continuous 50 year sampling interval with the nearest point regular interpolation method of the software PAST (Hammer et al., 2001). Lekens et al. (2006) have previously demonstrated, that the Ca/Fe ratios in core MD83 closely follow the carbonate content obtained from the same core.

Table 3
Overview of the sampling interval, sieving fractions and original references of the sediment data used in this study.

Core ID	Core depth (m)	Sampling interval (cm)	Time covered range (a)	Average time covered (a)	Fractions (μm)	References
MD83	0–13	2–5	50–100	50	< 63, 63–125, 125–150, 150–1000 and > 1000	Lekens et al. (2006)
MD83	3.5–4.5	2.5	10–50	50	< 63, 63–125, 125–150, 150–1000 and > 1000	This study
MD89	1.4–13	2–10	10–200 (15–25 ka) 200–1000 (25–35 ka)	80	< 63, 63–125, 125–150, 150–1000 and > 1000	Haflidason et al. (2003)
MD84	5.5–30	1	5–35	8.7	< 63, 63–150, 150–1000 and > 1000	This study

4. Results

The results of the performed analyses, plotted on depth scale and compared to the tentative tuning to Greenland ice core GISP2, demonstrate the large differences in accumulation rates within and between cores MD83, MD84 and MD89 (Fig. 3). In the following, the data will be presented in detail on the individual age model (Fig. 4).

4.1. Sedimentology

On average, about 80–90% of the deposits in the cores consist of silt and clay (Fig. 4). Distinct episodes with a higher content of coarser grain sizes are observed in all records. Before 26 ka BP, cores MD83 and MD84 show an influx of up to 50% very fine sorted sands for episodes of 500 to 1000 years (Figs. 4 and 5), in stark contrast to conditions after 26 ka BP, where similar influx episodes consist of coarse sand and pebbles (Figs. 4 and 6). The concentrations of grains > 150 μm and > 1 mm reflect this contrast, with relatively low coarse grain content before 26 ka BP and high after (Figs. 3 and 4). The coarse sediment composition after 26 ka BP is also recorded on the X-ray image of MD83 (Fig. 6), including pebbles of up to 8 cm in diameter. In MD89 the fine sand events before 26 ka BP are not as pronounced as in the southern cores, but the relative carbonate content inferred from the Ca/Fe data (Lekens et al., 2006) shows a similar pattern as in the southern cores (Fig. 4). In MD83, the Ca/Fe data and the carbonate content correlate well with the variations in grain size composition (Fig. 5). The Ca/Fe data in MD84 display a comparable, but more complex picture (Fig. 4), with a less precise correlation of the fine sand influx and the Ca/Fe ratio. After 26 ka BP, the Ca/Fe ratio and grain size composition appear not to show any co-variability, except within an episode between 25.8 and 24.5 ka BP, a short event around 21 ka BP in MD83 and around 16 ka BP in MD89 (Fig. 4). The pronounced episodes of medium to very coarse sand influx, especially between 25.8 and 18 ka BP, are interrupted by the deposition of almost pure silt and clay grain size content. In core MD83 these episodes are most distinct (Figs. 3 and 4) and make it possible to identify three coarse influx episodes, labelled “B” (21.2–19.8 ka BP), “C” (23.5–21.6 ka BP) and “D” (25.7–24.3 ka BP). A detailed look into the IRD counts of MD84 (light yellow graph in Fig. 4) shows similar episodes and opens the possibility for a fourth, younger, episode “A” (19.3–18.3 ka BP), that is not preserved in MD83. This is in agreement with the above-mentioned observation of the erosion of hemipelagic deposits on top of MD83, which predate the adjacent glacigenic debris flow (Figs. 1D and 4).

These episodes of coarser sediment input are each about 1.5 ka in duration and are followed by 400–800 years of reduced or no coarse input (Fig. 4). Minor changes in the content of lithic grains, interpreted to be IRD, suggest higher frequency variability within each episode. The input of IRD in the more northerly located MD89 during these episodes is similar in timing, but generally less pronounced. This appearance changes between 18.5 and 15 ka BP, where increased influx of coarse sands and IRD suggests ice sheet proximity (Fig. 4). The content of IRD is largely following the variability displayed in the grain size distribution, but also gives insights into the absolute amounts of IRD flux. In all three cores the apparent episodes of IRD input between 25.8 and 18 ka BP show about four times as high a content in the oldest episode, labelled D (Fig. 4), although we note that this is less pronounced in MD89. The timing of the initiation of these episodes appears to be the same in all records, but the input differs in scale and partly in duration. The latter is believed to be a function of uncertainty within the individual age models and the above-mentioned sampling resolution.

The upper 4.5 m (26–19 ka BP) of MD83 reveal clear differences in sediment composition between the different input episodes (Fig. 6). As mentioned above, episode D appears to be different from episodes B and C. The carbonate content is slightly enhanced above average values (14%), with spikes of 16 and 20%, the magnetic susceptibility values are at their lowest ($21 * 10^5$ SI units) and the sediment is almost barren of any foraminifera (not shown). At the same time the content of lithic particles is about four times higher, even though the absolute grain size composition appears similar to episodes B and C. Additionally, it appears that episode D can be divided into two distinct periods based on the Ca/Fe ratio, sediment composition and grain counts data (Fig. 6). This episode is additionally clearly different in sediment colour, appearing much lighter than the surrounding deposits (Fig. 6). Lekens et al. (2006) published chalk counts from this core, which show a high concentration within the depth corresponding to episode D, also reflected in the relatively high carbonate content in the core. However, a re-evaluation of the coarse fraction revealed that the light-coloured grains previously interpreted to be chalk are indeed mollusc and barnacle fragments. Finally, several samples of the layer in question were analysed in an electron microscope. This confirmed the absence of any coccolithophores, making the presence of large amounts of chalk particles unlikely. The conclusion is therefore, that the increased carbonate content in episode D is likely a product of ground down mollusc and barnacle shell fragments that are present in high concentration in all size fractions (Fig. 6).

Average sedimentation rates for the studied time period are calculated to be ca. 60 cm/ka (Fig. 7), with maximum values of 350 cm/ka at around 28 ka BP in core MD89. However, this short period of very high sedimentation rates in MD89 might be an erroneous effect of age modelling through a wide spread of densely sampled radiocarbon dates at this depth (Fig. 2). Calculating the sedimentation rate between the oldest and the youngest radiocarbon date within this date cluster around 28 ka BP, yields a more reasonable sedimentation rate of 160 cm/ka.

The sedimentation rate in core MD91 exceeds 300 cm/ka at 18.7 ± 0.23 ka BP, as 12.2 m of the core are modelled to have been deposited within only decades (Fig. 2), due to the previously described meltwater plume deposition (Reiche et al., 2011; Sejrup et al., 2016; Hjelstuen et al., this issue).

A striking feature in the calculated accumulation rates is the apparent similar change in magnitude through time within the studied cores (Fig. 7). Phases of relatively high sedimentation rates (100–150 cm/ka) in most cores are interrupted by periods of generally lower accumulation, with average rates of about 40 cm/ka, between 25.5 and 22.5 ka BP and after 18.5 ka BP.

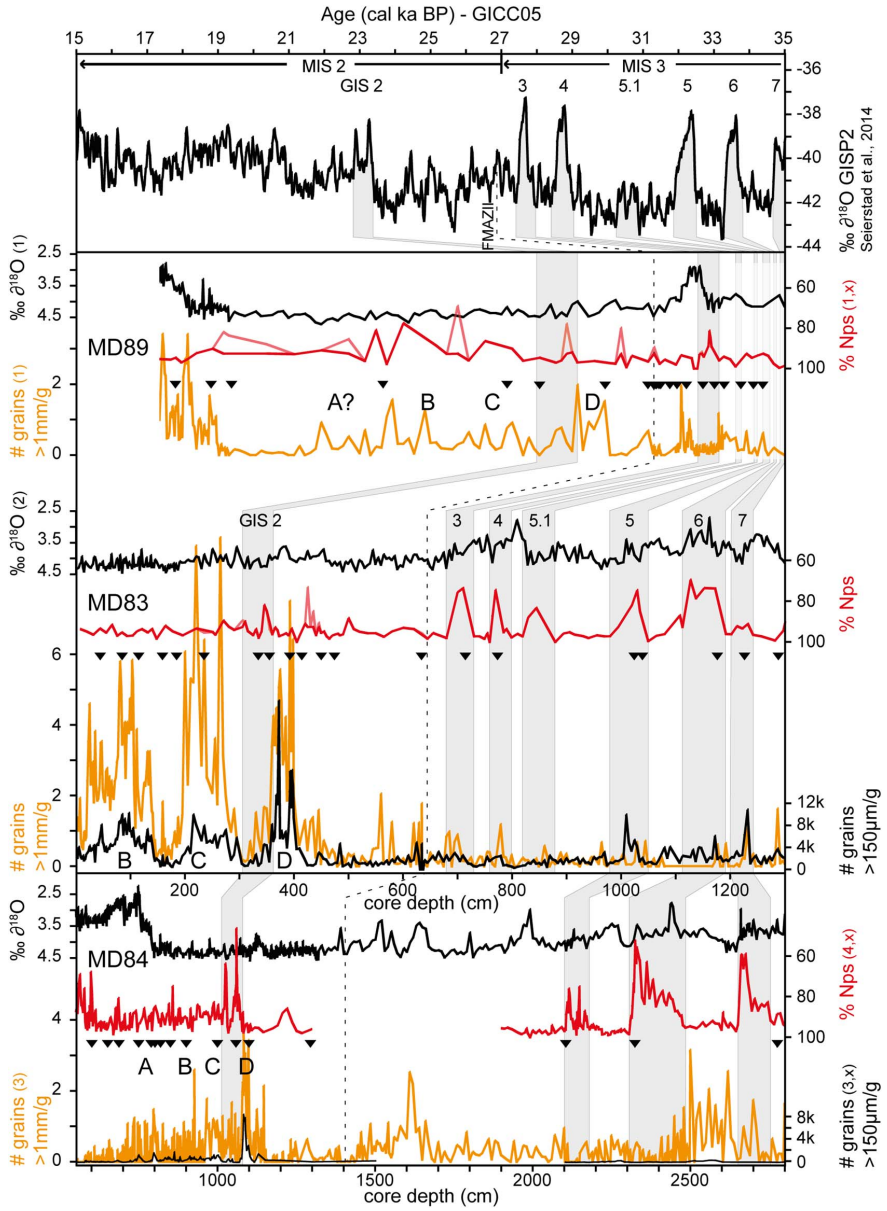

Fig. 3. Results of the analyses of cores MD99-2289, MD99-2283 and MD99-2284 on depth scale. The ∂18O data from Greenland ice core GISP2 are displayed on the GIIC05 time scale, Greenland Interstadials (GIS) and Marine Isotope Stages (MIS) are indicated. Planktonic ∂18O data from the cores is displayed in respect to the VPDB (Vienna Peedee Belemnite) standard. Relative abundances of *N. pachyderma* sinistral (Nps) in red, are displayed in light red, if < 200 planktonic foraminifera were counted (reversed scale). Grain content is displayed as counts > 1 mm per g dry sediment (orange) and counts > 150 µm for cores MD83 and MD84 (black). Radiocarbon dated levels (black triangles) and the stratigraphical position of the Faroe Marine Ash Zone (FMAZ) II are indicated. Grey shaded bars indicate tentative correlations between decreases in Nps and Greenland Interstadials. Capital letters D-A denote episodes of increased grain content > 150 µm. Numbers in paragraphs within graph captions correspond to the individual references of published data (see Table 2): (x or no symbol) this study, (1) (Berstad et al., 2003), (2) (Lekens et al., 2006), (3) (Dokken et al., 2013), (4) (Dokken et al., 2015b). (For interpretation of the references to colour in this figure legend, the reader is referred to the web version of this article.)

4.2. Oceanic conditions

Throughout most of the observed time period, the polar, planktonic foraminifera *N. pachyderma* sinistral generally accounts for more than 95% of the planktonic assemblage in our data (Fig. 4), suggesting full arctic conditions with close to perennial sea ice cover and near surface temperatures < 4 °C (Scourse et al., 2009). This state is perturbed by several 300–900 yearlong episodes with increased presence of sub-polar

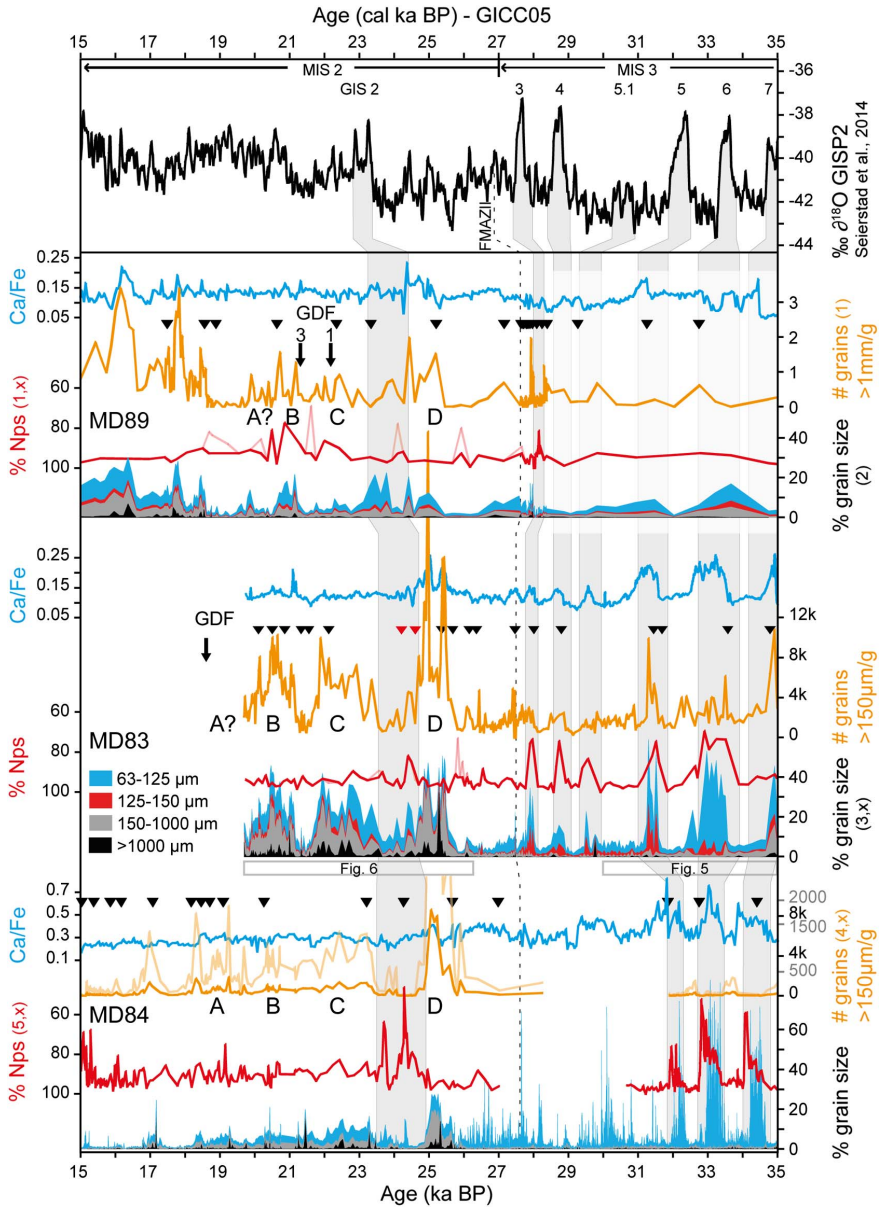

Fig. 4. Results of the analyses of core MD99-2289, MD99-2283 and MD99-2284 on individual age model. Coarse grain content is displayed as counts per g dry sediment (orange). Note that the grain size fraction used for counting differs in core MD89 (> 1 mm). The grain content in MD84 is additionally given in higher detail in yellow. Relative abundances of *N. pachyderma* sinistral (Nps) in red, are displayed in light red, if < 200 planktonic foraminifera were counted (reversed scale). Cumulative grain size values are displayed in their separate fractions. In MD84, fraction 63–150 µm was not subdivided. Radiocarbon dated levels are indicated with black triangles, red triangles denote dates that were removed. Ca/Fe core scanner data are resampled with the nearest point method (Hammer et al., 2001) every 50 years (blue). The ∂18O data from Greenland ice core GISP2 are displayed on the GIIC05 time scale, Greenland Interstadials (GIS) and Marine Isotope Stages (MIS) are indicated. Grey shaded bars indicate tentative correlations between decreases in Nps and Greenland Interstadials. The stratigraphical position of the Faroe Marine Ash Zone (FMAZ) II and the glacigenic debris flows (GDF) 3 and 1 (cf. Fig. 1D and E) are indicated. Capital letters D–A denote episodes of increased grain content > 150 µm. Numbers in paragraphs within graph captions correspond to the individual references of published data (see Table 2): (x or no symbol) this study, (1) (Berstad et al., 2003), (2) (Haflidason et al., 2003), (3) (Lekens et al., 2006), (4) (Dokken et al., 2013), (5) (Dokken et al., 2015b). (For interpretation of the references to colour in this figure legend, the reader is referred to the web version of this article.)

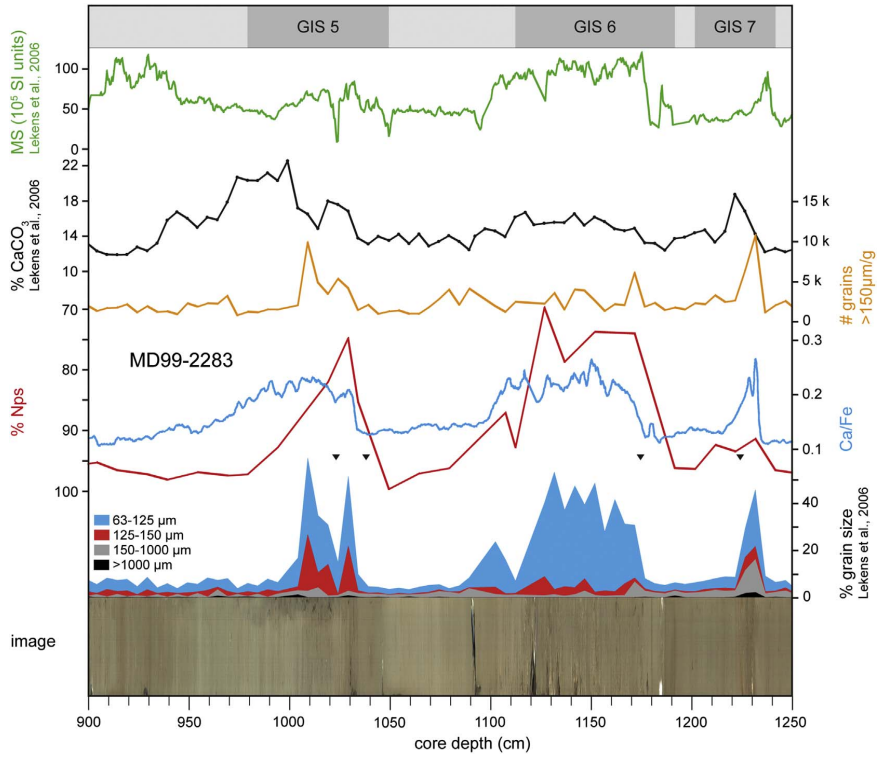

Fig. 5. Detail of core MD99-2283 between 900 and 1250 cm core depth, showing that the Ca/Fe counts, carbonates measurements, point measurements of magnetic susceptibility (MS), %Nps (*N. pachyderma* sinistral - reversed scale) and coarse grain contents correlate well with the variations in the displayed grain size distribution. Subtle changes in colour mark the change in sediment composition. Radiocarbon dated levels are indicated (black triangles). Tentatively correlated Greenland Interstadials (GIS) are also indicated.

species evidenced by *N. pachyderma* sinistral minima of 50% in MD84, 70% in MD83 and a minimum of 80% in MD89 (Fig. 4), implying periodic influx of warm Atlantic water into the Nordic Seas (e.g. Rasmussen and Thomsen, 2008). The relative timing of these events appears to coincide between the cores, within age model uncertainties. Cores MD83 and MD89 show in general lower *N. pachyderma* sinistral minima and less variability than MD84. However, the lowest values, that is, the warmest intervals in MD84, only have a duration of < 200 years, which makes it likely that the signal is missed or blurred in MD83 and MD89, where 2 cm sample slices are taken (0.5 cm in MD84) and the sampling resolution is commonly lower than 200 years (Table 3). Arguably, MD83 and MD89 might therefore also show a higher variability when denser sampled.

The above described episodes of sorted fine sand layers in MD83 and MD84 correspond roughly with the episodes of increases in sub-polar fauna before 26 ka BP. The relative temperatures increase briefly in MD84 when the sand layers disappear (Fig. 4). This might, however, be due to a dilutive effect during deposition of the fine sands, with parts of the assemblage being possibly exposed to reworking. The rapid change in sediment composition from 50% to < 5% fine sands at this boundary represents a large change in the depositional environment. Between 24.5 and 23.5 ka BP, two very distinctive peaks in sub-polar planktonic fauna are identified in core MD84, with *N. pachyderma* sinistral minima as low as 50%. These minima coincide with similarly low values in cores MD83 (81%) and MD89 (91%). Notably, the *N. pachyderma* sinistral values start to drop as soon as the coarse lithic grain content is decreasing, suggesting warm water intrusion to the coring location (Fig. 6).

5. Discussion

Based on the data presented above, the following discussion is structured into three distinct and quite different time periods in terms of the depositional environments along the studied margin. These are (Fig. 4): (1) Stadial/interstadial conditions (35–26 ka BP), (2) Full shelf edge glaciation (26–18.7 ka BP) and (3) Last deglaciation (18.7–15 ka BP).

5.1. Stadial/interstadial conditions (35–26 ka BP)

The climate system between 35 and 26 ka BP was dominated by, periodic, large-scale temperature variations, which left a global imprint in different types of climate archives including deep sea records from the Nordic Seas (Rasmussen et al., 2016). These Greenland Interstadials (GIS) or Dansgaard-Oeschger events are characterized by rapid warming at the onsets of interstadial conditions, gradual cooling throughout the interstadial, followed by rapid cooling to stadial conditions (Dansgaard et al., 1993; Rasmussen et al., 2016). Multiple paleoclimatic proxy studies and modelling efforts have suggested a link between Dansgaard-Oeschger events and variability in Atlantic Meridional Overturning Circulation strength, sea ice extent and polar front position variations in the Nordic Seas (Elliot et al., 2002; Scourse et al., 2009; Petersen et al., 2013; Peltier and Vettoretti, 2014; Hoff et al., 2016; Rasmussen et al., 2016; Wary et al., 2016). The large-scale changes in near sea-surface temperatures along the studied transect, inferred from the relative amounts of *N. pachyderma* sinistral, exhibit a clear Dansgaard-Oeschger pattern before 26 ka BP (Fig. 8). This pattern

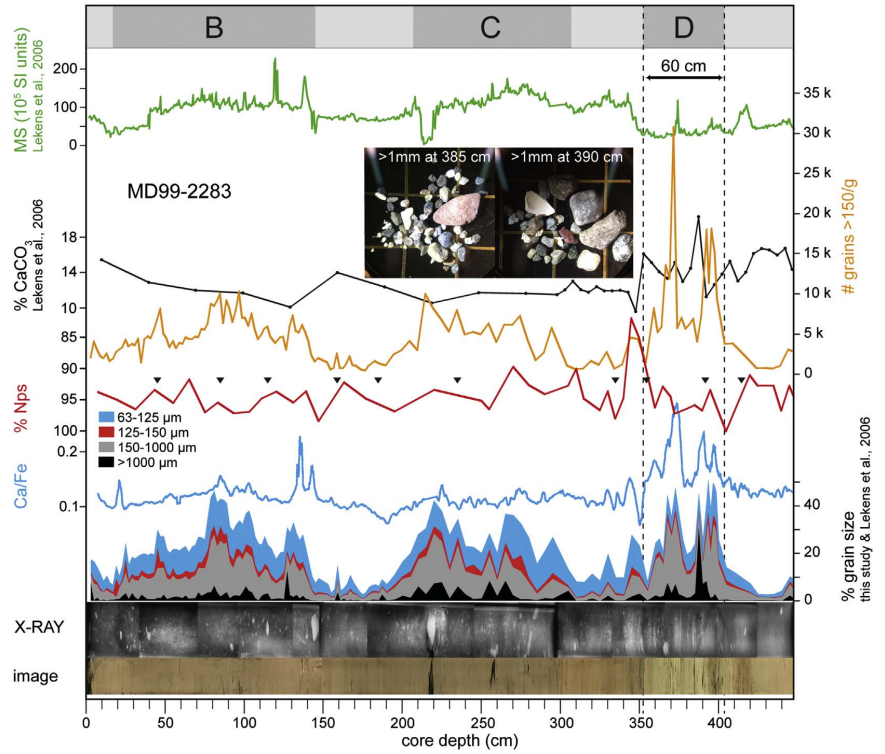

Fig. 6. The uppermost three sections of core MD99-2283, subdivided into the identified episodes D to B. Light sediment colour, high Ca/Fe and coarse grain counts, spikes in CaCO3, a high number of small fragments in the X-ray picture and low point measurements of magnetic susceptibility (MS) values mark episode D. Episodes C and B exhibit no sediment colour variation, relatively low and stable Ca/Fe counts, varying, but lower coarse grain counts, occasional pebbles of up to 8 cm in diameter on the X-ray image and high magnetic susceptibility values. %Nps (*N. pachyderma* sinistral) shows a distinct warm spike between episodes D and C (reversed scale). Radiocarbon dated levels are indicated (black triangles). Two colour image insets show fraction > 1 mm with mollusc fragments > 0.5 cm, raster in background is 1 cm.

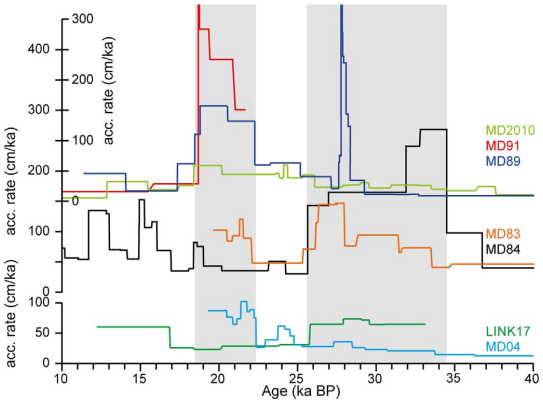

Fig. 7. Linear accumulation rates, calculated between every dated level of all cores. Core MD99-2291 exceeds the scale at around 18.5–19 ka BP. The amount of accumulation varies between 30 cm/ka and up to 350. Two zones of relatively high sedimentation (grey bars) between 35 and 25.5 ka BP and 22.5–18.5 ka BP are interrupted by periods with lower sedimentation rates.

is most pronounced in the southern section (Irish/Scottish margin) and not visible in the North (Mid-Norwegian margin).

The deposition of carbonate rich, sorted fine sands, coinciding with an apparent near-surface warming in cores MD83 and MD84 (Figs. 4 and 5) indicates a relatively high energy environment and the presence of Atlantic water along the margin (as described in Dahlgren and Vorren, 2003). The influx of lithic grains > 150 µm through ice rafting from 35 to 26 ka BP is likely limited, compared to the input between 26 and 15 ka BP, where the additional presence of particles > 1 mm clearly indicates ice rafting as the main contributor (Fig. 3). The apparent synchronous deposition in MD83 and MD84 coinciding with warm water influx might be due to winnowing effects of an increased overturning circulation through the Faroe-Shetland overflow during Interstadial conditions (Fig. 9A). Similar to present-day vigorous current speeds in the Faroe-Shetland Channel (Hansen and Østerhus, 2000). Sejrup et al. (1981) also described similar deposits during the Holocene, which they related to the vigorous NwAC along the upper slope in this area. An increased NwAC current speed would also agree with the stronger bio-productivity through elevated nutrient content as indicated by the increase in total planktonic foraminifera concentration during the episodes characterized by fine sand influx and higher carbonate content (Fig. 5). However, when directly comparing MD84 and MD83, with MD84 on the age model of Dokken et al. (2013), the magnetic susceptibility records appear to show the opposite behaviour (Fig. 5). The magnetic data of MD83 correlate well with the episodes of fine sand sorting and relatively warmer near-surface temperatures, linked to interstadial conditions (Lekens et al., 2006; Rasmussen and Thomsen, 2008; Scourse et al., 2009). Taking both approaches into account this would result in cores MD83 and MD84 being in anti-phase

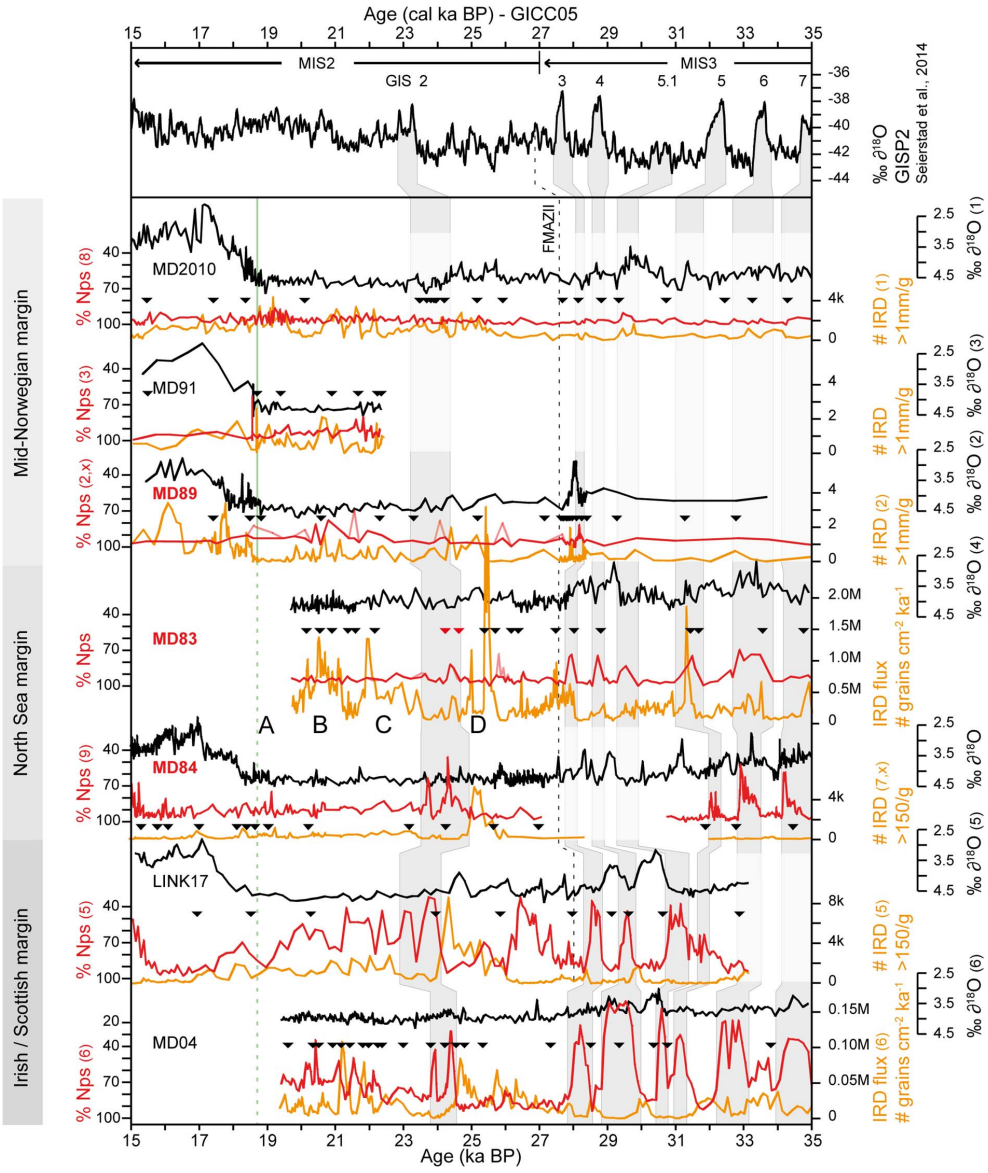

Fig. 8. Compilation of available data from all cores (plotted northeast to southwest), with the relative abundance of Nps (*N. pachyderma* sinistral) in red, the content of coarse grains, mainly interpreted as ice rafted debris (IRD), in orange and the isotopic measurements of planktonic ∂18O in black. The isotopic values are reported in respect to the VPDB (Vienna Peedee Belemnite) standard. Note, that the Nps and ∂18O scales are reversed and that the IRD values in MD83 and MD04 are displayed as flux values in [#IRD > 150 μm cm^{-2} ka^{-1}]. IRD counting was performed in the > 150 μm fraction, except of MD99-2291 and MD99-2289 (> 1 mm). Radiocarbon dated levels are indicated with black triangles, red triangles denote removed dates. The ∂18O data from the Greenland ice core GISP2 are displayed on the GIIC05 time scale, Greenland Interstadials (GIS) and Marine Isotope Stages (MIS) are indicated. Grey shaded bars indicate tentative correlations between decreases in Nps and Greenland Interstadials marked in ∂18O GISP2. The stratigraphical positions of the Faroe Marine Ash Zone (FMAZ) II and the meltwater drainage event (green line) are indicated, FMAZII was to date not found in MD04 to the authors knowledge. Numbers in paragraphs within graph captions correspond to the individual references of published data (see Table 2): (x or no symbol) this study, (1) (Dokken and Jansen, 1999), (2) (Berstad et al., 2003), (3) (Lekens et al., 2005), (4) (Lekens et al., 2006), (5) (Rasmussen and Thomsen, 2008), (6) (Scourse et al., 2009), (7) (Dokken et al., 2013), (8) (Dokken et al., 2015a), (9) (Dokken et al., 2015b). (For interpretation of the references to colour in this figure legend, the reader is referred to the web version of this article.)

between 35 and 26 ka BP, despite being raised only 75 km in distance and 555 m in water depth apart. Here, the events of the two records are regarded as synchronous (Fig. 4) and the sorted fine sand influxes are seen as effects of winnowing due to an increased overturning circulation during interstadials.

Further north, along the Mid-Norwegian margin, a similar sorting effect linked with warm planktonic assemblages as seen in MD83 and MD84, is not evident in MD89 (Fig. 4). However, it has to be noted, that

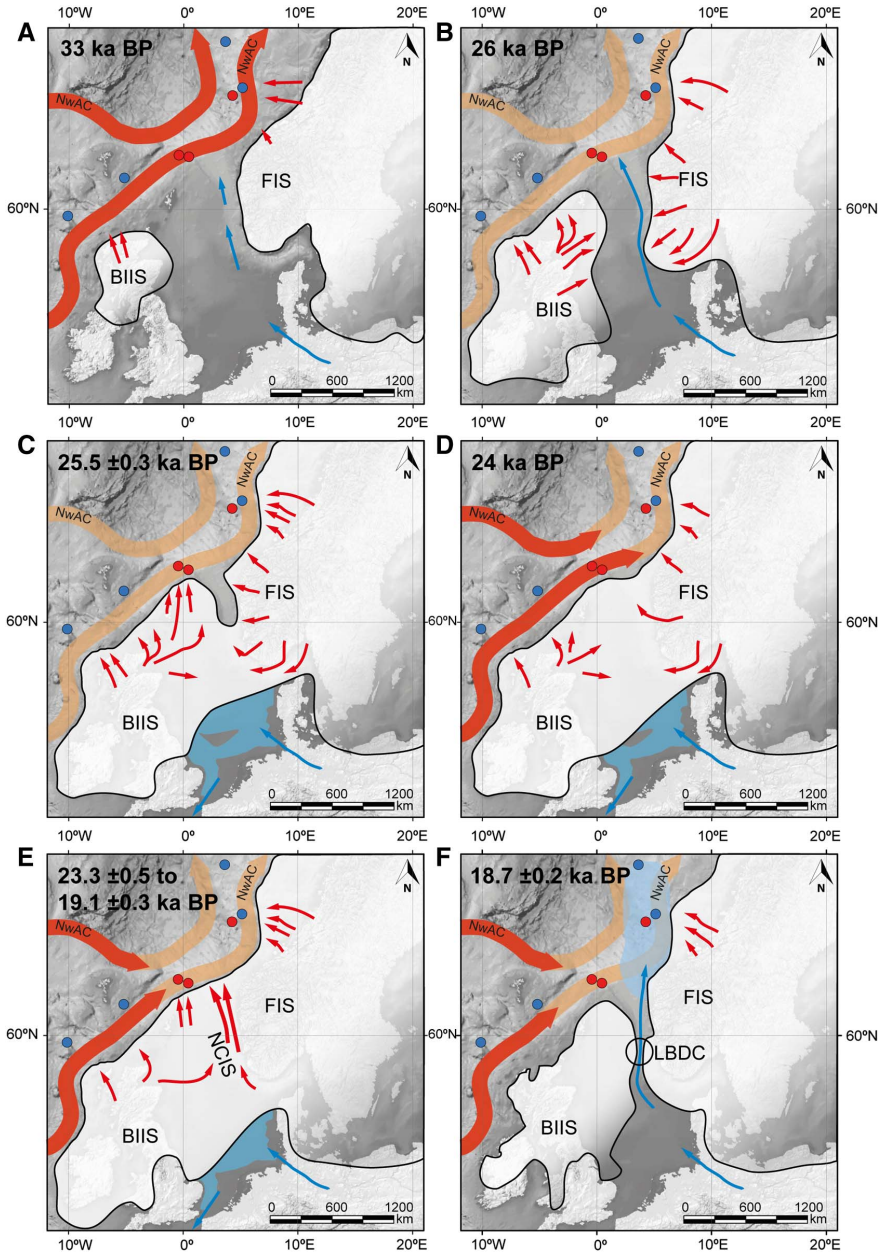

Fig. 9. Paleogeographic reconstructions with outlines without new data based on Hughes et al. (2015). The modern flow direction of the Norwegian Atlantic Current (NwAC) indicating warm water inflow (red) and no recorded inflow (orange). Fluvial sediment input (blue arrows) is separated from interpreted ice transport direction (red arrows). Interpreted freshwater pooling and meltwater plume sediments (blue areas) and glaciated areas (white areas) show their inferred extension. LBDC (Ling Bank Drainage Channel); NCIS (Norwegian Channel Ice Stream); FIS (Fennoscandian Ice Sheet); BIIS (British-Irish Ice Sheet). (For interpretation of the references to colour in this figure legend, the reader is referred to the web version of this article.)

the sampling resolution in MD89 in this period might be too coarse (Table 3) to capture these relatively short-lived events or the distance from the overflow threshold is simply too far.

5.2. Periods with full shelf edge glaciation (26–18.7 ka BP)

After about 26 ka BP, the positive correlation between sea surface conditions, as evidenced by the *N. pachyderma* sinistral content, and the

fine sand flux degenerates and is replaced by a distinct change to more unsorted sediments with an increase in coarser, middle sand to pebble sized material along the transect, with no simultaneous warming of the near surface waters. This is in agreement with marine and terrestrial evidence of the onset of FIS and BIIS, switching from a mostly continental to a marine-based margin after the Ålesund/Sandnes/Denekamp interstadial around 29 ka BP (Fig. 9B) (Sejrup et al., 2000; Scourse et al., 2009; Hall et al., 2011; Mangerud et al., 2011).

The IRD influx between 26 and 18.5 ka BP does not appear to be constant, but instead varies strongly, suggesting ice sheet instabilities with alternating advances, still stands or retreats (Fig. 4), as earlier described in e.g. Hjelstuen et al. (2005) for the Mid-Norwegian margin. Such a high degree of instability for the BIIS section of the Eurasian Ice Sheet has earlier been suggested for the Irish/Scottish margin from geological evidence (Scourse et al., 2009; Haapaniemi et al., 2010; Hall et al., 2011) and also from ice sheet modelling experiments (Hubbard et al., 2009; Patton et al., 2016).

The fact that the influx episodes D–A can generally be traced along the north-western European margin suggests an overarching forcing mechanism. The first episode "D" (25.7–24.3 ka BP) is most pronounced, exhibiting the highest IRD influx from the Irish/Scottish to the Mid-Norwegian margin, even though varying in absolute amounts and exhibiting two separate peaks (Fig. 8). Earlier studies have reported a similarly pronounced event during the same time period (Dahlgren and Vorren, 2003; Peck et al., 2006). We interpret this episode as the first widespread advance of the Eurasian Ice Sheet towards the respective shelf edges during the LGM. Simultaneously, the *N. pachyderma* sinistral content suggests full arctic water temperatures during this episode, while the sediments are almost barren of foraminifera, suggesting limited productivity (Fig. 6). Episode D ends with a rapid decrease in IRD and a simultaneous rise in relative near-surface temperatures (Figs. 6 and 8), indicating a retreat of the Eurasian Ice Sheet from the shelf edge.

The reduction in IRD influx in the southern cores, following episode D, might mark the early BIIS retreat from the shelf edge as reported from other studies (e.g. Scourse et al., 2009). This is also in line with terrestrial evidence from Ireland and the United Kingdom (summarized in Hughes et al., 2015). Scourse et al. (2009) link the rapid deterioration of the BIIS at the end of episode D to the rise in temperatures, which they correlated to GIS2. These two warming pulses at the end of episode D are clearly visible in cores MD83, MD84, LINK17 and MD04 at around 24 ka BP (Fig. 8), and is likely contributing to a substantial retreat of the calving front from the shelf edge.

The relative near-surface temperatures drop again at the onset of episode C and stay steady and low throughout the observed time period and the transect. The IRD influx north of MD83 in episode C and B is lower than during episode D, but follows similar trends as in MD83, suggesting that the FIS on the northern North Sea and Mid-Norwegian margin regained its shelf edge position within centuries, i.e., at around 23.5 ka BP. On the other hand, increased IRD influx in MD89 during episode A is not recorded, but two large influx episodes between 19 and 15 ka BP suggest late ice proximity on the Mid-Norwegian margin. South of MD83 the influx is greatly reduced after episode D (Fig. 8), supporting the above presented interpretation of the BIIS retreating from its maximum position after episode D.

The absence of further distinct warm spikes between the following episodes C–A in our data, suggests, that the apparent cyclicity of the glacial advances is at least not solely forced through increased ocean melt. Only the data from the Irish/Scottish margin suggests repeated intrusions of warm water during the period from 23 to 19 ka BP (Fig. 8), which might indicate a varying position of the polar front south of the northern North Sea margin, as suggested by Scourse et al. (2009). Especially core LINK17 exhibits relatively warm near-surface temperatures (Fig. 8), implying, that the large-scale influx of ice bergs and freshwater within this time period might have forced the path of the NwAC further westwards than suggested for pre-LGM times (Rasmussen and Thomsen, 2008).

Notably, at the same time as the data of LINK17 suggests rising near-surface temperatures, cores MD83 and MD84 show a gradual increase in the concentration of planktonic foraminifera from 24 to 19 ka BP (not shown), which varies in pace with the IRD influx. This could hint at improving oceanic conditions towards the end of the LGM, as proposed elsewhere (Bauch et al., 2001).

5.2.1. Norwegian Channel Ice Stream variability

The episodes of increased IRD influx in MD83, labelled B, C and D (Fig. 4) were earlier interpreted as indicators for periodic iceberg calving off the NCIS and shelf edge extension of the FIS and BIIS with an active ice stream (Lekens et al., 2006). However, the sediment composition, the high concentration of barnacle and mollusc fragments together with the other physical and geochemical parameters in MD83 (Fig. 6), and less pronounced in MD84, led us to hypothesize a provenance change between episode D and the younger episodes. If the deposits in episode D in cores MD83 and MD84 do have another provenance, this episode might offer a rare opportunity to understand the mechanisms and the timing of the NCIS onset during the LGM. Deciphering the provenance of episode D, we found three potential source regions.

Firstly, a BIIS source, which was previously suggested through the discovery of an increase in the clay mineral smectite, the presence of ordered layered clays and the above disproved chalk counts in MD83 (Lekens et al., 2006, 2009). The authors hypothesized, that the clays were an indicator for ice transport from the Moray Firth area, northeastern Scotland. Indeed, the most proximal source for the well-preserved barnacle and mollusc shells found in episode D in MD83 (Fig. 6) is the shallow shelf area around the Shetlands, 200 km to the southwest, supporting the notion of a south-westerly provenance. Today some of the beaches on the Shetlands consist almost purely of shell sands (e.g. Whittington and Edwards, 1993). Global sea level lowering during continental ice sheet build-up at the onset of the LGM would have left an extensive area of hard substrate available for mollusc growth around the Shetlands. These mollusc banks could have subsequently been eroded through an overriding grounded ice sheet, transported to and calved off at the shelf edge, and then deposited at the coring location (Fig. 9C). This transport direction and the associated early BIIS maximum extension is in accordance with above-mentioned earlier studies interpreting this time period as the maximum extension of the BIIS (e.g. Peck et al., 2006; Bigg et al., 2012). Dating of the best-preserved and most juvenile looking mollusc fragments could help resolve this issue and confirm its hypothetical Shetland provenance, as the youngest ages would give a minimum estimate of ice expansion off the islands. Secondly, a Scandinavian, FIS origin for this mollusc-rich layer cannot be excluded, as the direct transport distance from mainland Norway is of similar magnitude. However, this would imply FIS extension to the shelf edge and across the 400 m deep Norwegian Channel at a very early stage, suggesting rapid ice sheet build-up from an ice-free coast during the Hamnsund interstadial at around 29 ka BP (Mangerud et al., 2003) to a grounded ice sheet on the shelf edge within about 1000 years, which seems unlikely. Indeed, grounded ice on the shelf edge would likely indicate an active NCIS, which is reported to transport mainly FIS sourced material (Sejrup et al., 1996). This raises the question why episodes C–A are compositionally different from D, if they all would have been delivered by the same transport mechanism. In turn, a non-Scandinavian origin for the IRD in episode D appears reasonable. Thirdly, the timing, the exceptionally high amount of IRD and, on first glance, the composition of the IRD grains, are in favour of a North American, that is, Laurentide Ice Sheet origin of the deposits. Thus, the layer might belong to North Atlantic Heinrich event 2 (H2). This would fit with observations from the western United Kingdom margin, where clear evidence of Laurentide Ice Sheet sourced material during H-events H4, H2 and H1 were found, except for H3, which is hypothesized to have a largely European contribution (Peck et al.,

2007; Scourse et al., 2009; Hall et al., 2011). However, the very low magnetic susceptibility values in MD83 contradict this interpretation (Fig. 6), as H-events are commonly found to have high magnetic susceptibility values (Robinson et al., 1995). The magnetic susceptibility values are similarly low at the same time in MD84, supporting the notion, that the sediment deposited during episode D in MD84 might belong to a similar source. On the Faroe-Shetland side of the Faroe-Shetland Channel, a layer interpreted as H2 was also found to be light coloured and has a relatively low magnetic susceptibility (Ezat et al., 2014). On the other hand, the H2 deposits on the western United Kingdom margin have not been observed as such a light coloured, IRD and carbonate rich layer as in MD83 (Scourse, J., pers. comm., 2016), which underlines the interpretation, that this might be a local signal. In consequence, this episode might be a clear indication for early expansion of the BIIS to and beyond the Shetlands. Hence, the apparent difference in provenance within the episodes leads to the conclusion, that the NCIS might not have reached the outer parts of the Norwegian Channel within episode D (Fig. 9C), but rather only became more extensive after GIS2, that is, after 23.3 ± 0.5 ka BP (Fig. 9E). This might indicate, that the NCIS was not active as an ice stream before this time during the Weichselian, which is about 4000 years later than previously suggested (Nygård, 2003). The pronounced warming on the margin in core MD83 and MD84, tentatively correlated to GIS2, precedes the proposed onset of the NCIS only briefly (Fig. 6), which could indicate forcing of the NCIS streaming through increased ocean melt.

Following on from episode D, the ice stream appears to have advanced for about 1500 years (episode C) until it came to a standstill for a couple of centuries to then advance again (episode B), followed by another pause and potentially a final advance (episode A), before retreating from the shelf edge. This interpretation is supported by the similarity of sediment composition in episodes C–A. Considering todays surface circulation patterns (Hansen and Østerhus, 2000) the northeastwards surface transport (NwSC) along the shelf edge, allowed only a minority of the NCIS sourced icebergs to be transported south-westwards (Fig. 9E), which could explain the gradient in absolute sediment influx between MD83 and MD84.

5.2.2. FIS-BIIS confluence

Assuming that the conclusion of no NCIS activity in the northern parts of the channel before 23.3 ka BP is correct, the question is to which extent grounded ice was already reaching into the Norwegian Channel and to the shelf edge of the northern North Sea margin before that time. This conclusion effects the location and timing of FIS and BIIS confluence, which was, as described above, widely accepted to have been between about 31–24 ka BP, whereas a recent reinterpretation suggested a sustained confluence until 18.5 ka BP (Sejrup et al., 2016).

Both ice sheets are believed to gain a marine calving margin after the Ålesund/Sandnes/Denekamp interstadial. While the BIIS is interpreted to extend towards the east into the North Sea basin, the exact timing of this advance is, however, uncertain as there is a lack of datable material. Dates on the Fladen ground suggest ice proximal, but ice free conditions in the Fladen area until about 26 ka BP (Sejrup et al., 2016). On the Norwegian side, glacial ice in the northern section retreated back beyond the coastline during the Hamnsund interstadial (Mangerud et al., 2003). By 25.5 ka BP the presented data supports an eastwards extension of the BIIS from Scotland towards the North-east (Shetlands), the East (Fladen Plateau) and the South-east (Which Ground). This is interpreted to lead to confluence with the FIS, which by then extended into the Norwegian Channel, following a large-scale climatic deterioration after the Hamnsund interstadial, at the shallowest part of the Norwegian Channel, on the latitude of Stavanger, Western Norway (Fig. 9C). The timing of the confluence is therefore interpreted to be at around 25.5 ka BP, where a sharp drop in accumulation rate on the northern North Sea margin marks a sudden loss of sediment supply (Figs. 7 and 9B). This shifts earlier confluence interpretations by several thousands of years. Subsequently, the FIS and BIIS confluence potentially lead to a restructuring of the eastwards flow-direction of the BIIS. Deflecting the eastwards streaming BIIS north and south, delivering Shetland sourced IRD towards the region southwest of the Norwegian Channel and the location of MD83 and MD84 (25.5 to 24.5 ka BP). The observation of Shetland sourced glacial influx to the shelf edge on the northern North Sea margin in addition to the mapping of glacial landforms by Sejrup et al. (2016), suggests that the BIIS was more important for the glaciation of the central North Sea than previously anticipated. This would explain the apparent solely BIIS contribution to the northern North Sea margin around episode D (Fig. 6), as the Norwegian Channel north of the latitude of Stavanger is by then interpreted to be still mainly free of grounded ice (Fig. 8).

Evidence from freshwater drainage into the Gulf of Biscay (Toucanne et al., 2015) suggests freshwater drainage via the Fleuve Manche, when northwards transport is inhibited due to ice damming of a Eurasian Ice Sheet in confluence across the central North Sea. Finally, recent modelling efforts of the Eurasian Ice Sheet suggest a FIS and BIIS confluence around a similar latitude, with the FIS extending into the Skagerrak and the southern central North Sea about 1000 years prior to a confluence with the BIIS (Patton et al., 2016). The model comes to the same conclusion as our interpretation, with two largely independent ice sheets that merely “meet” in the eastern parts of the central North Sea and buttress each other during that time period. We interpret from the presented data that the NCIS reached the shelf edge about 1000–1500 years after initial confluence (Fig. 9D) at the start of episode C, roughly around 23.3 ka BP (Figs. 9E and 8).

The BIIS and the FIS are thus believed to be in confluence between 25.5 ± 0.3 and 18.7 ± 0.2 ka BP and therefore much later than the previously suggested 30–25 ka BP (Bradwell et al., 2008; Sejrup et al., 2009). The earlier described Tampen advance at around 21 ka BP (Sejrup et al., 2015) would by this interpretation not be a separate advance of the FIS, but instead the late, first advance of the FIS across the Norwegian Channel during the LGM. Advances into the Måløy area on the Mid-Norwegian margin are inferred to around 16 ka BP, the earlier described Bremanger event (Nygård et al., 2004).

5.3. Last deglaciation (18.7–15 ka BP)

The onset of deglaciation and as such the retreat of the grounded ice from the shelf edge is interpreted to have initiated at around 19 ka BP through a speed up in ice streaming through the NCIS (Nygård et al., 2007). This resulted in a draw down and thinning of the ice sheet in the central North Sea area (Sejrup et al., 2016) leading finally to the separation of the FIS and the BIIS. Sejrup et al. (2016) proposed that the separation is marked by the collapse of an ice dam in the central North Sea, which was holding back an ice-dammed lake in the southern North Sea. This lake is then interpreted to subsequently have drained northwards through the Ling Bank Drainage Channel (Fig. 9F). In favour of this, north of the North Sea Trough Mouth Fan an acoustically transparent unit, interpreted as a meltwater plume (in cores MD89, MD91 and MD2010), was mapped by Hjelstuen et al. (2004) and later described by several studies (Hjelstuen et al., 2005; Lekens et al., 2005; Reiche et al., 2011). This suspension plume is interpreted to originate from a point source in the direction of the Norwegian Channel (Lekens et al., 2005) and was, as discussed above, likely deposited within only centuries. This, including a detailed view into the fluvial deposits within the Norwegian Channel and the delta build up on the Ling Bank is further discussed in Hjelstuen et al. (this issue).

The timing of the deposition of the meltwater plume on the Mid-Norwegian margin is dated to 18.7 ± 0.2 ka BP in the three presented and independently age modelled cores MD89, MD91 and MD2010 (green line in Fig. 8). Within the oxygen isotope data, a 1‰ step in the cores on the Mid-Norwegian margin precedes a long 2‰ light oxygen isotope event in all cores by about 500 years (Fig. 8). The light isotope event in all cores between 18 and 15 ka BP likely shows the global, post LGM deglaciation signal. We interpret the 1‰ step, most pronounced in

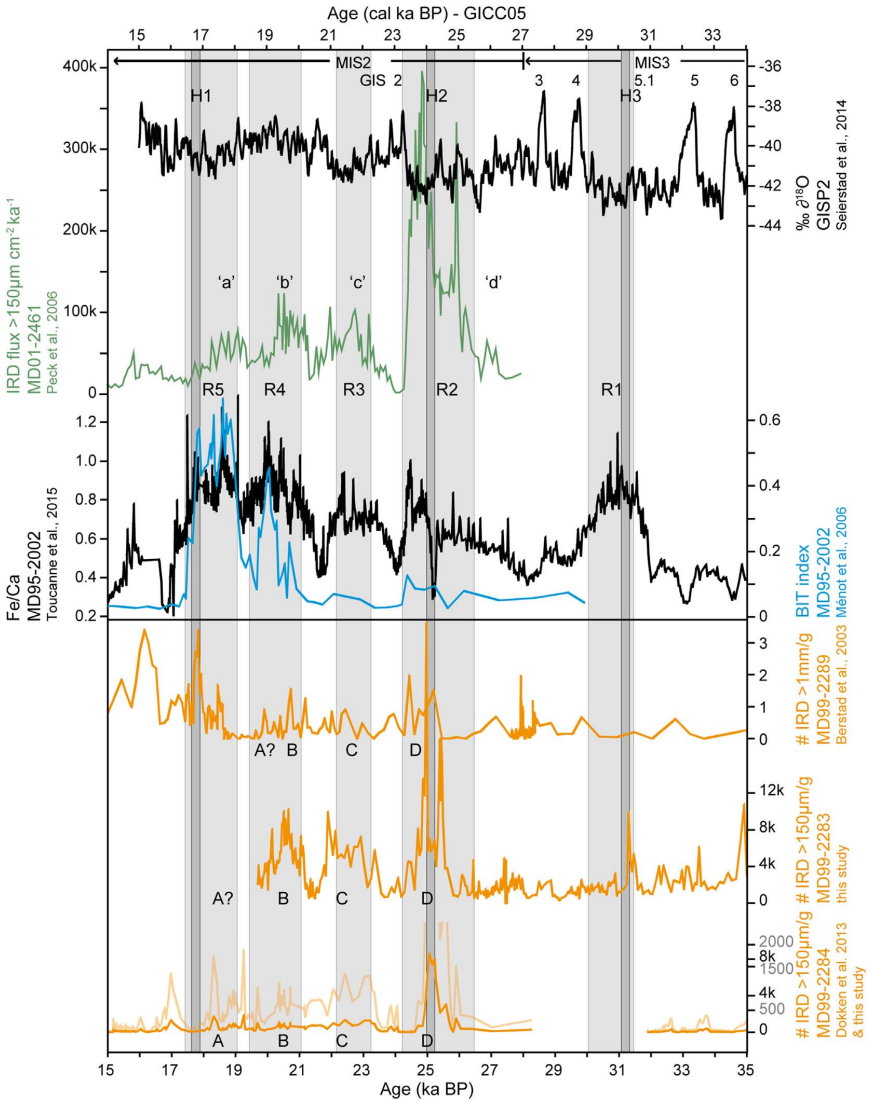

Fig. 10. Episodes (D–A) of increased content of ice rafted debris (IRD) from this study compared to IRD flux off the Irish margin in MD01-2461 (Peck et al., 2006) and riverine influx events (grey bars, R1–R5) observed in Fe/Ca data in the Bay of Biscay in MD95-2002 (Toucanne et al., 2015) and the branched and isoprenoid tetraether (BIT) index (Ménot et al., 2006). See Fig. 1A for the location of MD01-2461 and MD95-2002. North Atlantic IRD episodes are indicated in small letters (d–a) (Bond and Lotti, 1995), North Atlantic Heinrich events in dark grey bars. Note that the age scale of this study was shifted by − 1000 years to increase the fit with the data of the other studies on the absolute GIIC05 age scale.

MD91, as a trace of the freshwater perturbation of the glacially dammed lake collapse, released through the Ling Bank Drainage Channel (Sejrup et al., 2016; Hjelstuen et al., this issue). Hjelstuen et al. (this issue) estimate the duration of lake drainage to be only 5–15 months.

During deglaciation, the high IRD influx in MD89 and, to a lesser extent in MD91, after 19 ka BP appears to be restricted to the Mid-Norwegian margin (Fig. 8). This is in agreement with observations of a delayed deglaciation signal north of the North Sea Trough Mouth Fan and the mentioned Bremanger re-advance at around 16–17 ka BP (Nygård et al., 2004).

5.4. Regional implications

Comparing the above discussed IRD influx episodes D–A along the northern North Sea shelf edge with studies from the southern and the western (Irish) margin of the Eurasian Ice Sheet (Fig. 1A), there appears to be a good correlation between the individual events (Fig. 10). In fact, while anticipating a constant local reservoir correction of 1000 years for the presented age models, which is in agreement with the chronological offset of the FMAZII tephra layers (Table 2), episodes D–A have a very good fit with riverine runoff events in the Gulf of Biscay (Ménot et al., 2006; Toucanne et al., 2015) and IRD flux spikes off western Ireland (Peck et al., 2008) (Fig. 1A). These time series are displayed on

tuned, absolute chronologies. The riverine runoff events within the Gulf of Biscay (Fig. 1A) are interpreted as implications of Eurasian Ice Sheet fluctuations within the Baltics and the southern North Sea, e.g. the southern, continental margin of the Eurasian Ice Sheet (Toucanne et al., 2015). On the western margin, Peck et al. (2008) record the advance and retreat signal off western Ireland (Fig. 1A), agreeing with terrestrial and Irish/Scottish shelf studies on the retreat pattern (e.g. Peters et al., 2015). Offsets between the dataset in this study and the other data cannot be evaluated due to the large reservoir effect uncertainties. Under the assumption of age model comparability, it appears that all margins of the southern Eurasian Ice Sheet act simultaneous to one common forcing. Interestingly, as already indicated by Peck et al. (2008), a similar pattern (b–a in Fig. 10) is found throughout the southern North Atlantic (Bond and Lotti, 1995). Therefore, the forcing mechanism and the teleconnections might potentially not only be confined to the Eurasian Ice Sheet, but rather to the whole North Atlantic region, connecting influx from the Laurentide Ice Sheet and the Eurasian Ice Sheet. Additionally, the fact that not only marine margins appear to show the same signal, but also continental margins (Toucanne et al., 2015) strongly indicates atmospheric teleconnections as at least one important driver of these simultaneous changes.

6. Conclusions

Our compilation of new and previously published, well-dated cores, enables us to makes inferences about ice-sheet advances and instabilities along the south-eastern Nordic Seas continental margin and link this with the variability in ocean circulation between 35 and 15 ka BP. The established chronology, based on 146 AMS radiocarbon dates, is regarded as coherent within the presented transect of cores, but as no local reservoir correction has been applied, it should be emphasized that the absolute age of parts of the records may be significantly younger. The identification of the tephra FMAZII, dated to 26.7 ± 0.4 cal. ka BP, suggests that the local reservoir effect at this time might have been close to + 1000 years, confirming previously suggested reservoir ages in the region (Davies et al., 2008).

The following conclusions can be drawn from the analysed sedimentological, geochemical and micro-paleontological proxies in this study:

- Between 35 and 26 ka BP, the stadial/interstadial deposition pattern along the northern North Sea margin is characterized by 500–1000 year long periods dominated by strong current speeds with winnowing effects and periods which are influenced by glacimarine deposition.
- The possibly first Weichselian confluence of the FIS and the BIIS at 25.5 ± 0.3 ka BP is marked by a sharp drop in accumulation rates along the margin, suggesting cut-off from southern sediment sources. The confluence is interpreted to have lasted until the last inter-ice sheet connection collapsed in the central North Sea, releasing a rapidly deposited meltwater plume onto the Mid-Norwegian margin, which we dated in three cores to 18.7 ± 0.2 ka BP.
- Following the confluence, we propose that the BIIS expanded northeast of the Shetlands possibly for the first time within the Weichselian, between 25.5 and 24.5 ka BP. This is evidenced by a distinct change in sediment provenance on the northern North Sea margin.
- The change in provenance on the northern North Sea margin led us to suggest a late extension of grounded ice in the northern section of the Norwegian Channel, potentially restricting the only Weichselian NCIS activity to between 23.3 ± 0.5 ka BP and 19.0 ka BP. We note that the onset of the NCIS directly precedes a large-scale intrusion of warm near-surface waters into the study region, which may indicate forcing through ocean melt.
- Strong variations in the IRD flux on the northern North Sea margin indicate a highly variable NCIS, consisting of at least three streaming/advancing episodes, interrupted by 500–600 yearlong halts/retreats.
- The presented four episodes of high IRD flux on the northern Eurasian Ice Sheet margin compared to similar data off the western and eastern Eurasian Ice Sheet margin may indicate a common glacial forcing mechanism and potential atmospheric teleconnections.

Supplementary data to this article can be found online at http://dx.doi.org/10.1016/j.margeo.2017.09.003.

Acknowledgements

The research leading to these results has received funding from the GLANAM (GLAciated North Atlantic Margins) Initial Training Network, a People Program (Marie Curie Actions) of the European Union Seventh Framework Programme FP7/2007–2013 under REA grant agreement no 317217. This work was additionally supported by the gender program (“likestillingsprogrammet”) at the University of Bergen to B.O. Hjelstuen. All sediment analyses were done at the national infrastructure EARTHLAB (NRC 226171) at the University of Bergen. The authors acknowledge I. Berstad and T. Nilsen for the data of core MD99-2289. V. Hope, T. Richter, J. Kuvås, A. J.-G. Becker and H. Kinkel are thanked for their extensive laboratory work, B. Reinardy and B. Robson are thanked for language editing. Olex AS and the British Geological Survey, Natural Environment Research Council are thanked for their kind permission to use their bathymetric and shallow seismic data. Finally, the authors thank the guest editor, M. Bentley, and two anonymous reviewers for their helpful input.

References

Alvarez-Solas, J., Montoya, M., Ritz, C., Ramstein, G., Charbit, S., Dumas, C., Nisancioglu, K., Dokken, T., Ganopolski, A., 2011. Heinrich event 1: an example of dynamical ice-sheet reaction to oceanic changes. Clim. Past 7 (4), 1297–1306.

Andrews, J., 2000. Icebergs and iceberg rafted detritus (IRD) in the North Atlantic: facts and assumptions. Oceanography 13 (3), 100–108.

Anjar, J., Larsen, N.K., Håkansson, L., Möller, P., Linge, H., Fabel, D., Xu, S., 2014. A 10Be-based reconstruction of the last deglaciation in southern Sweden. Boreas 43, 132–148.

Austin, W.E.N., Wilson, L.J., Hunt, J.B., 2004. The age and chronostratigraphical significance of North Atlantic Ash Zone II. J. Quat. Sci. 19 (2), 137–146.

Bailey, I., Foster, G.L., Wilson, P.A., Jovane, L., Storey, C.D., Trueman, C.N., Becker, J., 2012. Flux and provenance of ice-rafted debris in the earliest Pleistocene sub-polar North Atlantic Ocean comparable to the last glacial maximum. Earth Planet. Sci. Lett. 341, 222–233.

Bauch, H.A., Erlenkeuser, H., Spielhagen, R., Struck, U., Matthiessen, J., Thiede, J., Heinemeier, J., 2001. A multiproxy reconstruction of the evolution of deep and surface waters in the subarctic Nordic seas over the last 30,000 yr. Quat. Sci. Rev. 20, 659–678.

Bé, A.W.H., Tolderlund, D.S., 1971. Distribution and ecology of living planktonic foraminifera in surface waters of the Atlantic and Indian Oceans. In: Funnel, B.M., Riedel, W.R. (Eds.), The Micropaleontology of Oceans, pp. 105–149.

Becker, L.W.M., Hjelstuen, B.O., Støren, E.W.N., 2017. Automated counting of sand sized particles in marine records. Sedimentology. http://dx.doi.org/10.1111/sed.12407.

Bentley, M.J., Cofaigh, C.Ó., Anderson, J.B., Conway, H., Davies, B., Graham, A.G.C., Hillenbrand, C.-D., Hodgson, D.A., Jamieson, S.S.R., Larter, R.D., Mackintosh, A., Smith, J.A., Verleyen, E., Ackert, R.P., Bart, P.J., Berg, S., Brunstein, D., Canals, M., Colhoun, E.A., Crosta, X., Dickens, W.A., Domack, E., Dowdeswell, J.A., Dunbar, R., Ehrmann, W., Evans, J., Favier, V., Fink, D., Fogwill, C.J., Glasser, N.F., Gohl, K., Golledge, N.R., Goodwin, I., Gore, D.B., Greenwood, S.L., Hall, B.L., Hall, K., Hedding, D.W., Hein, A.S., Hocking, E.P., Jakobsson, M., Johnson, J.S., Jomelli, V., Jones, R.S., Klages, J.P., Kristoffersen, Y., Kuhn, G., Leventer, A., Licht, K., Lilly, K., Lindow, J., Livingstone, S.J., Massé, G., McGlone, M.S., McKay, R.M., Melles, M., Miura, H., Mulvaney, R., Nel, W., Nitsche, F.O., O'Brien, P.E., Post, A.L., Roberts, S.J., Saunders, K.M., Selkirk, P.M., Simms, A.R., Spiegel, C., Stolldorf, T.D., Sugden, D.E., van der Putten, N., van Ommen, T., Verfaillie, D., Vyverman, W., Wagner, B., White, D.A., Witus, A.E., Zwartz, D., 2014. A community-based geological reconstruction of Antarctic ice sheet deglaciation since the last glacial maximum. Quat. Sci. Rev. 100, 1–9.

Berstad, I.M., 2003. Quaternary Climate Variability in the Eastern Nordic Sea Region Inferred From Speleotherm and Deep-sea Cores (PhD Thesis). University of Bergen, Bergen, Norway (140 pp.).

Berstad, I.M., Sejrup, H.P., Klitgaard-Kristensen, D., Haflidason, H., 2003. Variability in

temperature and geometry of the Norwegian current over the past 600 yr; stable isotope and grain size evidence from the Norwegian margin. J. Quat. Sci. 18 (7), 591–602.
Bigg, G.R., Clark, C.D., Greenwood, S.L., Haflidason, H., Hughes, A.L.C., Levine, R.C., Nygard, A., Sejrup, H.P., 2012. Sensitivity of the North Atlantic circulation to break-up of the marine sectors of the NW European ice sheets during the last Glacial: a synthesis of modeling and palaeoceanography. Glob. Planet. Chang. 98-99, 153–165.
Blaauw, M., Christen, J.A., 2011. Flexible paleoclimate age-depth models using an autoregressive gamma process. Bayesian Anal. 6, 457–474.
Bond, G.C., Lotti, R., 1995. Iceberg discharges into the North Atlantic on millennial time scales during the last glaciation. Science 267 (5200), 1005–1010.
Bradwell, T., Stoker, M.S., Golledge, N.R., Wilson, C.K., Merritt, J.W., Long, D., Everest, J.D., Hestvik, O.B., Stevenson, A.G., Hubbard, A.L., Finlayson, A.G., Mathers, H.E., 2008. The northern sector of the last British Ice Sheet: maximum extent and demise. Earth Sci. Rev. 88 (3–4), 207–226.
Brendryen, J., Haflidason, H., Sejrup, H.P., 2010. Norwegian Sea tephrostratigraphy of marine isotope stages 4 and 5: prospects and problems for tephrochronology in the North Atlantic region. Quat. Sci. Rev. 29 (7–8), 847–864.
Briner, J.P., Goehring, B.M., Mangerud, J., Svendsen, J.I., 2016. The deep accumulation of 10Be at Utsira, southwestern Norway: implications for cosmogenic nuclide exposure dating in peripheral ice sheet landscapes. Geophys. Res. Lett. 43.
Broecker, W., Peteet, D.M., Rind, D., 1985. Does the ocean-atmosphere system have more than one stable mode of operation? Nature 315, 21–26.
Clark, C.D., Hughes, A.L.C., Greenwood, S.L., Jordan, C., Sejrup, H.P., 2012. Pattern and timing of retreat of the last British-Irish Ice Sheet. Quat. Sci. Rev. 44, 112–146.
Crocker, A.J., Chalk, T.B., Bailey, I., Spencer, M.R., Gutjahr, M., Foster, G.L., Wilson, P.A., 2016. Geochemical response of the mid-depth Northeast Atlantic Ocean to freshwater input during Heinrich events 1 to 4. Quat. Sci. Rev. 151, 236–254.
Dahlgren, K.I.T., Vorren, T.O., 2003. Sedimentary environment and glacial history during the last 40 ka of the Vøring continental margin, mid-Norway. Mar. Geol. 193, 93–127.
Dahlgren, K.I.T., Vorren, T.O., Laberg, J.S., 2002. Late Quaternary glacial development of the mid-Norwegian margin—65 to 68° N. Mar. Pet. Geol. 19 (9), 1089–1113.
Dansgaard, W., Johnsen, S.J., Clausen, H.B., Dahljensen, D., Gundestrup, N.S., Hammer, C.U., Hvidberg, C.S., Steffensen, J.P., Sveinbjornsdottir, A.E., Jouzel, J., Bond, G., 1993. Evidence for general instability of past climate from a 250-kyr ice-core record. Nature 364 (6434), 218–220.
Davies, S.M., Wastegard, S., Rasmussen, T.L., Svensson, A., Johnsen, S.J., Steffensen, J.P., Andersen, K.K., 2008. Identification of the Fugloyarbanki tephra in the NGRIP ice core: a key tie-point for marine and ice-core sequences during the last glacial period. J. Quat. Sci. 23 (5), 409–414.
Dokken, T.M., Jansen, E., 1999. Rapid changes in the mechanism of ocean convection during the last glacial period. Nature 401 (6752), 458–461.
Dokken, T.M., Nisancioglu, K.H., Li, C., Battisti, D.S., Kissel, C., 2013. Dansgaard-Oeschger cycles: interactions between ocean and sea ice intrinsic to the Nordic seas. Paleoceanography 28 (3), 491–502.
Dokken, T., Andersson, C., Risebrobakken, B., 2015a. Relative abundance of planktic foraminifera and calculated SSTs and SST anomaly (11.1–25.5 ka BP) in sediment core MD95-2010. In: PANGAEA, http://dx.doi.org/10.1594/PANGAEA.841922.
Dokken, T., Andersson, C., Risebrobakken, B., 2015b. Relative abundance of planktic foraminifera and calculated SSTs and SST anomaly (0–25.5 ka BP) in sediment core MD99-2284. http://dx.doi.org/10.1594/PANGAEA.846924.
Dowdeswell, J.A., Elverhøi, A., 2002. The timing of initiation of fast-flowing ice streams during a glacial cycle inferred from glacimarine sedimentation. Mar. Geol. 188, 3–14.
Ehlers, J., Gibbard, P., 2008. Extent and chronology of Quaternary glaciation. Episodes 31 (2), 211–218.
Elliot, M., Labeyrie, L., Duplessy, J.C., 2002. Changes in North Atlantic deep-water formation associated with the Dansgaard–Oeschger temperature oscillations (60–10 ka). Quat. Sci. Rev. 21, 1153–1165.
Ezat, M.M., Rasmussen, T.L., Groeneveld, J., 2014. Persistent intermediate water warming during cold stadials in the southeastern Nordic seas during the past 65 k.y. Geology 42 (8), 663–666.
Haapaniemi, A.I., Scourse, J.D., Peck, V.L., Kennedy, H., Kennedy, P., Hemming, S.R., Furze, M.F.A., Pienkowski, A.J., Austin, W.E.N., Walden, J., Wadsworth, E., Hall, I.R., 2010. Source, timing, frequency and flux of ice-rafted detritus to the Northeast Atlantic margin, 30–12 ka: testing the Heinrich precursor hypothesis. Boreas 39 (3), 576–591.
Haflidason, H., Sejrup, H.P., Kristensen, D.K., Johnsen, S., 1995. Coupled response of the late-glacial climatic shifts of northwest Europe reflected in Greenland ice cores - evidence from the northern North-Sea. Geology 23 (12), 1059–1062.
Haflidason, H., King, E.L., Sejrup, H.P., 1998. Late Weichselian and Holocene sediment fluxes of the northern North Sea Margin. Mar. Geol. 152 (1–3), 189–215.
Haflidason, H., Sejrup, H.P., Berstad, I.M., Nygård, A., Richter, T., Bryn, P., Lien, R., Berg, K., 2003. A weak layer feature on the northern Storegga Slide Escarpment. In: European Margin Sediment Dynamics.
Hall, I.R., Moran, S.B., Zahn, R., Knutz, P.C., Shen, C.C., Edwards, R.L., 2006. Accelerated drawdown of meridional overturning in the late-glacial Atlantic triggered by transient pre-H event freshwater perturbation. Geophys. Res. Lett. 33 (16).
Hall, I.R., Colmenero-Hidalgo, E., Zahn, R., Peck, V.L., Hemming, S.R., 2011. Centennial-to millennial-scale ice-ocean interactions in the subpolar northeast Atlantic 18–41 kyr ago. Paleoceanography 26 (2), 1–18.
Hammer, Ø., Harper, D.A.T., Ryan, P.D., 2001. PAST: paleontological statistics software package for education and data analysis. Palaeontol. Electron. 4 (1).
Hansen, B., Østerhus, S., 2000. North Atlantic–Nordic seas exchanges. Prog. Oceanogr. 45, 109–208.
Hjelstuen, B., Sejrup, H.P., Haflidason, H., Nygård, A., Berstad, I.M., Knorr, G., 2004. Late Quaternary seismic stratigraphy and geological development of the south Vøring margin, Norwegian Sea. Quat. Sci. Rev. 23, 1847–1865.
Hjelstuen, B.O., Petter Sejrup, H., Haflidason, H., Nygård, A., Ceramicola, S., Bryn, P., 2005. Late Cenozoic glacial history and evolution of the Storegga Slide area and adjacent slide flank regions, Norwegian continental margin. Mar. Pet. Geol. 22 (1–2), 57–69.
Hjelstuen, B.O., Sejrup, H.P., Valvik, E., Becker, L.W.M., 2017. Evidence of a ice-dammed lake outburst in the North Sea during the last deglaciation. Mar. Geol (this issue).
Hoff, U., Rasmussen, T.L., Stein, R., Ezat, M.M., Fahl, K., 2016. Sea ice and millennial-scale climate variability in the Nordic seas 90 kyr ago to present. Nat. Commun. 7, 12247.
Houmark-Nielsen, M., Linge, H., Fabel, D., Schnabel, C., Xu, S., Wilcken, K.M., Binnie, S., 2012. Cosmogenic surface exposure dating the last deglaciation in Denmark: discrepancies with independent age constraints suggest delayed periglacial landform stabilisation. Quat. Geochronol. 13, 1–17.
Hubbard, A., Bradwell, T., Golledge, N.R., Hall, A.M., Patton, H., Sugden, D.E., Cooper, R., Stoker, M.S., 2009. Dynamic cycles, ice streams and their impact on the extent, chronology and deglaciation of the British–Irish ice sheet. Quat. Sci. Rev. 28, 758–776.
Hughes, A.L.C., Gyllencreutz, R., Lohne, Ø.S., Mangerud, J., Svendsen, J.I., 2015. The last Eurasian ice sheets – a chronological database and time-slice reconstruction, DATED-1. Boreas 10 (1111).
Jansen, E., Sejrup, H.P., Fjaeran, T., Hald, M., Holtedahl, H., Skarbo, O., 1983. Late Weichselian paleoceanography of the southeastern Norwegian Sea. Nor. Geol. Tidsskr. 63 (2–3), 117–146.
Joughin, I., Alley, R.B., Holland, D.M., 2012. Ice-sheet response to oceanic forcing. Science 338 (6111), 1172–1176.
Kellogg, T.B., 1980. Paleoclimatology and paleo-oceanography of the Norwegian and Greenland seas - glacial-interglacial contrasts. Boreas 9 (2), 115–137.
King, E.L., Sejrup, H.P., Haflidason, H., Elverhøi, A., Aarseth, I., 1996. Quaternary seismic stratigraphy of the North Sea Fan: glacially fed gravity flow aprons, hemipelagic sediments, and large submarine slides. Mar. Geol. 130, 293–315.
King, E.L., Haflidason, H., Sejrup, H.P., Løvlie, R., 1998. Glacigenic debris flows on the North Sea Trough Mouth Fan during ice stream maxima. Mar. Geol. 152 (1–3), 217–246.
Kissel, C., Laj, C., Mazaud, A., Dokken, T., 1998. Magnetic anisotropy and environmental changes in two sedimentary cores from the Norwegian sea and the North Atlantic. Earth Planet. Sci. Lett. 164 (3–4), 617–626.
Klitgaard-Kristensen, D., Sejrup, H.P., Haflidason, H., 2001. The last 18 kyr fluctuations in Norwegian Sea surface conditions and implications for the magnitude of climatic change: evidence from the North Sea. Paleoceanography 16 (5), 455–467.
Knutz, P.C., Zahn, R., Hall, I.R., 2007. Centennial-scale variability of the British Ice Sheet: implications for climate forcing and Atlantic meridional overturning circulation during the last deglaciation. Paleoceanography 22 (1), 1–14.
Lee, J.R., Busschers, F.S., Sejrup, H.P., 2012. Pre-Weichselian Quaternary glaciations of the British Isles, The Netherlands, Norway and adjacent marine areas south of 68° N: implications for long-term ice sheet development in northern Europe. Quat. Sci. Rev. 44, 213–228.
Lekens, W.A.H., Sejrup, H.P., Haflidason, H., Petersen, G.O., Hjelstuen, B., Knorr, G., 2005. Laminated sediments preceding Heinrich event 1 in the Northern North Sea and Southern Norwegian Sea: origin, processes and regional linkage. Mar. Geol. 216 (1–2), 27–50.
Lekens, W.A.H., Sejrup, H.P., Haflidason, H., Knies, J., Richter, T., 2006. Meltwater and ice rafting in the southern Norwegian Sea between 20 and 40 calendar kyr BP: implications for Fennoscandian Heinrich events. Paleoceanography 21 (3), PA3013.
Lekens, W.A.H., Haflidason, H., Sejrup, H.P., Nygard, A., Richter, T., Vogt, C., Frederichs, T., 2009. Sedimentation history of the northern North Sea Margin during the last 150 ka. Quat. Sci. Rev. 28 (5–6), 469–483.
Liu, W., Xie, S.P., Liu, Z., Zhu, J., 2017. Overlooked possibility of a collapsed Atlantic meridional overturning circulation in warming climate. Sci. Adv. 3 (1).
Malvern Instruments Ltd., 2017. Morphologi G3 - Advanced Particle Characterization Made Easy. https://www.malvern.com/en/products/product-range/morphologi-range/morphologi-g3/.
Mangerud, J., Løvlie, R., Gulliksen, S., Hufthammer, A.K., Larsen, E., Valen, V., 2003. Paleomagnetic correlations between Scandinavian Ice-Sheet fluctuations and Greenland Dansgaard–Oeschger events, 45,000–25,000 yr B.P. Quat. Res. 59, 213–222.
Mangerud, J., Gyllencreutz, R., Lohne, Ø., Svendsen, J.I., 2011. Glacial History of Norway. 15. pp. 279–298.
Margold, M., Stokes, C.R., Clark, C.D., 2015. Ice streams in the Laurentide Ice Sheet: identification, characteristics and comparison to modern ice sheets. Earth Sci. Rev. 143, 117–146.
Ménot, G., Bard, E., Rostek, F., Weijers, J.W.H., Hopmans, E.C., Schouten, S., Sinninghe Damsté, J.S., 2006. Early reactivation of European rivers during the last deglaciation. Science 313.
Morén, B.M., Sejrup, H.P., Hjelstuen, B.O., Borge, M.V., Schäuble, C., 2017. The last deglaciation of the Norwegian Channel; geomorphology, stratigraphy and radiocarbon dating. Boreas. http://dx.doi.org/10.1111/bor.12272.
Nilsen, T.E., 2014. Kronologi, askestratigrafi og utbredelse av store askeutbrudd fra de siste 40 ka i kjerne MD99-2289 fra Norskehavet. University of Bergen, Bergen (MSc Thesis, 114 pp.).
Nygård, A., 2003. Pleistocene Sedimentary Processes and Glacial History of the Southern Norwegian Continental Margin (PhD Thesis). University of Bergen, Bergen.
Nygård, A., Sejrup, H.P., Haflidason, H., Cecchi, M., Ottesen, D., 2004. Deglaciation history of the southwestern Fennoscandian Ice Sheet between 15 and 13 14C ka BP. Boreas 33, 1–17.

Nygård, A., Sejrup, H.P., Haflidason, H., Bryn, P., 2005. The glacial North Sea Fan, southern Norwegian Margin: architecture and evolution from the upper continental slope to the deep-sea basin. Mar. Pet. Geol. 22, 71–84.

Nygård, A., Sejrup, H.P., Haflidason, H., Lekens, W.A.H., Clark, C.D., Bigg, G.R., 2007. Extreme sediment and ice discharge from marine-based ice streams: new evidence from the North Sea. Geology 35 (5), 395–398.

Ottesen, D., Stokes, C.R., Bøe, R., Rise, L., Longva, O., Thorsnes, T., Olesen, O., Bugge, T., Lepland, A., Hestvik, O.B., 2016. Landform assemblages and sedimentary processes along the Norwegian Channel Ice Stream. Sediment. Geol. 338, 115–137.

Patton, H., Hubbard, A., Andreassen, K., Winsborrow, M., Stroeven, A.P., 2016. The build-up, configuration, and dynamical sensitivity of the Eurasian ice-sheet complex to Late Weichselian climatic and oceanic forcing. Quat. Sci. Rev. 153, 97–121.

Peck, V.L., Hall, I.R., Zahn, R., Elderfield, H., Grousset, F., Hemming, S.R., Scourse, J.D., 2006. High resolution evidence for linkages between NW European ice sheet instability and Atlantic Meridional Overturning Circulation. Earth Planet. Sci. Lett. 243 (3–4), 476–488.

Peck, V.L., Hall, I.R., Zahn, R., Grousset, F., Hemming, S.R., Scourse, J.D., 2007. The relationship of Heinrich events and their European precursors over the past 60 ka BP: a multi-proxy ice-rafted debris provenance study in the North East Atlantic. Quat. Sci. Rev. 26 (7–8), 862–875.

Peck, V.L., Hall, I.R., Zahn, R., Elderfield, H., 2008. Millennial-scale surface and sub-surface paleothermometry from the northeast Atlantic, 55–8 ka BP. Paleoceanography 23 (3), PA3221.

Peltier, W.R., Vettoretti, G., 2014. Dansgaard-Oeschger oscillations predicted in a comprehensive model of glacial climate: a "kicked" salt oscillator in the Atlantic. Geophys. Res. Lett. 41, 7306–7313.

Peters, J.L., Benetti, S., Dunlop, P., Cofaigh, C.Ó., 2015. Maximum extent and dynamic behaviour of the last British–Irish Ice Sheet west of Ireland. Quat. Sci. Rev. 128, 48–68.

Petersen, S.V., Schrag, D.P., Clark, P.U., 2013. A new mechanism for Dansgaard-Oeschger cycles. Paleoceanography 28 (1).

Pflaumann, U., Sarnthein, M., Chapman, M., d'Abreu, L., Funnell, B., Huels, M., Kiefer, T., Maslin, M., Schulz, H., Swallow, J., van Kreveld, S., Vautravers, M., Vogelsang, E., Weinelt, M., 2003. Glacial North Atlantic: sea-surface conditions reconstructed by GLAMAP 2000. Paleoceanography 18 (3), 1065.

Rahmstorf, S., Box, J.E., Feulner, G., Mann, M.E., Robinson, A., Rutherford, S., Schaffernicht, E.J., 2015. Exceptional twentieth-century slowdown in Atlantic Ocean overturning circulation. Nat. Clim. Chang. 5 (5), 475–480.

Rasmussen, T.L., Thomsen, E., 2008. Warm Atlantic surface water inflow to the Nordic seas 34-10 calibrated ka BP. Paleoceanography 23 (1).

Rasmussen, T.L., Thomsen, E., Moros, M., 2016. North Atlantic warming during Dansgaard-Oeschger events synchronous with Antarctic warming and out-of-phase with Greenland climate. Sci. Rep. 6, 20535.

Reiche, S., Hjelstuen, B.O., Haflidason, H., 2011. High-resolution seismic stratigraphy, sedimentary processes and the origin of seabed cracks and pockmarks at Nyegga, mid-Norwegian margin. Mar. Geol. 284 (1–4), 28–39.

Reimer, P.J., Bard, E., Bayliss, A., Beck, J.W., Blackwell, P.G., Ramsey, C.B., Buck, C.E., Cheng, H., Edwards, R.L., Friedrich, M., Grootes, P.M., Guilderson, T.P., Haflidason, H., Hajdas, I., Hatte, C., Heaton, T.J., Hoffmann, D.L., Hogg, A.G., Hughen, K.A., Kaiser, K.F., Kromer, B., Manning, S.W., Niu, M., Reimer, R.W., Richards, D.A., Scott, E.M., Southon, J.R., Staff, R.A., Turney, C.S.M., van der Plicht, J., 2013. Intcal13 and Marine13 radiocarbon age calibration curves 0–50,000 years Cal Bp. Radiocarbon 55 (4), 1869–1887.

Reinardy, B.T.I., Hjelstuen, B.O., Sejrup, H.P., Augedal, H., Jørstad, A., 2017. Late Pliocene-Pleistocene environments and glacial history of the northern North Sea. Quat. Sci. Rev. 158, 107–126.

Rise, L., Ottesen, D., Berg, K., Lundin, E., 2005. Large-scale development of the mid-Norwegian margin during the last 3 million years. Mar. Pet. Geol. 22 (1–2), 33–44.

Rise, L., Bøe, R., Ottesen, D., Longva, O., Olsen, H.A., 2008. Postglacial depositional environments and sedimentation rates in the Norwegian Channel off southern Norway. Mar. Geol. 251 (1–2), 124–138.

Risebrobakken, B., Dokken, T., Smedsrud, L.H., Andersson, C., Jansen, E., Moros, M., Ivanova, E.V., 2011. Early Holocene temperature variability in the Nordic Seas: the role of oceanic heat advection versus changes in orbital forcing. Paleoceanography 26.

Robinson, S.G., Maslin, M.A., Mccave, I.N., 1995. Magnetic-susceptibility variations in Upper Pleistocene deep-sea sediments of the Ne Atlantic - implications for ice rafting and paleocirculation at the last glacial maximum. Paleoceanography 10 (2), 221–250.

Rokoengen, K., Frengstad, B., 1999. Radiocarbon and seismic evidence of ice-sheet extent and the last deglaciation on the mid-Norwegian continental shelf. Nor. Geol. Tidsskr. 79 (2), 129–132.

Scourse, J.D., Haapaniemi, A.I., Colmenero-Hidalgo, E., Peck, V.L., Hall, I.R., Austin, W.E.N., Knutz, P.C., Zahn, R., 2009. Growth, dynamics and deglaciation of the last British-Irish ice sheet: the deep-sea ice-rafted detritus record. Quat. Sci. Rev. 28 (27–28), 3066–3084.

Seierstad, I.K., Abbott, P.M., Bigler, M., Blunier, T., Bourne, A.J., Brook, E., Buchardt, S.L., Buizert, C., Clausen, H.B., Cook, E., Dahl-Jensen, D., Davies, S.M., Guillevic, M., Johnsen, S.J., Pedersen, D.S., Popp, T.J., Rasmussen, S.O., Severinghaus, J.P., Svensson, A., Vinther, B.M., 2014. Consistently dated records from the Greenland GRIP, GISP2 and NGRIP ice cores for the past 104 ka reveal regional millennial-scale delta O-18 gradients with possible Heinrich event imprint. Quat. Sci. Rev. 106, 29–46.

Sejrup, H.P., Fjæran, T., Hald, M., Beck, L., Hagen, J., Miljeteig, I., Morvik, I., Norvik, O., 1981. Benthonic foraminifera in surface samples from the Norwegian continental margin between 62° N and 65° N. J. Foraminifer. Res. 11 (4), 277–295.

Sejrup, H.P., Haflidason, H., Aarseth, I., King, E., Forsberg, C.F., Long, D., Rokoengen, K., 1994. Late Weichselian glaciation history of the northern North-Sea. Boreas 23 (1), 1–13.

Sejrup, H.P., King, E.L., Aarseth, I., Haflidason, H., Elverhøi, A., 1996. Quaternary erosion and depositional processes: western Norwegian fjords, Norwegian Channel and North Sea Fan. Geol. Soc. Lond., Spec. Publ. 117 (1), 187–202.

Sejrup, H.P., Landvik, J.Y., Larsen, E., Janocko, J., Eiriksson, J., King, E., 1998. The Jæren area, a border zone of the Norwegian channel ice stream. Quat. Sci. Rev. 17 (9–10), 801–812.

Sejrup, H.P., Larsen, E., Landvik, J., King, E.L., Haflidason, H., Nesje, A., 2000. Quaternary glaciations in southern Fennoscandia: evidence from southwestern Norway and the northern North Sea region. Quat. Sci. Rev. 19 (7), 667–685.

Sejrup, H.P., Larsen, E., Haflidason, H., Berstad, I.M., Hjelstuen, B.O., Jonsdottir, H.E., King, E.L., Landvik, J., Longva, O., Nygard, A., Ottesen, D., Raunholm, S., Rise, L., Stalsberg, K., 2003. Configuration, history and impact of the Norwegian Channel Ice Stream. Boreas 32 (1), 18–36.

Sejrup, H.P., Hjelstuen, B.O., Dahlgren, K.I.T., Haflidason, H., Kuijpers, A., Nygard, A., Praeg, D., Stoker, M.S., Vorren, T.O., 2005. Pleistocene glacial history of the NW European continental margin. Mar. Pet. Geol. 22 (9–10), 1111–1129.

Sejrup, H.P., Nygard, A., Hall, A.M., Haflidason, H., 2009. Middle and Late Weichselian (Devensian) glaciation history of south-western Norway, North Sea and eastern UK. Quat. Sci. Rev. 28 (3–4), 370–380.

Sejrup, H.P., Hjelstuen, B.O., Nygard, A., Haflidason, H., Mardal, I., 2015. Late Devensian ice-marginal features in the central North Sea processes and chronology. Boreas 44 (1), 1–13.

Sejrup, H.P., Clark, C.D., Hjelstuen, B.O., 2016. Rapid ice sheet retreat triggered by ice stream debuttressing: evidence from the North Sea. Geology 44 (5), 355–358.

Stanford, J.D., Rohling, E.J., Bacon, S., Roberts, A.P., Grousset, F.E., Bolshaw, M., 2011. A new concept for the paleoceanographic evolution of Heinrich event 1 in the North Atlantic. Quat. Sci. Rev. 30 (9–10), 1047–1066.

Svendsen, J.I., Briner, J.P., Mangerud, J., Young, N.E., 2015. Early break-up of the Norwegian Channel Ice Stream during the last glacial maximum. Quat. Sci. Rev. 107, 231–242.

Toucanne, S., Zaragosi, S., Bourillet, J.-F., Marieu, V., Cremer, M., Kageyama, M., Van Vliet-Lanoë, B., Eynaud, F., Turon, J.-L., Gibbard, P.L., 2010. The first estimation of Fleuve Manche palaeoriver discharge during the last deglaciation: evidence for Fennoscandian ice sheet meltwater flow in the English Channel ca 20–18 ka ago. Earth Planet. Sci. Lett. 290 (3–4), 459–473.

Toucanne, S., Soulet, G., Freslon, N., Silva Jacinto, R., Dennielou, B., Zaragosi, S., Eynaud, F., Bourillet, J.-F., Bayon, G., 2015. Millennial-scale fluctuations of the European Ice Sheet at the end of the last glacial, and their potential impact on global climate. Quat. Sci. Rev. 123, 113–133.

Vaughan, D.G., Comiso, J.C., Allison, I., Carrasco, J., Kaser, G., Kwok, R., Mote, P., Murray, T., Paul, F., Ren, J., Rignot, E., Solomina, O., Steffen, K., Zhang, T., 2013. Observations: cryosphere. In: Stocker, T.F., Qin, D., Plattner, G.-K., Tignor, M., Allen, S.K., Boschung, J., Nauels, A., Xia, Y., Bex, V., Midgley, P.M. (Eds.), Climate Change 2013: The Physical Science Basis. Contribution of Working Group I to the Fifth Assessment Report of the Intergovernmental Panel on Climate Change. Cambridge University Press, Cambridge, United Kingdom and New York, NY, USA.

Wary, M., Eynaud, F., Rossignol, L., Lapuyade, J., Gasparotto, M.-C., Londeix, L., Malaizé, B., Castére, M.-H., Charlier, K., 2016. Norwegian Sea warm pulses during Dansgaard-Oeschger stadials: zooming in on these anomalies over the 35–41 ka cal BP interval and their impacts on proximal European ice-sheet dynamics. Quat. Sci. Rev. 151, 255–272.

Werner, J.P., Tingley, M.P., 2015. Technical note: probabilistically constraining proxy age–depth models within a Bayesian hierarchical reconstruction model. Clim. Past 11 (3), 533–545.

Whittington, G., Edwards, K.J., 1993. Vegetation change on Papa Stour, Shetland, Scotland: a response to coastal evolution and human interference? The Holocene 3 (1), 54–62.

Core	Lab number	core depth, void corrected (cm)	Material	14C Age, uncorrected (ka BP)	calendar age (ka BP)	S.D. 1 σ (ka)	calibrated, modelled age (cal ka BP)	S.D. 2 σ (ka) (max)	S.D. 2 σ (ka) (min)	S.D. 2 σ (ka) (average of both errors)	Original reference	Info
MD95-2010	KIA-6550	9.5	N. pachyderma sinistral	3.57		0.04	3.00	0.14	0.12	0.13	this study	
MD95-2010	KIA-6551	54.5	N. pachyderma sinistral	11.42		0.06	12.92	0.17	0.15	0.16	Dokken and Jansen (1999)	included
MD95-2010	KIA-6552	136.5	N. pachyderma sinistral	13.25		0.06	15.45	0.26	0.22	0.24	Dokken and Jansen (1999)	included
MD95-2010	KIA-6553	173.5	N. pachyderma sinistral	14.75		0.11	17.52	0.32	0.34	0.33	Dokken and Jansen (1999)	included
MD95-2010	KIA-6554	197.5	N. pachyderma sinistral	15.62		0.07	18.50	0.19	0.23	0.21	Dokken and Jansen (1999)	included
MD95-2010	KIA-6555	300.5	N. pachyderma sinistral	16.99		0.11	20.17	0.30	0.31	0.31	Dokken and Jansen (1999)	included
MD95-2010	GifA-96476	449.5	N. pachyderma sinistral	19.83		0.13	23.61	0.23	0.27	0.25	Dokken and Jansen (1999)	included
MD95-2010	GifA-96477	450.5	N. pachyderma sinistral	20.03		0.11	23.63	0.23	0.27	0.25	Dokken and Jansen (1999)	included
MD95-2010	GifA-96487	459.5	N. pachyderma sinistral	19.93		0.12	23.79	0.24	0.25	0.25	Dokken and Jansen (1999)	included
MD95-2010	GifA-96489	464.5	N. pachyderma sinistral	20.34		0.12	24.05	0.15	0.16	0.15	Dokken and Jansen (1999)	included
MD95-2010	GifA-96683	467.5	N. pachyderma sinistral	22.26		0.18	24.21	0.14	0.14	0.14	Dokken and Jansen (1999)	included
MD95-2010	GifA-96490	469.5	N. pachyderma sinistral	20.34		0.13	24.32	0.17	0.17	0.17	Dokken and Jansen (1999)	included
MD95-2010	GifA-96684	470.5	N. pachyderma sinistral	20.39		0.16	24.35	0.18	0.18	0.18	Dokken and Jansen (1999)	included
MD95-2010	GifA-96492	484.5	N. pachyderma sinistral	20.45		0.12	24.45	0.17	0.17	0.17	Dokken and Jansen (1999)	included
MD95-2010	GifA-96685	521.5	N. pachyderma sinistral	21.59		0.19	24.84	0.30	0.21	0.25	Dokken and Jansen (1999)	included
MD95-2010	KIA-6556	554.5	N. pachyderma sinistral	20.49		0.14	25.13	0.26	0.23	0.25	Dokken and Jansen (1999)	included
MD95-2010	GifA-96686	594.5	N. pachyderma sinistral	24.33		0.22	26.09	0.51	0.20	0.36	Dokken and Jansen (1999)	included
MD95-2010	GifA-96491	606.5	N. pachyderma sinistral	20.42		0.17	26.16	0.55	0.19	0.37	Dokken and Jansen (1999)	included
MD95-2010	GifA-96493	624.5	N. pachyderma sinistral	25.54		0.20	27.96	0.64	0.39	0.52	Dokken and Jansen (1999)	included
MD95-2010	KIA-6557	640.5	N. pachyderma sinistral	25.52		0.24	29.63	0.54	0.43	0.49	Dokken and Jansen (1999)	included
MD95-2010	GifA-96496	670.5	N. pachyderma sinistral	27.45		0.20	31.05	0.33	0.44	0.39	Dokken and Jansen (1999)	included
MD95-2010	GifA-96497	716.5	N. pachyderma sinistral	28.94		0.24	32.74	0.56	0.59	0.58	Dokken and Jansen (1999)	included
MD95-2010	GifA-96687	737.0	N. pachyderma sinistral	29.67		0.26	33.55	0.42	0.51	0.47	Dokken and Jansen (1999)	included
MD95-2010	GifA-96688	757.5	N. pachyderma sinistral	31.24		0.30	34.67	0.55	0.54	0.55	Dokken and Jansen (1999)	included
MD95-2010	GifA-96494	790.5	N. pachyderma sinistral	33.42		0.37	36.70	0.70	0.71	0.70	Dokken and Jansen (1999)	included
MD95-2010	GifA-96689	816.5	N. pachyderma sinistral	33.82		0.39	37.76	0.75	0.82	0.79	Dokken and Jansen (1999)	included
MD95-2010	GifA-96690	827.5	N. pachyderma sinistral	35.48		0.55	38.89	0.78	0.79	0.79	Dokken and Jansen (1999)	included
MD95-2010	KIA-6558	861.5	N. pachyderma sinistral	38.56		0.91	42.06	1.39	1.44	1.41	Dokken and Jansen (1999)	
MD95-2010	KIA-6559	903.5	N. pachyderma sinistral	45.94		2.46	46.75	3.33	2.58	2.96	Dokken and Jansen (1999)	
MD99-2291	KIA-18160	10.0	N. pachyderma dextral	15.86		0.10	4.06	0.92	1.14	1.03	Lekens et al. (2005)	rejected - reworked
MD99-2291	ETH-257121	16.5	N. pachyderma sinistral and N. pachyderma dextral	4.24		0.28	4.48	0.76	0.75	0.75	Lekens et al. (2005)	
MD99-2291	KIA-19317	60.8	N. labradorica	13.02		0.07	7.28	2.53	2.14	2.34	Lekens et al. (2005)	rejected - reworked
MD99-2291	ETH-25488	100.0	benthic foraminifera	10.74		0.17	9.23	2.84	2.64	2.74	Lekens et al. (2005)	
MD99-2291	ETH-25495	180.0	benthic foraminifera	13.05		0.11	15.48	1.20	0.95	1.08	Lekens et al. (2005)	included
MD99-2291	ETH-25958	280.0	benthic foraminifera	15.40		0.14	18.69	0.22	0.25	0.23	Lekens et al. (2005)	included

Core	Lab number	core depth, void corrected (cm)	Material	14C Age, uncorrected (ka BP)	calendar age (ka BP)	S.D. 1 σ (ka)	calibrated, modelled age (cal ka BP)	S.D. 2 σ (ka) (max)	S.D. 2 σ (ka) (min)	S.D. 2 σ (ka) (average of both errors)	Original reference	Info
MD99-2291	Poz-3950	367.0	Yoldiella lenticula	16.12		0.07	18.69	0.20	0.20	0.20	Lekens et al. (2005)	included
MD99-2291	Poz-3951	455.0	Yoldiella lenticula	16.11		0.07	18.70	0.20	0.20	0.20	Lekens et al. (2005)	included
MD99-2291	Poz-3952	614.5	Yoldiella lenticula	16.20		0.06	18.70	0.20	0.20	0.20	Lekens et al. (2005)	included
MD99-2291	ETH-22959	1690.0	N. pachyderma sinistral	16.10		0.25	19.39	0.31	0.32	0.32	Lekens et al. (2005)	included
MD99-2291	ETH-22960	2040.0	N. pachyderma sinistral	17.05		0.25	20.88	0.38	0.40	0.39	Lekens et al. (2005)	included
MD99-2291	Poz-3956	2168.0	Yoldiella lenticula	18.62		0.08	21.66	0.24	0.32	0.28	Lekens et al. (2005)	included
MD99-2291	Poz-3957	2375.0	Yoldiella lenticula	18.61		0.08	22.23	0.20	0.21	0.21	Lekens et al. (2005)	included
MD99-2291	ETH-22961	2523.0	N. pachyderma sinistral	16.63		0.25	22.35	0.21	0.22	0.21	Lekens et al. (2005)	included
MD99-2289	ETH-55533	86.8	N. pachyderma sinistral	11.78		0.18	13.25	0.35	0.37	0.36	this study	included
MD99-2289	AAR-6234	124.5	N. pachyderma sinistral	12.41		0.14	14.07	0.59	0.36	0.48	Reiche et al. (2011)	included
MD99-2289	Beta-414663	182.0	planktonic foraminifera	14.72		0.04	17.39	0.18	0.21	0.19	this study	included
MD99-2289	Beta-380040	248.8	N. pachyderma sinistral	15.63		0.05	18.47	0.14	0.14	0.14	this study	included
MD99-2289	AAR-6235	285.8	planktonic foraminifera	16.16		0.17	18.81	0.22	0.21	0.21	Reiche et al. (2011)	included
MD99-2289	AAR-6236	563.2	N. pachyderma sinistral	17.31		0.16	20.57	0.31	0.31	0.31	Reiche et al. (2011)	included
MD99-2289	ETH-25496	790.1	N. pachyderma sinistral	18.56		0.13	22.29	0.20	0.26	0.23	Reiche et al. (2011)	included
MD99-2289	Beta-380041	850.1	N. pachyderma sinistral	19.79		0.07	23.29	0.27	0.29	0.28	this study	included
MD99-2289	ETH-25497	969.8	N. pachyderma sinistral	21.37		0.16	25.18	0.39	0.49	0.44	Reiche et al. (2011)	included
MD99-2289	Beta-376421	1049.9	N. pachyderma sinistral	23.24		0.10	27.14	0.34	0.40	0.37	this study	included
MD99-2289	Beta-376422	1059.8	N. pachyderma sinistral	24.08		0.09	27.64	0.13	0.20	0.17	this study	included
MD99-2289	Beta-373227	1062.8	N. pachyderma sinistral	24.14		0.12	27.68	0.11	0.15	0.13	this study	included
MD99-2289	FMAZ II	1063.8	Tephra		26.69	0.39	27.70	0.10	0.13	0.11	Nilsen (2014)	not in age model
MD99-2289	Beta-365943	1064.8	N. pachyderma sinistral	23.83		0.11	27.71	0.09	0.11	0.10	this study	included
MD99-2289	Beta-376423	1069.8	N. pachyderma sinistral	24.40		0.11	27.78	0.07	0.07	0.07	this study	included
MD99-2289	Beta-380041	1072.8	N. pachyderma sinistral	24.20		0.09	27.79	0.07	0.07	0.07	this study	included
MD99-2289	ETH-23313	1089.8	N. pachyderma sinistral	22.95		0.20	27.84	0.07	0.07	0.07	Reiche et al. (2011)	included
MD99-2289	Beta-380043	1102.8	N. pachyderma sinistral	25.54		0.11	27.88	0.09	0.06	0.07	this study	included
MD99-2289	ETH-25498	1119.8	N. pachyderma sinistral	23.99		0.20	27.95	0.14	0.09	0.11	Reiche et al. (2011)	included
MD99-2289	ETH-23314	1150.3	N. pachyderma sinistral	23.69		0.20	28.09	0.19	0.14	0.17	Reiche et al. (2011)	included
MD99-2289	Beta-380044	1171.8	N. pachyderma sinistral	27.79		0.13	28.24	0.23	0.19	0.21	this study	rejected - reworked
MD99-2289	ETH-25499	1189.3	N. pachyderma sinistral	23.32		0.24	28.38	0.24	0.24	0.24	Reiche et al. (2011)	included
MD99-2289	ETH-23315	1219.8	N. pachyderma sinistral	25.46		0.32	29.26	0.75	0.60	0.68	Reiche et al. (2011)	included
MD99-2289	Beta-380045	1242.8	N. pachyderma sinistral	28.50		0.14	31.27	0.84	0.88	0.86	this study	included
MD99-2289	ETH-24870	1259.8	N. pachyderma sinistral	29.42		0.27	32.77	0.74	0.75	0.75	Reiche et al. (2011)	included
MD99-2289	ETH-24871	1299.8	N. pachyderma sinistral	34.25		0.43	37.01	1.35	1.30	1.32	Reiche et al. (2011)	included
MD99-2283	Poz-3945	45.0	N. pachyderma sinistral	17.08		0.07	20.12	0.23	0.24	0.23	Lekens et al. (2006)	included

Core	Lab number	core depth, void corrected (cm)	Material	14C Age, uncorrected (ka BP)	calendar age (ka BP)	S.D. 1 σ (ka)	calibrated, modelled age (cal ka BP)	S.D. 2 σ (ka) (max)	S.D. 2 σ (ka) (min)	S.D. 2 σ (ka) (average of both errors)	Original reference	Info
MD99-2283	Poz-3946	85.0	N. pachyderma sinistral	17.36		0.07	20.51	0.20	0.20	0.20	Lekens et al. (2006)	included
MD99-2283	Poz-3947	115.0	N. pachyderma sinistral	17.75		0.08	20.86	0.23	0.22	0.22	Lekens et al. (2006)	included
MD99-2283	Poz-3948	159.0	N. pachyderma sinistral	18.19		0.08	21.34	0.29	0.31	0.30	Lekens et al. (2006)	included
MD99-2283	ETH-26404	185.0	N. pachyderma sinistral	17.68		0.14	21.55	0.34	0.34	0.34	Lekens et al. (2006)	included
MD99-2283	ETH-24515	235.0	N. pachyderma sinistral	18.28		0.13	22.11	0.46	0.42	0.44	Lekens et al. (2006)	included
MD99-2283	ETH-72933	334.8	N. pachyderma sinistral	19.90		0.07	24.18	0.62	0.71	0.67	this study	rejected - too young
MD99-2283	ETH-26405	354.8	N. pachyderma sinistral	19.74		0.15	24.60	0.53	0.66	0.60	Lekens et al. (2006)	rejected - too young
MD99-2283	BETA-429895	392.3	N. pachyderma sinistral	21.51		0.07	25.37	0.25	0.31	0.28	this study	included
MD99-2283	ETH-24514	414.8	N. pachyderma sinistral	20.87		0.18	25.69	0.29	0.32	0.30	Lekens et al. (2006)	included
MD99-2283	BETA-429889	449.4	N. pachyderma sinistral	22.48		0.08	26.14	0.22	0.23	0.23	this study	included
MD99-2283	Poz-7179	474.4	N. pachyderma sinistral	22.74		0.12	26.36	0.24	0.24	0.24	Lekens et al. (2006)	included
MD99-2283	ETH-26406	634.4	N. pachyderma sinistral	23.67		0.22	27.47	0.29	0.30	0.29	Lekens et al. (2006)	included
MD99-2283	FMAZ II	634.4	Tephra		26.69	0.39	27.47	0.29	0.30	0.29	this study	not in age model
MD99-2283	ETH-24513	714.4	N. pachyderma sinistral	24.03		0.21	28.01	0.44	0.35	0.39	Lekens et al. (2006)	included
MD99-2283	ETH-24512	773.7	N. pachyderma sinistral	26.13		0.22	28.80	0.63	0.56	0.60	Lekens et al. (2006)	included
MD99-2283	ETH-24511	1024.3	N. pachyderma sinistral	26.82		0.25	31.46	0.88	0.62	0.75	Lekens et al. (2006)	included
MD99-2283	Poz-7180	1039.3	N. pachyderma sinistral	28.60		0.26	31.69	0.82	0.58	0.70	Lekens et al. (2006)	included
MD99-2283	Poz-3953	1176.9	N. pachyderma sinistral	29.24		0.18	33.57	0.74	0.55	0.65	Lekens et al. (2006)	included
MD99-2283	ETH-24516	1226.9	Gastropode	31.52		0.28	34.79	0.56	0.57	0.56	Lekens et al. (2006)	included
MD99-2283	Poz-3954	1288.9	Bivalve	32.44		0.23	36.13	0.91	0.59	0.75	Lekens et al. (2006)	included
MD99-2283	Laschamp	1408.9	magnetic reversal		40.65	0.95	39.98	1.39	1.30	1.34	Lekens et al. (2006)	included
MD99-2284	KIA-10676	2.5	N. pachyderma sinistral	1.69		0.03	1.32	0.06	0.07	0.07	Risebrobakken et al. (2014)	
MD99-2284	Poz-10150	19.5	N. pachyderma sinistral	3.52		0.04	3.46	0.10	0.11	0.10	Risebrobakken et al. (2014)	
MD99-2284	Poz-10151	36.5	N. pachyderma sinistral	5.30		0.04	5.75	0.14	0.09	0.11	Risebrobakken et al. (2014)	
MD99-2284	Poz-10157	53.5	N. pachyderma sinistral	7.30		0.04	7.75	0.08	0.08	0.08	Risebrobakken et al. (2014)	
MD99-2284	Poz-33098	71.5	N. pachyderma sinistral	7.94		0.07	8.55	0.15	0.12	0.13	Risebrobakken et al. (2014)	
MD99-2284	TUa-3301	100.5	N. pachyderma sinistral	8.68		0.09	9.32	0.18	0.23	0.21	Risebrobakken et al. (2014)	included
MD99-2284	Poz-33098	165.5	N. pachyderma sinistral	9.34		0.09	10.22	0.24	0.26	0.25	Risebrobakken et al. (2014)	included
MD99-2284	TUa-3302	213.5	N. pachyderma sinistral	10.05		0.10	11.07	0.19	0.25	0.22	Risebrobakken et al. (2014)	included
MD99-2284	TUa-3304	249.5	N. pachyderma sinistral	10.70		0.09	11.73	0.39	0.34	0.37	Risebrobakken et al. (2014)	included
MD99-2284	Poz-29526	423.5	N. pachyderma sinistral	11.44		0.08	13.04	0.18	0.21	0.19	Risebrobakken et al. (2014)	included
MD99-2284	Tua-3305	450.5	N. pachyderma sinistral	11.96		0.09	13.42	0.16	0.14	0.15	this study	included
MD99-2284	Tua-3987	472.5	N. pachyderma sinistral	12.24		0.08	13.73	0.16	0.17	0.17	this study	included
MD99-2284	Tua-3988	502.5	N. pachyderma sinistral	12.60		0.13	14.17	0.42	0.28	0.35	this study	included
MD99-2284	Tua-3989	543.5	N. pachyderma sinistral	12.98		0.13	14.92	0.24	0.26	0.25	this study	included

Core	Lab number	core depth, void corrected (cm)	Material	14C Age, uncorrected (ka BP)	calendar age (ka BP)	S.D. 1 σ (ka)	calibrated, modelled age (cal ka BP)	S.D. 2 σ (ka) (max)	S.D. 2 σ (ka) (min)	S.D. 2 σ (ka) (average of both errors)	Original reference	Info
MD99-2284	POZ-10154	546.5	N. pachyderma sinistral	13.08		0.06	14.94	0.23	0.24	0.23	this study	included
MD99-2284	KIA-10678	600.5	N. pachyderma sinistral	13.15		0.07	15.30	0.24	0.19	0.22	this study	included
MD99-2284	Tua-3306	650.5	N. pachyderma sinistral	13.55		0.10	15.77	0.23	0.25	0.24	this study	included
MD99-2284	POZ-10155	687.5	N. pachyderma sinistral	13.71		0.06	16.09	0.18	0.20	0.19	this study	included
MD99-2284	Tua-3990	749.5	N. pachyderma sinistral	14.32		0.12	17.00	0.36	0.34	0.35	this study	included
MD99-2284	POZ-10156	788.5	N. pachyderma sinistral	15.33		0.07	18.11	0.24	0.25	0.24	this study	included
MD99-2284	Tua-3307	800.5	N. pachyderma sinistral	15.55		0.19	18.41	0.24	0.26	0.25	this study	included
MD99-2284	POZ-10157	819.5	N. pachyderma sinistral	15.73		0.07	18.64	0.16	0.19	0.17	this study	included
MD99-2284	Tua-3991	849.5	N. pachyderma sinistral	16.11		0.12	19.04	0.27	0.21	0.24	this study	included
MD99-2284	Tua-3308	900.5	N. pachyderma sinistral	17.20		0.09	20.22	0.27	0.27	0.27	this study	included
MD99-2284	Tua-3309	1000.5	N. pachyderma sinistral	19.73		0.12	23.19	0.38	0.39	0.39	this study	included
MD99-2284	BETA-429891	1058.5	N. pachyderma sinistral	20.59		0.08	24.26	0.26	0.28	0.27	this study	included
MD99-2284	TUa-3310	1100.5	N. pachyderma sinistral	21.98		0.16	25.67	0.32	0.38	0.35	Dokken et al. (2013)	included
MD99-2284	BETA-429890	1295.5	N. pachyderma sinistral	23.02		0.08	26.99	0.30	0.32	0.31	this study	included
MD99-2284	FMAZ II	1407.5	Tephra		26.69	0.39	27.67	0.52	0.47	0.49	Dokken et al. (2013)	not in age model
MD99-2284	POZ-29522	2106.5	N. pachyderma sinistral	29.10		0.24	31.91	0.45	0.38	0.41	Dokken et al. (2013)	included
MD99-2284	POZ-29523	2324.5	N. pachyderma sinistral	29.90		0.60	32.82	0.49	0.48	0.48	Dokken et al. (2013)	included
MD99-2284	POZ-17620	2775.5	N. pachyderma sinistral	29.92		0.24	34.50	0.36	0.46	0.41	Dokken et al. (2013)	included
MD99-2284	POZ-17621	2996.5	N. pachyderma sinistral	32.50		0.30	36.77	0.97	0.81	0.89	Dokken et al. (2013)	included
MD99-2284	POZ-29524	3075.5	N. pachyderma sinistral	34.60		0.70	38.81	1.26	1.23	1.25	Dokken et al. (2013)	included
LINK17	AAR-7236	135.0	N. pachyderma sinistral	13.16		0.15	15.00	0.64	0.80	0.72	Rasmussen and Thomsen (2008)	included
LINK17	AAR-7237	250.0	N. pachyderma sinistral	14.12		0.12	16.93	0.69	0.54	0.61	Rasmussen and Thomsen (2008)	included
LINK17	AAR-8137	290.0	N. pachyderma sinistral	15.73		0.11	18.52	0.35	0.43	0.39	Rasmussen and Thomsen (2008)	included
LINK17	AAR-7238	331.0	N. pachyderma sinistral	17.28		0.14	20.27	0.51	0.56	0.53	Rasmussen and Thomsen (2008)	included
LINK17	AAR-7239	436.5	Bivalve	20.33		0.19	23.93	0.63	0.69	0.66	Rasmussen and Thomsen (2008)	included
LINK17	AAR-8138	496.5	N. pachyderma sinistral	22.30		0.22	25.85	0.58	0.94	0.76	Rasmussen and Thomsen (2008)	included
LINK17	AAR-7240	633.0	N. pachyderma sinistral	24.25		0.35	27.95	0.56	0.59	0.57	Rasmussen and Thomsen (2008)	included
LINK17	AAR-8139	718.5	N. pachyderma sinistral	25.35		0.30	29.11	0.54	0.54	0.54	Rasmussen and Thomsen (2008)	included
LINK17	AAR-8140	754.0	N. pachyderma sinistral	25.65		0.35	29.61	0.59	0.54	0.56	Rasmussen and Thomsen (2008)	included
LINK17	AAR-8141	818.5	N. pachyderma sinistral	26.85		0.35	30.61	0.55	0.68	0.62	Rasmussen and Thomsen (2008)	included
LINK17	AAR-8142	965.0	N. pachyderma sinistral	28.45		0.45	32.87	1.02	0.99	1.01	Rasmussen and Thomsen (2008)	included
MD04-2829	SUERC-8793	312.5	N. pachyderma sinistral	16.73		0.07	19.60	0.17	0.16	0.16	Hall et al. (2011)	included
MD04-2829	SUERC-8794	376.5	N. pachyderma sinistral	17.25		0.07	20.33	0.15	0.16	0.16	Hall et al. (2011)	included
MD04-2829	SUERC-8795	391.5	N. pachyderma sinistral	17.38		0.07	20.51	0.14	0.15	0.15	Hall et al. (2011)	included
MD04-2829	SUERC-8797	422.5	N. pachyderma sinistral	17.71		0.07	20.91	0.16	0.16	0.16	Hall et al. (2011)	included

Core	Lab number	core depth, void corrected (cm)	Material	14C Age, uncorrected (ka BP)	calendar age (ka BP)	S.D. 1 σ (ka)	calibrated, modelled age (cal ka BP)	S.D. 2 σ (ka) (max)	S.D. 2 σ (ka) (min)	S.D. 2 σ (ka) (average of both errors)	Original reference	Info
MD04-2829	SUERC-8798	438.5	N. pachyderma sinistral	17.99		0.08	21.16	0.17	0.16	0.16	Hall et al. (2011)	included
MD04-2829	SUERC-8799	457.5	N. pachyderma sinistral	18.23		0.08	21.42	0.16	0.17	0.16	Hall et al. (2011)	included
MD04-2829	SUERC-8802	495.5	N. pachyderma sinistral	18.31		0.08	21.79	0.14	0.15	0.15	Hall et al. (2011)	included
MD04-2829	SUERC-8803	510.5	N. pachyderma sinistral	18.57		0.08	21.97	0.15	0.14	0.15	Hall et al. (2011)	included
MD04-2829	SUERC-8804	534.5	N. pachyderma sinistral	18.67		0.08	22.24	0.13	0.14	0.14	Hall et al. (2011)	included
MD04-2829	SUERC-8805	544.5	N. pachyderma sinistral	18.80		0.08	22.37	0.12	0.13	0.12	Hall et al. (2011)	included
MD04-2829	SUERC-8807	560.5	N. pachyderma sinistral	19.60		0.09	22.98	0.26	0.25	0.25	Hall et al. (2011)	included
MD04-2829	SUERC-8808	592.5	N. pachyderma sinistral	20.33		0.10	23.79	0.22	0.23	0.23	Hall et al. (2011)	included
MD04-2829	SUERC-8809	618.5	N. pachyderma sinistral	20.51		0.10	24.21	0.21	0.20	0.20	Hall et al. (2011)	included
MD04-2829	SUERC-8812	636.5	N. pachyderma sinistral	20.70		0.11	24.54	0.31	0.22	0.26	Hall et al. (2011)	included
MD04-2829	SUERC-8813	648.5	N. pachyderma sinistral	21.38		0.12	24.79	0.36	0.23	0.30	Hall et al. (2011)	included
MD04-2829	SUERC-8814	664.5	N. pachyderma sinistral	21.45		0.12	25.31	0.26	0.27	0.27	Hall et al. (2011)	included
MD04-2829	SUERC-8815	720.5	N. pachyderma sinistral	23.51		0.15	27.32	0.27	0.30	0.29	Hall et al. (2011)	included
MD04-2829	SUERC-8816	762.5	N. pachyderma sinistral	24.78		0.17	28.50	0.29	0.33	0.31	Hall et al. (2011)	included
MD04-2829	SUERC-8817	784.5	G. bulloides	25.71		0.20	29.34	0.38	0.39	0.38	Hall et al. (2011)	included
MD04-2829	SUERC-10904	807.5	N. pachyderma sinistral	26.48		0.15	30.35	0.31	0.38	0.35	Hall et al. (2011)	included
MD04-2829	SUERC-10899	816.5	N. pachyderma sinistral	26.96		0.15	30.74	0.25	0.29	0.27	Hall et al. (2011)	included
MD04-2829	SUERC-10900	880.5	N. pachyderma sinistral	30.07		0.22	33.79	0.43	0.48	0.45	Hall et al. (2011)	included

Evidence of an ice-dammed lake outburst in the North Sea during the last deglaciation

Berit O. Hjelstuen, Hans Petter Sejrup, Espen Valvik, Lukas W.M. Becker

In press in Marine Geology, GLANAM special issue,
https://doi.org/10.1016/j.margeo.2017.11.021

III

Evidence of an ice-dammed lake outburst in the North Sea during the last deglaciation

Berit O. Hjelstuen*, Hans Petter Sejrup, Espen Valvik, Lukas W.M. Becker
Department of Earth Science, University of Bergen, Allégaten 41,
N-5007 Bergen, Norway
*Corresponding author, e-mail: berit.hjelstuen@uib.no

Abstract

Recent reconstructions suggest that the British-Irish and Fennoscandian ice sheets coalesced and covered the central and northern North Sea from ca. 26 cal. ka BP and until ca. 19 cal. ka BP. At ca. 19 cal. ka BP the Norwegian Channel Ice Stream started to retreat and the ice sheets broke apart at ca. 18.7 cal. ka BP. This led to a drainage of an ice-dammed lake in the southern North Sea northwards via the Norwegian Channel into the SE Nordic Seas. In this paper, we combine information from high resolution TOPAS profiles, bathymetric records and shallow borings to study the ice-dammed lake outburst, a common deglaciation process but which rarely has been evidenced in such a detail from the marine realm. A 12 m deep and 3 km wide incision at the northeastern part of the Dogger Bank is suggested to represent the point where the ice-dammed lake breached. The glacial lake outburst flood, which had an estimated peak discharge of 9.8 x 10^4 - 2.9 x 10^5 m^3s^{-1} and lasted for about 5-15 months, flowed between the withdrawing British-Irish and Fennoscandian ice sheets following the crest of the Ling Bank northwards. Along this path, about 300 km downstream of the break-through point, an up to 10 m thick sediment package with a prograding-aggrading sedimentation pattern, typical for ice-dammed lake outburst deposits, has been deposited. This sediment package was deposited in a high-energy environment, immediately following extensive erosion of the underlying till unit of Last Glacial Maximum age. An oxygen isotope anomaly and an associated ultra-rapidly deposited meltwater plume on the

Norwegian continental margin, dated to ca. 18.7 cal. ka BP, also witness this lake outburst. The ice-dammed lake outburst flood occurred when evidence suggest a sea level at least 110 m lower than at present in the region. As the sea level rose, following the melting of the Last Glacial Maximum ice sheet, the Ling Bank Delta developed on top the outburst deposits. The delta, indicating a sealevel close to 80 m below present, has an extent of 80 km and up to 12 m deep fluvial channels are associated with the topset beds. This fluvial environment may have lasted until the end of the Younger Dryas time period when the Ling Bank was submerged and attained its present water depth.

Keywords: North Sea, ice-dammed lake, glacial lake outburst flood, Last Glacial Maximum, deglaciation, delta

1. Introduction

Ice-dammed lakes develop supraglacially, subglacially or ice-marginally and their formation and length of existence are strongly dependent on the dynamics of the ice sheet and the character of the neighboring environment (Carrivick and Tweed, 2013). Well-studied examples of paleo ice-dammed lakes are Lake Agassiz (Laurentide Ice Sheet) which existed for a time period of 4000 years during the last deglaciation, the late Wisconsin Glacier Lake Missoula (Cordilleran Ice Sheet), and the Younger Dryas Baltic Ice Lake (Scandinavian Ice Sheet) (e.g. Jensen et al., 1997; Teller et al., 2004; Alho et al., 2010). Such ice-dammed lakes can cover considerable areas and contain huge volumes of water. The 9700 km^2 Glacier Lake Missoula held a water volume of 2600 km^3, whereas the Baltic Ice Lake was nearly four times larger in area and 10 times larger in volume (Björck, S., 1995; Smith, 2006; Jakobsson et al., 2007; Alho et al., 2010). On the other hand, Lake Agassiz covered a total area of 841,000 km^2 and contained a water volume of 163,000 km^3 when it merged with Lake Ojibway about 8200 years ago (Teller et al., 2002). For comparison, the largest lake on Earth today, the Caspian Sea, covers 371,000 km^2 and has a volume of 78,200 km^3 (Rodionov, 2012).

Ice-dammed lakes can be drained, often periodically, and such glacial lake outburst floods (GLOFs) commonly represent abrupt discharges of large volumes of water. It has been estimated that the prominent 8.2 cal. ka BP drainage of Lake Agassiz was ongoing for 6 months, with an average flux of 5 Sv, and involved a total water volume of 10^{14} m^3 (Clarke et al., 2004). Signatures of GLOFs are reported from onshore areas as canyons and giant gravel bars, whereas in the marine domain such sudden release of dense fresh water can give rise to prominent meltwater peaks (e.g. Alley and Ágústsdóttir, 2005; Høgaas and Longva, 2016).

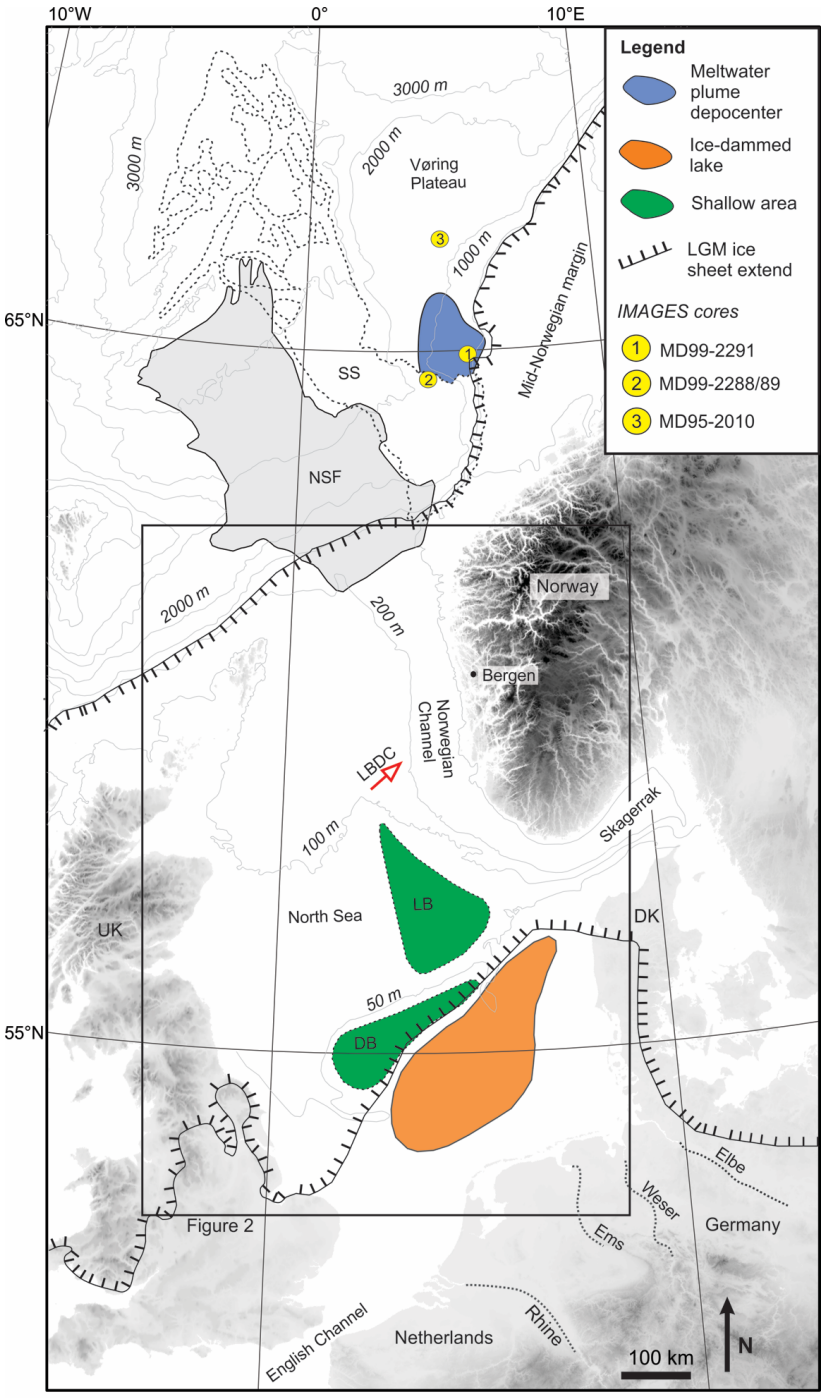

Figure 1. a) *Overview map of North Sea and Norwegian continental margin. Outline of meltwater plume depocentre on the south Vøring Plateau (from Hjelstuen et al.,*

2004), Late Weichselian North Sea Lake, Dogger Bank, Ling Bank, Ling Bank Drainage Channel (from Sejrup et al. (2016]), North Sea Fan (from Nygård et al. (2005]), Storegga Slide (from Haflidason et al. (2004)) and LGM ice extent (based on Sejrup et al. (2005)) are shown. Location of major rivers entering the southern North Sea and sediment cores mentioned in this study are also indicated. SS: Storegga Slide; NSF: North Sea Fan; LBDC: Ling Bank Drainage Channel; DB: Dogger Bank; LB: Ling Bank; LGM: Last Glacial Maximum.

It is of importance to have knowledge on GLOFs, and their associated processes, as they give information on deglaciation character and as they may have a strong impact on climate and ocean circulation (Carrivick and Tweed, 2013). Notably, the around 1000 year-long Younger Dryas event has been suggested to be related to the 9500 km^3 Herman Drainage Stage of Lake Agassiz (Broecker et al., 1989; Teller et al., 2002). Smaller ice-dammed lakes are at present located on e.g. Iceland, in Scandinavia and in the Central European Alps and it is suggested that the number of such lakes will increase in the years to come due to the inferred warming climate (Carrivick and Tweed, 2016). Thus, outburst floods may increase in frequency and become an increasing threat to infrastructure and buildings.

In this study we investigate the drainage route of a paleo-GLOF from an ice-dammed lake predicted by many authors (e.g. Hijma et al., 2012; Sejrup et al., 2016) to have existed during the Last Glacial Maximum (LGM) in the southern North Sea (Fig. 1), and which we here name the Late Weichselian North Sea Lake. In this effort, we integrate high resolution acoustic data and information from already analysed shallow borings, and **(1)** identify outburst processes using seismic facies analyses, **(2)** evaluate seabed features and their possible relationship with the GLOF, **(3)** study sediment character of identified seismic facies and seismic units, and **(4)** discuss a chronological framework for the identified processes. Finally, we put the ice-dammed lake outburst in context of the late glacial-Holocene paleo-environmental history of the North Sea region.

2. Background

The epicontinental North Sea is characterized by water depths of <150 m except for in the Norwegian Channel, a prominent seabed depression along the south and west coast of Norway that reaches a maximum water depth of 700 m in the Skagerrak (Figs. 1-3). In general, the water depth in the North Sea shows a gradual increase from south to north. South of Dogger Bank the water depth does not exceed 60 m. North of Dogger Bank the North Sea is characterized by an embayment. This embayment reaches a maximum water depth of 150 m in the Fladen Basin (Witch Ground Basin) and is bounded to the east by the Ling Bank (Figs. 2 and 3). Several larger-sized rivers, including the Rhine, Elbe, Weser and Ems, are at present entering the southern North Sea (Fig. 1). The effect these rivers had on shaping the seabed morphology during glacial low sea level stands is easily visible in the bathymetric data (Fig. 3a).

It has been suggested that the northern and central North Sea have been partly or fully ice covered several times during the Late Quaternary Northern Hemisphere Glaciations (Sejrup et al., 2005; Graham et al., 2011; Lee et al., 2012), and that the British-Irish (BIIS) and Fennoscandian (FIS) ice sheets coalesced in this region for the last time during the LGM (Sejrup et al., 2016). Evidence of these ice advances are imprinted in the sediment stratigraphy as moraine packages, and as networks of buried and exposed tunnel valleys (Sejrup et al., 1987; Sejrup et al., 1995; Stewart and Longergan, 2011). The last glacial-deglaciation cycle of the North Sea region is partly evidenced in the present-day seabed, which shows a complex pattern of ice marginal features, lateral shear zone moraines and glacial lineations (Fig. 3) (Bradwell et al., 2008; Sejrup et al., 2016).

During maximum glacial stages, global eustatic sea level was around 120 m lower than today (e.g. Lambeck et al., 2014), and parts of the North Sea were located above sea level for some time after the withdrawal of the LGM ice sheet. The Dogger and Ling banks (Figs. 1 and 2), in particular, must have been sub-aerially exposed for a considerable time span, and these now “lost lands” have attracted strong interest as they may have been sites for early settlements during post-glacial times (e.g. Coles, 2000; Hammer et al., 2015).

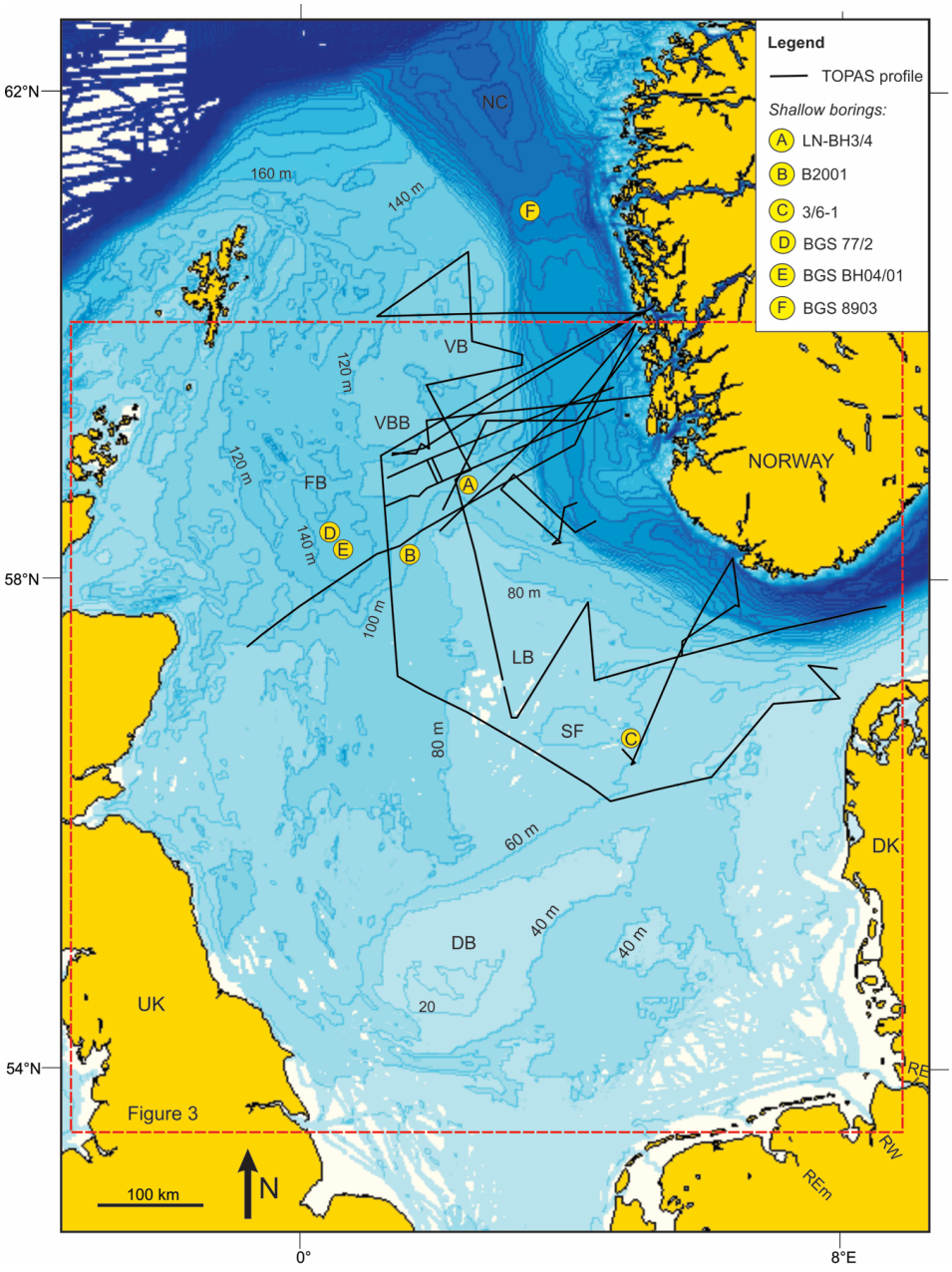

Figure 2. *North Sea bathymetric map based on the Olex bathymetric database (www.olex.no). Location of shallow borings, sediment cores and TOPAS profiles applied or mentioned in this study are shown (For full TOPAS database see Fig. 1a in*

Sejrup et al. (2016)). DB: Dogger Bank; SF: Store Fiskebank; LB: Ling Bank; FB: Fladen Basin; VBB: Viking Bank Basin; VB: Viking Bank; NC: Norwegian Channel; RE: River Elbe; RW: River Weser; REm: River Ems.

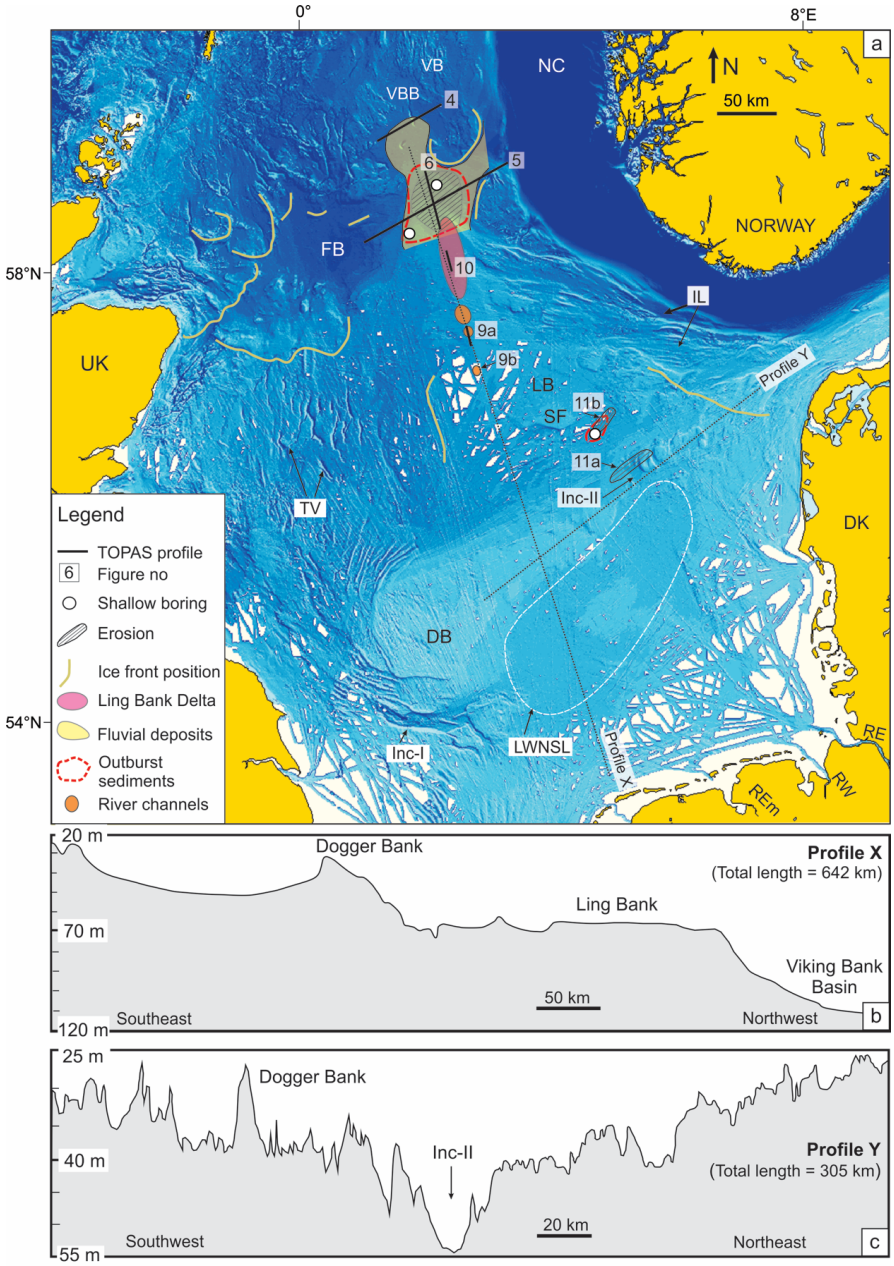

Figure 3. a) *3D bathymetric view, based on the Olex bathymetric database, of southern and central North Sea. Location of Ling Bank Delta, channels, Late Weichselian North Sea Lake and ice-dammed lake outburst sediments are indicated. The shown ice front positions are based on Sejrup et al. (2016). For core names see Fig. 2. DB: Dogger Bank; SF: Store Fiskebank; LB: Ling Bank; FB: Fladen Basin; VBB: Viking Bank Basin; VB: Viking Bank; NC: Norwegian Channel; TV: Tunnel valley; Inc: Incision; IL: Inclined ledge (from Sejrup et al. (2016)); RE: River Elbe; RW: River Weser; REm: River Ems; LWNSL: Late Weichselian North Sea Lake* ***b)*** *and* ***c)*** *Bathymetric profiles across the Dogger and Ling banks. For location see Fig. 3a. The profiles are generated from the Olex bathymetric database.*

It has been suggested that an ice-dammed lake has occupied the region south of the Dogger Bank during various glacial stages, including Marine Isotope Stage (MIS) 12, MIS 6 and MIS 2 (e.g. Hijma et al., 2012; Murton and Murton, 2012). The Late Weichselian North Sea Lake outburst was suggested by Sejrup et al. (2016) to follow an ice-free corridor that existed between the BIIS and FIS as these ice sheets started to unzip, flowing into the Norwegian Channel through the proposed Ling Bank Drainage Channel (Fig. 1). Also, a light spike in oxygen-isotopes in planktonic foraminifera, possibly reflecting enhanced input of freshwater to the ocean, is identified close to 18.7 cal. ka BP in cores MD99-2289, MD99-2291 and MD95-2010 (Fig. 1) from the SE Nordic Seas margin (Lekens et al., 2005). This light spike probably reflects the Late Weichselian North Sea Lake drainage event (Sejrup et al., 2016). The ice-dammed lake has, based on maximum North Sea ice margins and bathymetric variations in the area, been estimated to be 3900 km^3 (Bigg et al., 2012). Thus, the Late Weichselian North Sea Lake is comparable to the proposed Late Wisconsion Glacier Lake Missoula in North America (Teller et al., 2002).

3. Data and methods

The data base used in this study includes TOPAS high resolution profiles, bathymetric data and shallow borings (Figs. 2 and 3).

The seismic profiles, which were collected during several University of Bergen cruises onboard R/V G.O. Sars between 2006 and 2014, define a broad grid within the study area (Fig. 2). During data acquisition, the TOPAS PS18 parametric sonar system from Kongsberg AS was used (www.kongsberg.no), giving seismic profiles with a vertical resolution of around 30 cm and a maximum penetration of ca. 100 m. The seismic profiles analysed for this study have an overall good quality and were processes to .segy files before imported and interpreted using the Petrel 2013 software from Schlumberger AS. We base the seismic interpretation on seismic facies character and changes in this throughout the study area.

An isopach map, in millisecond (two-way travel time) [ms (TWT)], showing thickness and distribution of the sediments deposited in the Norwegian Channel between the last deglaciation (19-17.5 cal. ka BP) and the end of the Younger Dryas (11.6 cal. ka BP) has been generated. In addition to the TOPAS profiles presented in this study, this map is also based on numerous other TOPAS lines collected in the Norwegian Channel (see Fig. 1a in Sejrup et al., 2016). For conversion of sediment thickness and sediment depth in ms (TWT) to depth in meter, a velocity in the sediments of 1500 m/s has been applied.

The bathymetric database used in this study, Olex, has been made available by Olex AS (www.olex.no). In Olex, individual data sets, acquired by fishing and research vessels, have been merged into a single database with a horizontal resolution of 5x5 m. The vertical resolution of the database is <1 m, and positioning errors are commonly less than 10 m. The Olex database has good coverage in the northern part of the North Sea, whereas regions with more scattered data coverage are identified in the central part and particularly in the southern part of the North Sea (Figs. 2 and 3). The analyses of the bathymetric data were done both in the Olex system, where the bathymetry can be viewed as 2D contours, 2D shaded relief, 3D views or as 2D profiles, and on exported

.tiff files which were georeferenced and interpreted in the ArcGIS 10.3 software from Esri.

We have also utilized information from three previously analysed shallow borings in the study area, B2001 (1.72°E, 58.39°N), LH-BH3/4 (2.26°E, 58.79°N) and 3/6-1 (4.89°E, 56.58°N) (Fig. 2). B2001 was drilled in 110 m water depth and penetrated to a depth of 119.3 m below the seabed, and information on the upper 20 m on grain-size, shear strength and chronology have previously been published by Sejrup et al. (1987) and Sejrup et al. (1994). Boring 3/6-1 was raised from a water depth of 64 m at the southern part of the Ling Bank (Fig. 2), and penetrates 37 m into the sediments. The upper 12 m of this boring has been sub-divided into five units based on grain size and various geotechnical parameters (Hammer et al., 2015). LN-BH3/4 is 97 m in length and is located in a water depth of 109 m at the northern tip of the Ling Bank Information on grain size and shear strength are available from this borehole (Reinardy et al., 2017). In addition to these study area specific borings we have also used published information from sediment cores located elsewhere in the North Sea and on the Norwegian continental margin (Figs. 2 and 3).

4. Results

4.1 Bathymetry and seabed character

In the southernmost North Sea maximum water depths of 50 m are reached in an elongated bathymetric depression bounded by the coastlines of Denmark, Germany, the Netherlands and UK in east, west and south and the Dogger Bank to the north (Fig. 2). A ridge, standing up to 10 m above the surrounding seabed, interrupts the otherwise flat sea floor of the depression (Fig. 2 and 3). Two prominent seabed incisions, Inc-I and Inc-II (Fig. 3), are observed at the western and eastern edges of the bathymetric depression. Inc-I has an east-west trend, is up to 30 km wide and reaches a maximum water depth of 83 m, whereas Inc-II has a width of around 10-15 km and a maximum water depth of 56 m. The SW-NE trending Dogger Bank (Fig. 2) is a prominent elevated area located at the boundary between the southern and central North Sea. The bank has a length of nearly 300 km in the E-W direction and is up to 100 km wide. The shallowest

part of the Dogger Bank is located to the southwest, where the seafloor is situated only 11 m below the present-day sea level. Towards the northeast the Dogger Bank is both narrowing and deepening, and at its north-eastern tip, where the Dogger Bank is incised by Inc-II (Fig. 3), the water depth is around 40 m. The northern boundary of the Dogger Bank is characterized by a $<0.2^{o}$ slope, along where the water depth is increasing from 40-50 m to approximately 60-80 m.

Northeast of the Dogger Bank is the Ling Bank located (Figs. 1 and 3). Along the crest of this bank the water depth is only 65 m, shallowing to 45 m across Store Fiskebank ("SF" in Figs. 2 and 3). The shape of Store Fiskebank resembles a typical moraine ridge, with a northern flank that is much steeper than the southern. The Ling Bank is approximately 200 km wide nearby Dogger Bank, narrowing to only around 40 km at its northern tip where a rather abrupt deepening in the water depth to 110-120 m, across a 0.03^{o} slope, is observed (Fig. 3b). The Ling Bank has a slope of up to 0.6^{o} towards the Norwegian Channel, whereas the western slope is more gentle. East and west of the Ling Bank the water depth is around 80-90 m and the seabed reveals a glacial landscape, where tunnel valleys, inclined ledges and ice marginal features have been identified (Sejrup et al., 2016). In the northern North Sea the seabed is dominated by a fresh glacial landscape (Bradwell et al., 2008; Sejrup et al., 2016), except for in the Fladen and Viking Bank basins areas (Fig. 3) where a relatively flat and smooth seabed in water depths of 150 m and 110 m is observed.

4.2 Seismic facies and sediment character

Two seismic facies dominate in the study area; acoustically transparent and acoustically well laminated. The acoustically transparent seismic facies has been shown to represent till, as documented both by sediment core-seismic profile correlation in this study and by previous work in the region on similar data (e.g. Sejrup et al., 2015). The acoustically well laminated seismic pattern comprises medium to high amplitude continuous and parallel reflectors, and are, based on a comparison to studies by Graham et al. (2010) and Sejrup et al. (2015), suggested to represent glacimarine deposits.

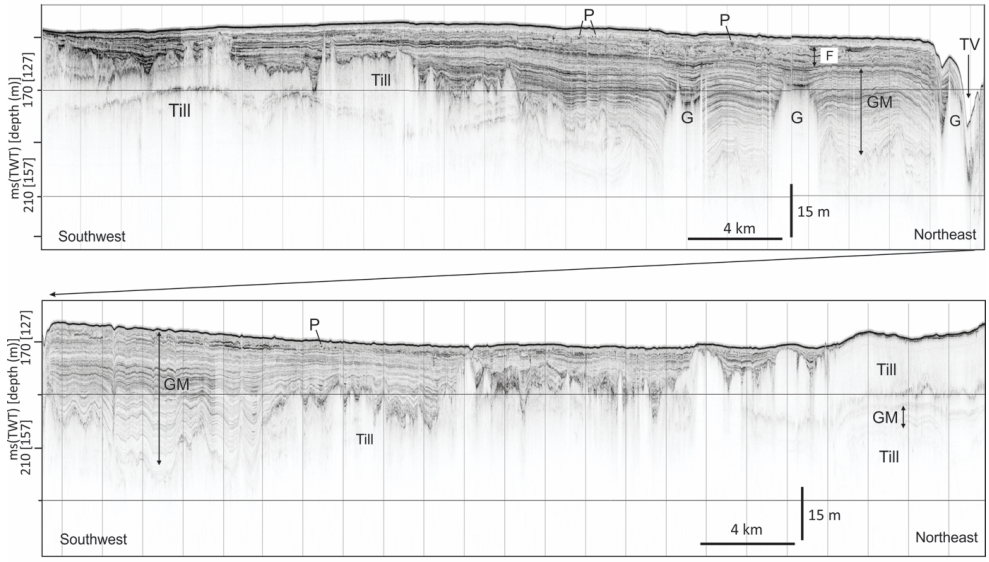

Figure 4. *TOPAS profile across Viking Bank Basin. Profile location in Fig. 3a. G: Gas; GM: Glacimarine sediments; P: Point source reflection; F: Fluvial-dominated sediments; TV: Tunnel valley.*

4.2.1 Area north of Ling Bank

The region north of the Ling Bank comprises two prominent accumulation areas of postglacial sediments, the Fladen Basin and the not previously studied Viking Bank Basin (Fig. 2). The Fladen Basin contains an up to 25 m thick unit of acoustically well laminated glacimarine sediments which are interfingered by several glacigenic debris flows (Sejrup et al., 2015). The Viking Bank Basin covers an area of around 3500 km^2, and contains an up to 35 m thick sediment package that drapes one or several acoustically transparent till units (Fig. 4). Several deep incisions, both exposed at the seabed and buried, are observed, and we infer these features to represent tunnel valleys. Tunnel valleys are commonly identified in the North Sea (e.g. Huuse and Lykke-Andersen et al., 2000). The acoustic data also show that the Viking Bank Basin contains shallow gas (Fig. 4), locally reducing the seismic penetration. The sediment package deposited in the Viking Bank Basin is characterized by an acoustically well laminated

seismic facies, inferred to represent glacimarine sediments. However, in the uppermost 15-20 ms(TWT) (ca. 12-15 m) of the deposited sequence a wavier and more contorted seismic pattern is identified ("F" in Fig. 4). Furthermore, numerous point source reflectors ("P" in Fig. 4) are identified in this part of the sediment column, most likely representing more coarse-grained sediments.

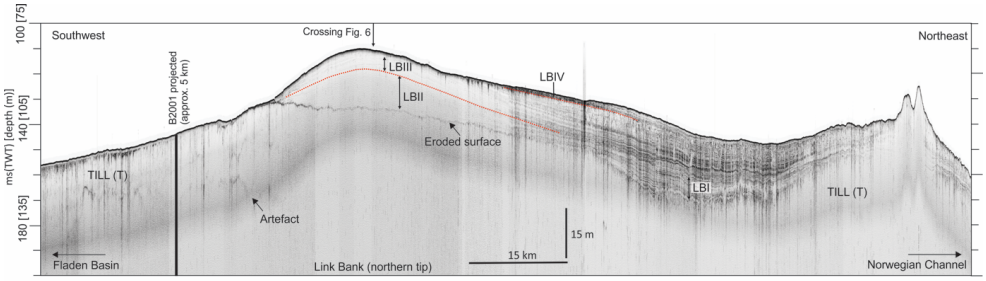

Figure 5. *TOPAS profile across the northern tip of Ling Bank showing typical seismic facies characters in this area. Profile location in Fig. 3a. LBI-LBIV and T: Identified seismic units.*

At the northern tip of the Ling Bank, prominent changes in the seismic facies allow us to divide the sediment succession in this region into four sub-units, LBI (oldest) - LBIV (Figs. 5 and 6a). Sub-unit LBI comprises continuous, parallel medium to high amplitude reflectors and seems to represent typical glacimarine sediments deposited above a till unit. This till unit isdefining the base of the Fladen and Ling Bank sediment basins, and can also be followed into the Norwegian Channel.

LBII reaches a maximum thickness of about 10 m, and is characterized by medium to high amplitude continuous reflections that define a prograding-aggrading seismic pattern (Fig. 6a). This seismic facies covers an area of ca. 3400 km^2 (Fig. 3a), and can be followed for a distance of up to 40 km. At the base of sub-unit LBII several mounds, up to 5 m in height and 2 km in diameter, are observed (Fig. 6b). Commonly, sub-unit LBII is overlying sub-unit LBI. We note, however, that LBII, locally, downlap the mapped till unit (Fig. 6a). In this downlapping region the surface of the till unit is extremely flat.

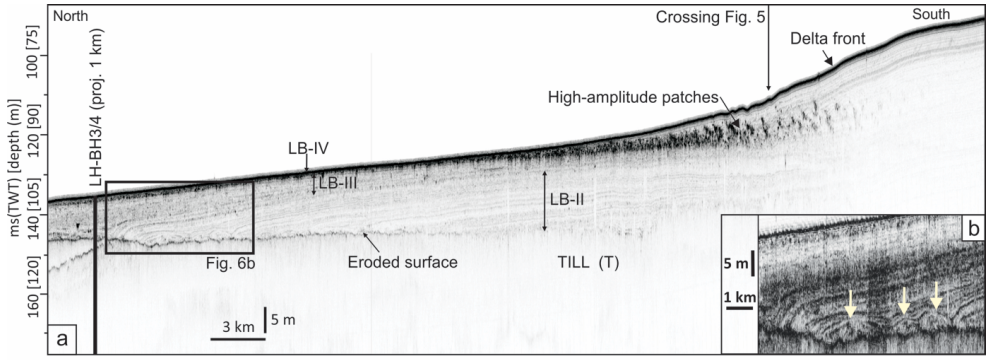

***Figure 6**. **(a)** TOPAS profile, location in Fig. 3a, showing assumed lake outburst deposits (LBII) north of Ling Bank. Note also the delta front pinch out. LBI-LBIV and T: Identified seismic units. **(b)** Zoom-in on ice dammed lake-outburst deposits. Arrows point at observed mounds at the base of sub-unit LBII. Figure location in Fig. 6a.*

Sub-unit LBIII has been deposited stratigraphically above LBII, and is characterized by an acoustically contorted seismic facies where point-source reflectors are frequently identified (Fig. 5). Towards the Norwegian Channel this sediment package increases in thickness and incisions, up to 500 m in width and 5 ms(TWT) (ca. 3.5 m) deep, are observed. These incisions are commonly observed at two levels in the sediment package. The uppermost identified sub-unit, LBIV, has an acoustically transparent to acoustically weakly layered character.

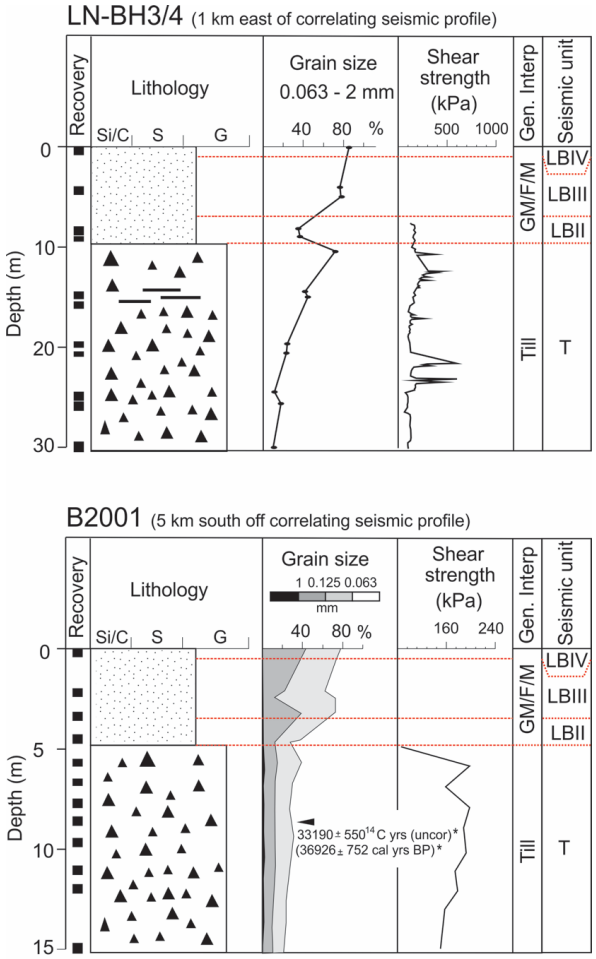

Figure 7. *Lithology, grain size and shear strength of LGM till and post-LGM sediments (from Sejrup et al. (1994) [B2001) and Reinardy et al. (2017) [LN-BH3/4]). (*) Age information from Sejrup et al. (2016). Correlation to seismic units identified in this study (T and LBII-IV) is indicated. Please note the long correlation distance of 5 km between B2001 and the seismic profile (Fig. 5), which results in the upper and lower boundaries of seismic units only being inferred. Si: Silt; C: Clay; S: Sand; G: Gravel; GM: Glacimarine; F: Fluvial; M: Marine.*

Shallow borings B2001 and LH-BH3/4 (Fig. 2) penetrate sub-units LBII-LBIV, and reveal that the observed changes in acoustic facies mirror lithology variations in the deposited sediment package (Fig. 7). Mapping of LBI-LBIV time-equivalent sediments

in the Norwegian Channel shows that these deposits reach a maximum thickness of 160 ms (TWT) (ca. 120 m) in the Skagerrak region (Fig. 8). In the central part of the Norwegian Channel the sediment thickness is much less, reaching a maximum of 70 ms (TWT) (ca. 50 m) in a depocentre along the western edge of the Norwegian Channel. The outermost part of the Norwegian Channel is characterized by sediment thicknesses of less than 20 ms (TWT) (ca. 15 m).

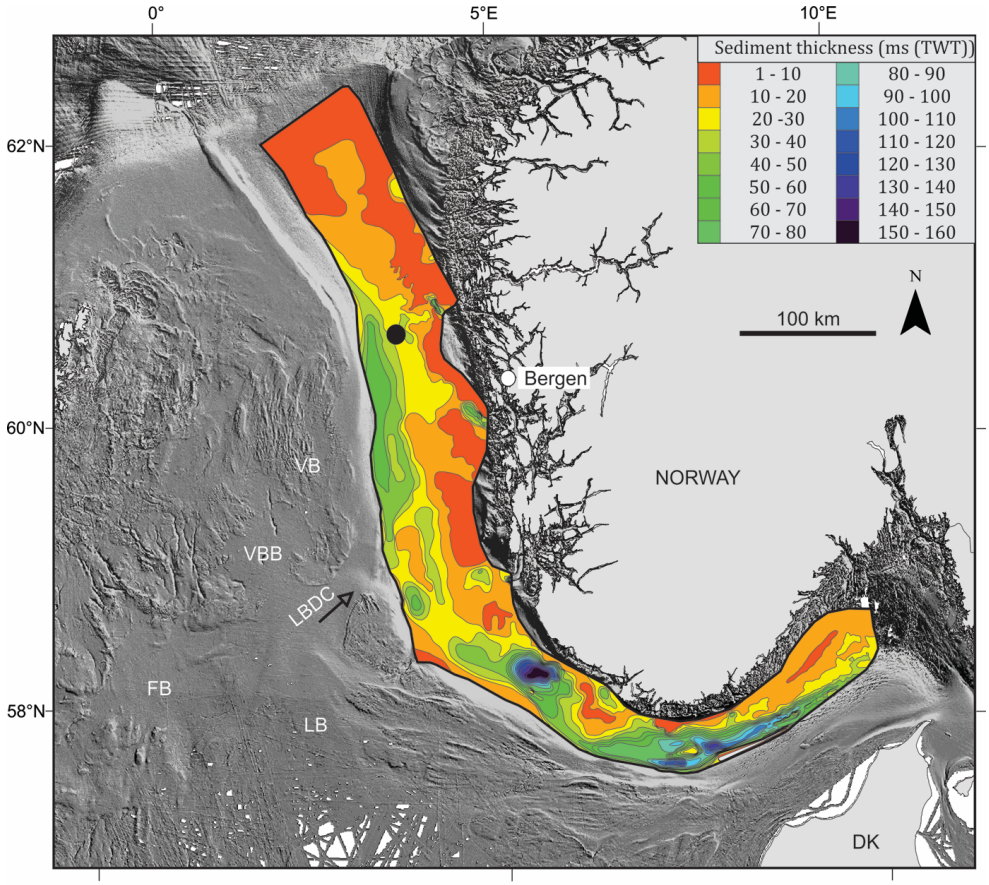

Figure 8. *Isopach map in ms (TWT) of sediments deposited in the Norwegian Channel between ca. 19 cal. ka BP (end LGM) and ca. 11.6 cal. ka BP (start of the Holocene). Black dot shows location of boring BGS 8903. LB: Ling Bank, VBB: Viking Bank Basin, VB: Viking Bank, FB: Fladen Basin, LBDC: Ling Bank Drainage Channel.*

4.2.2. Ling Bank

Along the Ling Bank stacks of acoustically transparent units, which we suggest to represent till units, dominate the sub-seabed sediment succession (Fig. 9). Several major incisions, some of which are assumed to represent tunnel valleys, have eroded into these units. Still, these incisions have remnants of their presumed original sediment infill, represented by an acoustically well-laminated seismic facies, and which we infer to represent glacimarine deposits (Fig. 9). However, mostly such possible infills have been removed and replaced by till packages.

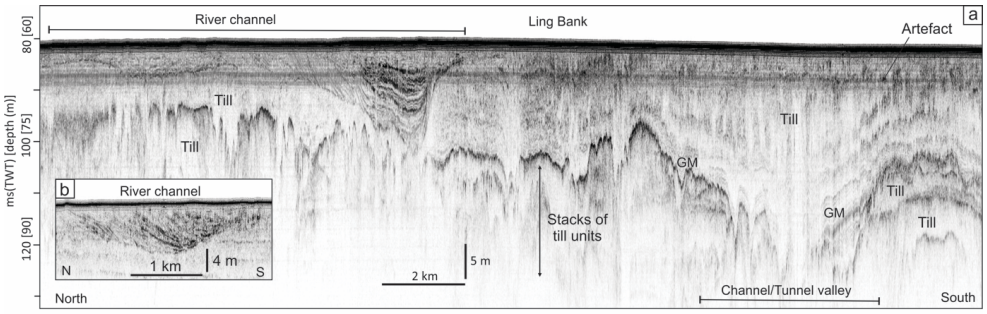

Figure 9. (a) *TOPAS example showing typical seismic stratigraphy, including tunnel valleys, possible river channels, glacimarine sediments (GM) and till units, across the Ling Bank. The indicated artefact is related to the acquisitions of the data. Profile location in Fig. 3a.* ***(b)*** *TOPAS example highlighting sediment infill in an assumed river channel observed at the crest of the Ling Bank. Profile location in Fig. 3a.*

At the northernmost part of the Ling Bank, in present water depths of 65-70 m, a unit composed of northward dipping clinoforms is identified (Figs. 3 and 10). The clinoforms are most likely topset, foreset and possibly bottomset beds of a delta, which we name the Ling Bank Delta. The delta is about 80 km in length, up to 10 m thick and shows a well-defined pinch-out at its southern boundary. The TOPAS profiles show indications of several incisions in the topset beds (Fig. 10). At the northern tip of the Ling Bank, the delta front seems to downlap the upper surface of sub-unit LBII, and the

boundary between the downlapping clinoforms and sub-unit LBII are identified as a zone of high amplitude patches (Fig. 6a).

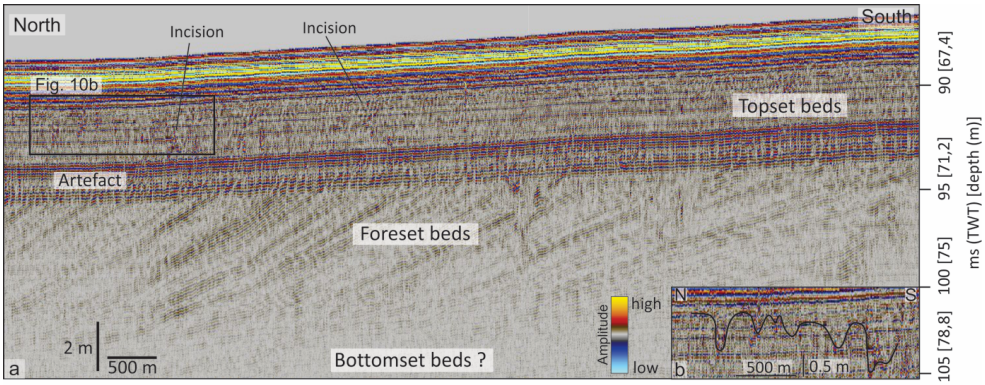

***Figure 10**. a) TOPAS example from the northern part of the Ling Bank, showing the presumed Ling Bank Delta with bottomset, foreset and topset beds. The indicated artefact is related to the acquisitions of the data. Profile location in Fig. 3a. b) Interpretation (white line) of incision mapped in the topset beds. Figure location in Fig. 10a.*

Along the crest of the Ling Bank, near the present-day seabed, three incisions are identified (Figs. 3, 9a and 9b). These incisions have eroded 10-20 ms (TWT) (7-15 m) into the sub-seabed sediment succession and can be traced for up to 6 km in the available seismic profiles. A draping or prograding infill style characterizes these features.

At the southern part of the Ling Bank, at the boundary towards the Dogger Bank, the present-day current system in the region have caused sand waves and sand dunes to develop, prohibiting seismic penetration with the TOPAS system (Fig. 11a). The TOPAS profiles, however, reveal a 20 ms (TWT) (ca. 15 m) deep cut in the sediment succession at the location where a prominent bathymetric depression is observed (Inc-II in Fig. 3c). In this region we also observe erosion of the surrounding sediment packages (Fig. 11a). Southeast of Store Fiskebank, in an area where glacial imprints in the seabed are not observed, we identify erosion of the surface of the uppermost identified till unit (Figs. 3 and 11b). Furthermore, the sub-bottom data show that a less than 10 ms (TWT) (ca. 7 m) thick sediment package, displaying the same prograding

pattern as sub-unit LBII further north, has been deposited in this region. Boring 3/6-1 (Hammer et al., 2015) indicates that this sediment package is dominated by sand.

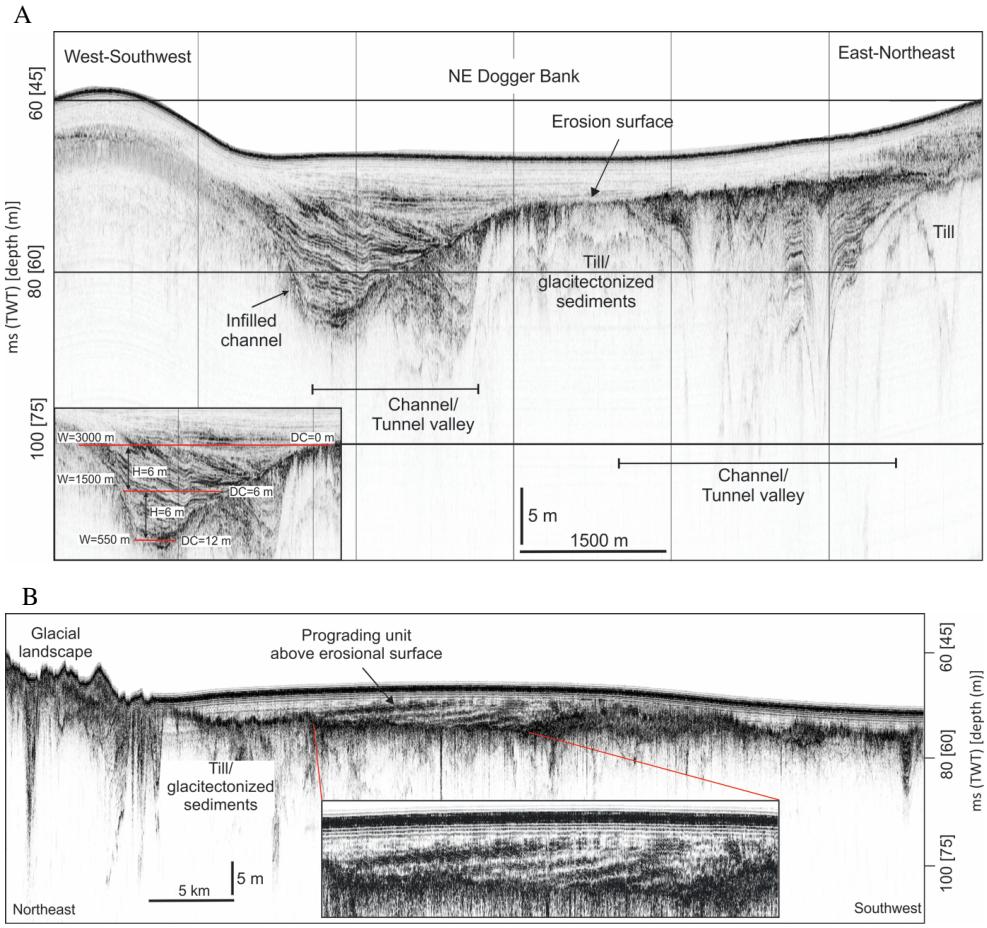

Figure 11. ***(a)*** *Sub-seabed incision observed at the Inc-II bathymetric low at the northeastern part of Dogger Bank. Location of TOPAS profile in Fig. 3a. Inset: Cut out image of infilled channel where the drawn white lines illustrated the geometries used in discharge estimation (see Equation 1). W: Width of channel; DC: Depth of channel; H: Pass height.* ***(b)*** *Seismic facies character northwest of Store Fiskebank. Location of TOPAS profile in Fig. 3a.*

5. Discussion

5.1 Acoustic evidence of a lake outburst flood, its transport route and its dimensions

The studied bathymetric and seismic data give several indications about both the existence of a GLOF in the North Sea and the transport route it followed after the collapse of the lake-supporting ice-barrier. A strong indication is the identified seismic sub-unit LBII, mapped at the northern tip of the Ling Bank (Figs. 3, 5 and 6a). The observed northward prograding direction of this unit (Fig. 6a) suggests that LBII has had a southerly sediment source, which is in line with the existence of an ice-dammed lake south of Dogger Bank (Fig. 1). The prograding-aggrading character of this unit also resembles closely the typical depositional signature of lake-outburst deposits, as reported from field studies of terrestrial GLOFs (Russell et al., 2001; Smith, 2006; Carling et al., 2013).

Seismic sub-unit LBII is in the study area, furthermore, overlying a seismically homogenous unit, which can be traced over large distances in the Northern North Sea. Based on its seismic character, and lithological information (Fig. 7) this unit has been identified as till or glacially overridden sediments (Sejrup et al., 1994). AMS ^{14}C datings of cores B2001, BGS BH04/01 and BGS 77/2 (Sejrup et al., 1994; Graham et al., 2010; Sejrup et al., 2012) suggest that seismic sub-unit LBII represents the last glacial phase in the area. . The boundary of the till towards LBII is characterized by a very flat and smooth surface when comparing it with regions where LBI is deposited on top of this unit (Fig. 5). This relationship between LBII deposits and the flat surface leads us to infer that sub-unit LBII had a strong erosion capacity during deposition, and reshaped the upper boundary of the till to a smooth and slightly westward dipping surface over an approximately 2200 km^2 large area (Figs. 3a and 5). This inferred high-sedimentation rate environment is also supported by the seismic signature observed near the bottom of LBII. Here, smaller-sized mounds are observed, which, when comparing to land-based field data from GLOFs in NW Germany (Fig. 16 in Meinsen et al., 2011), may represent convoluted bedding formed during high energy deposition. We note that analogous erosional boundaries between GLOF deposits and underlying strata are

frequently reported from land-based studies (e.g. Hanson and Clague, 2016). Additionally, Alho et al. (2010) show, from a paleohydraulic drainage reconstruction of Glacier Lake Missoula, that the shear stress affecting the bed during a GLOF is high and capable of eroding the substrata. Thus, the combined observation of erosion, its location, at the till-LBII boundary, and the character of LBII suggests that this unit is related to a lake outburst flood. Similar indications of outburst sediments and associated erosional surfaces are observed at the southern part of the Ling Bank (Figs. 3 and 11b).

We note that there is a distance of about 300 km from the assumed Late Weichselian North Sea Lake (Fig. 1) and the sediments in LBII, but large travel distances seem to be common for GLOFs. During the Glacier Lake Missoula drainage, outburst flood features covered distances of up to 700 km (Hanson et al., 2012). Two borings, B2001 and LN-BH3/4, penetrate the assumed GLOF deposits at the tip of the Ling Bank (Figs. 2, 5 - 7), documenting that 40-60% of the outburst sediments consist of sand and coarser material, indicating high energy environments. The borings further indicate that the GLOF deposits represent an upward-coarsening sequence. However, the relative low core recovery, and also the distance between borings and seismic profiles (up to 5 km) requires caution in making firm interpretation at the present time. Boring 3/6-1 (Figs. 2 and 3) (Hammer et al., 2015), suggest a similar composition of the possible outburst sediments on the southern Ling Bank, noting that this assumption is based on only one sediment sample from these deposits.

Our bathymetric data give further evidence for the pathway of the proposed outburst. At the NE part of the Dogger Bank the water depth reaches a maximum of 56 m, and the seafloor thus lies about 15 m deeper than the surrounding areas (Inc-II in Fig. 3c). We infer that this seabed depression represents the transport pathway that developed when the ice-barrier broke, causing the GLOF to flow northwards. The seabed morphology (Fig. 3a) also suggests that this region of the North Sea has been a lake-outburst point, showing the same characteristic features as found in a DTM (Digital Terrain Model) from the Lower Rhine Embayment where a moraine ridge has been dissected by a Middle Pleistocene glacial lake outburst flood (Lang and Winsemann, 2013). It should, however, be noted that the TOPAS profiles reveal that large regions in the southern North Sea are draped by post-glacial deposition of cover sand and sand

waves, thereby concealing some of the drainage features in bathymetric maps. Across the observed bathymetric incision (Inc-II in Fig. 3) our sub-bottom data also reveal an infilled 15 m deep and 3 km wide depression with associated erosional surfaces at its flanks (Fig. 11a). This adds supporting evidence that this region at the NE part of the Dogger Bank represents the out-burst point of the ice dammed lake.

Thus, based on observations in the available acoustic data we infer that the Late Weichselian North Sea Lake had a catastrophic drainage and formed a prominent seabed/sub seabed incision at the NE part of the Dogger Bank (Figs. 3c and 11b). The outburst flood followed the Ling Bank east of Store Fiskebank (Fig. 3a) northwards before depositing unit LBII (Fig. 6a) at the northernmost tip of the Ling Bank. A first estimate of the flood discharge can be calculated in a similar way as demonstrated by Meinsen et al. (2011) for a Saalian glacial outburst flood in NW German by using:

$$Q = V \times 0.5(A_1 + A_2) \times H \quad (1)$$

Where Q is peak discharge (m^3/s), V is velocity (m/s), A_1 and A_2 is minimum and maximum width (m) of the outburst channel and H is the pass height (m)..

A pass height of 6 m and channel widths of 555 m (channel bottom), 1500 m and 3000 m (channel top) were utilized to calculated discharge for two depth intervals (0-6 m and 6-12 m) of the assumed break-out channel (Fig. 11a). We used 5 and 15 m/s, which is suggested to be characteristic velocities for GLOFs (Baker, 2009), as a minimum and maximum velocity. Thus, a peak discharge in the range of 9.8×10^4 m^3/s - 2.9×10^5 m^3/s is estimated for the Late Weichselian North Sea Lake, suggesting that this outburst is a "major" jökulhlaup (see Meinsen et al. (2011) and references herein for classification system of jökulhlaup). The estimated discharge of the Late Weichselian North Sea Lake is similar to that of Glacier Lake Nedre Glomsjø in southeast Norway (Høgaas and Longva, 2016), but ten times less than the calculated discharge of the Glacier Lake Missoula (Alho et al., 2010).

If utilizing the estimated lake volume of 3900 km^3 (Bigg et al., 2012) along with our peak discharge estimates, we hypothesis that it took between 5 and 15 months to drain the Late Weichselian North Sea Lake.

5.2 Late Glacial – Holocene paleo-environmental history

It has been suggested that between ca. 26 and ca. 19 cal. ka BP the central and northern North Sea was covered by the BIIS and FIS, with a southern ice margin at the Dogger Bank and the northern margin at the present-day shelf edge (Figs. 1, 12 and 13) (Sejrup et al., 2016, Becker et al., this issue). During this time period the Late Weichselian North Sea Lake was possibly draining southwards, through the English Channel (Toucanne et al., 2010).

In the Norwegian Channel the Norwegian Channel Ice Stream (NCIS) was operating, transporting huge amounts of sediments to the North Sea Fan (Figs. 1 and 13) (Sejrup et al., 2003; Nygård et al., 2005; Nygård et al., 2007; Hjelstuen et al., 2012). These sediments were transported downslope as glacigenic debris flows (GDFs), considered to represent signature deposits for shelf edge located ice streams (King et al., 1996). At ca. 19 cal. ka BP the last pulse of GDF activity is recorded at the North Sea Fan (King et al., 1998; Nygård et al., 2007), and the NCIS started to retreat into the Norwegian Channel. Soon after the NCIS had left its position at the shelf edge, an up to 20 m thick fine-grained unit was deposited along the Norwegian margin (e.g. Hjelstuen et al., 2004) (Figs. 1, 12 and 13). Age constrains from several IMAGES cores along the Norwegian margin (Fig. 1) reveal that this unit was deposited nearly instantaneously, at ca. 18.7 cal. ka BP (Lekens et al., 2005; Becker et al., this issue). It was earlier assumed that this unit, interpreted to represent a meltwater plume, was related to the withdrawal and rapid melting of the NCIS (Sejrup et al., 2003; Hjelstuen et al., 2004; Lekens et al., 2005). We now suggest, however, that this meltwater flux is closely related to the sudden drainage of the Late Weichselian North Sea Lake. Seismic correlation of the till unit identified at the northern tip of the Ling Bank (Figs. 5 and 6) to shallow borings in the Fladen Basin (Fig. 2) suggests that it is related to the LGM. The observed deep erosion of this unit and the undisturbed outburst sediments superimposed (Figs. 5 and 6a) also evidence that the GLOF must have occurred in relation to the last deglaciation of the central and northern North Sea.

Thus, we build upon the reconstruction of Sejrup et al. (2016) suggesting that there was a corridor between the BIIS and FIS at ca. 18.7 cal. ka BP, allowing for

transportation of GLOF sediments and freshwater to the SE Nordic Seas (Fig. 13). As the GLOF entered the Norwegian Channel, through the proposed Ling Bank Drainage Channel, it flowed along the western edge of the retreating NCIS. The ice stream was at this time located about 200 km inside the Norwegian Channel, close to the location of boring 8903 (Sejrup et al., 1995; Morén et al. in press) (Figs. 3 and 13). The observation of a grounding zone wedge in this region (Sejrup et al., 2016) indicates that the NCIS stood still at this location for a period before it continued to retreat.

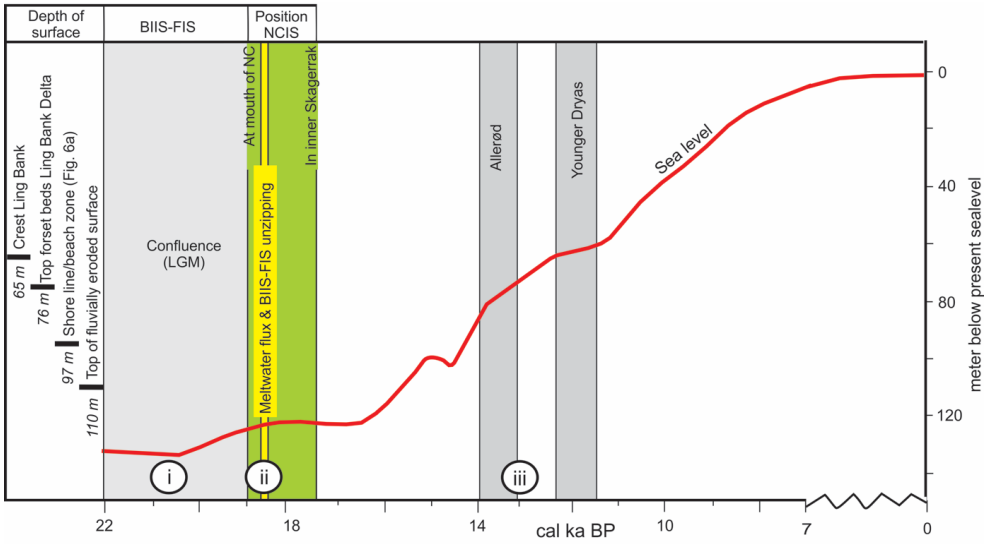

Figure 12. *Post-glacial sea level curve, from Lambeck et al. (2014). Main glacial events, post-glacial processes, and depth to significant surfaces observed in the seismic profiles are indicated. Numbers (i) - (ii) - (iii) refer to time slices shown in Figure 13. Note change in horizontal scale. NC: Norwegian Channel; NCIS: Norwegian Channel Ice Stream; BIIS: British-Irish Ice Sheet; FIS: Fennoscandian Ice Sheet; LGM; Last Glacial Maximum.*

After a time period of up to 15 months, which is based on estimated peak discharge and lake volume in the present study, the Late Weichselian North Sea Lake was drained. Notably, Lekens et al. (2005) counted 854 laminae, deposited in a rhythmic pattern, in the assumed meltwater plume deposits on the southern Vøring Plateau (Figs. 1 and 13).

If assuming the rhythmic lamina pattern to represent tidal influence on an ice-dammed lake outburst, the drainage of the Late Weichselian North Sea Lake is close to have taken 15 months (which represent about 450 days and 900 tidal cycles). Thus, this supports our discharge calculations for the glacial lake outburst. Following this assumed short-lived outburst event the NCIS continued its retreat though the Norwegian Channel, and by 17.6 cal. ka BP the NCIS had withdrawn to a position in the innermost Skagerrak (Morén et al., in press). Larger parts of the central and northern North Sea are likely ice free by this point, with an ice cap over the British and the Shetland islands extending into the Fladen Basin region (Clark et al., 2012; Becker et al., this issue).

After the glacial ice-dammed lake outburst event a fluvial depositional environment developed in the study area, as evidenced by the build-up of the Ling Bank Delta at the northern part of the Ling Bank (Figs. 3, 10, 12 and 13). We interpret the observed incisions at a shallow depth beneath the present-day seabed (Fig. 9) to be channels in a meandering river system, transporting sediments to the steadily growing delta. The characteristic sediment infill pattern of these incisions (Fig. 9b) also supports their association with a river system (e.g. Toonen et al., 2012). The assumed GLOF break-through point, at the NE part of the Dogger Bank (Fig. 11a), was also presumably used by rivers after the drainage of the Late Weichselian North Sea Lake.

Borings B2001 and LN-BH3/4 (Figs. 3 and 7) also evidence the changes in depositional environments after the Late Weichselian North Sea Lake outburst event. Sediments with a sand content of up to 80% are now deposited, suggested to reflect the input of fluvial-dominated sediments. Based on inspection of seismic facies character, where we infer that coarse-grained sediments are reflected in the seismic data as point source reflectors, it seems that such sediments were deposited in a wide area north of the Ling Bank including the Viking Bank Basin (Figs. 3 and 4). The thick sediment depocentre at the western edge of the Norwegian Channel (Fig. 8) also seems mostly to be built up by fluvial deposits fed through the Ling Bank delta system. This assumption is based on analysis of boring 8903 (Fig. 2) (Sejrup et al., 1994) and interpretation of the acoustic data, which indicate that sediments related to the GLOF and the withdrawal of the NCIS are only represented as a thin, uniform sediment package in this region.

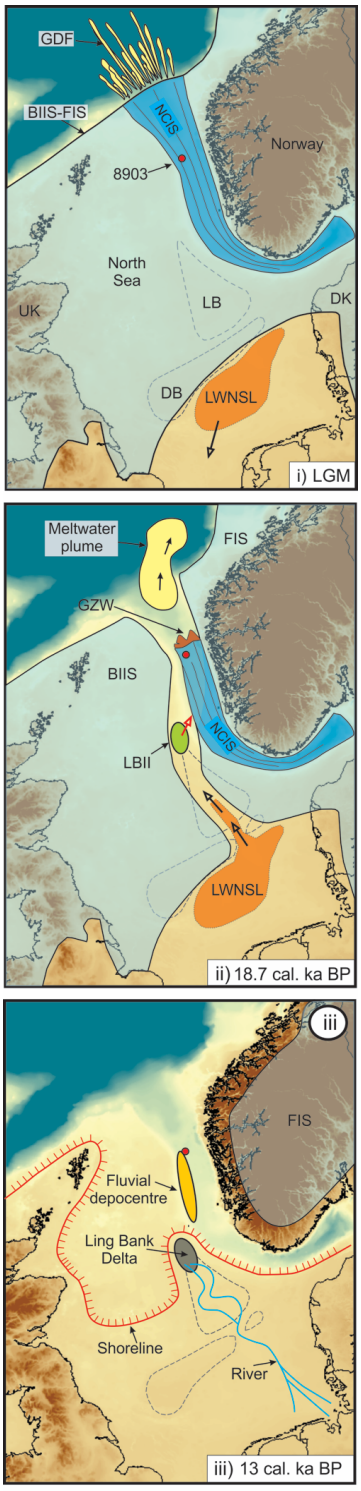

Figure 13. *Conceptual models for selected time slices of the Late glacial-Holocene paleo-environmental development of the North Sea.* ***(i) LGM***. *Confluence of the British-Irish (BIIS) and Fennoscandian (FIS) ice sheets in the North Sea and formation of the Late Weichselian North Sea ice-dammed lake (LWNSL) south of Dogger Bank (DB). Location of boring 8903 (red dot) and drainage direction of LWNSL are indicated (open black arrow). LB: Ling Bank; NCIS: Norwegian Channel Ice Stream; GDF: Glacigenic Debris Flow.* ***(ii) 18.7 cal. ka BP***. *Initiation of Late Weichselian North Sea Lake (LWNSL) outburst, deposition of outburst sediments (LBII) at the northern tip of Ling Bank and meltwater flux along the Norwegian margin. Ling Bank Drainage Channel indicated with a red arrow. GZW: Grounding Zone Wedge; NCIS: Norwegian Channel Ice Stream; FIS: Fennoscandian Ice Sheet; BIIS: British-Irish Ice Sheet.* ***(iii) 13 cal. ka BP***. *Build-up of Ling Bank Delta, meandering rivers across Ling Bank and development of fluvial depocentre in the Norwegian Channel. Indicated shoreline is drawn approximately along present day 80 m water depth contour.*

After the break-up and withdrawal of the BIIS and FIS from the main study area, the FIS margin was located along the coast of Norway until the start of the Allerød time period, at ca. 14 cal. ka BP. Thereafter, the ice sheet continued to withdraw onshore with a short-lived terrestrial readvance during the Younger Dryas (e.g. Mangerud et al., 2011). Throughout this

time period sea level was rising, but with observed still stands at around 15 cal. ka BP, 13.5 cal. ka BP (Allerød) and 12 cal. ka BP (Younger Dryas) (Fig. 12). We note that the ca. 1000 year-long halt in sea level rise at around 15 cal. ka BP seems to coincide with the level of identified high-amplitude patches at the Ling Bank Delta front (Figs. 6a and 12), suggesting that these features may be related to a shoreline and an associated beach zone.

The fluvial-dominated environment within the central North Sea, including a period with an active delta system on the Ling Bank, may have lasted for almost 7000 years until the Ling Bank submerged at the end of the Younger Dryas time period (Fig. 12).

It should be noted that the North Sea was influenced by a combined effect of glacioisostatic adjustment and tectonic subsidence during the latest part of the Quaternary (Sejrup et al., 1987; Sejrup et al., 1998; Peltier et al., 2015), making it challenging to reconstruct the exact sea level in the North Sea at a given time. The eroded till surface at the northern tip of the Ling Bank ("T1" in Fig. 6), assumed to be subaerial formed, is located at ca. 110 m below present day sealevel. In the Fladen Basin area a tectonic subsidence of up to 0.9 mm/yr has been estimated (Sejrup et al., 1987), and Peltier et al. (2015) suggest a negative glasioisostatic adjustment of around 1 mm/yr since LGM in our study area. This accounts for a total subsidence of up to 40 m in the study area. However, we have no firm evidence of sealevel or subaerial exposure deeper than 110 m in this region.

6. Conclusions

Based on high resolution acoustic records and information from shallow borings we have mapped the pathway and processes related to a glacial lake outburst flood in the North Sea. The main findings are:

- The existence of a Late Weichselian North Sea Lake outburst is evidenced from:
  - An incision, about 12 m deep and 3000 m wide, at the NE part of the Dogger Bank. This incision is located in a water depth of about 56 m and is thought to represent the break-through point of the ice-dammed lake.
  - A prograding-aggrading unit (LBII) deposited at the northern tip of the Ling Bank which resembles typical characteristics of GLOF deposits. A similar depositional pattern is also observed on the southernmost part of the Ling Bank.
  - Erosional surfaces in glacial sediments are associated with the identified prograding-aggrading sediment sequences. Such surfaces are commonly associated with GLOFs.
- Dates from the North Sea and the Norwegian continental slope suggest that the outburst took place at ca. 18.7 cal. ka BP. The flood followed the Ling Bank northwards for about 300 km before depositing an up to 10 m thick prograding-aggrading unit (LBII) at the northern tip of the Ling Bank. A meltwater plume and an associated meltwater spike, observed in sediment cores and acoustic data from the Norwegian continental margin, are suggested to represent the far-field evidence of the GLOF.
- A first approximation in estimating GLOF peak discharge resulted in values between 9.8×10^4 and 2.9×10^5 m^3/s, indicating that the Late Weichselian North Sea Lake outburst is a “major” jökulhlaup. Thus, the discharge of the Late Weichselian North Sea Lake appears to be about 10 times smaller than that estimated for Glacier Lake Missoula.
- The Late Weichselian North Sea Lake is estimated to have drained in 5-15 months.
- The Late Weichselian North Sea Lake GLOF event was followed by a fluvial-dominated environment, where the Ling Bank Delta built up at the northern part of the Ling Bank during a rising sea level. A meandering river system seems to have

existed in association with this delta. This fluvial environment may have existed as long as 7000 years, until the end of the Younger Dryas time period when the Ling Bank got submerged.

Acknowledgements

We thank Jørgen Bergeland for mapping of post-LGM sediments in the Norwegian Channel and for generating the isopach map in Figure 8. The captains and crews onboard R/V G.O.Sars are thanked for all help during several UiB cruises to the North Sea, collecting data for this study. Thanks to Olex AS, Trondheim, who gave us permission to use their bathymetric database. We are grateful for valuable comments from Alastair G.C. Graham and an anonymous reviewer. This study has been supported by the European Union's Seventh Framework Programme FP7/2007–2013/ under the REA (Research Executive Agency) grant agreement 317217, the GLANAM ITN (Glaciated North Atlantic Margins Initial Training Network). The manuscript was written during a research stay at OGS, Trieste, Italy, which was partly funded by L. Meltzers Høyskolefond.

References

Alho, P., Baker, V.R., Smith, L.N., 2010. Paleohydraulic reconstruction of the largest Glacial Lake Missoula draining(s). Quat. Sci. Rev. 29(23), 3067-3078.

Alley, R.B., Ágústsdóttir, A.M., 2005. The 8k event: cause and consequences of a major Holocene abrupt climate change. Quat. Sci. Rev. 24(10), 1123-1149.

Baker, V.R., 2009. High-energy megafloods: planetary settings and sedimentary dynamics, in: Martini, P.I., Baker, V.R., Garzon, G. (Eds.), Flood and megaflood processes and deposits: recent and ancient examples. Special Publication of the International Association of Sedimentologists, 32. Blackwell Science, Oxford, pp. 3-15.

Becker, L.W.M., Sejrup, H.P., Hjelstuen, B.O., Haflidason, H., Dokken, T.M. Ocean - ice sheet interaction along the SE Nordic Seas margin from 35 - 15 ka BP. Marine Geology. This issue.

Bigg, G.R., Clark, C.D., Greenwood, S.L., Haflidason, H., Hughes, A.L.C., Levine, R.C., Nygård, A., Sejrup, H.P., 2012. Sensitivity of the North Atlantic circulation to break-up of marine sectors of the NW European ice sheets during the last Glacial: A synthesis of modelling and palaoceanography. Global Planet. Change 98-99, 153-165.

Björck, S., 1995. A review of the history of the baltic sea, 13.0-8.0 ka BP. Quat. Inter. 27, 19-40.

Bradwell, T., Stoker, M.S., Golledge, N.R., Wilson, C.K., Merritt, J.W., Long, D., Everest, J.D., Hestvik, O.B., Stevenson, A.G., Hubbard, A.L., Finlayson, A.G., Mathers, H.E., 2008. The northern sector of the last British Ice Sheet: Maximum extent and demise. Earth-Sci. Rev. 88, 207-226.

Broecker, W.S., Kennett, J.P., Flower, B.P., Teller, J.T., Trumbore, S., Bonani, G., Wolfli, W., 1989. Routing of meltwater from the Laurentide Ice Sheet during the Younger Dryas cold episode. Nature 341, 318-321.

Carling, P.A., 2013. Freshwater megaflood sedimentation: What can we learn about generic processes? Earth-Sci. Rev. 125, 87-113.

Carrivick, J.L., Tweed, F.S., 2013. Proglacial lakes: character, behaviour and geological importance. Quat. Sci. Rev. 78, 34-52.

Carrivick, J.L., Tweed, F.S., 2016. A global assessment of the societal impacts of glacier outburst floods. Global Planet. Change 144, 1-16.

Clark, C.C., Hughes, A.L.C., Greenwood, S.L., Jordan, C., Sejrup, H.P., 2012. Pattern and timing of the last British-Irish Ice Sheet. Quat. Sci. Rev. 44, 112-146.

Clarke, G.K., Leverington, D.W., Teller, J.T. and Dyke, A.S., 2004. Paleohydraulics of the last outburst flood from glacial Lake Agassiz and the 8200BP cold event. Quat. Sci. Rev. 23(3), 389-407.

Coles, B.J., 2000. Doggerland: the cultural dynamics of a shifting coastline. Geol. Soc. London Spec. Pub. 175(1), 393-401.

Graham, A.G.C, Stoker, M.S., Lonergan, L., Bradwell, T., Stewart, M.A., 2011. The Pleistocene glaciations of the North Sea Basin, in: Ehlers, J., Gibbard, P.L., Hughes, P.D., (Eds.), Quaternary glaciations: extent and chronology: a closer look. Elsevier, pp. 261-278.

Graham, A.G.C, Lonergan, L., Stoker, M.S., 2010. Depositional environments and chronology of Late Weichselian glaciation and deglaciation in the central North Sea. Boreas 39(3), 471-491.

Haflidason, H., Sejrup, H.P., Nygård, A., Mienert, J., Bryn, P., Lien, R., Forsberg, C.F., Berg, K., Masson, D., 2004. The Storegga Slide: architecture, geometry and slide development. Mar. Geol. 213, 201-234.

Hammer, Ø., Planke, S., Hafeez. A., Hjelstuen, B.O., Faleide, J.I., Kvalø. F., 2015. Agderia – a postglacial lost land in the southern Norwegian North Sea. Nor. J. Geol. 96, 43-60.

Hanson, M.A., Clague, J.J., 2016. Record of glacial Lake Missoula floods in glacial Lake Columbia, Washington. Quat. Sci. Rev. 133, 62-76.

Hanson, M.A., Lian, O.B., Clague, J.J., 2012. The sequence and timing of large late Pleistocene floods from glacial Lake Missoula. Quat. Sci. Rev. 31, 67-81.

Hijma, M.P., Cohen, K.M., Roebroeks, W., Westerhoff, W.E., Busschers, F.S., 2012. Pleistocene Rhine–Thames landscapes: geological background for hominin occupation of the southern North Sea region. J. Quat. Sci. 27(1), 17-39.

Hjelstuen, B.O., Nygård, A., Sejrup, H.P., Haflidason, H., 2012. Quaternary denudation of southern Fennoscandia - evidence from the marine realm. Boreas 41(3), 379-390.

Hjelstuen, B.O., Sejrup, H.P., Haflidason, H., Nygård, A., Berstad, I.M., Knorr, G., 2004. Late Quaternary seismic stratigraphy and geological development of the south Vøring margin, Norwegian Sea. Quat. Sci. Rev. 23, 1847-1865.

Høgaas, F., Longva, O., 2016. Mega deposits and erosive features related to the glacial lake Nedre Glomsjø outburst flood, southeastern Norway. Quat. Sci. Rev. 151, 273-291.

Huuse, M., Lykke-Andersen, H., 2000. Overdeepened Quaternary valleys in the eastern Danish North Sea: morphology and origin. Quat. Sci. Rev. 19(12), 1233-1253.

Jakobsson, M., Björck, S., Alm, G., Andrén, T., Lindeberg, G., Svensson, N.O., 2007. Reconstructing the Younger Dryas ice dammed lake in the Baltic Basin: Bathymetry, area and volume. Global Planet. Change 57(3), 355-370.

Jensen, J.B., Bennike, O., Witkowski, A., Lemke, W., Kuijpers, A., 1997. The Baltic Ice Lake in the southwestern Baltic: sequence-, chrono-and biostratigraphy. Boreas 26(3), 217-236.

King, E.L., Haflidason, H., Sejrup, H.P., Løvlie, R., 1998. Glacigenic debris flows on the North Sea Trough Mouth Fan during ice stream maxima. Mar. Geol. 152, 217-246.

King, E.L., Sejrup, H.P., Haflidason, H., Elverhøi, A., Aarseth, I. 1996. Quaternary seismic stratigraphy of the North Sea Fan: Glacially-fed gravity flow aprons, hemipelagic sediments, and large submarine slides. Mar. Geol. 130, 293-315.

Lambeck, K., Rouby, H., Purcell, A., Sun, Y., Sambridge, M., 2014. Sea level and global ice volumes from the Last Glacial Maximum to the Holocene. Proc. National Academy of Science 111(43), 15296-15303.

Lang, J., Winsemann, J., 2013. Lateral and vertical facies relationships of bedforms deposited by aggrading supercritical flows: from cyclic steps to humpback dunes. Sed. Geol. 296, 36-54.

Lee, J.R., Busschers, F.S., Sejrup., H.P., 2012. Pre-Weichselian Quaternary glaciations of the British Isles, The Netherlands, Norway and adjacent marine areas south of

68°N: implications for long-term ice sheet development in Northern Europe. Quat. Sci. Rev. 44, 213-228.

Lekens, W.A.H., Sejrup, H.P., Haflidason, H., Petersen, G.Ø., Hjelstuen, B.O., Knorr, G., 2005. Laminated sediments preceding Heinrich event 1 in the Northern North Sea and Southern Norwegian Sea; origin, processes and regional linkage. Mar. Geol. 216, 27-50.

Mangerud, J., Gyllencreutz, R., Lohne, Ø., Svendsen, J. I., 2011. Glacial history of Norway, in: Ehlers, J., Gibbard, P.L., Hughes, P.D., (Eds.), Quaternary glaciations: extent and chronology: a closer look. Elsevier, pp 279-298.

Meinsen, J., Winsemann, J., Weitkamp, A., Landmeyer, N., Lenz, A., Dölling, M., 2011. Middle Pleistocene (Saalian) lake outburst floods in the Münsterland Embayment (NW Germany): impacts and magnitudes. Quat. Sci. Rev. 30(19), 2597-2625.

Morén, BM., Sejrup, H.P., Hjelstuen, B.O., Borge, M.V., Schäuble, C. In press. The last deglaciation of the Norwegian Channel; geomorphology, stratigraphy and radiocarbon dating. Boreas. DOI: 10.1111/bor.12272

Murton, D.K., Murton, J.B., 2012. Middle and Late Pleistocene glacial lakes of lowland Britain and the southern North Sea Basin. Quat. Int. 260, 115-142.

Nygård, A., Sejrup, H. P., Haflidason, H., Bryn, P., 2005. The glacial North Sea Fan, southern Norwegian Margin: Architecture and evolution from the continental slope to the deep-sea basin. Mar. Pet. Geol. 22, 71-84.

Nygård, A., Sejrup, H.P., Haflidason, H., Lekens, W.A.H., Clark, C.D., Bigg, G.R., 2007. Extreme sediment and ice discharge from marine-based ice streams: New evidence from the North Sea. Geology 35, 395-398.

Peltier, W.R., Argus, D.F. and Drummond, R., 2015. Space geodesy constrains ice-age terminal deglaciation: The global ICE-6G_C (VM5a) model. J. Geophys. Res. Solid Earth 120, 450-487.

Reinardy, B.T., Hjelstuen, B.O., Sejrup, H.P., Augedal, H., Jørstad, A., 2017. Late Pliocene-Pleistocene environments and glacial history of the northern North Sea. Quat. Sci. Rev., 158, 107-126.

Rodionov, S.N., 2012. Global and regional climate interaction: the Caspian Sea experience. Springer Science and Business Media, ISBN 978-94-010-4468-4, 242 pp.

Russell, A.J., Knudsen, O., Fay, H., Marren, P.M., Heinz, J., Tronicke, J., 2001. Morphology and sedimentology of a giant supraglacial, ice-walled, jökulhlaup channel, Skeiðarárjökull, Iceland: implications for esker genesis. Global Planet. Change 28(1), 193-216.

Sejrup, H.P., Clark, C.D., Hjelstuen, B.O., 2016. Rapid ice sheet retreat triggered by ice stream buttressing: Evidence from the North Sea. Geology 44(5), 355-358.

Sejrup, H.P., Haflidason, H., Aarseth, I., King, E., Forsberg, C.F., Long, D., Rokoengen, K., 1994. Late Weichselian glaciation history of the northern North Sea. Boreas 23, 1-13.

Sejrup, H.P., Hjelstuen, B.O., Dahlgren, K.I.T., Haflidason, H., Kuijpers, A., Nygård, A., Praeg, D., Stoker, M.S., Vorren, T.O., 2005. Pleistocene glacial history of the NW European continental margin. Mar. Pet. Geol. 22, 1111-1129.

Sejrup, H.P., Hjelstuen, B.O., Nygård, A., Haflidason, H., Mardal, I., 2015. Late Devensian ice marginal features in the central North Sea – processes and chronology. Boreas 44, 1-13.

Sejrup, H.P., Landvik, J.Y., Larsen, E., Janocko, J., Eiriksson, J., King, E., 1998. The Jæren Area; a Border Zone of the Norwegian Channel Ice Stream. Quat. Sci. Rev. 17, 801-812.

Sejrup, H.P., Larsen, E., Haflidason, H., Berstad, I.M., Hjelstuen, B.O., Jonsdottir, H.E., King, E.L, Landvik, J., Longva, O., Nygård, A., Ottesen, D., Raunholm, S., Rise, L., Stalsberg, K., 2003. Configuration, history and impact of the Norwegian Channel Ice Stream. Boreas 32, 18-36.

Sejrup, H.P., Aarseth, I., Ellingsen, K.L., Reither, E., Jansen, E., Løvlie, R., Bent, A., Brigham-Grette, J., Larsen, E., Stoker, M.S., 1987. Quaternary stratigraphy of the Fladen area, central North Sea: A multidisciplinary study. J. Quat. Sci. 2, 35-58.

Sejrup, H.P., Aarseth, I., Haflidason, H., Løvlie, R., Bratten, Å., Tjøstheim, G., Forsberg,C.F., Ellingsen, K.I., 1995. Quaternary of the Norwegian Channel: glaciation history and palaeoceanography. Nor. J. Geol. 75, 65-87.

Smith, L.N., 2006. Stratigraphic evidence for multiple drainings of glacial Lake Missoula along the Clark Fork River, Montana, USA. Quat. Res. 66, 311-322.

Stewart, M.A., Lonergan, L., 2011. Seven glacial cycles in the middle-late Pleistocene of northwest Europe: Geomorphic evidence from buried tunnel valleys. Geology 39(3), 283-286.

Teller, J.T., Leverington, D.W., Mann, J.D., 2002. Freshwater outbursts to the oceans from glacial Lake Agassiz and their role in climate change during the last deglaciation. Quat. Sci. Rev. 21(8), 879-887.

Teller, J.T., Leverington, D.W., 2004. Glacial Lake Agassiz: A 5000 yr history of change and its relationship to the δ18O record of Greenland. Geol. Soc. Am. Bull. 116(5-6), 729-742.

Toonen, W.H., Kleinhans, M.G., Cohen, K.M., 2012. Sedimentary architecture of abandoned channel fills. Earth Surf. Proc. Landforms 37(4), 459-472.

Toucanne, S., Zaragosi, S., Bourillet, J.F., Marieu, V., Cremer, M., Kageyama, M., Van Vliet-Lanoë, B., Eynaud, F., Jean-Louis Turon, J.-L., Gibbard, P.L., 2010. The first estimation of Fleuve Manche palaeoriver discharge during the last deglaciation: evidence for Fennoscandian ice sheet meltwater flow in the English Channel ca 20–18 ka ago. Earth Planet. Sci. Let. 290(3), 459-473.

www.km.kongsberg.com, Kongsberg Maritime, Kongsberg, Norway, 27.10.2017

Glacigenic sedimentation pulses triggered post-glacial gas hydrate dissociation

Jens Karstens, Haflidi Haflidason, Lukas W. M. Becker, Christian Berndt, Lars Rüpke, Sverre Planke, Volker Liebetrau, Mark Schmidt, Jürgen Mienert

In press in Nature communications

IV

Glacigenic sedimentation pulses triggered post-glacial gas hydrate dissociation

Jens Karstens[1,2*], Haflidi Haflidason[1], Lukas W.M. Becker[1], Christian Berndt[2], Lars Rüpke[2], Sverre Planke[3,4], Volker Liebetrau[2], Mark Schmidt[2], Jürgen Mienert[5]

[1]Department of Earth Science, University of Bergen, Norway

[2]GEOMAR Helmholtz Centre for Ocean Research Kiel, Germany

[3]Volcanic Basin Petroleum Research (VBPR), Oslo, Norway

[4]The Centre for Earth Evolution and Dynamics (CEED), University of Oslo, Norway

[5]CAGE - Centre for Arctic Gas Hydrate, Environment and Climate, UiT - The Arctic University of Norway, Norway

[*]jkarstens@geomar.de

Abstract

Large amounts of methane are stored in continental margins as gas hydrates. They are stable under high pressure and low, but react sensitively to environmental changes. Bottom water temperature and sea level changes were considered as main contributors to gas hydrate dynamics after the last glaciation. However, here we show with numerical simulations that pulses of increased sedimentation dominantly controlled hydrate stability during the end of the last glaciation offshore mid-Norway. Sedimentation pulses triggered widespread gas hydrate dissociation and explains the formation of ubiquitous blowout pipes in water depths of 600 to 800 m. Maximum gas hydrate dissociation correlates spatially and temporally with the formation or reactivation of pockmarks, which is constrained by radiocarbon dating of Isorropodon nyeggaensis bivalve shells. Our results highlight that rapid changes of sedimentation can have a strong impact on gas hydrate system affecting fluid flow and gas seepage activity, slope stability and the carbon cycle.

Introduction

Continental margin sediments represent the largest methane reservoir on earth[3]. Most methane is stored as free gas or gas hydrate - ice-like clathrates that form under high pressure and low temperature conditions - in the pore space of marine sediments[4]. High gas hydrate saturations can lower the permeability of the host sediment and prevent diffusive migration of gas resulting in its accumulation beneath the base of the gas hydrate stability zone (BGHSZ)[5]. Such gas accumulations result in the build-up of high pore-overpressure, which can lead to the formation or reactivation of focused fluid conduits[6]. Pressurized fluids are released by natural blowout events and create sea floor craters known as pockmarks[7], which are abundant in many gas hydrate provinces around the world. The southern Vøring Plateau gas hydrate province is located at the northern sidewall of the Storegga Slide and received significant amounts of glacigenic sediments related to ice-stream activity during the decay of the Fennoscandian Ice-Sheet at the end of the Last Glacial Maximum[8]. It hosts the Nyegga pockmark field, which consists of several hundred sea floor depressions (Fig. 1, ref. 9). Seismic data show that gas hydrates occur from beneath the pockmark field towards the South into the Storegga Slide scar[10]. The pockmarks are located on top of pipe structures, which penetrate the gas hydrate layer and root in the free gas zone beneath the BGHSZ or even deeper (Figs. 1b, 2). Several pockmarks host large authigenic carbonate mounds indicating phases with increased and long lasting seepage activity[11].

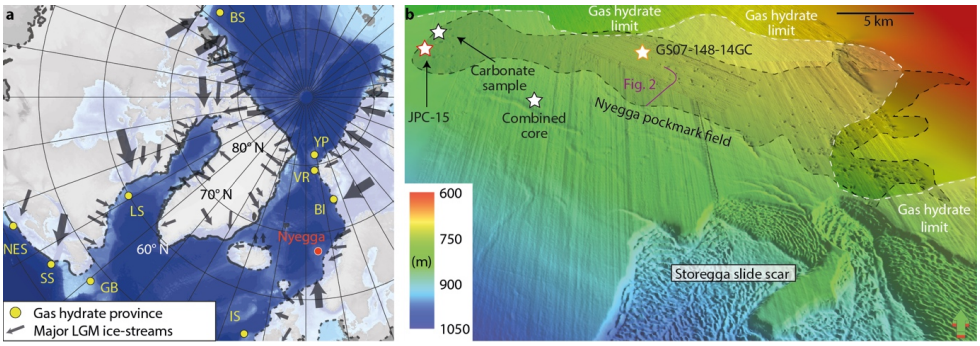

Fig. 1 – a) Map showing modelled gas hydrate occurrence around the Nordic Sea's shelves, proven gas hydrate deposits (BI: Bear Island trough mouth fan and Håkon Mosby mud volcano, BS: Beaufort Sea, GB: Grand Banks, IS: Irish Sea, LS: Labrador Sea, NES: New England Shelf, SS: Scotian Shelf, VR: Vestnesa Ridge, YP: Yermak Plateau[24], the location of the LGM Fennoscandian, Eurasian and Laurentian ice-sheets[25,26] and the major ice-streams[27]. b) 3D view on seismic bathymetry from the Southern Vøring Plateau showing the location of the Nyegga pockmark field, the extent of gas hydrates[40] (white dashed line) and the Storegga slide scar. Locations of sediments cores, carbonate sample and the combined cores are marked with stars.

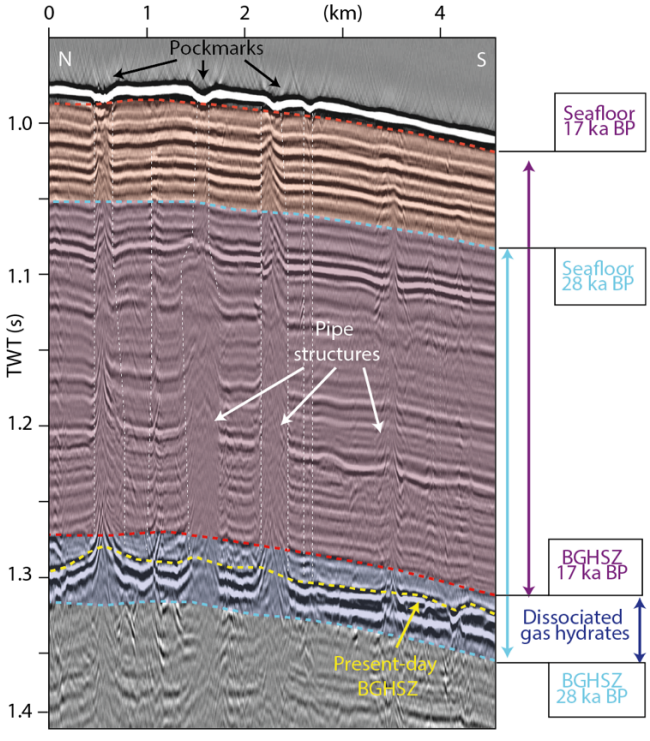

Fig. 2 - Seismic profile with pipe structures, pockmarks, the present-day base of the gas hydrate stability zone (yellow) and calculated bases of the gas hydrate stability zone at 17 ka BP (blue) and 28 ka BP (red).

The dynamic redistribution of gas hydrates within the sediment column due to external forces is a well-established process known as gas hydrate recycling [12, 13]. During glacial cycles, gas hydrate dynamics is governed by sea level changes, regional bottom water temperature fluctuations and local sedimentation rate changes. The local sea floor depth is controlled by the global sea level and regional uplift or subsidence. Bottom water temperature changes during deglaciations are mainly controlled by the reorganization of ocean currents and warming of water masses affecting the sediment temperature profile[14]. This study has a focus on the impact of sedimentation on gas hydrate dynamics. Sediment accumulation influences both the sea floor depth and the sediment temperature profile (Fig. 3). When sediment is deposited, the sediment temperature profile leaves the equilibrium temperature gradient. Conductive heat transfer gradually warms the sedimentary column, which begins with the adjustment of the sediment temperature close to the sea floor and then propagates towards greater depth. As a consequence, gas hydrates at the BGHSZ dissociate into free gas, which dissolves in the pore water or migrate upward, where it may form hydrates again. Only if concentrations are very low the gas may stay in situ as the buoyancy may not be great enough to overcome capillary forces withholding gas migration. Otherwise the buoyancy of gas and related volumetric expansion of the pore fluid during hydrate dissociation will cause increasing pore overpressure and the formation or reactivation of focused fluid conduits involving the cracking of sediment formations. This process concentrates gas hydrates at the BGHSZ and reduces sediment permeability, which impedes further gas migration and therefore leads to gas accumulation beneath the BGHSZ (Fig. 3).

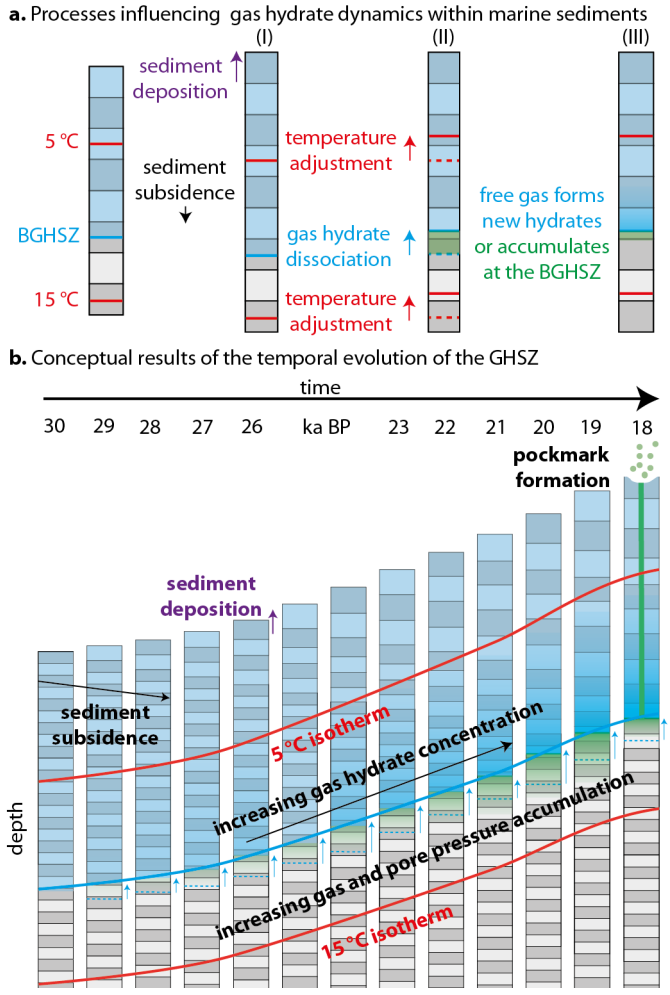

Fig. 3 - a) Processes influencing the gas hydrate dynamics within marine sediments: Sediment gets deposited and the sedimentary column subsides (I), the temperature profile and the base of the gas hydrate stability zone (BGHSZ) adjusts and gas hydrate dissociates (II). Free gas migrates back in the GHSZ and forms hydrates again, while hydrate concentration increases and free gas accumulates beneath the base of the GHSZ (III). b) Conceptual evolution of isotherms, hydrate concentrations and free gas accumulations during ongoing sedimentation and subsidence for a single location.

We have analysed the gas hydrate dynamics beneath the Nyegga pockmark field with numerical simulations for the period between 30,000 and 15,000 years before present (BP). The analysis built on the global sea level curve[15], local subsidence constraints[16], bottom water temperature information and a local sedimentation history reconstruction. Our dynamic gas hydrate stability simulations integrated time-dependent sediment temperature profiles with a time-dependent sea floor depth reconstruction (Figs. 4a, e). The sea floor depth was calculated combining a global sea level reconstruction[14] with a

regional subsidence rate of 1.2 mm/a (ref. 16) and a local sedimentation rate reconstruction. The sediment temperature profiles used the sedimentation reconstruction as well and were calculated with a finite difference heat-flow simulation building on Fourier's law for heat flow (see methods). We used a homogenous thermal diffusivity for the glacigenic sediments (4.2 x 10^{-7} m^2/s, ref 2). The evolution of the bottom water temperature at the mid-Norwegian margin during the LGM is controversial. The stable oxygen isotope analysis of benthic foraminifera reveals a pronounced $\delta^{18}O$ anomaly around the LGM, which may be explained by brine formation[17], freshening by melt water input[18] or warming of immediate water masses[19]. For our simulations, we assume constant bottom water temperature of -1°C (ref. 2). We base this assumption on the analysis of stable oxygen isotope from benthic foraminifera from two cores that have been affected by the same bottom water masses. One of the sediment cores from the Vøring Plateau shows stable deep-water conditions during the Last Glacial Maximum[17], while the oxygen isotope record of a core from the northern North Sea indicates that an increase of bottom water temperature did not occur before the end of the Younger Dryas (~11.800 years BP) [20], which correlates with the onset of the Norwegian Atlantic Current[21, 22]. All parameters were combined to calculate the pressure and temperature fields (Fig. 4d) to determine the BGHSZ following the approach of Tishchenko et al. (2005; ref. 23). We conducted a sensitivity analysis for the input parameters of our simulations by testing different bottom water temperature profiles, sedimentation rate reconstructions, subsidence rates, thermal diffusivity values and geothermal gradients. The sensitivity analysis revealed that variations of these input parameters had no significant impact on the timing and trend of gas hydrate dissociation (see methods and supplement). The sensitivity analysis includes simulation scenarios, which assume bottom water warming before or during the LGM.

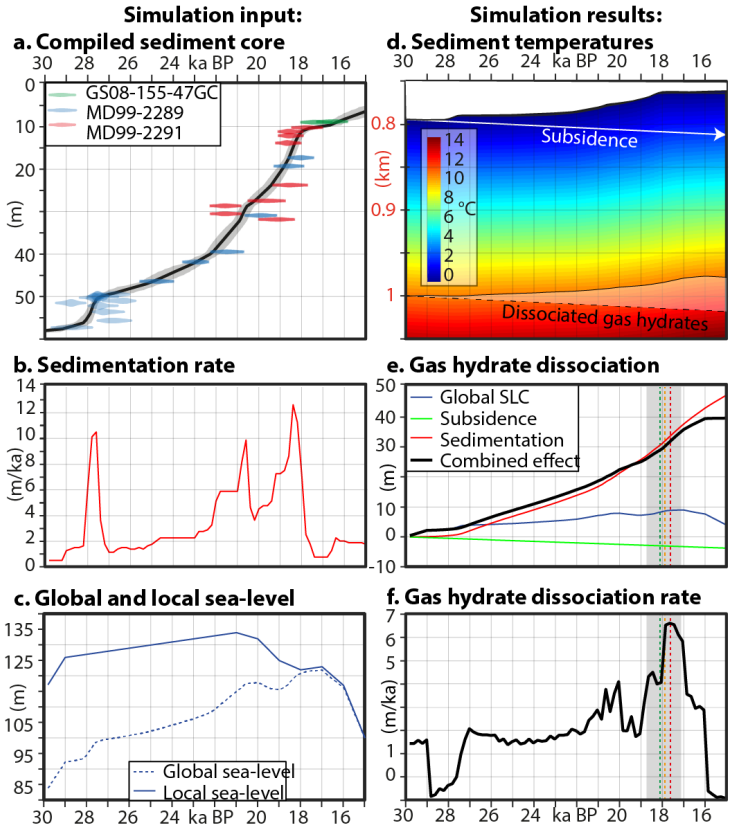

Fig. 4 - a) Age-depth-model and radiocarbon ages from the combined core. b) Sedimentation rate evolution. c) Global and local sea level anomaly in comparison to the present-day sea level and phases with enhanced methane seepage. d) Sediment temperature reconstruction and the effect on gas hydrate dissociation (compare with Fig. 2b). e) Absolute gas hydrate dissociation with time: effect of sedimentation (red line), effect of subsidence (green line), effect of sea level fluctuation (blue line), effect of all combined (black line) and phase with enhanced methane seepage (green dashed line mean calibrated age of carbonate sample, orange dashed line mean calibrated age of Isorropodon nyeggaensis horizon in core GS07-148-14GC, red dashed line mean calibrated age of Isorropodon nyeggaensis horizon in core JCP-15 (ref. 31) and grey box indicating the error margins of the calibrations. f) Gas hydrate dissociation rate and phase with enhanced methane seepage.

Results

Sedimentation rate reconstruction

The most important input parameter for our simulations is a spatial sedimentation history reconstruction that builds on combining a local age-depth model compiled from 43 radiocarbon dates from five sediment cores (Fig. 4a) into a high-resolution seismo-stratigraphic framework of the study area (see methods). The sedimentation rate reconstruction shows distinct differences between periods characterized by decreased sedimentation rates between 0.5 and 1 mm/a and phases of increased rates of glacigenic input with peak rates of 9 mm/a (Fig. 4b). The sedimentation rate shows a first maximum at 28,000 years BP, which coincides with the first advance of the Fennoscandian ice sheet on the nearby shelves[25]. At around 25,000 years BP, sedimentation rates started to increase again and had a second maximum at 20,500 years BP, which correlates with the deposition of glacial debris lobes. There was a third maximum between 19,500 and 18,500 years BP associated with sediment-rich melt water plumes[8].

Modelling the dynamic changes of the hydrate stability zone

The finite difference heat flow simulations demonstrate, how the diffusive heat transfer warms the newly deposited sediments and affects the sediment temperature profile and the BGHSZ (Figs. 3, 4d). The sediment temperature adjustment causes a significantly shoaling of the BGHSZ within the sedimentary column during the simulation period (Fig. 4d). The change of the BGHSZ is the result of the combined effects of sedimentation, sea level change and subsidence. In the period between 30,000 to 15,000 years BP, the eustatic sea level fluctuation alone would have resulted in a maximum BGHSZ shoaling of ~10 m, while continuous local subsidence would have caused a deepening of the BGHSZ of ~3 m over the entire simulation period (Fig. 4e). During the same period, the sedimentation alone would have caused a shoaling of the GHSZ by ~47 m outpacing the effects of sea level fluctuation and subsidence by far. All factors combined resulted in a net dissociation of ~40 m. Therefore, sedimentation was the

most important driver of gas hydrate dynamics in the study area during and after the Last Glacial Maximum (Fig. 4f). A possible bottom water temperature increase after the Last Glacial Maximum would have amplified further sedimentation-related gas hydrate dissociation. The gas hydrate dissociation rate follows the trend of sedimentation rate with a delay of about 1000 years having its maximum around 17,800 years BP.

Timing of enhanced seepage from radiocarbon analysis

High-resolution 3D seismic analysis of the Nyegga fluid pipes indicates that sea floor seepage is episodic correlating with Pleistocene climate fluctuations[28]. Reflection seismic data and radiocarbon dating of sediment cores reveal that the pipes crosscut sediments, which was deposited before and during the LGM (Fig. 2). This is a clear indicator for seepage activity during at the end of the LGM. To have more detailed constraints about the timing of enhanced methane seepage during that period, we further analysed seep fauna and seafloor carbonates. The chemosynthetic symbiotic bacteria containing bivalve species *Isorropodon nyeggaensis* (Fig. 5; ref. 29) provide a model-independent time marker for methane seepage in the Nyegga pockmark field. Sediment coring (GS07-155-14GC in Fig. 1b) of a seep-related mound structure with a central depression revealed a 60 cm-thick layer of *Isorropodon nyeggaensis* shells at a depth of 100 cm (Fig. 5). Radiocarbon dating of these shells points towards two episodes of pronounced methane seepage about 17,900 and about 15,700 years BP[30]. A similar shell-bearing horizon was cored within a pockmark (JPC-15) in the western part of the field, providing analogue ages of around 17,600 years BP[30].

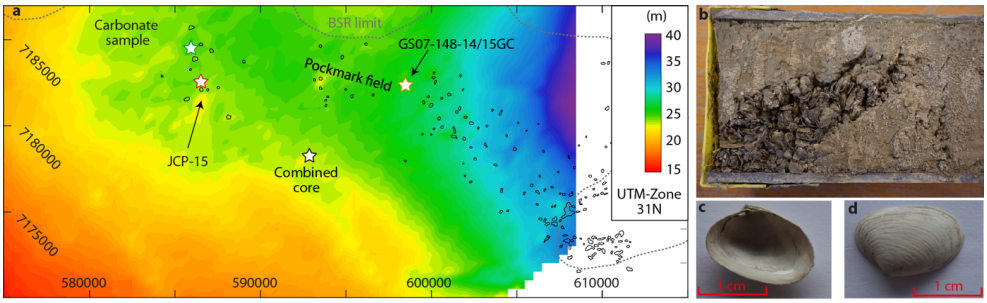

Fig. 5 - a) Map showing the distribution of gas hydrate dissociation at 17.8 ka with pockmark location[9], extent of gas hydrates indicated by a BSR (Bottom simulating reflector; dashed black lines; ref.10) and coring and sample locations. b) Photograph showing the beginning of section 2 of gravity core GS07-148-14GC with a pronounced accumulation of intact and fragmented shells of Isorropodon nyeggaensis. c) and d) Photographs of Isorropodon nyeggaensis shell from this core.

Additionally, mineralogical and geochemical analyses of a sea floor-exposed sediment crust (Fig. 1b) indicate a maximum age around 18,000 years BP (see methods). The sample consists of 30-50 wt.% of Ca(Mg)-carbonate with calcite and dolomite in approximately equal abundancy, which is similar to sediment samples from JPC-15 (ref. 27). The bulk $\delta^{13}C$ values between -0.4 and -5.2 ‰ relative to Vienna Pee Dee Belemnite for binary mixtures of calcite and dolomite from three sub-samples suggest an endmember $\delta^{13}C$ signature of -11 ‰ for the dolomitic mineral phase. This value is less negative than known from other authigenic carbonate concretions from the study area[32], however, still indicative for seep-related overgrowth or recrystallization of biotic mineral precursors[33, 34]. Probably the dolomitic phase precipitated either outside the main methane seep site from pore fluids ascending with the methane or after vigorous methane seepage ceased. The $\delta^{18}O$-values of the carbonaceous mixtures indicate a slight enrichment of ^{16}O in dolomite compared to calcite. This is contrary to the oxygen fractionation during precipitation at the same sea floor temperature and possibly rather reflects pore water freshening than increased temperatures during dolomite formation[35]. These observations combined, suggest a simultaneous pulse of methane seepage in the pockmark field starting around 18,000 years BP.

Excess pore pressure quantification

The overpressure resulting from the buoyancy of free gas can be calculated by $P = H_{gas} *(g*(\rho_w-\rho_{CH4\_10\ MPa}))$ (ref. 36), where H_{gas} represents the gas column height, g is gravitational acceleration (9.81 m/s^2), ρ_w is density of the formation water (~1025 kg/m^3) and $\rho_{CH4\_10\ MPa}$ is density of methane for pressure of 10 MPa C (~84 kg/m^3; ref. 37). The volume of the gas formed by gas hydrate dissociation is 164 times greater than the hydrate volume under atmospheric pressure conditions[38], while density of methane under atmospheric pressure condition (0.656 kg/m^3) is about 128 times smaller than at 10 MPa. The gas column height is consequently: $H_{gas} = 164/128\ H_{hydrate} * s_{hydrate}$, where $s_{hydrate}$ is the gas hydrate concentration (3 – 12%, ref. 39) and $H_{hydrate}$ is the height of dissociated gas hydrates (40 m from simulations). The resulting overpressure due to buoyancy lies between 15.1 and 60.6 kPa.

Discussion

The radiometrically-deduced timing of enhanced seepage coincides well with the independently modelled maximum of gas hydrate dissociation around 17,800 years BP (Fig. 4). For this time slice, the gas hydrate dissociation peaks (Fig. 4h) and the simulation even reproduces the location of the western pockmark group (Fig. 5). These areas received most of the gas released by dissociation due to the locally increased gas hydrate dissociation rate and as the result of the topography of the BGHSZ focussing lateral gas migration towards the pockmark field[40]. The temporal and spatial correlation between the maximum gas hydrate dissociation and the pockmark activity strongly suggests that gas hydrate dynamics related to increased glacigenic sediment accumulation controlled methane seepage after the Last Glacial Maximum at the Nyegga pockmark field.

Gas hydrate dissociation results in high pore overpressure by volume expansion during phase transition and buoyancy of the released gas. Considering 40 m of dissociated hydrates and hydrate concentrations of 3 – 12% (refs. 39, 41), the buoyancy of the resulting gas column would cause pore-overpressures of 15 – 61 kPa. This calculation

assumes that gas formed by the gas hydrate dissociation is mobile and accumulates beneath the BGHSZ, which is plausible considering the well-developed bottom-simulating reflector indicating the presence of a gas column beneath the highly dynamic BGHSZ (Fig. 3).

More detailed quantification of excess pore-pressure due to volume expansion would require detailed knowledge of past gas hydrate concentration, distribution and hydraulic properties of the host sediments. However, excess pore pressure is expected to be highest at times of maximum gas hydrate dissociation rate[42] and hence to correlate with the timing of enhanced methane seepage.

Depending on the average gas hydrate concentration, the methane seepage potential from gas hydrate dissociation in the modelled area accrues to between 26 and 212 Mt (see methods). Our model covers only a tenth of the local gas hydrate province implying a total seepage potential of more than 1 Gt of methane. Ice-stream activity and the rapid melting of the Fennoscandian, Eurasian and Laurentide ice-sheets released pulses of high sedimentation discharge to gas hydrate provinces along the North Atlantic and Artic Ocean margins (Fig. 1a). This high sediment discharge might have triggered wide-spread and simultaneous gas hydrates dissociation implying a global seepage potential of several billion tons of methane. Even if a large fraction of the methane has been recycled within the hydrate stability zone or consumed by the benthic filter, it is likely that the sudden hydrate dissociation due to sediment input has released large amounts of methane into the water column. It is difficult to constrain, if the methane release from pockmarks at Nyegga occurred continuously with low seepage rates or catastrophically with high seepage rates comparable to drilling-induced blowout events. Numerical simulations indicate that methane released from natural seeps deeper than 100 m below sea level will not reach the atmosphere via bubble transport due to oxidisation and dissolution, while a catastrophic methane release allows a more efficient transport of methane to the sea surface[43]. Consequently, it is speculative if the focused methane release at Nyegga after the LGM directly affected the atmosphere methane budget. Nevertheless, the dissolution and oxidisation of methane in the water column has likely reduced the ocean's potential of absorbing atmospheric methane. Assuming that the sedimentation controlled gas hydrate dissociation and methane seepage occurred

simultaneously around glaciated gas hydrate provinces after the LGM, this process would have contributed to the increase of global atmospheric methane concentrations after the Last Glacial Maximum[44].

Our simulations indicate that sedimentation on its own is able to cause significant hydrate dissociation independent of bottom water temperature warming or sea level fluctuation. The link between sedimentation, gas hydrate dynamics and pore-pressure evolution is a key to understand slope stability. Glacial and fluvial depocenters on passive margins host some of the largest submarine slope failures. The resulting landslides have mainly been attributed to pore-overpressure due to increased sediment load or gas hydrate dissociation, which is commonly explained by post-glacial bottom water temperature warming[45]. However, many large slope failures occurred after phases with enhanced sediment accumulation with a delay of several thousand years[46]. We observe a similar delay for hydrate dissociation, in which the timing is mainly controlled by thermal sediment properties. Although there is so far no proof for hydrate-related slope failure, our results show that sedimentation-induced gas hydrate dissociation may play an important part in pore-overpressure accumulation and trigger or precondition slope failures in trough mouth and river fan systems.

Unlike sea level and bottom water temperature fluctuations, the effect of sedimentation on the absolute thickness of the gas hydrate stability zone is relatively small, because basin subsidence counteracts sedimentation and heat flow re-adjusts sediment temperatures. However, sedimentation results in a large shift of the BGHSZ within the sedimentary column and causes the redistribution of large volumes of hydrates (Figs. 3b, 4f). If redistribution is not possible via diffusive fluid flow due to lithological or gas hydrate-related permeability barriers, it has the potential to create pore-overpressure and trigger focused fluid flow. The discharge of methane via focused fluid flow has significant impact on local and global carbon budgets and fluxes[47]. Therefore, sedimentation has to be considered, when understanding gas hydrate and fluid flow systems not only in glaciated margins, but also in other areas with high sedimentation rates. Increased sedimentation is key to understand the formation of focused fluid conduits and slope failures in gas hydrate systems around the world.

Methods

Seismo-stratigraphic framework

The seismo-stratigraphy of the Nyegga area is characterized by the presence of six pronounced reflections, which are well-defined in echosounder data throughout the study area[48]. We traced these reflection in a dense network of echosounder profiles collected with the TOPAS echosounder system on-board RV G.O. Sars by University in Bergen in 2004 and a Parasound echosounder system on board of RV Meteor by Geomar in 2012 (Fig. 6). The stratigraphic section defined by the deepest and shallowest interpreted seismic reflections consists of spatially homogenous, laminated sediments and shows no unconformities indicating phases of erosion. The thickness of specific intervals within this stratigraphic section varies depending on the proximity to glacigenic depositional centres to the West[9]. The seismo-stratigraphy represents a continuous record of the sedimentation history of the study area and allows constraining a stratigraphic framework for the Nyegga pockmark field.

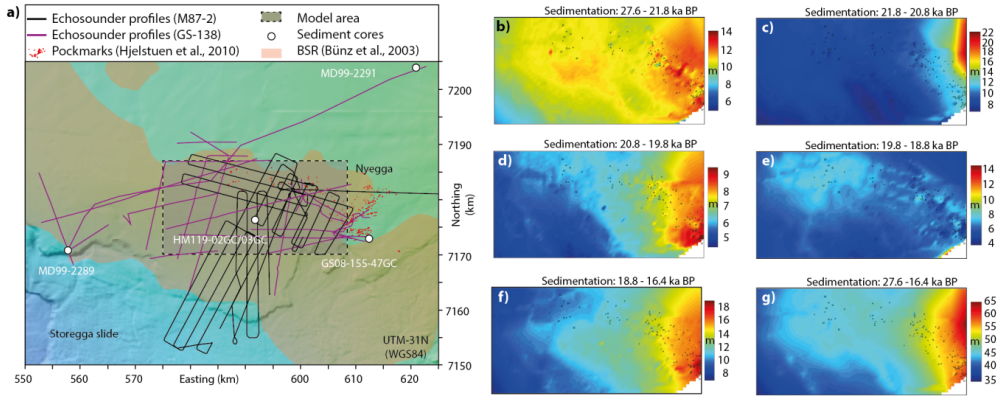

Fig. 6 - a) Map showing the location of the echosounder profiles used for the seismo-stratigraphic framework, pockmarks, sediment core locations, model area, and area with mapped BSR (Bottom simulating reflector). b-g) Sediment thickness maps for different intervals of the seismo-stratigraphic framework.

Radiocarbon age calibration

The calibration of radiocarbon dates from marine sources need to be corrected for the global and local reservoir effects. The global reservoir effect is set to 405 years within the Marine13 calibration curve[49]. The local reservoir effect depends on time-varying oceanographic parameters, which are not well-constrained for the study area during the analysed period. Numerical modelling of the local reservoir effect for the North Atlantic suggests values between 200 and 600 years[50], while the comparison of terrestrial and marine ^{14}C reservoir ages revealed variations of the local reservoir effects between 100 and 400 years for the Younger Dryas[51]. To acknowledge this uncertainty, we used a local reservoir effect of 400 years with an uncertainty of ± 200 years for the calibration tool Calib7.1 using the Marine13 calibration curve for all radiocarbon based dates in this study[48, 51] to make them self-consistent.

Age-depth-model

The age depth model builds on integrating radiocarbon dates from the five sediment cores MD99-2289, MD99-2291, HM119-02GC, HM119-03GC and GS08-155-47GC (Fig 7; Tab. 1). Sediment core MD99-2291 is located close to the depositional centre in the West of the study area and has a high-resolution record of the shallow to intermediate interval of the seismo-stratigraphic framework, while sediment core MD99-2289 is located more than 60 km away close to the Storegga Slide side-wall and provides age information for the intermediate to deep interval of the seismo-stratigraphic framework. Sediments cores HM119-02GC, HM119-03GC and GS08-155-47GC targeted the shallowest seismic reflections of the seismo-stratigraphic framework.

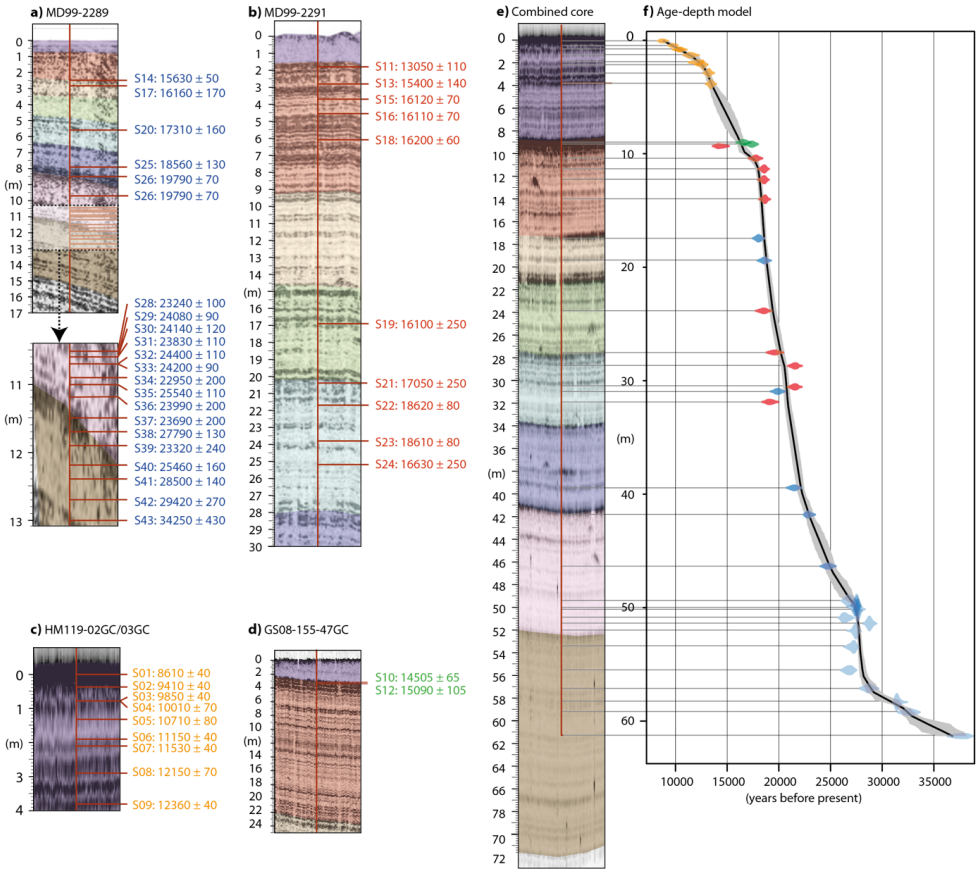

Fig. 7 - a-d) Echosounder profiles showing the locations of radiocarbon dates from the different sediment cores. The intervals of the seismo-stratigraphic framework are coloured. e) Locations of the radiocarbon dates in the combined core. f) Age-depth model from the combined core (calibrated ages) with the 2 sigma standard deviation in grey.

The analysis of the seismo-stratigraphy of the modelled area suggests that the shape of the sedimentation curve is approximately constant throughout the study area and only the magnitude of sedimentation varies depending on the proximity to the depositional centres. This implies that the relative depth of a specific date within an interval of the stratigraphic framework at its coring location should be approximately constant within the stratigraphic framework. Therefore, we transferred the depth from cores MD99-

2289, MD99-2291, HM119-03GC and GS08-155-47GC, to the coring location of HM119-03GC with the following equation:

$depth_k^0 = top_i^0 + \frac{top_i^j - depth_k^j}{base_i^j - top_i^j} \times (base_i^0 - top_i^0)$, whereas $depth_k^0$ is the transferred depth of sample k from core site j, which lies in coring depth $depth_k^j$ within the stratigraphic interval i. The radiocarbon ages including their measurement errors and their transferred depth within the virtual core were the input for the Bayesian statistics based age-depth modelling script Bacon[54], which provided a high-resolution age-depth model for the Nyegga pockmark field (Fig. 3d; Fig. 7). The cores MD99-2289, MD99-2291 and GS08-155-47GC provide overlapping age-depth information for the section between 8 and 33 m of the combined core (7f). The age-depth information from MD99-2289 and MD99-2291 reveal very similar sedimentation rates. The age depth information provided by GS08-155-47GC is in good agreement with the trend from MD99-2289 and MD99-2291. The shallow-most radiocarbon age from MD99-2291 is about 1500 years younger than the shallow-most radiocarbon age from GS08-155-47GC. However, the Bayesian age-depth modelling prefers the age-depth information from GS08-155-47GC leading to a smoother sedimentation curve than following the shallow-most radiocarbon age from MD99-2291. The “too young” radiocarbon age of the shallow-most radiocarbon age from MD99-2291 is most likely the result of reworking as the sample was taken directly below an erosional surface (between purple and red intervals in 7b).

Table 1 –Radiocarbon dated samples used for the age-depth model and sedimentation history reconstruction. Radiocarbon ages are not corrected for reservoir effect.

ID	Sample name	Core name	Sample depth (cm)	Combined core depth (cm)	Radio-carbon age (a)	St. dv. (a)	Reference
S01	Beta-226957	HM119-02GC	6.5	5	8610	40	this study
S02	Beta-226958	HM119-02GC	54	45	9410	40	this study
S03	Beta-226959	HM119-02GC	95	80	9850	40	this study
S04	Beta-229428	HM119-03GC	13.25	83	10010	70	this study
S05	Beta-229429	HM119-02GC	155.5	131	10710	80	this study
S06	Beta-226960	HM119-03GC	146	195	11150	40	this study
S07	Beta-226961	HM119-03GC	170.25	215	11530	40	this study
S08	Beta-229427	HM119-03GC	256.5	288	12150	70	this study
S09	Beta-226962	HM119-03GC	372	385	12360	40	this study
S10	ETH-38626	GS08-155-47GC	319	900	14505	65	this study
S11	ETH-25495	MD99-2291	180	932	13050	110	8
S12	ETH-38628	GS08-155-47GC	339	916	15090	105	this study
S13	ETH-25958	MD99-2291	280	1040	15400	140	8
S14	Beta-380040	MD99-2289	249	1745	15630	50	53
S15	Poz-3950	MD99-2291	367	1134	16120	70	8
S16	Poz-3951	MD99-2291	455	1229	16110	70	8
S17	AAR-6235	MD99-2289	285	1941	16160	170	48
S18	Poz-3952	MD99-2291	614.5	1401	16200	60	8
S19	ETH-22959	MD99-2291	1690	2384	16100	250	8
S20	AAR-6236	MD99-2289	563	3094	17310	160	48
S21	ETH-22960	MD99-2291	2040	2751	17050	250	8
S22	Poz-3956	MD99-2291	2168	2869	18620	80	8
S23	Poz-3957	MD99-2291	2375	3055	18610	80	8
S24	ETH-22961	MD99-2291	2523	3187	16630	250	8
S25	ETH-25496	MD99-2289	790	3944	18560	130	48
S26	Beta-380041	MD99-2289	850	4180	19790	70	53
S27	ETH-25497	MD99-2289	970	4635	21370	160	48
S28	Beta-376421	MD99-2289	1050	4938	23240	100	53
S29	Beta-376422	MD99-2289	1060	4976	24080	90	53
S30	Beta-373227	MD99-2289	1063	4987	24140	120	53

S31	Beta-365943	MD99-2289	1065	4995	23830	110	53
S32	Beta-376423	MD99-2289	1070	5014	24400	110	53
S33	Beta-380041	MD99-2289	1073	5025	24200	90	53
S34	ETH-23313	MD99-2289	1090	5090	22950	200	48
S35	Beta-380043	MD99-2289	1103	5139	25540	110	53
S36	ETH-25498	MD99-2289	1120	5204	23990	200	48
S37	ETH-23314	MD99-2289	1150	5346	23690	200	48
S38	Beta-380044	MD99-2289	1172	5459	27790	130	53
S39	ETH-25499	MD99-2289	1189	5551	23320	240	48
S40	ETH-23315	MD99-2289	1220	5711	25460	320	48
S41	Beta-380045	MD99-2289	1243	5832	28500	140	53
S42	ETH-24870	MD99-2289	1260	5921	29420	270	48
S43	ETH-24871	MD99-2289	1300	6132	34250	430	48

4D sedimentation reconstruction

The local age-depth model and the seismo-stratigraphic framework were then integrated into 4D sedimentation history reconstruction. The age-depth-model provided absolute age information for each seismic reflections and the local sedimentation rate evolution. The sedimentation rate constrained by the age-depth model was then adjusted for every location within the seismo-stratigraphic framework by scaling the sedimentation rate for each interval and each location of the seismo-stratigraphic framework with the thickness of that interval at a specific position divided by the thickness of the interval in the combined core. This approach was not possible for the stratigraphic record younger than 16.2 ka BP and for the western-most part of the Nyegga pockmark field, where buried glacigenic debris lobes were deposited in between the laminated sediments.

Analyses of carbonate crusts sampled from Nyegga pockmark area

A carbonate crust sample was collected during a dive on submersible MIR (on board RV Akademik Mstislav Keldysh during GEOMAR cruise 40 in 1998). The sample was analysed for C and O isotope composition by dissolving three finely powdered sub-samples with 100% H_3PO_4 at 72 ºC in the Carbo Kiel IV preparation line and thereby releasing CO_2, which was isotopically analysed using a Finnigan MAT 253 mass spectrometer. $^{18}O/^{16}O$ and $^{13}C/^{12}C$ ratios were determined against a working calcite standard and are expressed in the common δ-notation relative to Vienna Pee Dee Belemnite (VPDB). The uncertainty of this sample set accompanying standard measurements (n = 8) was 0.16‰ (2σ) for $\delta^{18}O$ and 0.04‰ (2σ) for $\delta^{13}C$. Table 2 shows the results with their individual measurement uncertainties on 2SD level. No further corrections for different acid fractionation factors of calcite and dolomite were applied. Mineral composition of fine-grained carbonaceous material was determined by using x-ray diffraction analysis (Philips PW 1820, Co-K ✔, 0.02°/s). X-ray diffraction patterns were interpreted by using the XPowder® software. Identified carbonate minerals (i.e. calcite and dolomite) were quantified by Rietveld refinement.

Table 2: Mineralogical and geochemical characterisation of carbonate concretion

ID	Dissolvable fraction[1] (wt.%)	Calcite/dolomite ratio[2]	$\delta^{13}C_{bulk}$ (‰ VPDB)	2SD (‰ VPDB)	$\delta^{18}O_{bulk}$ (‰ VPDB)	2SD (‰ VPDB)
Mie1-3729-1	33	1.32	-0.44	0.04	0.91	0.18
Mie1-3729-2	46	0.46	-5.22	0.07	-0.67	0.07
Mie1-3729-3	38	0.54	-3.84	0.08	-0.74	0.10

[1]dissolved by 2.25 N HNO3

[2]XRD detection

In addition, we applied U-Th geochronology methods for methane-derived authigenic carbonates to constrain the precipitation age of the carbonates[55, 56]. However, the analysis indicated different formation ages for the calcitic and dolomitic dominated subsamples of the same carbonate sample. A too high contribution of detrital Th in both carbonate phases prevented deducing reasonable isochron-based age information. The finding of different formation ages for the different carbonate phases is in agreement with the light stable isotope findings. The ^{14}C data from the carbonate crust sample Mie 1-3729-1 represent a rather robust maximum formation age of 18,000 years BP (15,710 ^{14}C). This maximum age interpretation is based on the assumption that any carbon contributed from the sediment system below would be relatively depleted in ^{14}C by ongoing decay during burial, resulting in apparent higher ages.

Finite difference temperature modelling

The temperature profile modelling builds on Fourier's law for heat flow and the assuming homogenous thermal properties of the deposited glacigenic sediments, which allows using the thermal diffusivity κ (4.2 x 10^{-7} m^2/s; ref. 2) for calculating the heat flow: $q = \kappa \nabla T$. We transferred this simple differential equation in a 1D finite difference algorithm:

$T_i^{n+1} = \frac{\kappa \Delta t}{\Delta x^2}(T_{i+1}^n - 2T_i^n + T_{i-1}^n) + T_i^n$, whereas Δt is the temporal discretization of 1 second and Δs the spatial discretization of 0.1 meter. The simulation started with equilibrium temperature profile with a length of 300 m following the local temperature gradient of 55 ºC/km (ref. 2). This profile was then extended at the top by the amount of sediments deposited within a time step of 200 years according to the 4D sedimentation history reconstruction. The sediments had the bottom water temperature of -1ºC, which was also used as boundary condition, the lower boundary was defined as a gradient and the heat flow adjustment was simulated over 200 years using an implicit approximation. The resulting temperature profile was then the starting model for the following time step.

Gas hydrate stability calculation

The gas hydrate stability calculations followed the approach by Tishchenko[23], which build on thermodynamic stability and solubility calculation for methane hydrates. The dissociation temperature for specific depths below sea floor z is calculated following the empirical function: $T_{diss}(z) = a + b * \log(P(z)) + c*(d-\log(P(z)))^3$, whereas T_{diss} is the dissociation temperature, P is the hydrostatic pressure and a, b, c, d are empiric parameters calculated by fitting the stability curve of methane hydrates for a given salinity of 3.5% and pure methane (a = -25.1391, b = 7.9832, C = -0.0959 and d = 6.0687). The hydrostatic pressure at the sea floor and within the top 300 m within the sediments for a given point at a given time was calculated analytically by implementing the sea level fluctuation, subsidence and the sedimentation reconstruction. The T_{diss} profile was then compared with the temperature profile from the finite difference heat flow simulations to determine the BGHSZ, which is defined by the shallowest depth in the modelled temperature is higher than T_{diss}.

Sensitivity analysis

In order to test the robustness of our simulations, we performed sensitivity analyses for different sedimentation rates, bottom water temperature profiles, the subsidence rates affecting the local sea level curve, bulk thermal conductivity values and the geothermal gradients (Fig. 8; the input parameter and simulations results used in the main part of the manuscript are marked with dashed black lines). We tested the impact of bottom water temperature on the gas hydrate dynamics by applying different temperature evolution profiles. These simulations included scenarios with constant temperatures of -1°C (dashed black line in Fig. 8a) and -2°C (yellow line) and repeatedly fluctuating temperatures between -1.75 and -2.25°C (orange line). These input parameters result in very similar curves for the dissociation rate of gas hydrates. In addition, we performed simulations with four potential warming scenarios with an absolute warming of ~0.5 °C (green line) and ~1°C (red, light blue and dark blue). All simulations result in similar shaped gas hydrate dissociation curves with a peak of dissociation after 18,000 years before present. The absolute thickness of gas hydrate dissociation at the end of the simulations lies between 35 and 47 m, which shows that bottom water temperatures had only a secondary impact on gas hydrate dynamic during the LGM at Nyegga. The solution space of the Bayesian age-depth reconstruction allows different sedimentation rate reconstructions (Fig. 8b). In addition to the statistically most likely reconstruction (dashed black line), we tested the sedimentation rate reconstructions, which bound the solution space (blue and yellow lines; marked in grey in Fig. 7f). These sedimentation rate reconstructions result in very similar gas hydrate dissociation rates and absolute dissociation curves.

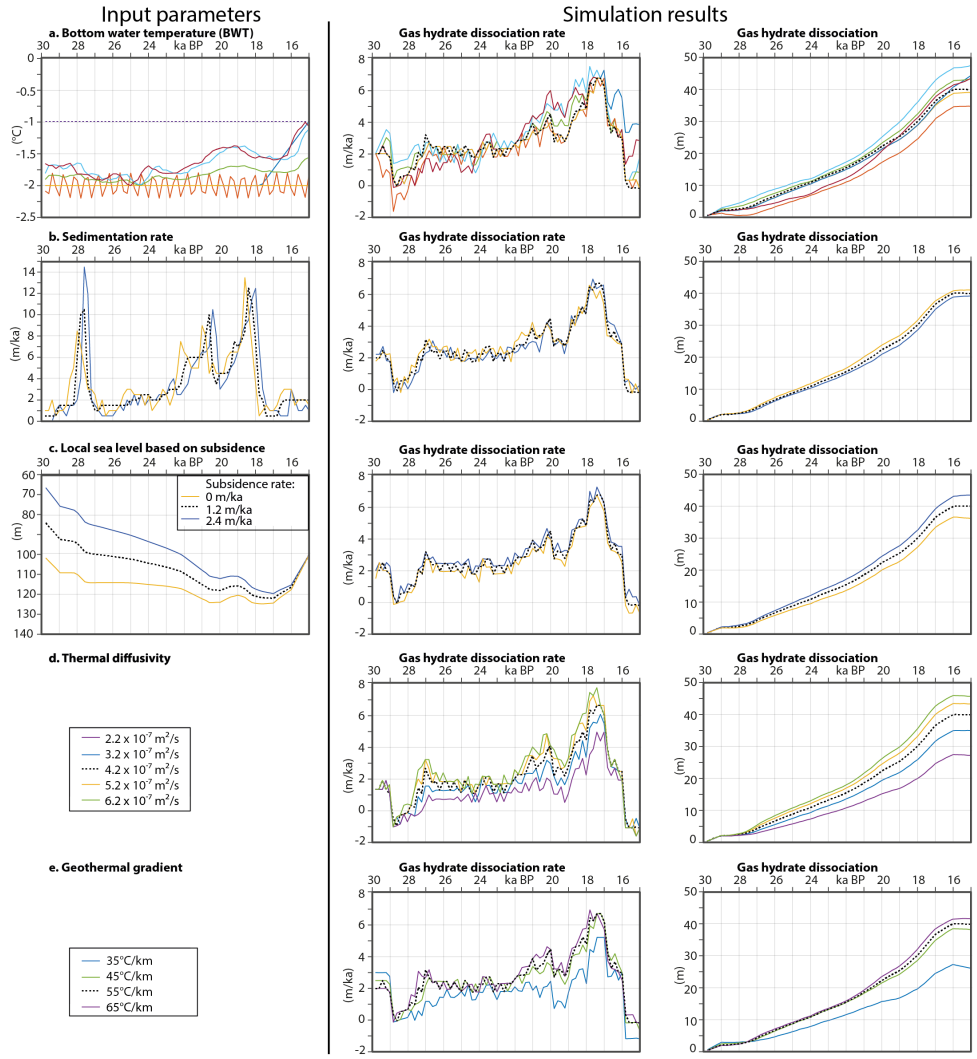

Fig. 8 – Results of the sensitivity analyses showing simulation *results of the individual input parameter test runs: a) Bottom water temperature profiles. b) Sedimentation rates: minimum, maximum and best-fit sedimentation rate reconstructions. c) Subsidence rate and their impact on the local sea level anomaly. d) Thermal diffusivity. e) Geothermal gradient.*

The analysis of different local subsidence rate (Fig. 8c), which influence the local sea level curve reveals that subsidence had only a minor impact on gas hydrate dynamics,

even when neglecting subsidence (yellow line) or assuming a twice as high subsidence rate (blue line). The analyses of the thermal diffusivity of the sediments and the geothermal gradients reveal that the effect of sedimentation on gas high dynamics becomes more important for sediments with a high thermal diffusivity and in areas with high geothermal gradients (Fig. 8d and e). However, the timing of enhanced gas hydrate dissociation remains stable for various thermal property values. The sensitivity analysis revealed that the gas hydrate dissociation rate and the absolute value of dissociated gas hydrates are robust and the observed gas hydrate dynamics can be observed using a wide range of parameters.

Seepage potential calculation

The seepage potential can be calculated by multiplying the average thickness of dissociated gas hydrates (40 m from our simulations) with the area of gas hydrate occurrence A (model area: 540 km²), the gas hydrate concentration (3 – 12%, ref. 39), the sediment porosity Φ (0.38 – 0.76, ref 57), the gas hydrate expansion factor under atmospheric pressure conditions (164, ref. 38) and the density of methane under atmospheric conditions $\rho_{CH4\_atmospheric}$ (~ 0.656 kg/m^3):

$SP = H_{hydrate} * A * s_{hydrate} * \Phi * 164 * \rho_{CH4\_atmospheric}$

The resulting seepage potential for the modelled area lies between 26 and 212 Mt.

Data availability statement

The datasets analysed during the current study are available from the corresponding author on reasonable request.

References

1. Berndt, C., Feseker, T., Treude, T., Krastel, S., Liebetrau, V., Niemann, H., et al. Temporal constraints on hydrate-controlled methane seepage off Svalbard. Science, 343(6168), 284–287 (2014).

2. Mienert, J., Vanneste, M., Bünz, S., Andreasen, K., Haflidason, H., Sjerup, H. P. Ocean warming and gas hydrate stability on the mid-Norwegian margin at the Storegga Slide. Marine and Petroleum Geology 22, 233–244 (2005).

3. Falkowski, P., et al. The Global Carbon Cycle: A Test of Our Knowledge of Earth as a System. Science, 290, 291-296 (2000).

4. Sloan, E. D. Fundamental principles and applications of natural gas hydrates. Nature 426, 353–363 (2003).

5. Nimblett, J. & Ruppel, C. Permeability evolution during the formation of gas hydrates in marine sediments. Journal of Geophysical Research: Solid Earth 108(B9), 2420 (2003).

6. Clayton, C. J. & Hay, S. J. Gas migration mechanisms from accumulation to surface. Bulletin of the Geological Society of Denmark, Vol. 41, pp. 12-23. (1994).

7. Judd, A., Hovland, M. Seabed fluid flow: the impact on geology, biology and the marine environment. Cambridge University Press, pp. 475 (2007).

8. Lekens, W. A. H., Sejrup, H. P., Haflidason, H., Petersen, G. Ø., Hjelstuen, B., Knorr, G. Laminated sediments preceding Heinrich event 1 in the Northern North Sea and Southern Norwegian Sea: Origin, processes and regional linkage. Marine Geology 216, 27-50 (2005).

9. Hjelstuen, B. O., Haflidason, H., Sejrup, H. P. & Nygård, A. Sedimentary and structural control on pockmark development—evidence from the Nyegga pockmark field, NW European margin. Geo-Marine Letters 30, 221–230 (2009).

10. Bünz, S., Mienert, J. & Berndt, C. Geological controls on the Storegga gas-hydrate system of the mid-Norwegian continental margin. Earth and Planetary Science Letters 209, 291–307 (2003).

11. Hovland, M. et al. Complex pockmarks with carbonate-ridges off mid-Norway: Products of sediment degassing. Marine Geology 218, 191–206 (2005).

12. Kvenvolden, K.A. Gas hydrates— geological perspective and global change. Rev. Geophys. 31, 173–187 (1993).

13. Haacke, R.R., Westbrook, G.K., Hyndman, R. Gas hydrate, fluid flow and free gas: Formation of the bottom-simulating reflector. Earth and Planetary Science Letters 261, 407–420 (2007).

14. Bauch, H. A., Erlenkeuser, H., Spielhagen, R. F., Struck, U., Matthiessen, J., Thiede, J. & Heinemeier, J. A multiproxy reconstruction of the evolution of deep and surface waters in the subarctic Nordic seas over the last 30,000 yr. Quaternary Science Reviews 20, 659-678(2001).

15. Lambeck, K., Rouby, H., Purcell, A., Sun, Y. & Sambridge, M. Sea level and global ice volumes from the Last Glacial Maximum to the Holocene. Proceedings of the National Academy of Sciences 111, 15296-15303 (2014).

16. Dahlgren, K. I. T., Vorren, T. O. & Laberg, J.-S. Late Quaternary glacial development of the mid-Norwegian margin—65 to 68°N. Marine and Petroleum Geology 19, 1089-1113 (2002).

17. Dokken, T. M. & Jansen, E. Rapid changes in the mechanism of ocean convection during the last glacial period. Nature 401, 458-461 (1999).

18. Stanford, J.D. , Rohling, E.J. , Bacon, S. , Roberts, A.P., Grousset, F.E., Bolshaw, M. A new concept for the paleoceanographic evolution of Heinrich event 1 in the North Atlantic, Quaternary Science Reviews, Volume 30, Issue 9, 1047-1066 (2011).

19. Ezat, M.M., Rasmussen, T.L., Groeneveld, J. Persistent intermediate water warming during cold stadials in the southeastern Nordic seas during the past 65 k.y. Geology 42, 8, 663 – 666 (2014).

20. Haflidason, H., Sejrup, H.P., Klitgaard Kristensen, D., Johnsen, S. Coupled response of the late glacial climatic shifts of northwest Europe reflected in Greenland ice cores: Evidence from the northern North Sea. Geology 23, 12, 1059-1062 (1995).

21. Eldevik, T. et al. A brief history of climate – the northern seas from the Last Glacial Maximum to global warming. Quaternary Science Reviews 106, 225-246 (2014).

22. Klitgaard-Kristensen, D., Sejrup, H. P., Haflidason, H. The last 18 kyr fluctuations in Norwegian Sea surface conditions and implications for the magnitude of climatic change: Evidence from the North Sea. Paleoceanography, Vol 16, No 5, 455-467 (2001).

23. Tishchenko, P., Hensen, C., Wallmann, K., Wong. C.S. Calculation of the stability and solubility of methane hydrate in seawater. Chemical Geology 219, 37-52 (2005).

24. Collett, T. S., Johnson, A. H., Knapp, C. C., Boswell, R. Natural gas hydrates—Energy resource potential and associated geologic hazards: AAPG Memoir 89, 146 – 219 (2009).

25. Hughes, A. L. C., Gyllencreutz, R., Lohne, Ø. S., Mangerud, J., Svendsen, J.-I. The last Eurasian ice sheets - a chronological database and time-slice reconstruction, DATED-1. Boreas 45, 1 (2015).

26. Ehlers, J., P.L. Gibbard, and P.D. Hughes, eds. Quaternary Glaciations - Extent and chronology: A closer look. Developments in Quaternary Science, Vol. 15, pp. 1126 (2011).

27. Stokes, C.R. and C.D. Clark, Palaeo-ice streams. Quaternary Science Reviews, 20, 1437-1457 (2001).

28. Plaza-Faverola, A., Bünz, S., Mienert, J. Repeated fluid expulsion through sub-seabed chimneys offshore Norway in response to glacial cycles. Earth and Planetary Science Letters 305, 297-308 (2011).

29. Krylova, E.M., Gebruk, A. V., Portnova, D.A., Todt, C., Haflidason, H. New species of the genus Isorropodon (Bivalvia: Vesicomyidae: Pliocardiinae) from cold methane seeps at Nyegga (Norwegian Sea, Vøring Plateau, Storrega slide). Journal of the Marine Biological Association of the United Kingdom, 1-10 (2011).

30. Chen, Y., Bian, Y., Haflidason, H., Matsumoto, R. Present and past methane seepage in pockmark CN03, Nyegga, offshore mid-Norway. Proceedings of the 7th International Conference on Gas Hydrates (ICGH 2011), Edinburgh, Scotland, United Kingdom, 1-10 (2011).

31. Paull, C. K. et al. Origin of pockmarks and chimney structures on the flanks of the Storegga Slide, offshore Norway. Geo-Marine Letters 28, 43–51 (2008).

32. Mazzini, A., Svensen, H., Hovland, M. & Planke, S. Comparison and implications from strikingly different authigenic carbonates in a Nyegga complex pockmark, G11, Norwegian Sea. Marine Geology 231, 89–102 (2006).

33. Schmidt, M., Botz , R., Winn , K., Stoffers , P., Thiessen , O., Herzig, P. Seeping hydrocarbons and related carbonate mineralisations in sediments south of Lihir Island (New Ireland fore arc basin, Papua New Guinea). Chemical Geology, 186 (3/4), 249-264 (2002).

34. Panieri, G., C., Graves, A. , James, R. H. Paleo-methane emissions recorded in foraminifera near the landward limit of the gas hydrate stability zone offshore western Svalbard. Geochem. Geophys. Geosyst. 17, 521–537 (2016).

35. Sheppard, S.M.F. and Schwarcz, H.P. Fractionation of carbon and oxygen isotopes and magnesium between coexisting metamorphic calcite and dolomite. Contr. Mineral. and Petrol. 26, 161-198 (1970).

36. Harrington, J. F., Noy, D. J., Horseman, S. T. & Birchall, D. J. & Chadwick, R.A. Laboratory study of gas and water flow in the Nordland Shale, Sleipner, North Sea. in Grobe, MPashin, ., J. C. & Dodge, R. L., eds., Carbon dioxide sequestration in geological media-State of the science: AAPG Studies in Geology 59, 521-543 (2009).

37. Pieperbeck, N., Kleinrahm, R., Wagner, W., Jaeschke, M. Results of (pressure, density, temperature) measurements on methane and on nitrogen in the temperature range from 273.15 K to 323.15 K at pressures up to 12 MPa using a new apparatus for accurate gas-density measurements. The Journal of Chemical Thermodynamics, Vol 23, Issue 2, February 1991, 175-194 (1991).

38. Sloan E. D. Clathrate Hydrates of Natural Gases, Second Edition, Revised and Expanded, CRC Press, pp. 705 (1998).

39. Bünz, S., Mienert, J., Vanneste, M. & Andreassen, K. Gas hydrates at the Storegga Slide: Constraints from an analysis of multicomponent, wide-angle seismic data. Geophysics 70, B19–B34 (2005).

40. Bünz. S., Mienert, J., Berndt, C. Geological controls on the Storegga gas-hydrate system of the mid-Norwegian continental margin. Earth and Planetary Science Letters 209, 291-307 (2003).

41. Attias, E., Weitemeyer, K., Minshull, T. A., Best, A. I., Sinha, M., Jegen-Kulcsar, M., Höz, S., Berndt, C. Controlled-source electromagnetic and seismic delineation of subseafloor fluid flow structures in a gas hydrate province, offshore Norway. Geophys J Int 206(2), 1093-1110 (2016).

42. Xu, W. & Germanovich, L. N. Excess pore pressure resulting from methane hydrate dissociation in marine sediments: A theoretical approach. Journal of Geophysical Research 111, B01104 (2006).

43. McGinnis, D. F., Greinert, J., Artemov, Y. S., Beaubien, E., Wüest, A. Fate of rising methane bubbles in stratified waters: How much methane reaches the atmosphere? Journal of Geophysical Research, Vol. 111, C09007 (2006).

44. Blunier, T., Chappellaz, J., Schwander, J. & Stauffer, B. Variations in atmospheric methane concentration during the Holocene epoch. Nature 374, 46-49 (1995).

45. Maslin, M., Owen, M., Day, S.,Long, D. Linking continental-slope failures and climate change: Testing the clathrate gun hypothesis. Geology 32, 53-56 (2004).

46. Urlaub, M., Talling, P.J., Masson, D.G. Timing and frequency of large submarine landslides: implications for understanding triggers and future geohazards. Quaternary Science Reviews 72, 63-82 (2013).

47. Mau, S., Römer, M., Torres, M.E., Bussmann, I., Pape, T., Damm, E., Geprägs, P., Wintersteller, P., Hsu, C.-w., Loher, M., Bohrmann, G. Widespread methane seepage along the continental margin off Svalbard - from Bjørnøya to Kongsfjorden. Scientific Reports 7, Article number: 42997 (2017).

48. Reiche, S., Hjelstuen, B. O. & Haflidason, H. High-resolution seismic stratigraphy, sedimentary processes and the origin of seabed cracks and pockmarks at Nyegga, mid-Norwegian margin. Marine Geology 284, 28–39 (2011).

49. Reimer, P. J.,Bard, E., Bayliss, A., Beck, J. W. IntCal13 and Marine13 radiocarbon age calibration curves 0–50,000 year Cal BP. Radiocarbon, 55, 1869–1887 (2013).

50. Francke, J., Paul, A., Schulz, M. Modeling variations of marine reservoir ages during the last 45000 years. Clim. Past, 4, 125–136, (2008).

51. Bondevik, S., Mangerud, J., Birks, H. H., Gulliksen, S., Reimer, P. Changes in North Atlantic Radiocarbon Reservoir Ages During the Allerød and Younger Dryas. Science 09, Vol 312, Issue 5779, 1514-1417 (2006).

52. Stuiver, M., Reimer, P. J., Braziunas, F. High-precision radiocarbon age calibration for terrestrial and marine samples. Radiocarbon, Vol. 40, No. 3, 1127-1151 (1998).

53. Becker, L.W.M., Sejrup, H.P., Hjelstuen, B., Haflidason, H. and Dokken, M., accepted. Ocean-ice sheet interaction along the SE Nordic Seas margin from 35 - 15 ka BP. Mar. Geol. (GLANAM Special Issue).

54. Blaauw, M., Christen, J. A. Flexible Paleoclimate Age-Depth Models Using an Autoregressive Gamma Process. Bayesian Analysis 6, Number 3, 457-474 (2011).

55. Bayon, G.; Henderson, GM; Bohn, M. U-Th stratigraphy of a cold seep carbonate crust, Chemical Geology, 2 60, 1, 47-56 (2009).

56. Liebetrau, V., Augustin, N., Kutterolf, S., Schmidt, M., Eisenhauer, A., Garbe-Schönberg, D., Weinrebe, W. Cold-seep-driven carbonate deposits at the Central American forearc: contrasting evolution and timing in escarpment and mound settings. International Journal of Earth Sciences, Volume 103, Issue 7, pp 1845–1872 (2014).

57. Hustoft, S., Dugan, B., Mienert, J. Effects of rapid sedimentation on developing the Nyegga pockmark field: Constraints from hydrological modeling and 3-D seismic data, offshore mid-Norway. Geochemistry, Geophysics, Geosystems, Vol 10, 6, 1-17 (2009).

Acknowledgements

The research leading to these results has received funding from the People Programme (Marie Curie Actions) of the European Union's Seventh Framework Programme FP7/2007-2013/ under REA grant agreement n° 317217. The research forms part of the GLANAM (GLAciated North Atlantic Margins) Initial Training Network. We would like to thank the Department of Earth Science of the University of Bergen for providing funding for publishing this manuscript. S.P. acknowledges the support from the Research Council of Norway through its Center of Excellence funding scheme, project 223272 (CEED). We would like to thank W. Wood and to anonymous reviewers for improving the quality of the manuscript with their comments.

Author contributions

J.K., H.H., C.B., S.P. designed the study and wrote the manuscript. L.B. and J.K. compiled the sediment history reconstruction and J.K. and L.R. performed heat flow and gas hydrate stability simulations. V.L. and M.S. carried out the analysis of a sea floor sediment samples collected by J.M. H.H. collected and analysed sediment cores. All authors helped editing the manuscript.

Competing financial interests

The authors declare no competing financial interests.

Holocene primary productivity fluctuations in the SE Nordic Seas

Lukas W. M. Becker, Hans Petter Sejrup, Berit O. Hjelstuen,
Haflidi Haflidason, Heidi Kjennbakken, Johannes Werner

To be submitted to Paleoceanography

V

Graphic design: Communication Division, UiB / Print: Skipnes Kommunikasjon AS

uib.no

ISBN: 978-82-308-3789-4